Materials Science & Engineering R 171 (2026) 101248

Contents lists available at ScienceDirect

Materials Science & Engineering R

journal homepage: www.elsevier.com/locate/mser

Advancing MOFs for electrocatalytic ORR, UOR, and CO_2RR: From fundamentals to device integration and deployment challenges

Sheraz Muhammad [a], Hao Sun [b], Sana Zahoor [a], Sumayya Khan [a], Rahmat Ullah [a], Biao Fu [a], Sana Ullah [c], Tayirjan Taylor Isimjan [d,*], Shohreh Azizi [e,*], Xiulin Yang [a,*]

[a] Guangxi Key Laboratory of Low Carbon Energy Materials, School of Chemistry and Pharmaceutical Sciences, Guangxi Normal University, Guilin 541004, China
[b] Wolfson Institute for Biomedical Research, UCL Division of Medicine,University College London, Gower St, London WC1E 6BT, United Kingdom
[c] Institute for Advanced Study, Shenzhen University, Shenzhen 518060, China
[d] Saudi Arabia Basic Industries Corporation (SABIC) at King Abdullah University of Science and Technology (KAUST), Thuwal 23955-6900, Saudi Arabia
[e] UNESCO-UNISA Africa Chair in Nanosciences/Nanotechnology, College of Graduate Studies, University of South Africa, Muckleneuk Ridge, Pretoria 0181, South Africa

ARTICLE INFO

Keywords:
Metal organic framework
Oxygen reduction reaction
Urea oxidation reaction
Carbon dioxide reduction reaction and Density functional theory

ABSTRACT

Metal-organic frameworks (MOFs) offer a uniquely tunable platform for electrocatalysis, yet their path from fundamental promise to industrial application remains a critical challenge. This review comprehensively examines the role of MOFs in three pivotal electrochemical reactions: oxygen reduction reaction (ORR), urea oxidation reaction (UOR), and carbon dioxide reduction reaction (CO_2RR). The fundamental mechanisms of these reactions, bolstered by insights from density functional theory (DFT) calculations, are discussed to provide a foundational understanding of the electrocatalytic processes at the molecular level. The review further explores the integration of MOFs into real-world electrochemical devices, including fuel cells, metal-air batteries, urea electrolysis and CO_2 electrolyzers, with an emphasis on their potential for energy production, hydrogen generation, wastewater treatment, and carbon utilization. The challenges of scaling up MOF-based technologies for industrial applications are critically analyzed, covering technoeconomic considerations, sustainability factors, and mitigation strategies such as MOF hybrids, post-synthetic modifications, as well as advanced composite systems such as polyoxometalate@MOF (POM@MOF) and covalent organic framework@MOF (COF@MOF) heterostructures. Finally, this review maps a forward-looking roadmap to address the deployment challenges for MOFs in ORR, UOR, and CO_2RR systems. This integrated perspective underscores the potential of MOFs to bridge the gap from fundamental mechanisms to real-world application, accelerating their role in sustainable electrochemical energy devices.

1. Introduction

The global community stands at a critical juncture in its energy evolution, as global temperatures have already risen by approximately 1.0°C since pre-industrial times. With fossil fuel reserves rapidly depleting and carbon emissions continuing to rise at their current pace, the temperature is expected to increase by 1.5°C between 2030 and 2052 [1–3]. The urgency for sustainable energy solutions has never been greater, as we face mounting pressure on resources and a rapidly changing climate. The growing global population and accelerating industrialization are intensifying pressure on energy resources, creating a widening gap between energy supply and sustainable demand [4,5]. International policy frameworks, such as the Paris Agreement, coupled with national-level climate mandates, have further intensified the pursuit of carbon neutrality [6,7]. However, realizing these ambitious goals requires a transformative shift in how we generate, store, and utilize energy.

In this context, electrochemical reactions have emerged as a cornerstone of the clean energy transition. These reactions underpin a range of key technologies, including fuel cells and metal-air batteries reliant on the ORR for direct electricity conversion, UOR systems for energy-dense fuel cells and simultaneous wastewater remediation, and electrochemical CO_2RR for producing value-added chemicals and fuels [8–12]. Such technologies are uniquely compatible with renewable

* Corresponding authors.
E-mail addresses: isimjant@sabic.com (T.T. Isimjan), azizis@unisa.ac.za (S. Azizi), xlyang@gxnu.edu.cn (X. Yang).

https://doi.org/10.1016/j.mser.2026.101248
Received 28 February 2026; Received in revised form 15 May 2026; Accepted 28 May 2026
Available online 3 June 2026

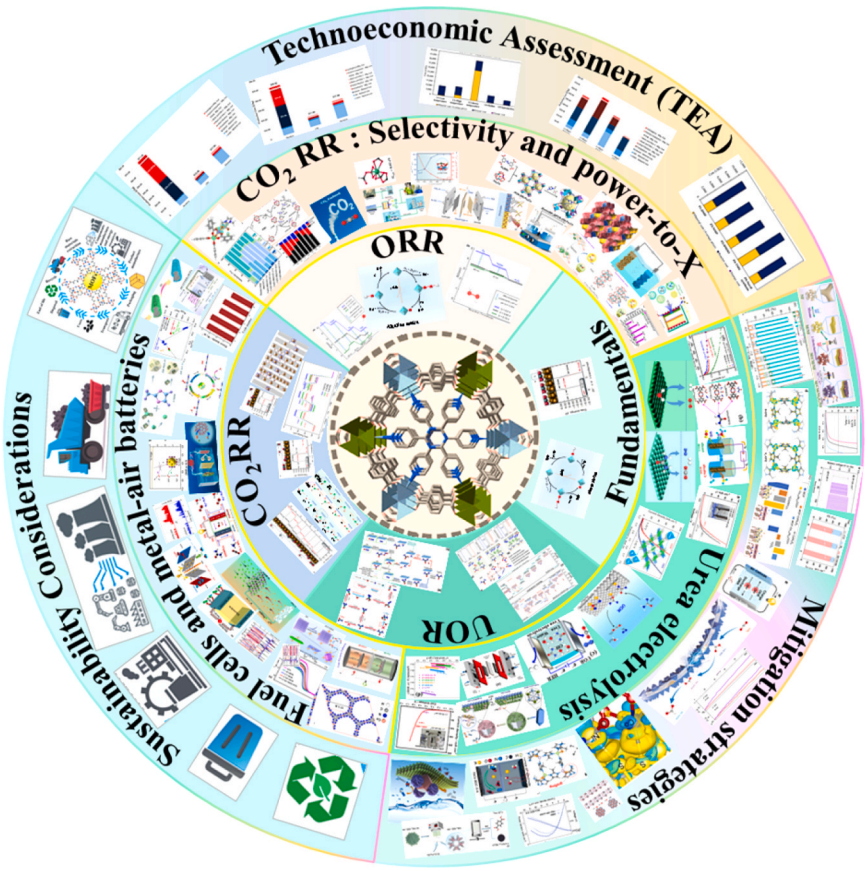

Fig. 1. Main contents of the review.

energy sources like solar and wind, which are characterized by high energy efficiency, scalability, and modularity [13–15]. Therefore, the performance and cost-effectiveness of these electrochemical platforms critically depend on the development of advanced electrocatalysts capable of optimizing these processes. While traditional noble-metal-based catalysts, such as platinum (Pt), ruthenium (Ru), and iridium (Ir), have historically dominated electrocatalysis due to their excellent intrinsic activity and stability, they present significant challenges for large-scale implementation [16–18]. The high cost, scarcity, and poor tunability of these materials hinder their widespread use, particularly in industrial applications. Moreover, these catalysts often exhibit suboptimal selectivity, with performance limited by fundamental scaling relationships among reaction intermediates, preventing the simultaneous optimization of activity, selectivity, and stability a persistent issue in electrocatalysis [19].

To overcome these limitations, researchers have turned to materials that offer greater design flexibility, atomic-level tunability, and abundant elemental composition. Among these, MOFs have emerged as a promising alternative [20,21]. Composed of metal nodes linked by organic ligands into crystalline porous networks, MOFs present a uniquely modular architecture that allows for precise control over structure and properties [22]. Their key advantages include high porosity and surface area for improved reactant accessibility, tunable coordination environments for catalytic metal centers, incorporation of redox-active ligands and metals, and the ability to control defects and structural anisotropy [23–26]. Additionally, MOFs are capable of multi-functionality, acting as catalysts, supports, and sacrificial templates for derived materials, further enhancing their utility in a variety of electrochemical reactions. Furthermore, the ability of MOFs to enable non-traditional catalytic mechanisms such as the single-site activation in CO_2 reduction offers a significant advantage over conventional catalysts [27–32]. These mechanisms can bypass the scaling relationships that limit traditional materials, opening new avenues for designing highly efficient electrocatalysts that could perform better across a range of electrochemical reactions.

The exceptional structural and compositional tunability of MOFs has established them as a transformative platform for a broad spectrum of electrochemical energy conversion and storage reactions. While existing reviews have often focused on singular niches such as pristine MOFs, specific synthesis methods, MOFs-derived, or a single reaction like the ORR, this work provides a unified and systematic examination with an exclusive focus on the integrated trio of ORR, UOR, and CO_2RR [33–39]. Our review uniquely bridges the critical gap between fundamental mechanistic understanding, unlocked by DFT insights, and practical deployment in real-world devices. It offers a detailed progression from catalytic mechanisms to performance in functional systems like fuel cells, urea, and CO_2 electrolyzers, while consolidating a suite of next-generation strategies for scalability and sustainability.

In this review, we provide a comprehensive analysis of MOFs for multi-functional electrocatalysis, integrating foundational mechanistic insights with cutting-edge application engineering. We begin by establishing the fundamental reaction mechanisms and active sites for ORR, UOR, and CO_2RR. The discussion then progresses to the integration of these MOF catalysts within real-world electrochemical devices, critically examining their performance, durability, and efficiency metrics in fuel cells, direct urea fuel cells, metal-air batteries, and CO_2 electrolyzers. A dedicated section tackles the pivotal challenges of commercialization, introducing technoeconomic assessment and life-cycle analysis to evaluate scalability and environmental impact (Fig. 1). Finally, we conclude with a forward-looking perspective that outlines a strategic research roadmap, proposing mitigation strategies through MOF hybrids, post synthetic modifications, POM@MOF, COF@MOF and emerging frontiers like AI-guided discovery and circular MOF design. By systematically traversing the journey from fundamental mechanisms to market-

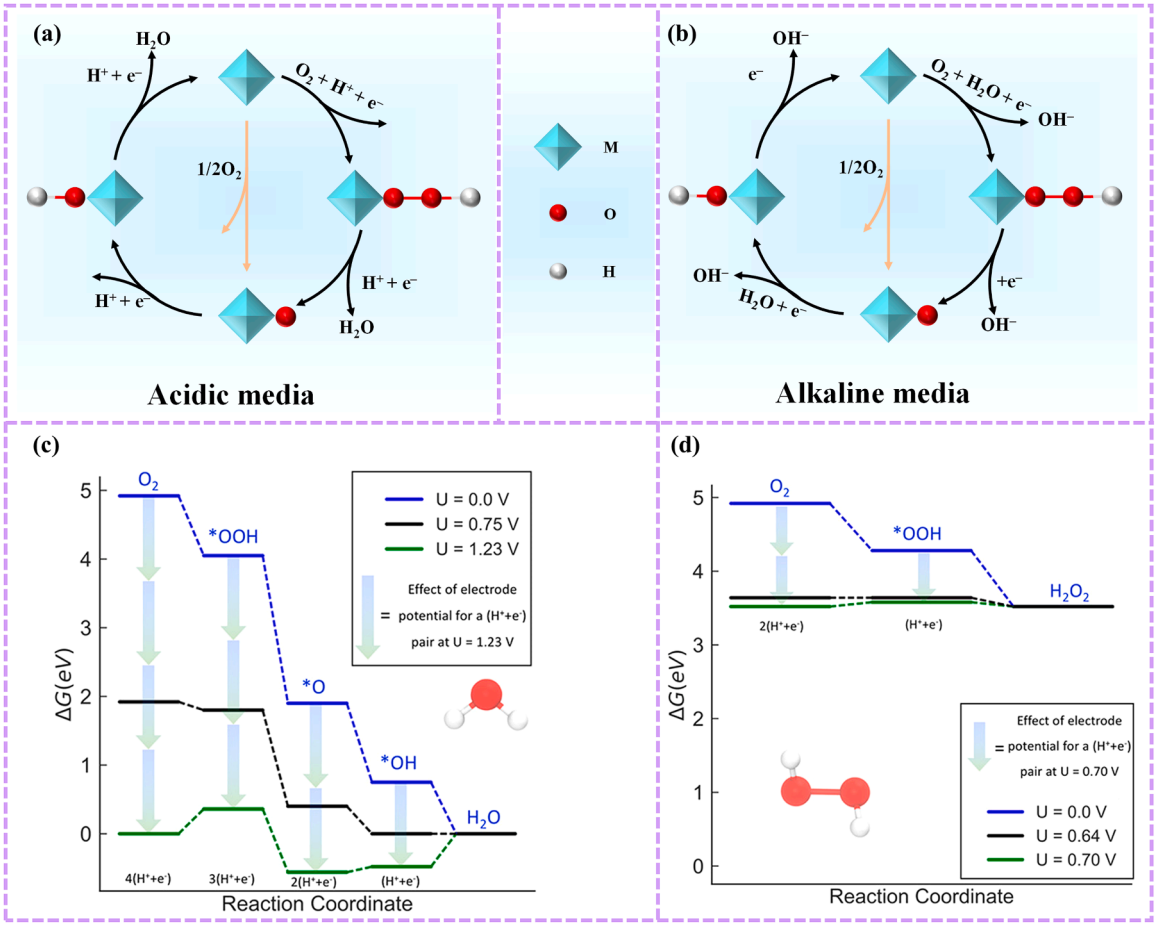

Fig. 2. (a) ORR mechanism in acidic media showing a 4-electron reduction process. (b) ORR mechanism in alkaline media showing a 2-electron reduction process. (c) Free energy diagram for the ORR process in acidic media at different electrode potentials. Reproduced with permission from ref [46]. Copyright 2008 Royal Society of Chemistry. (d) Free energy diagram for the ORR process in alkaline media at different electrode potentials [44,45]. Copyright 2013 Springer Nature and Copyright © 2018. American Chemical Society.

oriented deployment, this review aims to serve as a foundational guide for developing high-performance, commercially viable MOF-based electrochemical systems, thereby accelerating the transition to a sustainable and carbon-neutral energy landscape.

2. Fundamentals of ORR, UOR and CO_2RR

The foundational principles of modern energy conversion lie in understanding electrocatalytic reactions such as the ORR, UOR, and CO_2RR. These reactions involve complex pathways dictated by the catalyst's electronic structure and coordination environment. For instance, the ORR diverges between a 4-electron pathway to water and a less efficient 2-electron pathway to peroxide. Similarly, the UOR involves a complex 6-electron transfer process with challenges in achieving complete oxidation to N_2 and CO_2 while avoiding catalyst poisoning. The CO_2RR, meanwhile, branches into a wide range of C_1 and C_{2+} products. DFT is a critical tool for unraveling this complexity, offering insights into adsorption energies, rate-limiting steps, and electronic descriptors that govern activity and selectivity. Here, we will examine the core mechanisms of the ORR, UOR, and CO_2RR, highlighting how specific catalyst structures facilitate distinct reaction pathways and suppress competing side reactions.

2.1. Oxygen reduction reaction (ORR)

ORR electrocatalysis is a crucial process in various electrochemical applications, where oxygen molecules are reduced to form water or hydroxide ions through electron transfer. The efficiency of ORR is significantly influenced by the catalyst material properties, which affect the reaction kinetics and overall energy efficiency. Effective electrocatalysts improve performance by lowering activation energy and enhancing reaction rates. In this section, we will explore ORR mechanisms in acidic and alkaline media.

The ORR mechanism involves the reduction of oxygen molecules to water or hydroxide ions, typically through either a 4-electron transfer process in acidic media or a 2-electron transfer process in alkaline media, each pathway influencing the reaction's efficiency and the resulting products. In acidic media (Fig. 2a,c), the ORR begins with the adsorption of O_2 onto the catalyst, where it interacts with H^+ and e^-. The oxygen molecule undergoes a 4-electron reduction, where two electrons and two protons are transferred in the first step to form the peroxo intermediate (OOH). In the next step, another two electrons and two protons are transferred, resulting in the formation of H_2O, completing the reaction. This entire process is characterized by the reduction of O_2 to water with a 4-electron transfer [40]. Furthermore, Fig. 2b,d illustrates the ORR in alkaline media, where O_2 is reduced to OH^- on a catalyst surface. Initially, oxygen adsorbs onto the catalyst, interacting with OH^- and e^-. The reaction proceeds with a 2-electron transfer, where oxygen is reduced to a superoxide intermediate (O_2^-). This intermediate then reacts to form OH^- or H_2O. The overall process involves the reduction of oxygen to OH^-, with potential intermediate formation of H_2O_2, depending on the reaction conditions [41–45]. The key difference is that in acidic media, the reaction completes as H_2O, while in alkaline media, OH^- or H_2O_2 are the products, depending on the electron and

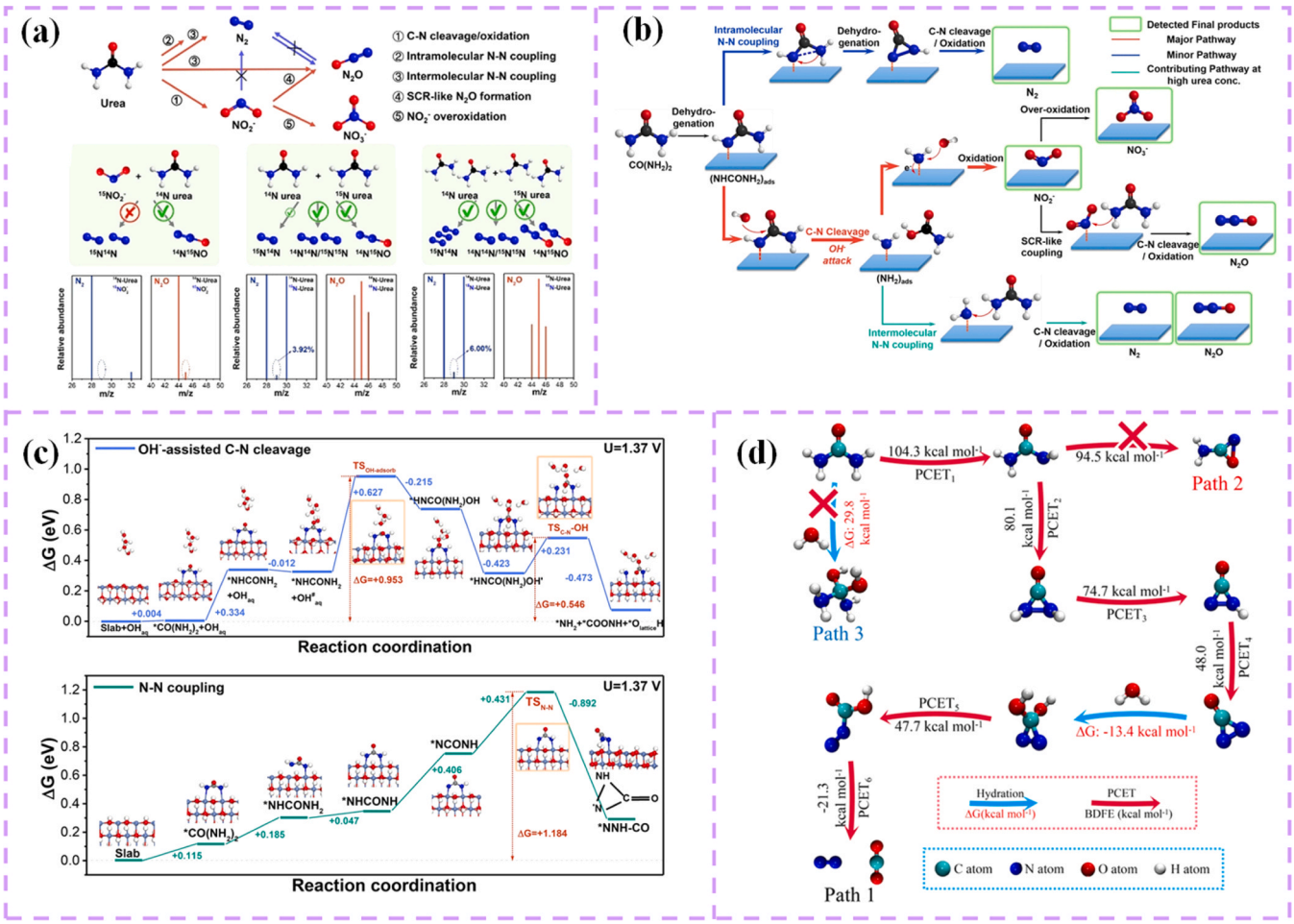

Fig. 3. (a) Schematic representation showing the relationships between N_2, N_2O, NO_2^-, and NO_3^- formed during UOR, along with MS spectra of gaseous products obtained under three conditions: UOR with $^{15}NO_2^-$ pre-added to 0.33 M ^{14}N-urea; a mixture of 0.33 M ^{14}N-urea and ^{15}N-urea in a 1:1 molar ratio; and a mixture of 1.00 M ^{14}N-urea and ^{15}N-urea in a 1:1 molar ratio, all in 1 M KOH. DFT analysis of potential urea dissociation pathways on nickel active sites, including: (b) schematic illustration of possible urea oxidation routes; and (c) intramolecular N-N coupling on NiOOH and OH^--assisted C-N cleavage. Copyright 2021 © Wiley-VCH. (d) Urea dehydrogenative oxidation pathway involving PCET, hydration, and rearrangement steps, as revealed by molecular simulations performed with Gaussian. Copyright 2021 © Wiley-VCH.
(a-c) Reproduced with permission from ref [54]. (d) Reproduced with permission from ref [55].

proton transfer steps.

2.2. Urea oxidation reaction (UOR)

Urea, commonly found in industrial wastewater and toilet waste, is produced in large quantities, with over 2 million tons generated daily by the fertilizer industry, and human urine contributing even more [47]. However, untreated urea-rich wastewater poses environmental and health risks as it can decompose into harmful pollutants like ammonia, nitrites, nitrates, and nitric oxides. Effective treatment methods include biodegradation, enzymolysis, oxidation, adsorption, and catalytic decomposition. Recently, urea-based energy technologies, such as urea oxidation for hydrogen production and direct urea fuel cells, have gained attention [48,49]. The UOR has gained attention as an efficient route for producing hydrogen energy and sustainable nitrogen. Understanding its reaction mechanism is essential. While UOR can occur in acidic, neutral, or alkaline electrolytes, alkaline media offer the best performance based on both products and theoretical potentials [50]. The equilibrium potential for UOR (0.37 V vs. RHE) is far lower than that for water splitting (1.23 V vs. RHE), making it a low-energy alternative for hydrogen generation from wastewater. This not only cuts energy costs but also benefits water treatment [51]. To advance commercialization, researchers are developing low-cost, high-efficiency electrocatalysts, with nickel-based materials being especially promising for alkaline electrooxidation due to their low resistance and high activity.

While great progress has been made in developing low-overpotential UOR electrocatalysts, the detailed transformation of urea molecular structure remains insufficiently explored. Ideally, urea undergoes electrochemical oxidation through a six-electron, six-proton transfer, yielding CO_2, N_2, and H_2O [52,53]. For instance, *Li et al.* revealed that nickel-based catalysts can over-oxidize urea to NO_2^- with high Faradaic efficiency, alongside trace NO_3^- and N_2O. Using ^{15}N isotopes and urea analogues, they mapped a nitrogen-fate network involving an OH^--assisted C-N cleavage pathway leading to NO_2^- formation, along with two N_2-generation routes via intra- and intermolecular coupling. Isotopic labeling further revealed that NO_2^- does not convert to N_2 during UOR, while N_2O can form through a selective catalytic reduction–like process involving urea or its intermediates. Higher urea concentrations promoted intermolecular coupling, increasing cross-labeled N_2 and N_2O formation and reducing NO_2^- yields, highlighting competitive pathways within the nitrogen product network (Fig. 3a). DFT calculations further clarified the reaction network. In Fig. 3b, urea adsorbs onto the NiOOH surface and is oxidized to a $*NHCONH_2$ intermediate, which can follow three routes. The intramolecular N-N coupling pathway involves $*NHCONH_2$ undergoing PCET steps to form *NCONH, followed by N-N

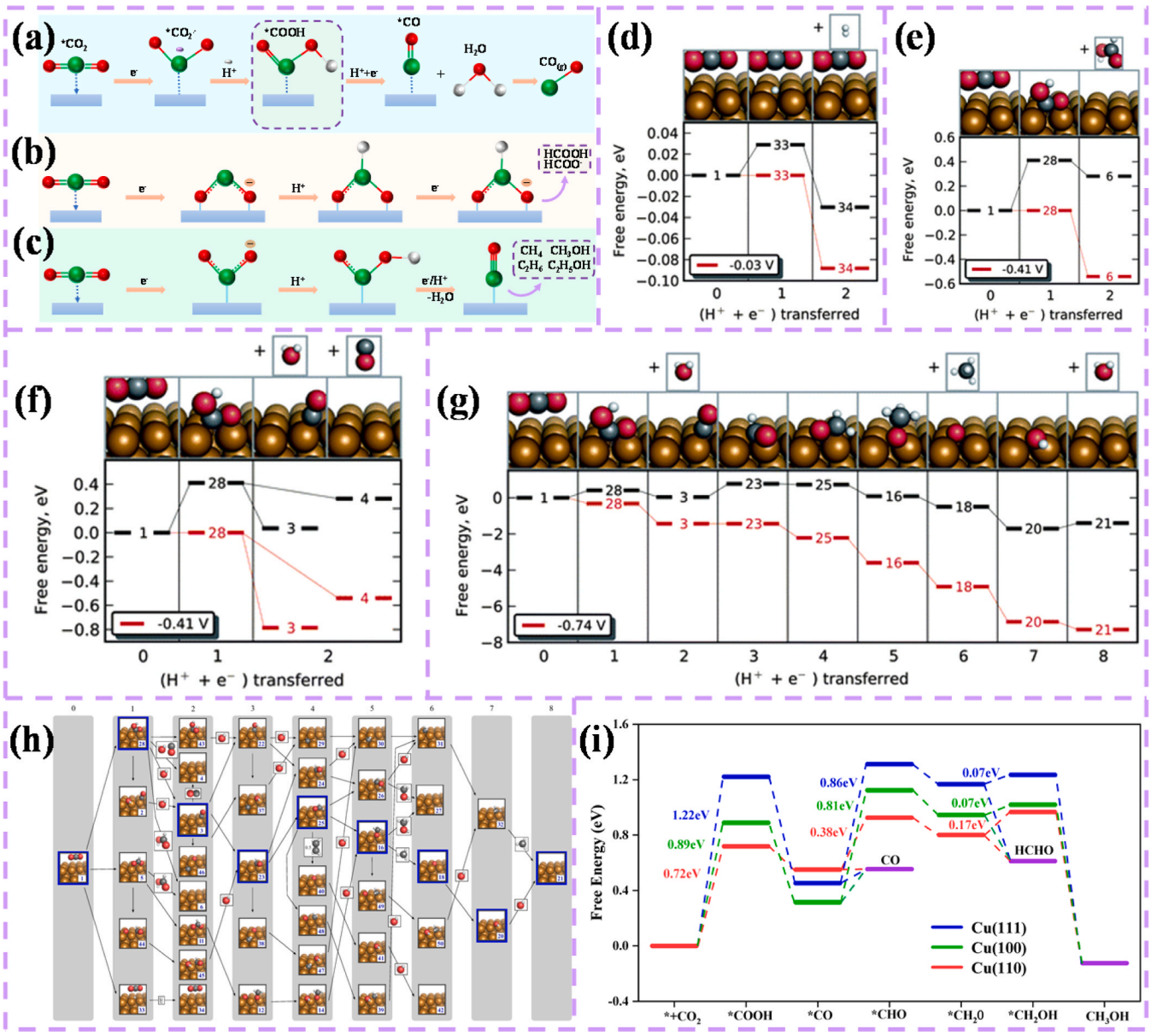

Fig. 4. (a) CO_2 reduction mechanism to CO via *COOH intermediate. (b) CO_2 reduction pathway to formic acid (HCOOH) or formate ($HCOO^-$). (c) CO_2 reduction mechanism to multi-carbon products such as methane (CH_4), methanol (CH_3OH), ethanol (C_2H_5OH) and other. Calculated free-energy profiles for CO_2 electroreduction pathways. (d-g) Show the lowest-energy routes to H_2, HCOOH, CO, and CH_4, respectively. In each case, the black curve (upper) corresponds to the free energy at 0 V vs. RHE, while the red curve (lower) represents the free energy at the applied potential. (h) Lists the numerical labels assigned to each intermediate state. Copyright 2010 Royal Society of Chemistry. (i) Free-energy profiles for CO_2 reduction to CO, formaldehyde (HCHO), and methanol (CH_3OH) on Cu(111), Cu (100), and Cu(110) surfaces, respectively. (Under CC license).
(d-h) Reproduced with permission from ref [76]. (i) Reproduced with permission from ref [77].

bond formation into a cyclic *NNH-CO intermediate. This intermediate is further oxidized to CO_2 and N_2, with an overall energy barrier of 1.184 eV. The direct C-N cleavage pathway proceeds through C-NH_2 bond scission in *$NHCONH_2$, producing *NH_2 and *CONH. The *NH_2 species is then oxidized to NO_2^-. The lowest energy barrier for this route is 1.299 eV. The OH^--assisted C-N cleavage pathway (Fig. 3c) involves OH^- attacking the carbon center of *$NHCONH_2$, breaking the C-NH_2 bond via a 0.953 eV rate-determining step. This is the most favorable route, explaining the experimentally observed dominance of NO_2^- formation (~80% FE). The small energy gap between the OH^--assisted cleavage and N-N coupling pathways allows both N_2 and NO_2^- to form, but cleavage is strongly favored under alkaline conditions. At higher urea concentrations, intermolecular N-N coupling becomes more significant, leading to increased N_2 and N_2O formation and influencing the overall product distribution [54]. Analysis of the liquid by-products showed that urea was not fully converted to N_2, indicating the need for further work on UOR catalysts with higher selectivity. While intramolecular N-N coupling has been observed during Ni^{3+}-driven UOR, this behavior may also arise from reactive species other than NiOOH. To clarify the mechanism, *Chen et al.* investigated nitrogen nucleophilic electrooxidation (NOR) on a β-$Ni(OH)_2$ electrode. Using *in-situ* SERS, quasi-*in-situ* XPS, and potentiostatic measurements under varying conditions (1 M KOH, 1 M KOH + 50 mM urea, and 1 M KOH + 0.5 M urea), they confirmed a two-step UOR pathway: first, β-$Ni(OH)_2$ undergoes electrocatalytic dehydrogenation to β-Ni(OH)O, followed by spontaneous nucleophilic dehydrogenation oxidation back to β-$Ni(OH)_2$. DFT calculations further indicated that after intramolecular N-N coupling, urea most likely proceeds through a spontaneous dehydrogenation

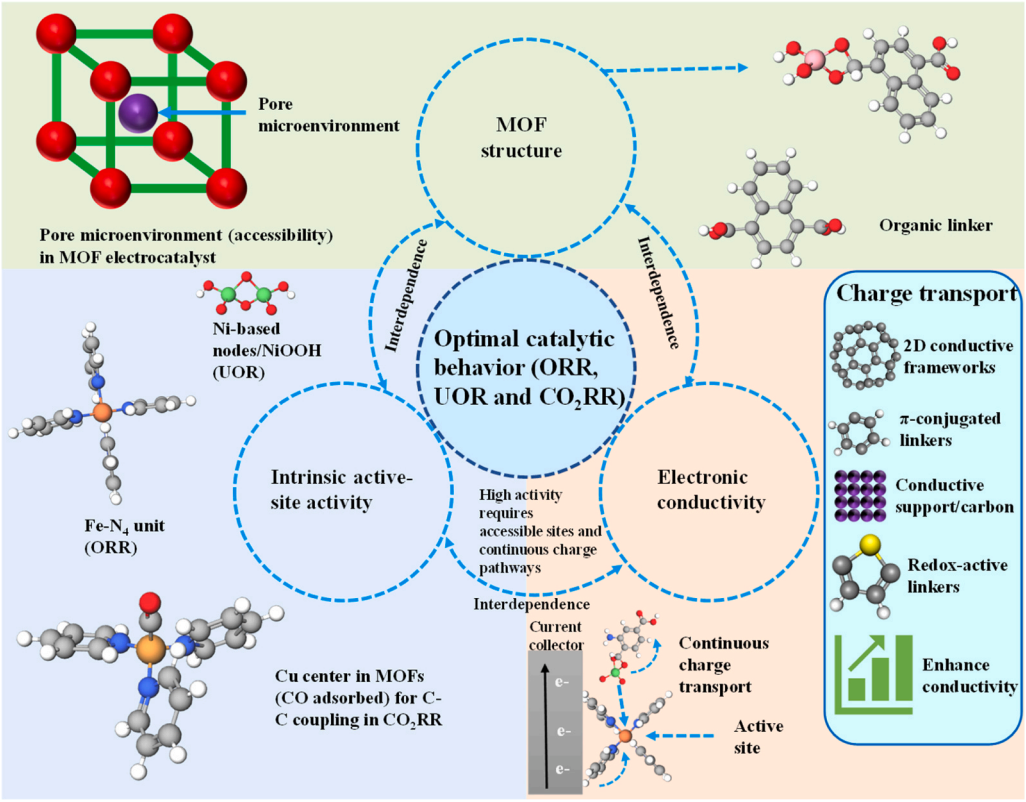

Fig. 5. Schematic illustrating the interplay among MOF structure, intrinsic active-site activity, electronic conductivity, and pore microenvironment in determining electrocatalytic performance for ORR, UOR, and CO_2RR. Key components include metal nodes, charge transport pathways, and the current collector, all converging to optimal catalytic behavior.

oxidation sequence involving PCET, hydration, and structural rearrangement (Fig. 3d) [55]. These results imply that multiple active species may drive N-N coupling, highlighting the need for deeper understanding of the catalyst-product relationship in UOR.

2.3. CO_2 reduction reaction (CO_2RR)

The CO_2RR is a transformative electrochemical process that converts CO_2 into valuable chemical fuels, thus helping to mitigate climate change by recycling CO_2 into sustainable energy sources [56–58]. This reaction typically occurs at the cathode of an electrochemical cell and requires a catalyst to overcome the significant energy barrier associated with CO_2 reduction. CO_2RR is a multi-electron process, and its products can range from carbon monoxide (CO), formate ($HCOO^-$), and methane (CH_4) to methanol (CH_3OH), ethanol (C_2H_5OH), and even higher hydrocarbons like ethylene (C_2H_6) [59]. These products are the result of different reaction pathways that vary based on the catalyst, operating conditions, and reaction kinetics.

The electrochemical reduction of CO_2RR proceeds through various pathways that depend on the catalyst and reaction conditions. The process involves the conversion of CO_2 into different products such as CO, $HCOO^-$, CH_4, CH_3OH, (C_2H_5OH) and other hydrocarbons. As shown in Fig. 4a, the CO_2RR begins with the absorption of a CO_2 molecule onto the cathode surface of the electrode. The absorbed CO_2 molecule is then reduced by an electron, forming a highly energetic $*CO_2^{\bullet-}$ anion radical. This radical reacts with a H^+, resulting in the formation of the *COOH intermediate. The *COOH intermediate then gains another electron and reacts with a proton, leading to the formation of *CO. Finally, *CO desorbs from the electrode surface, releasing CO as the final product [60–62]. This mechanism demonstrates the process of electron and proton transfer in converting CO_2 to CO in electrochemical CO_2 reduction. As shown in Fig. 4b, the electrochemical CO_2RR can also proceed through a pathway that leads to the formation of $HCOO^-$ or HCOOH. In this process, CO_2 is first adsorbed onto the catalyst surface, followed by the reduction of the CO_2 molecule with an electron to form the CO_2^- intermediate. This intermediate then undergoes protonation to form a COOH species, which is further reduced by another electron and proton to produce $HCOO^-$ or HCOOH [63,64]. The reaction occurs via a combination of electron and proton transfer steps, ultimately producing formate or formic acid, a valuable chemical that can be used in various applications. In Fig. 4c, another pathway for CO_2RR leads to the formation of higher-value products such as CH_4, CH_3OH, C_2H_6, and C_2H_5OH. Similar to the previous pathway, CO_2 is first adsorbed onto the catalyst, where it is reduced by electrons to generate a CO_2^- intermediate. This intermediate can undergo multiple electron and proton transfer reactions to form CH_4, CH_3OH, C_2H_6, and C_2H_5OH, depending on the specific conditions and the catalyst used [65–68]. This pathway highlights the potential for CO_2RR to produce a wide range of valuable hydrocarbon fuels and chemicals, which offer sustainable alternatives to fossil-derived products.

Among the various metals studied for CO_2RR, copper stands out as the only catalyst capable of producing significant quantities of multi-carbon (C_{2+}) products in addition to single-carbon compounds such as CO, formate, and methane [69,70]. Its unique catalytic behavior arises from a balanced binding strength for key intermediates, allowing both efficient CO formation and subsequent C-C coupling. The activity and selectivity of copper are highly sensitive to its surface morphology, with low-index facets such as Cu(211) and Cu(110) exhibiting distinct adsorption energies and reaction pathways compared to Cu(100) or stepped surfaces. DFT calculations have been instrumental in elucidating the molecular-level mechanism of CO_2RR on Cu(211) and Cu(110). The studies reveal how the surface facilitates CO_2 activation through the formation of $*CO_2^-$ and *COOH intermediates, the subsequent hydrogenation to *CO, and further proton-electron transfer steps

leading to CH_4, CH_3OH, and C_{2+} products [71–75]. By mapping out free energy diagrams and potential-dependent transition states, DFT analyses not only clarify the rate-determining steps but also provide design principles for tailoring Cu surfaces to enhance activity, suppress competing hydrogen evolution, and improve product selectivity. For instance, *Peterson et al.* used the computational hydrogen electrode (CHE) model to study CO_2 electroreduction on Cu(211), evaluating 41 possible intermediates that could lead to CO, H_2, HCOOH, CH_4, and C_2H_4. The limiting potential was defined as the least negative voltage at which a pathway becomes thermodynamically favorable. While proton electron transfer barriers were assumed to be small, reactions between two adsorbed species such as C-C coupling may involve higher activation energies. As shown in Fig. 4d, the first pathway to open corresponds to H_2 evolution, limited by the adsorption of the first proton. Fig. 4e depicts HCOOH formation through CO_2 protonation to a carboxyl intermediate, requiring −0.41 V. The CO pathway in Fig. 4f follows the same initial step and limiting potential. Hydrocarbon production, including CH_4, begins with hydrogenation of *CO to *CHO at −0.74 V. The lowest-energy CH_4 route in Fig. 4g proceeds via *CHO → H_2CO → $*OCH_3$, with CH_4 released upon protonation of the methyl group, followed by water formation from the remaining oxygen. Experimental studies support these predictions, showing that hydrocarbon generation proceeds through CO while the formate pathway is largely a dead end. The model also explains why electrochemical CO_2 reduction on Cu favors CH_4 over CH_3OH: proton attack from solution on the methyl end of methoxy favors CH_4 formation by 0.27 eV, whereas in gas-phase catalysis, hydrogen addition to the oxygen end enables methanol synthesis. Reaction pathways for CO_2 electroreduction on a Cu(211) surface. The numbers above each section indicate the total proton–electron pairs transferred relative to CO_2. Atoms are color-coded: carbon (gray), oxygen (red), hydrogen (white), and copper (orange). The pathway with the lowest free energy leading to methane is emphasized (Fig. 4h) [76]. Furthermore, *Xue et al.* compared the CO_2 reduction mechanisms on three low-index copper surfaces Cu(100), Cu(110), and Cu(111). They found that Cu(110) delivered the most favorable performance for producing methanol, following the CO_2 → *COOH → *CO → *CHO → $*CH_2O$ → $*CH_2OH$ → CH_3OH pathway (Fig. 4i). In this sequence, the formation of *COOH from CO_2 was identified as the potential-determining step (PDS) [77]. The superior activity of Cu(110) was attributed to its higher d-band center, which promotes stronger *COOH adsorption and, consequently, more efficient methanol synthesis compared to the other facets.

2.4. Structural and transport determinants of MOF electrocatalysis

2.4.1. Interplay among MOF structure, intrinsic activity, and electronic conductivity

The electrocatalytic behavior of MOF-based materials toward ORR, UOR, and CO_2RR is governed by the coupled effects of framework structure, intrinsic active-site activity, and electronic conductivity, three interdependent pillars [78–81]. The structure of a MOF determines the identity, density, accessibility, and electronic environment of catalytic sites [82,83]. Metal nodes or metal-ligand coordination motifs, such as Fe-N_4, Ni-O/N, Cu-N/O, Bi-O, or bimetallic centers, regulate the adsorption strength of reaction intermediates, while the organic linker controls metal-ligand orbital coupling, charge distribution, local polarity, and pore microenvironment [84–87]. Consequently, intrinsic activity is strongly influenced by metal oxidation state, coordination geometry, ligand field strength, and local electronic structure [88,89].

For ORR, metal-N coordination units such as Fe-N_4 can provide favorable adsorption energies for *OOH, enabling the four-electron reduction pathway when binding is neither too weak nor too strong (Fig. 5) [90]. For UOR, Ni-based nodes or reconstructed NiOOH-like species promote urea adsorption and dehydrogenation, while secondary metals (Fe, Co, Mn) modulate the electronic structure of Ni sites and facilitate C-N bond cleavage [91]. For CO_2RR, Cu-based centers favor *CO adsorption and C-C coupling under suitable electronic and structural environments, whereas Bi-based centers generally promote C_1 products such as formate by stabilizing oxygen-bound intermediates and suppressing hydrogen evolution [92,93].

However, intrinsic activity alone is insufficient. Many pristine MOFs possess limited electrical conductivity, which restricts electron transport from the current collector to internal active sites. Poor conductivity increases charge-transfer resistance, lowers active-site utilization, and limits current density, especially during multi-electron reactions such as UOR and CO_2RR [81,94,95]. Conductivity can be improved by using π-conjugated ligands, two-dimensional conductive frameworks, redox-active linkers, metal-ligand orbital hybridization, conductive substrates, carbon integration, or guest-mediated charge transport [96]. Thus, optimal MOF electrocatalysts must balance active-site electronic structure with efficient electron delivery, ensuring that accessible active sites, favorable intermediate binding, and continuous charge transport work in concert.

2.4.2. Role of porosity and mass transport in electrocatalytic performance

In addition to electronic structure and conductivity, pore architecture strongly affects electrocatalytic performance by controlling the transport of reactants, electrolytes, ions, and products within the electrode [97,98]. The optimal pore structure is not defined by maximum surface area alone, but by a balance among pore size, connectivity, volume, wettability, and hierarchical organization.

Micropores provide high surface area and abundant exposed active sites, which can enhance reactant adsorption and local concentration. However, excessive microporosity may restrict diffusion, especially for solvated ions, urea molecules, and gas-derived reactants under elevated current densities [99]. Mesopores reduce diffusion resistance, improve electrolyte penetration, and facilitate the transport of O_2, CO_2, urea, and reaction intermediates to internal active sites. Macropores further improve bulk electrolyte access and gas bubble release, which is particularly important for practical electrodes operating at high current density. Hierarchical porous structures containing micro-, meso-, and macropores are generally more favorable than purely microporous frameworks [100,101].

For ORR, interconnected mesoporous channels improve oxygen diffusion and water management in the catalyst layer, reducing mass-transfer polarization [102,103]. For UOR, larger and interconnected pores facilitate urea transport and product removal, preventing local accumulation of intermediates [52,104]. For CO_2RR, mesoporous and hierarchical structures help maintain CO_2 supply near active sites, reduce concentration gradients, and suppress the hydrogen evolution reaction by improving local reactant availability [105,106]. Pore wettability is also important: hydrophilic channels improve electrolyte contact in aqueous UOR systems, while balanced hydrophilic-hydrophobic interfaces benefit gas-involving reactions (ORR, CO_2RR) by enabling simultaneous gas, ion, and electron transport [107–109]. Rational pore engineering enhances electrochemical performance by shortening diffusion pathways, increasing active-site utilization, reducing concentration polarization, accelerating product desorption, and maintaining stable operation at high current density.

2.4.3. Regulating intermediates via metal nodes, ligands, and pores

While the previous subsections addressed general electronic conductivity and mass transport, this subsection focuses specifically on how metal nodes, ligands, and pore confinement regulate reaction intermediates. The adsorption and conversion of key intermediates are primarily determined by the electronic structure of metal nodes, the functional chemistry of organic ligands, and the confined pore microenvironment.

Metal nodes dictate the binding strength and activation mode of adsorbed intermediates [110]. In ORR, Fe-N_4 sites optimize *OOH adsorption for the four-electron pathway, whereas alternative metal centers may shift selectivity toward H_2O_2. In UOR, Ni-based nodes (or

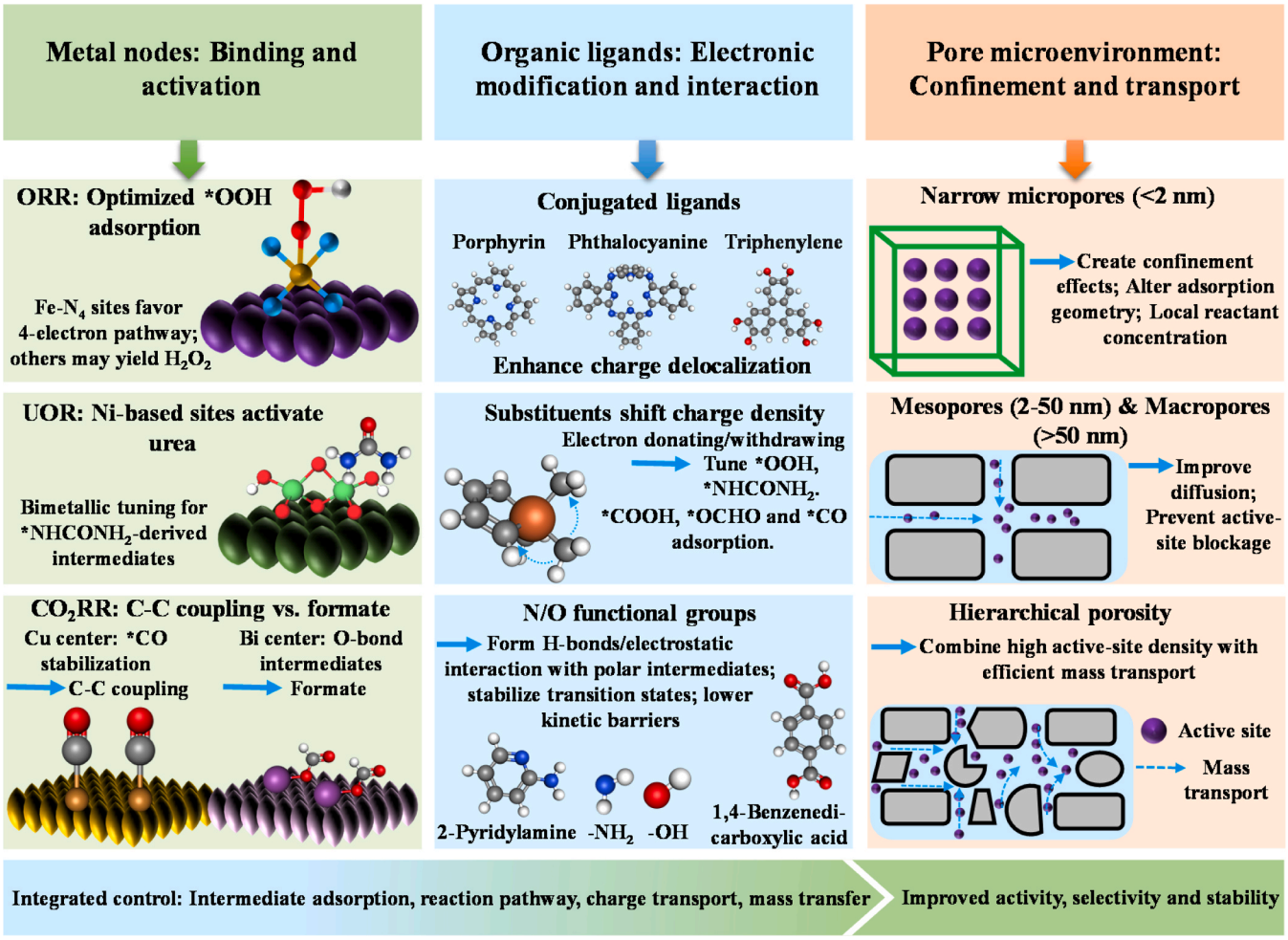

Fig. 6. Regulation of reaction intermediates in MOF electrocatalysts through metal nodes, organic ligands, and pore microenvironment for ORR, UOR, and CO_2RR.

in-situ generated NiOOH-like sites) activate urea, while bimetallic modulation tunes the adsorption and transformation of *$NHCONH_2$-derived intermediates. In CO_2RR, Cu centers stabilize *CO and promote C-C coupling to C_{2+} products, whereas Bi centers favor formate production by stabilizing oxygen-bound intermediates and weakening hydrogen adsorption.

Ligand structure further modifies the electronic properties of active sites. Conjugated ligands (porphyrin, phthalocyanine, triphenylene−2,3,6,7,10,11-hexaol (HHTP)) enhance charge delocalization and electronic coupling between metal nodes (Fig. 6) [111–114]. Electron-donating or electron-withdrawing substituents shift local charge density at the metal center, thereby changing the adsorption strength of *OOH, *$NHCONH_2$, *COOH, *OCHO, or *CO intermediates. N/O-containing functional groups (-NH_2, -OH, 2-Pyridylamine and 1, 4-benzenedicarboxylic acid) form hydrogen-bonding or electrostatic interactions with polar intermediates, stabilizing transition states and lowering kinetic barriers [115–117]. However, excessive stabilization may inhibit product desorption; therefore, ligand design must follow the principle of moderate adsorption strength.

Pore size and porosity complement these electronic effects by influencing intermediate residence time, reactant accessibility, and product removal. Narrow micropores create confinement effects that alter adsorption geometry and local reactant concentration, while mesopores and macropores improve diffusion and prevent active-site blockage. Hierarchical porosity is especially beneficial because it combines high active-site density with efficient mass transfer. Overall, the integration of suitable metal nodes, electronically active ligands, and well-connected pore architectures enable simultaneous control over intermediate adsorption, reaction pathway, charge transport, and mass transfer, thereby improving the activity, selectivity, and stability of MOF-based electrocatalysts.

3. MOFs in real-world electrochemical devices

MOFs are being translated from promising materials into integral components of real-world electrochemical devices, leveraging their exceptional porosity, tunable structures, and abundant catalytic sites to address pressing energy and environmental challenges. Their function as high-performance electrocatalysts, selective electrode modifiers, or versatile precursors enables enhanced efficiency, selectivity, and stability across various sustainable technologies, often surpassing traditional catalysts. This section details the integration of MOFs into key electrochemical platforms, examining their role in, fuel cells and metal-air batteries for efficient power generation via the ORR, direct urea fuel cells and urea electrolysis systems that valorize waste streams while producing energy or hydrogen, CO_2 reduction electrolyzers designed for selective conversion to valuable fuels and chemicals within power-to-X frameworks and emerging hybrid, multi-functional systems that combine these processes. The following discussion critically assesses device performance, durability, and the specific material engineering strategies that enable MOF functionality in each application.

3.1. *Fuel cells and metal-air batteries*

Fuel cells and metal-air batteries represent critical electrochemical technologies for sustainable energy conversion and storage. Their

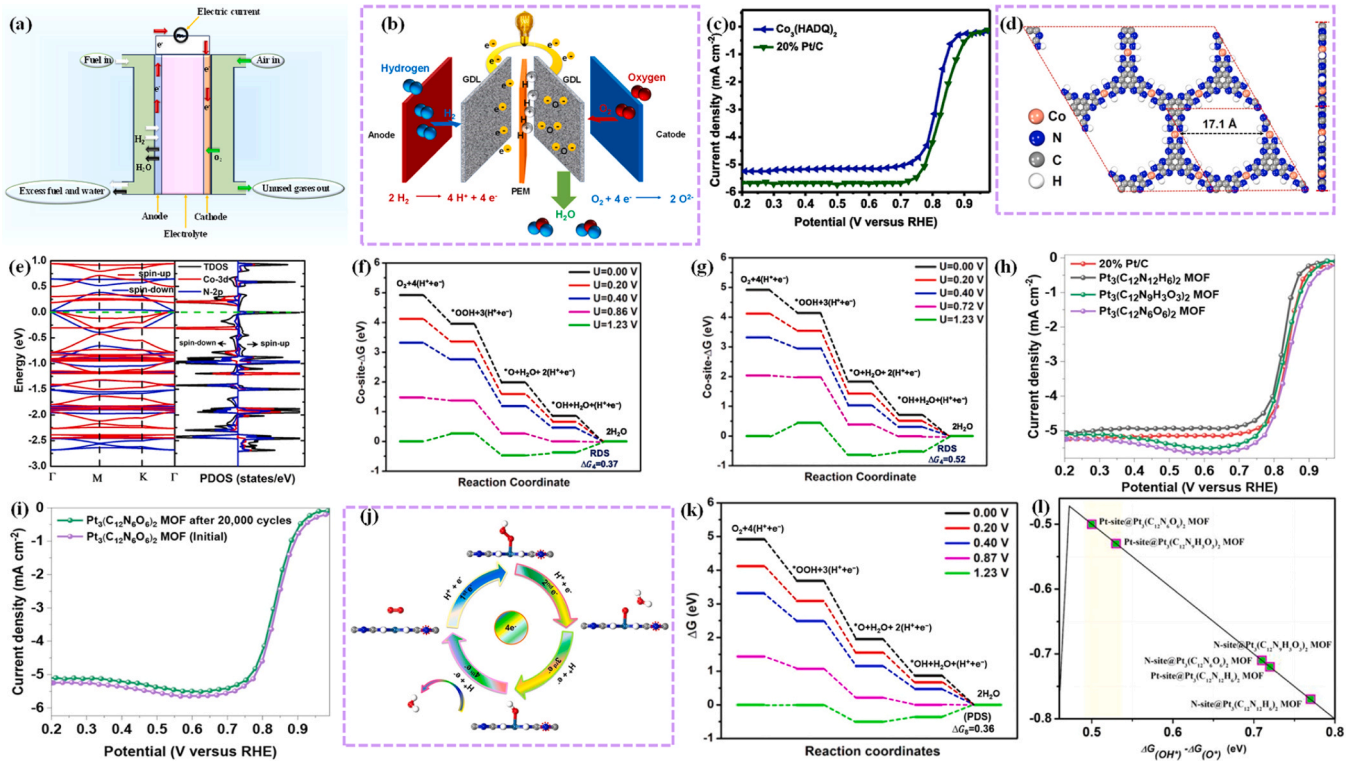

Fig. 7. (a) Schematic of a hydrogen fuel cell showing the flow of hydrogen and oxygen, electron movement, and electric current generation. (b) Schematic of a PEMFC, showing the hydrogen and oxygen reactions, proton and electron movement, and water production at the anode and cathode. (Under CC license) (c) Electrocatalytic activity for ORR in O_2-saturated 0.5 M H_2SO_4 solution was evaluated using LSV at 1600 rpm, comparing $Co_3(HADQ)_2$ with commercial 20% Pt/C. (d) Top and side views of the 2 × 2 supercell and (e) calculated band structure and PDOS for $Co_3(HADQ)_2$. The free energy profiles for ORR at both zero and applied potential versus RHE for $Co_3(HADQ)_2$ are presented for (f) Co-sites and (g) pyridinic N-sites. Copyright 2022 Elsevier. (h) LSV curves of $Pt_3(C_{12}N_6O_6)_2$ MOFs compared to 20% Pt/C at 1600 rpm. (i) LSV curves for ORR before and after 20,000 cycles in the CV test at 1600 rpm. (j) A schematic showing the 4e− ORR process on a Pt-MOF monolayer, where dark green, blue, grey, red, and white represent Pt, N, C, O, and H atoms, respectively. The red dotted circle highlights the involvement of pyridinic N atoms in the pyrazine ring during the reaction. (k) ORR of the Pt-site in $Pt_3(C_{12}N_6O_6)_2$ MOFs at zero and applied potential vs RHE. (l) Volcano plot of ORR performance. Copyright 2023 Elsevier.
(b) Reproduced with permission from ref [128]. (c-g) Reproduced with permission from ref [130]. (h-i) Reproduced with permission from ref [131].

performance hinges on efficient electrocatalytic reactions. In fuel cells, the ORR at the cathode is the pivotal step that converts the chemical energy of fuels like hydrogen into electricity. For metal-air batteries most prominently, zinc-air batteries that use atmospheric oxygen at the cathode the ORR similarly governs the discharge process, enabling systems with exceptionally high energy density. Concurrently, DUFCs utilize the UOR, offering an alternative pathway for power generation that valorizes a waste product, thereby addressing energy and environmental challenges simultaneously. In this section we will discuss fuel cell and metal air batteries in details.

3.1.1. ORR in hydrogen fuel cells

Hydrogen fuel cells generate electricity by converting chemical energy into electrical energy through the electrochemical reactions of hydrogen and oxygen. At the anode, hydrogen is oxidized, releasing electrons that travel through an external circuit to generate electricity, while protons (hydrogen ions) pass through an electrolyte to the cathode. At the cathode, oxygen combines with the protons and electrons to form water. Due to their high energy efficiency, power density, and clean operation emitting only water and heat hydrogen fuel cells are considered ideal for use in automotive and stationary applications [118, 119]. As shown in Fig. 7a a hydrogen fuel cell, where hydrogen (fuel) and oxygen (from air) react to generate electricity. At the anode, hydrogen undergoes the hydrogen oxidation reaction (HOR): it splits into H^+ and e^-. The electrons flow through an external circuit, creating electric current, while protons move through the electrolyte to the cathode. At the cathode, oxygen undergoes the ORR: it combines with protons and electrons to form water [120]. These two reactions (HOR and ORR) drive the cell operation, producing electricity cleanly and efficiently, with only water as a byproduct. There are several types of hydrogen fuel cells, each designed to operate under different conditions and applications. The main types of hydrogen fuel cells include proton exchange membrane fuel cells (PEMFCs), alkaline fuel cells (AFCs), phosphoric acid fuel cells (PAFCs), solid oxide fuel cells (SOFCs), and molten carbonate fuel cells (MCFCs) [121,122]. However, here we will focus on PEMFCs and AFCs, as these two types are particularly relevant due to their wide-ranging commercial applications and significant role in advancing clean energy solutions. While other types like PAFCs, SOFCs, and MCFCs offer certain benefits, they also come with notable drawbacks. For example, PAFCs operate at relatively high temperatures (160–220°C), making them less efficient in some applications, while SOFCs (600–1000°C) and MCFCs operate at even higher temperatures (600–800°C), leading to issues with material degradation, slow startup times, and overall complexity [123–125]. Additionally, SOFCs require specific fuels and high thermal management, limiting their versatility. In contrast, PEMFCs and AFCs operate at lower temperatures (10–100 °C and 20–120 °C) and offer advantages in terms of efficiency, quick start-up, and simplicity, making them better suited for applications like transportation and portable power generation [126].

3.1.1.1. ORR in proton exchange membrane fuel cells. PEMFCs are highly efficient in converting hydrogen into electricity with no pollution, low noise, and strong endurance [127]. The fuel cell operates by introducing hydrogen gas at the anode, where it splits into H^+ and e^-. The electrons

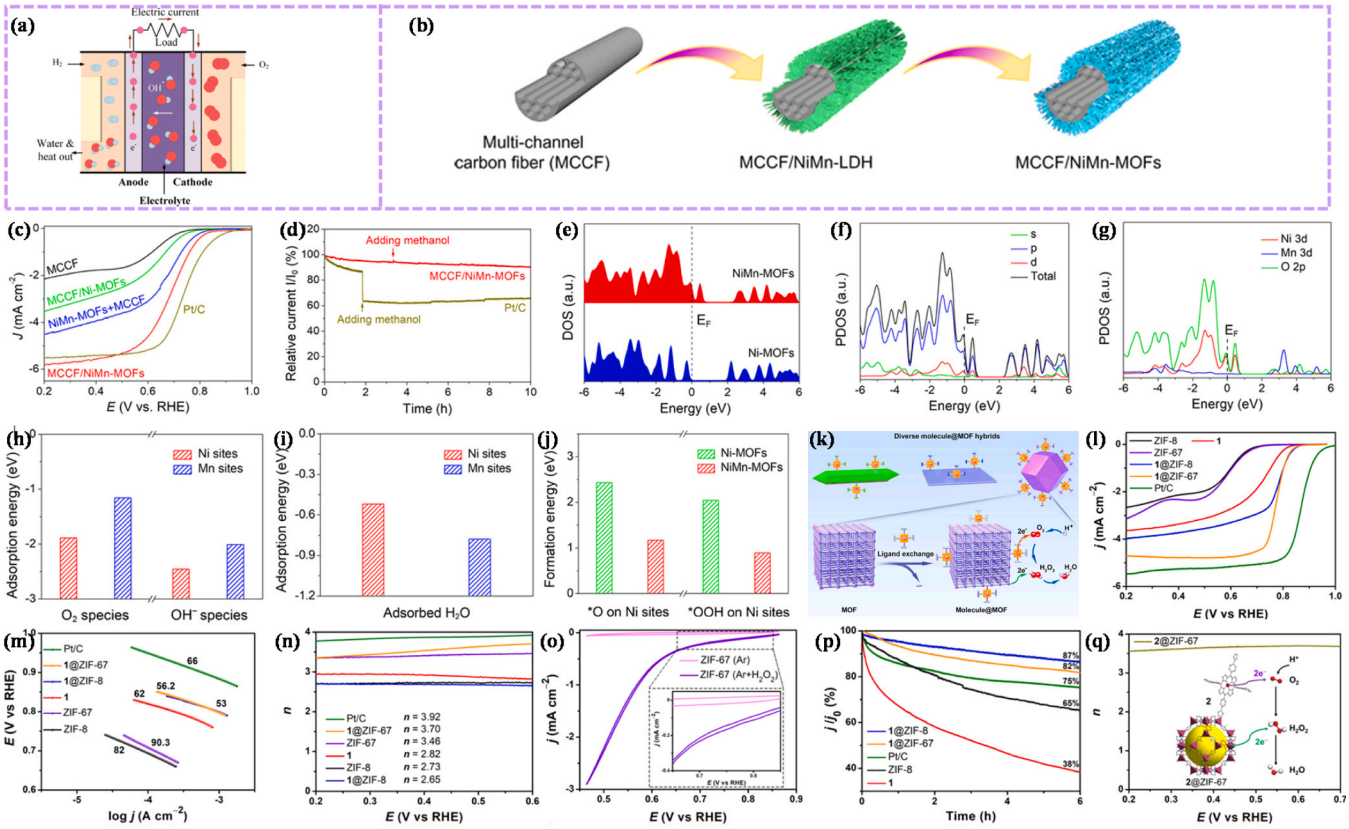

Fig. 8. (a) Schematic of AFCs showing hydrogen and oxygen flow, electricity generation, and water production. (Under CC license). (b) Synthesis of MCCF/NiMn-MOFs hydrothermal reaction to form MCCF/NiMn-LDH and conversion to MCCF/NiMn-MOFs via ligand exchange. (c) LSV plots for ORR at 1600 rpm. (d) chronoamperometric (i-t) curves with methanol addition for Pt/C and MCCF/NiMn-MOFs. (e) DOS for Ni-MOFs and NiMn-MOFs. (f, g) PDOS for NiMn-MOFs. (h, i) Adsorption energy of O_2 and OH^- and H_2O on Ni and Mn sites in NiMn-MOFs. (j) Formation energy of *O and *OOH intermediates for Ni-MOFs and NiMn-MOFs. Copyright 2020 © Wiley-VCH. (k) Molecular catalysts can be converted to heterogeneous catalysts by grafting them onto MOF surfaces through ligand exchange, where the reduction of O_2 occurs in a sequential manner at both the porphyrin and MOF sites, as depicted in the enlarged section. (l) LSV measured at 10 mV/s and at 1600 rpm with an oxygen-saturated 0.1 M KOH solution, (m) corresponding Tafel plots measured at 2 mV/s, and (n) electron transfer number (n) values determined from RRDE of ZIF−8, ZIF−67, 1, 1@ZIF−8, 1@ZIF−67, and Pt/C. (o) CV data of ZIF−67 with and without H_2O_2 under argon using RDE at 50 mV/s. (p) Long-term stability tests of ZIF−8, 1, 1@ZIF−8, 1@ZIF−67, and Pt/C measured with RDE at a controlled potential (0.46 V). (q) Schematic illustration of ORR and n of 2@ZIF−67 determined from RRDE. Copyright 2021 © Wiley-VCH.
(a) Reproduced with permission from ref [132]. (b-j) Reproduced with permission from ref [133]. (k-q) Reproduced with permission from ref [134].

travel through an external circuit, generating electrical power, while the protons pass through the PEM to the cathode. At the cathode, they combine with oxygen and electrons to form water as a byproduct (Fig. 7b) [128]. However, the ORR at the cathode is slower than the HOR at the anode, limiting fuel cell performance. While platinum-based catalysts are commonly used for ORR, their high cost and scarcity hinder PEMFC commercialization. To overcome these challenges, there is a need for efficient, stable, and low-cost PGM-free catalysts [129]. MOFs offer a promising solution, potentially addressing these limitations with their high efficiency, stability, and cost-effectiveness in acidic environments. For instance, *Iqbal et al.* introduced a new layer-stacked two-dimensional MOF, $Co_3(HADQ)_2$, as an efficient electrocatalyst for acidic ORR. As shown in Fig. 7c that this novel MOF exhibits exceptional conductivity, high activity ($E_{1/2}$ = 0.836 V vs. RHE), Tafel slope 79 mV dec^{-1} and outstanding stability (up to 20,000 cycles), outperforming many state-of-the-art electrocatalysts. The geometry and electronic properties of $Co_3(HADQ)_2$ were analyzed using DFT calculations. As shown in Fig. 7d, the 2D $Co_3(HADQ)_2$ has a planar, porous structure with a hexagonal grid and a pore size of 17.01 Å, facilitating ion and proton dispersion for the ORR process. Band structure and PDOS analysis (Fig. 7e) reveal metallic behavior and high electrical conductivity, attributed to electron delocalization in the Co-N_4 motif and conjugated pyrazine and benzene units, suggesting its high activity for ORR. The ORR reaction pathways on Co-sites and pyridinic N-sites in $Co_3(HADQ)_2$ were studied, with the results shown in Fig. 7f-g. The Co-sites, possessing positive charge, act as active sites for ORR, with a lower limiting potential (UL = 0.86 V) compared to pyridinic N-sites (UL = 0.72 V), indicating superior ORR activity at Co-sites, which is comparable to or even better than state-of-the-art catalysts like Pt [130]. Furthermore, *Iqbal et al.* developed electrically conductive $Pt_3(C_{12}N_6O_6)_2$ MOF, which demonstrated the best performance for acidic ORR, with high activity ($E_{1/2}$ = 0.836 V vs. RHE) and exceptional durability (20,000 cycles) in acidic media (pH = 0.29) (Fig. 7h-i). To evaluate the catalytic performance of Pt-MOF monolayers for ORR, the Gibbs free energy changes (ΔG) of key reaction steps were calculated using the 4e- scheme (Fig. 7j). The ORR process involves the hydrogenation of O_2 to form *OOH, followed by its conversion to *OH and water, with Pt and N-sites in the pyrazine ring acting as active sites. Bader charge analysis indicates that the Pt ion is positively charged, facilitating electron transfer between Pt-sites and ORR intermediates during the process. Moreover, the calculated value of ΔG for the RDS is 0.36 eV for $Pt_3(C_{12}N_6O_6)_2$ at 1.23 V (Fig. 7k). The value is comparatively lower than the value for pyridinic N-sites, which indicates that the Pt-sites in Pt-MOFs exhibit better ORR performance than the pyridinic N-sites in the same materials. To explain the varying ORR activity between the Pt-site in the Pt-X_4 unit and the pyridinic N-site in the pyrazine ring, Bader charge analysis (Fig. 7l) reveals that charge transfer from Pt atoms to adsorbed intermediates enhances electron interaction, leading to better catalytic

performance, with $Pt_3(C_{12}N_6O_6)_2$ exhibiting the highest ORR activity among the Pt-MOFs [131]. The superior ORR performance of MOF-based catalysts in acidic PEMFC environments is closely linked to their structural features. The 4e⁻ ORR pathway requires optimized *OOH adsorption and efficient electron/proton transfer. In $Co_3(HADQ)_2$, the planar 2D structure with Co-N_4 motifs embedded in a highly conjugated pyrazine-benzene framework enables metallic conductivity and favorable electronic delocalization, resulting in a low limiting potential on Co sites. Similarly, in $Pt_3(C_{12}N_6O_6)_2$, the positively charged Pt sites in the Pt-N_4 coordination environment strengthen interaction with ORR intermediates while maintaining structural stability in strong acid. These atomic-level structural advantages, combined with high porosity, facilitate mass transport and contribute to the observed high half-wave potential, low Tafel slope, and excellent durability.

The development of efficient electrocatalysts, such as MOFs, presents a promising pathway to overcome the limitations of PEMFCs, particularly in enhancing the ORR at the cathode. These materials not only offer improved catalytic performance but also demonstrate exceptional stability and cost-effectiveness, making them strong candidates for future fuel cell technologies. These advancements highlight the promising role of MOFs in addressing the challenges of PEMFCs commercialization and enhancing their efficiency for various applications.

3.1.1.2. Alkaline fuel cells. AFCs are one of the earliest fuel cell types, known for their successful use in space missions. These cells use an alkaline aqueous electrolyte, usually potassium hydroxide (KOH), and operate at low temperatures. In this solution, KOH dissociates into potassium (K^+) and OH^- ions. The HOR occurs at the anode, where hydrogen reacts with OH^- to form water, and electrons flow through an external circuit to provide power. At the cathode, oxygen undergoes the ORR, where it combines with water and electrons to produce OH^- ions, keeping the electrolyte intact (Fig. 8a) [132]. AFCs face several challenges, including the need for efficient and durable catalysts for both the HOR and the ORR. The slow kinetics of ORR at the cathode, along with catalyst degradation over time, hinders the overall performance and stability of AFCs. Additionally, the sensitivity of conventional catalysts to impurities, such as CO_2, further complicates their widespread use. MOFs offer a promising solution to these challenges, providing tunable structures with high surface areas and the potential for efficient catalytic activity in electrochemical reactions. For instance, *Cheng et al.* developed a method to grow NiMn-based bimetallic MOF nanosheets on multi-channel carbon fibers (MCCF) through a hydrothermal reaction to form MCCF/NiMn-LDH, followed by a ligand exchange to convert it into MCCF/NiMn-MOFs (Fig. 8b). The MCCF/NiMn-MOFs demonstrated excellent electrocatalytic performance for ORR, with an onset potential of 0.85 V vs. RHE and a large limiting current density of 5.6 mA cm^{-2}, comparable to Pt/C (Fig. 8c). Furthermore, the MCCF/NiMn-MOFs

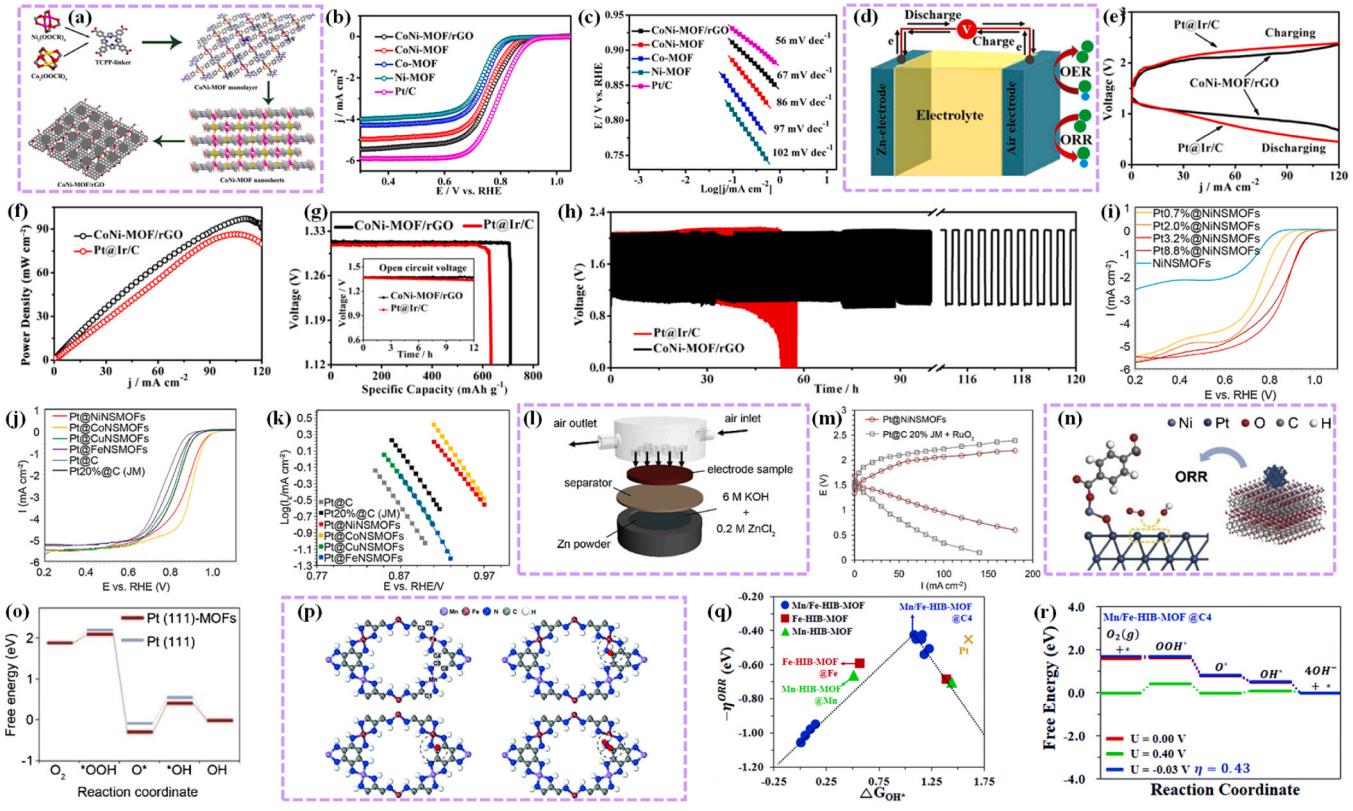

Fig. 9. (a) A schematic diagram depicting the synthesis of the CoNi-MOF/rGO catalyst, with the following color representation: gray for carbon (C), red for oxygen (O), pink for nickel (Ni), yellow for cobalt (Co), and blue for hydrogen (H). (b) ORR polarization curves, recorded at a scan rate of 5 mV s^{-1} in O_2-saturated 0.1 M KOH at 1600 rpm. (c) The corresponding Tafel plots for ORR. (d) Schematic illustration of the ZAB setup. (e) Charge/discharge polarization curves for ZABs with CoNi-MOF/rGO and Pt@Ir/C as electrocatalysts. (f) Corresponding power densities for ZABs. (g) Specific capacity and open-circuit voltage plot (inset) for the CoNi-MOF/rGO- and Pt@Ir/C-based ZABs, normalized to the zinc consumed. (h) Galvanostatic charge/discharge cycling performance of ZABs. Copyright © 2019 American Chemical Society. Electrochemical activity of prepared catalysts: (i, j) ORR polarization curves and (k) corresponding Tafel plots in 0.1 M KOH saturated with oxygen, at a rotation rate of 1600 rpm and a scan rate of 10 mV s^{-1}. (l) Schematic of rechargeable ZAB fabrication; (m) Charge-discharge polarization curves for ZABs with different electrodes. (n) Schematic model of Pt-embedded MOFs for DFT calculations; (o) Free energy profiles for ORR. Copyright 2019 Elsevier. ORR mechanistic study: (p) Initial structure and structures after the adsorption of hydroxyl (OH*), oxyl (O*), and hydroperoxyl (OOH*) intermediates on Mn/Fe-HIB-MOF, with active sites labeled and shown in the inset. (q) Volcano plots for ORR activity for Mn-HIB-MOF, Fe-HIB-MOF, and Mn/Fe-HIB-MOF catalysts. (r) Free energy diagrams illustrating the ORR pathways on Mn/Fe-HIB-MOF in an alkaline environment. Copyright 2019 Royal Society of Chemistry.
(a-h) Reproduced with permission from ref [142]. (i-o) Reproduced with permission from ref [143]. (p-r) Reproduced with permission from ref [144].

exhibited impressive stability and methanol tolerance, retaining 95% and 92% of the initial current after 10 and 30 h of ORR operation, respectively, as shown in Fig. 8d. Theoretical investigations using DFT calculations reveal that the incorporation of Mn into Ni-MOFs enhances electron density around the Fermi level, with Ni sites acting as active centers for ORR (Fig. 8e-g). The adsorption energies of O_2 and OH^- species on Ni sites are significantly lower than on Mn sites, suggesting that Ni is the primary active site for oxygen electrocatalysis, while Mn enhances the process by promoting water adsorption (Fig. 8h-i). The formation energy barriers for key intermediates (*O and *OOH) on Ni sites in NiMn-MOFs are much lower than in Ni-MOFs, indicating improved ORR kinetics (Fig. 8j) [133].

Furthermore, *Liang et al.* developed Co porphyrin@MOF hybrids through ligand exchange for enhanced ORR activity and selectivity. The grafted Co porphyrins showed a significant anodic shift of over 70 mV in the half-wave potential and increased electron transfer from 2.65 to 3.70, improving $4e^-$ ORR selectivity. As shown in Fig. 8k, the use of MOFs as supports offers tunable compositions, optimized electron transfer, and improved catalytic activity. The electrocatalytic ORR performance of 1@ZIF−8 was evaluated, showing an onset potential (E1/2) of 0.79 V, with a Tafel slope of 53 mV dec^{-1} (Fig. 8l-m). The electron transfer number (n) for 1@ZIF−8 was 2.65, indicating partial $4e^-$ selectivity, which was enhanced to 3.70 when 1 was grafted onto Co-based ZIF−67 (Fig. 8n). Stability tests revealed a 13% and 18% current loss for 1@ZIF−8 and 1@ZIF−67, respectively, with 1@ZIF−67 exhibiting superior $4e^-$ selectivity and stability (Fig. 8o-p). Additionally, Co tetra(4-imidazolylphenyl) porphyrin (2) was grafted onto both ZIF−8 and ZIF−67. The resulting 2@ZIF−8 showed an ORR activity with a n value of 2.70, while 2@ZIF−67 displayed a n value of 3.70 (Fig. 8q). Due to the distance between the porphyrin sites and the MOF surface in 2@ZIF−67, generated H_2O_2 desorbs and is further reduced on ZIF−67 [134]. In alkaline media, the ORR performance of MOF-based catalysts is governed by bimetallic synergy, ligand engineering, and support effects. In MCCF/NiMn-MOFs, incorporation of Mn into the Ni-MOF framework increases electron density near the Fermi level and lowers the formation energy barriers of *O and *OOH intermediates on Ni active sites, while Mn promotes water adsorption. This bimetallic modulation leads to enhanced ORR kinetics, high limiting current density, and superior methanol tolerance. Likewise, in Co-porphyrin@MOF hybrids, ligand-exchange grafting enables synergistic cooperation between molecular Co-porphyrin sites and the MOF support. The optimized distance between porphyrin and ZIF−67 surface facilitates H_2O_2 desorption and subsequent reduction, boosting the $4e^-$ selectivity and overall stability. These examples demonstrate how rational design of metal nodes, bimetallic composition, and hybridization directly translates into improved activity, selectivity, and durability in alkaline ORR. These advancements in MOF-based catalysts offer significant promise in overcoming the challenges facing AFCs and enhancing their commercial viability.

3.1.2. ORR in metal-air batteries

Metal-air batteries, including zinc-air, lithium-air, and aluminum-air batteries, are promising energy storage devices that utilize oxygen from the air as a cathode reactant. In these batteries, the ORR plays a crucial role during discharge, where oxygen molecules are reduced at the cathode to form either hydroxide ions or peroxides, depending on the specific battery chemistry. This process enables the battery to produce electricity efficiently. Metal-air batteries are highly regarded for their high energy densities, making them ideal for applications in electric vehicles, portable electronics, and grid storage.

Rechargeable ZABs are a promising energy storage technology for applications like smart grids, electric vehicles, and wearable electronics due to their high energy density, safety, and environmentally benign nature [135]. However, their commercialization is hindered by poor cycle life and energy conversion efficiency, primarily due to slow oxygen reduction. While precious metals like Pt, Ru, and Ir offer effective catalytic performance, their high cost and scarcity limit large-scale use [136–138]. Efforts have shifted to developing precious metal-free catalysts, including transition metal oxides, nitrides and phosphides, but challenges such as corrosion susceptibility and low conductivity persist [139–141]. MOFs can address these challenges due to their tunable structure, high surface area, and potential for improved catalytic activity and stability. For instance, *Zheng et al.* reported the design of bimetallic CoNi-MOF nanosheets/reduced graphene oxide (rGO) hybrid electrocatalysts to enhance the catalytic activity of metal–air batteries for ORR. CoNi-MOF nanosheets, prepared using TCPP as the ligand and PVP as the surfactant, offer enhanced electrocatalytic activity due to their larger surface area and more exposed active sites compared to bulk MOFs (Fig. 9a). Furthermore, CoNi-MOF/rGO exhibits an onset over-potential of 0.88 V, a diffusion limiting current density of 5.35 mA cm^{-2} at 1600 rpm, and a small Tafel slope of 67 mV dec^{-1}, indicating superior ORR performance compared to other catalysts (Fig. 9b-c). A rechargeable ZAB was constructed with CoNi-MOF/rGO as the air electrode, a zinc plate as the anode, and a KOH/$ZnCl_2$ mixture as the electrolyte (Fig. 9d). The charge and discharge polarization curves of CoNi-MOF/rGO and Pt@Ir/C-based ZABs were compared, highlighting CoNi-MOF/rGO superior OER performance (Fig. 9e). CoNi-MOF/rGO achieved a peak power density of 97 mW cm^{-2}, outperforming the Pt@Ir/C mixture (86 mW cm^{-2}) (Fig. 9f). The CoNi-MOF/rGO-based battery demonstrated a voltage plateau of 1.31 V for 30 h with a specific capacity of 711 mA h g^{-1}, surpassing the performance of Pt@Ir/C-based batteries (Fig. 9g). Additionally, CoNi-MOF/rGO exhibited better cycling stability and rechargeability, as shown in the charge/discharge cycle curves (Fig. 9h) [142].

Furthermore, *Xia et al.* developed a new strategy for bifunctional electrocatalysts by designing a synergistic nano-architecture of Pt NPs and ultrathin 2D MOFs. The unique nano-architecture and electron interaction between Pt NPs and MOF nanosheets enhance electrochemical performance for ORR. As Pt loading increases from 0.7% to 3.2%, ORR activity improves, with a positive onset potential shift from 0.902 V to 1.024 V, as seen in Fig. 9i. However, further increasing Pt loading to 8.8% reduces ORR performance. The Pt@NiNSMOFs sample (3.2% Pt) outperforms Pt@C with similar Pt loading (5%) and shows a 110-mV shift in half-wave potential, as shown in Fig. 9j. The ORR performance is further confirmed by the Tafel plots in Fig. 9k, demonstrating fast ORR kinetics and enhanced activity for the Pt@NiNSMOFs composite compared to commercial Pt@C. The Pt3.2%@NiNSMOFs catalyst shows superior performance in rechargeable ZABs, with a 0.097 V and 0.252 V reduction in over-potential at 10 mA cm^{-2} compared to commercial Pt/C and RuO_2 (Fig. 9l-m). At 100 mA cm^{-2}, it outperforms the commercial catalyst mixture, achieving a discharge voltage of 0.95 V and charge voltage of 2.07 V. The peak power density reaches 108 mW cm^{-2}, 2.5 times higher than the commercial catalysts. A theoretical study using DFT was conducted to explore the relationship between electron structural modification and catalytic activity of the composite catalyst. Simplified models for ORR were constructed, as shown in Fig. 9n. The adsorption energy of intermediates on active sites revealed that anchoring the metal-organic group on the Pt surface lowers the energy level of intermediates, enhancing ORR activity, as seen in the free energy profile in Fig. 9o [143]. In another study, *Shinde et al.* developed advanced ZABs using Mn/Fe-HIB-MOF bifunctional electrocatalysts and superionic bio-cellulose electrolytes. The Mn/Fe-HIB-MOFs exhibited superior ORR activity with a half-wave potential of 0.883 V, outperforming Pt/C. The cathode demonstrated remarkable cycle life, achieving 1000 h over 6000 cycles at 10 mA cm^{-2} and 600 h over 3600 cycles at 25 mA cm^{-2}, with excellent flexibility for both liquid and solid-state ZABs. The DFT calculations reveal that Mn/Fe-HIB-MOFs exhibit superior catalytic performance for ORR. The optimized structures, shown in Fig. 9p, demonstrate that the unique carbon-active sites in Mn/Fe-HIB-MOF enhance conductivity and reduce overpotentials. Theoretical analysis, including free energy diagrams (Fig. 9q), shows Mn/Fe-HIB-MOF has the lowest overpotential for ORR

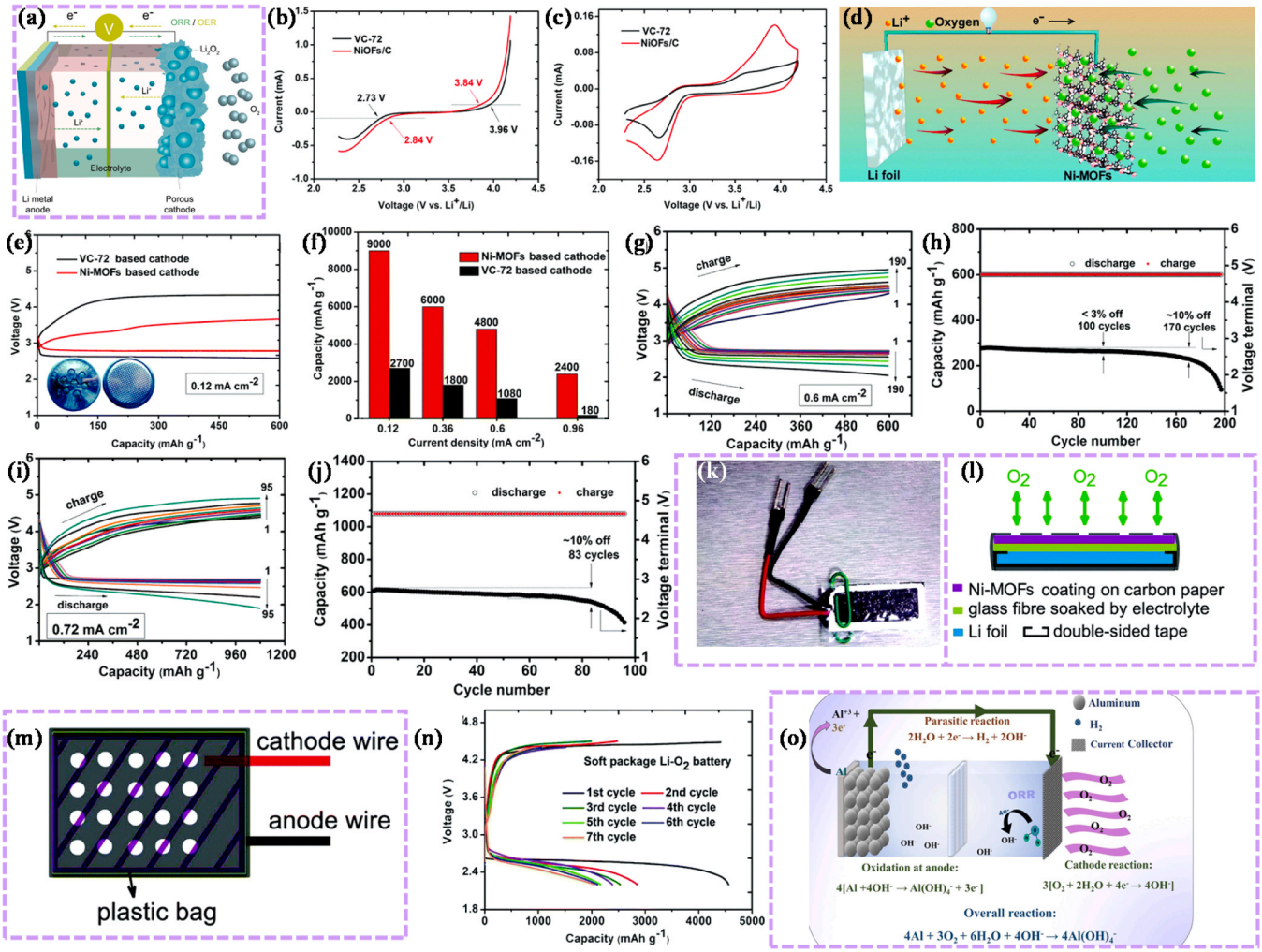

Fig. 10. (a) Schematic of a typical LAB showing the Li metal anode, porous cathode, and electrolyte with the ORR/OER. Copyright 2023 Elsevier. (b) ORR and OER polarization curves of VC−72 and Ni-MOFs/C on a RDE in an O_2-saturated aprotic electrolyte of 1 M LiTFSI in TEGDME. (c) CVs at a scan rate of 20 mV s^{-1} on RDE in O_2-saturated 1 M LiTFSI in TEGDME. (d) Schematic of a LAB, consisting of a lithium anode and an O_2 cathode, with 1 M LiTFSI in TEGDME as the electrolyte. The Ni-MOFs-coated NF cathode produces discharge products through the reaction between Li^+ and O_2 during discharge, which are decomposed back to Li^+ and O_2 during charging. (e) Voltage profiles of Ni-MOFs-based and VC−72-based LABs with a fixed capacity of 600 mA h g^{-1} at 0.12 mA cm^{-2}. The inset shows the CR2032 coin-type battery. (f) Discharge capacity comparison of Ni-MOFs and VC−72-based cathodes at different current densities. (g, i) Galvanostatic discharge-charge curves and (h, j) voltage variation on the discharge terminal for batteries with a fixed capacity of (g, h) 600 mA h g^{-1} at 0.6 mA cm^{-2} and (j, i) 1080 mA h g^{-1} at 0.72 mA cm^{-2}. Capacities are based on the total mass loading of the cathode. (k) Photograph of a plastic LAB. (l) Cross-sectional and (m) top view schematics of the plastic LAB, consisting of a lithium anode, electrolyte-soaked separator, Ni-MOFs/C-coated cathode, and a plastic case with holes for oxygen transfer. (n) Voltage variation with capacity, where the capacity is based on the mass of Ni-MOFs/C (~16 mg) in the cathode. Copyright 2015 Royal Society of Chemistry. (o) A diagram illustrating the operational mechanism of a full AAB, showing the corresponding electrodes and the overall reaction. Copyright 2024 Royal Society of Chemistry.
(a) Reproduced with permission from ref [145]. (b-n) Reproduced with permission from ref [149]. (o) Reproduced with permission from ref [150].

(0.43 V), outperforming Mn-HIB-MOF, Fe-HIB-MOF, and commercial RuO_2 and Pt/C (Fig. 9r). The improvement is attributed to the enhanced electronic structure, carbon contribution, and large active surface area of Mn/Fe-HIB-MOF, making it an efficient electrocatalyst in alkaline environments [144]. Advanced MOF-based electrocatalysts significantly enhance the performance of rechargeable ZABs by improving ORR activity, reducing overpotentials, and increasing cycling stability. These catalysts outperform traditional precious metals, providing a cost-effective and efficient solution for energy storage. The above results underscore the potential of MOFs and similar materials in advancing rechargeable battery performance for practical applications. Ongoing research into MOFs will continue to unlock their full potential, further advancing energy storage technologies.

Moreover, LABs have attracted significant attention due to their high theoretical energy density (3155 Wh kg^{-1}, based on Li_2O_2). A typical LAB comprises a lithium foil anode, a separator, and a cathode electrocatalyst, where the ORR takes place during discharge, and the OER occurs during charge (Fig. 10a) [145]. However, slow ORR at the cathode lead to high overpotentials, low round-trip efficiency, poor cycling life, and limited rate capability, which seriously hinder the overall performance of LABs [146,147]. Consequently, considerable efforts have been dedicated to developing cathode catalysts that can enhance ORR performance. Porous gold has shown promise in promoting ORR by effectively accommodating the insoluble Li_2O_2 produced during discharge [148]. MOFs offer a solution to these limitations by providing a highly tunable and porous structure that enhances ORR catalytic activity. With their large surface area, adjustable pore size, and the ability to modify metal nodes, MOFs are ideal candidates for improving the performance of LABs. For instance, *Hu et al.* demonstrated the use of Ni-MOFs as high-performance cathode catalysts for rechargeable LABs. Ni-MOFs, with their 3D micro-nano structure, open catalytic sites, and large surface area, facilitate efficient O_2 transfer and

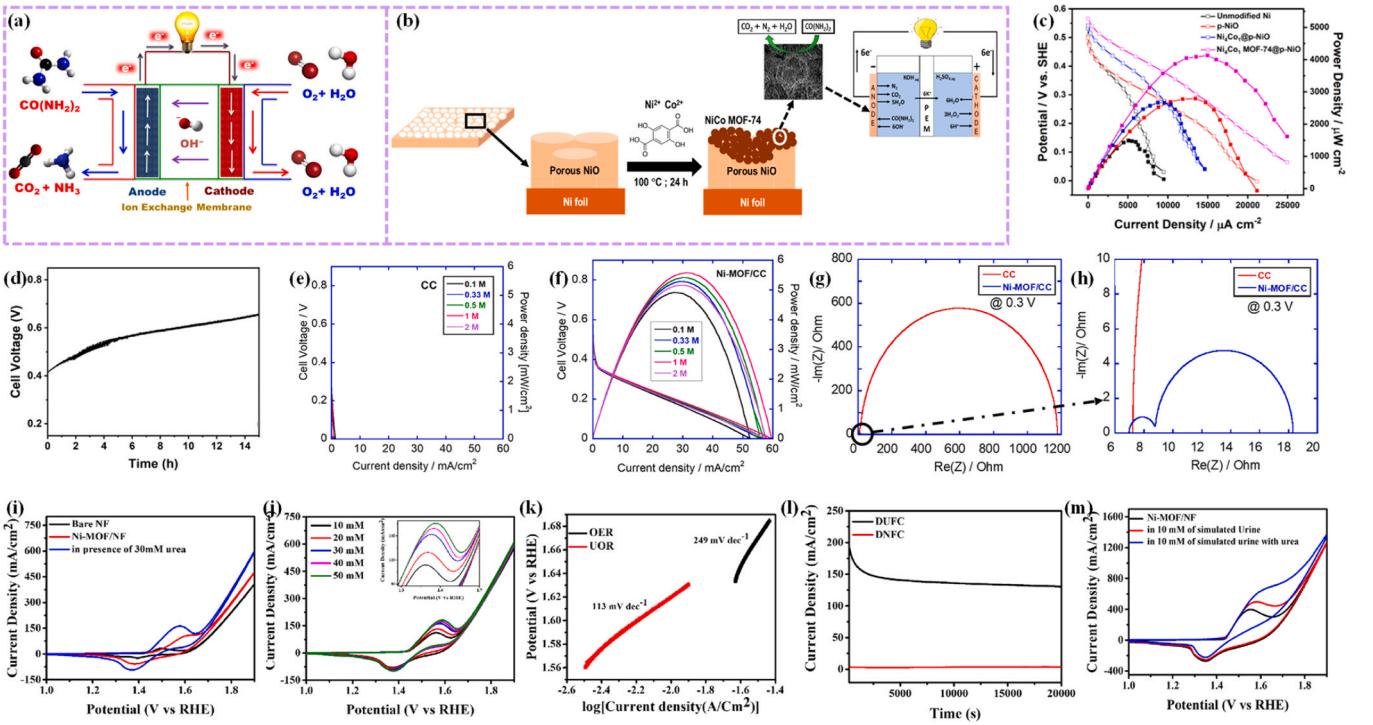

Fig. 11. (a) Schematic of a DUFCs with ion exchange membrane, showing the anode and cathode reactions. Copyright © 2025 American Chemical Society. (b) Schematic illustration of the preparation of NiCo MOF−74 on porous NiO and its application in a DUFCs. (c) Performance comparison of urea/H_2O_2 fuel cell using NiCo MOF−74@p-NiO and other electrodes. (d) Potential vs. time during a 15-h test at a 10-mA cm^{-2}. Copyright © 2023 American Chemical Society. (e-f) LSV measurements were conducted on the synthesized electrode in a real fuel cell, operating with various urea concentrations in 1 M KOH. (g) EIS of the real fuel cell using CC and Ni-MOF/CC electrodes. (h) High magnification of the EIS spectra at high frequency. Copyright 2024 Elsevier. (i) CV curves with 30 mM urea at 50 mV/s. (j) CV curves of in 1 M KOH with varying urea concentrations from 10 mM to 50 mM. (k) Corresponding Tafel plot comparing OER (Ni-MOF/NF) and UOR with 30 mM urea. (l) CP studies of DUFC in 1 M KOH with 50 mM urea (onset potential: 1.56 V (vs RHE)). (m) CV of Ni-MOF/NF in the presence of simulated urine and simulated urine with varying concentrations of urea in 1 M KOH. Copyright 2023 Elsevier.
(a) Reproduced with permission from ref [162]. (b-d) Reproduced with permission from ref [163]. (e-h) Reproduced with permission from ref [164]. (i-m) Reproduced with permission from ref [165].

electrolyte contact. Ni-MOFs/C demonstrated better catalytic performance for LABs, showing more positive ORR (2.84 V vs. Li+/Li) and more negative OER (3.84 V vs. Li+/Li) potentials than pure VC−72 (Fig. 10b). Cyclic voltammetry (Fig. 10c) further confirmed their superior activity, with a larger current density and smaller ORR/OER peak gap. Ni-MOFs were used as the cathode catalyst for LABs, with a lithium foil anode and 1 M LiTFSI in TEGDME electrolyte (Fig. 10d). The Ni-MOFs-based cathode showed superior ORR/OER activity, with a low discharge overpotential of 0.16 V and a round-trip efficiency of 80% (Fig. 10e). The Ni-MOFs-based cathode delivered higher discharge capacity than the VC−72-based cathode, reaching 9000 mA h g^{-1} at 0.12 mA cm^{-2} (Fig. 10f). The cycling stability of Ni-MOFs-based LABs was evaluated at a fixed capacity retention of 600 mA h g^{-1}, showing minimal voltage drop (below 3%) after 100 cycles (Fig. 10g-h). Notably, the batteries operated for 170 cycles with no significant polarization increase. When the capacity and current density were increased to 1080 mA h g^{-1} and 0.72 mA cm^{-2}, the discharge voltage maintained 90% retention after over 80 cycles (Fig. 10i-j). These results demonstrate the impressive stability and reversibility of Ni-MOFs-based batteries. Furthermore, a plastic LABs was designed with a Ni-MOFs-based cathode, lithium foil anode, glass fiber separator, and a plastic case for O_2 transfer (Fig. 10k-m). The first cycle provided an initial capacity of 4650 mA h g^{-1} and an energy density of 478 Wh kg^{-1} (Fig. 10n). After the 7th cycle, the capacity decreased to 2150 mA h g^{-1} with an energy density of 239 Wh kg^{-1}. The plastic LABs performance is significantly higher than that of commercial LABs, though the preparation process is still being optimized [149]. The development of advanced cathode catalysts, such as Ni-MOFs, plays a crucial role in overcoming the limitations of LABs. By enhancing key aspects like catalytic efficiency, cycling stability, and energy density, these innovations contribute to the progress of next-generation energy storage technologies. Ongoing research and optimization will continue to refine these systems, ultimately leading to more reliable and efficient solutions for a range of applications in the energy sector.

Similarly, aluminum-air batteries (AABs) have gained significant attention due to the numerous advantages of using aluminum as the anode material [151]. Aluminum is abundant, sustainable, and has a higher energy density than metals like zinc and iron, offering the potential for improved specific energy and power compared to traditional metal-air batteries. This makes AABs highly promising for applications in electric vehicles, grid-scale energy storage, and other critical sectors. In addition to their high energy density, AABs are environmentally friendly, as aluminum is easily recyclable and presents fewer environmental concerns than other metals. In AABs, the aluminum anode undergoes oxidation, releasing electrons and forming aluminum hydroxide ($Al(OH)_4^-$), as shown in Fig. 10o [150,152]. At the cathode, ORR occurs, where oxygen molecules react with water to form OH^-. However, a parasitic reaction can also occur, where water is reduced to hydrogen and hydroxide ions, leading to some inefficiency. The overall reaction combines these processes: $4Al + 3\ O_2 + 6\ H_2O \rightarrow 4Al(OH)_4^-$, generating energy. The reaction emphasizes the critical role of both the anode and cathode in the performance of AABs, highlighting the need for efficient catalysts to minimize energy loss from parasitic reactions and enhance overall efficiency. Despite the promising advantages of AABs, several challenges remain that hinder their commercial viability and overall performance. These include limited cycle life, poor rechargeability, and inefficiencies due to parasitic reactions, such as the reduction of water to hydrogen, which lowers energy efficiency [153,154]. Additionally, the

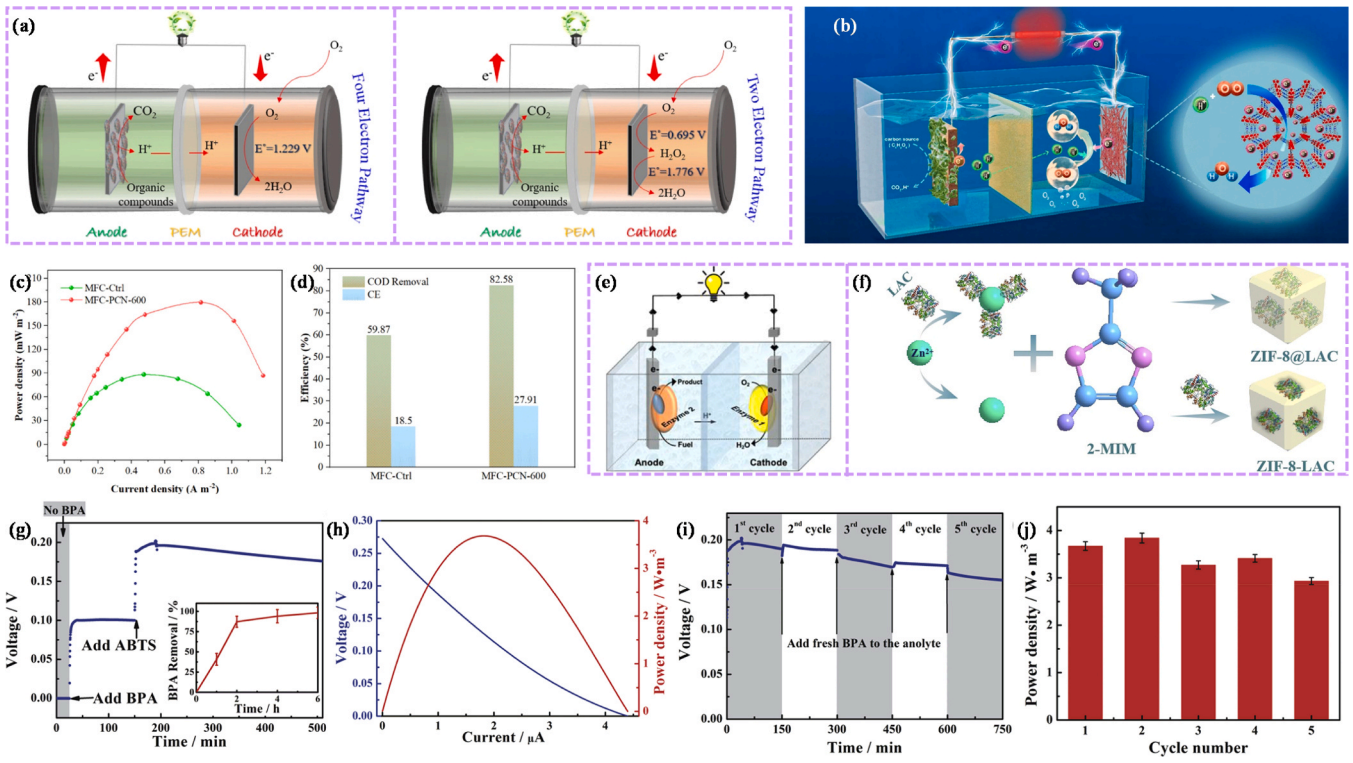

Fig. 12. (a) The potential pathways for electron transfer during the ORR in microbial fuel cells (MFCs). Copyright 2022 Elsevier. (b) Schematic of MFCs using metalloporphyrin MOF (PCN−600). (c) Power density graphs and (d) chemical oxygen demand (COD) removal efficiency and coulombic efficiency (CE) for MFCs with PCN−600-modified and unmodified cathodes. Copyright 2024 Elsevier. (e) Enzymatic fuel cell (EFC) schematic showing the anode and cathode catalyzed by enzymes for fuel oxidation and oxygen reduction, respectively. (Under CC license). (f) Schematic diagram depicting the preparation of ZIF−8@LAC and ZIF−8-LAC. (g) Operating voltage of a single EBFC (with inset showing BPA removal efficiency). (h) Power and polarization curves of a single EBFC, long-term sustainability of a single EBFC. (i) Voltage output during operation. (j) Power density (using BC/c-MWCNTs/ZIF−8@LAC electrode, with 0.4 mM BPA in the anolyte and 0.05 mM ABTS in the catholyte). Copyright 2020 Elsevier.
(a) Reproduced with permission from ref [169]. (b-d) Reproduced with permission from ref [173]. (e-j) Reproduced with permission from ref [175]. (d) Reproduced with permission from ref [176].

development of effective catalysts for the ORR at the cathode is critical for enhancing the efficiency of AABs. MOFs can potentially address these challenges [155]. MOFs offer a tunable structure, high surface area, and the ability to modify metal nodes, making them ideal candidates for enhancing ORR activity. Their unique properties can help reduce overpotentials, improve cycle life, and minimize energy loss due to parasitic reactions. Although there is limited literature specifically focusing on MOFs for AABs, their success in other metal-air and fuel cell systems suggests that they could be highly effective in addressing these challenges and improving the performance of AABs. Further research into MOFs could unlock their potential in advancing AAB technology.

In conclusion, MOFs serve as versatile electrocatalysts for the ORR in both fuel cells and metal-air batteries. Their structural tunability allows for performance optimization across diverse systems, from acidic PEMFCs to alkaline zinc-air batteries. The key activity and stability metrics for these applications are compiled in Table 2.1, highlighting their significant potential as efficient alternatives to noble-metal catalysts for sustainable energy conversion and storage.

3.1.3. Direct urea fuel cells (DUFCs)

DUFCs utilize the UOR at the anode to generate electricity from urea-rich wastewater [156]. DUFCs are preferred due to their high efficiency, economic viability, eco-friendliness, and sustainability. Operating at low temperatures (ambient to 60 °C), DUFCs allow the direct use of urea as fuel, making them a promising energy generation technology [157]. They offer advantages such as fuel flexibility, low flammability, and easy transportation, compared to other fuel cell types. The principle of DUFCs is similar to PEMFCs, but instead of hydrogen, urea is used as the fuel. Anion exchange membranes (AEM) replace cation exchange membranes (CEM) in DUFCs because urea breakdown produces NH_3. There are two types of DUFCs based on the type of exchange membrane used, with the main difference being the exchanged ions. The energy generation process involves the electrochemical oxidation of urea at the anode, producing N_2, CO_2, and H_2O, along with the release of $6e^-$ [158–161]. These electrons support the ORR at the cathode, where OH^- ions are generated. The OH^- ions move through the AEM toward the anode, as shown in Fig. 11a [162]. DUFCs offer a sustainable solution for clean energy generation and environmental preservation, converting urea from wastewater or urine into electrical energy. A typical adult produces enough urea annually to power a car for 2700 km using a DUFC. The process involves the urea oxidation at the anode and reduction at the cathode. However, challenges remain related to urea's generation, storage, and mobilization, as well as the sluggish kinetics of UOR, which limits the widespread adoption of DUFCs. MOFs can address these limitations by enhancing reaction kinetics, improving electrocatalytic performance, and optimizing urea utilization, making DUFCs more efficient and practical for large-scale applications. For instance, *Putri et al.* developed a NiCo-MOF−74 electrocatalyst crystallized on a porous NiO (p-NiO) film using a solvothermal method for use in the anode of DUFCs (Fig. 11b). A Ni-to-Co ratio of 4:1 showed optimal catalytic activity, outperforming other electrodes like Ni foil and p-NiO. Under optimized conditions with 3.0 M KOH and 1.0 M urea, a current density of 110 mA cm^{-2} and a power density of 4131 μW cm^{-2} was achieved, thanks to the enhanced active surface area. The catalyst showed excellent stability with a cell voltage of ~0.6 V over 15 h of operation (Fig. 11c-d) [163]. Furthermore, *Sayed et al.* reported a Ni-MOF

synthesized directly on CC via a simple ball milling method at room temperature for application as an anode in DUFCs. The Ni-MOF/CC electrode was tested in a two-electrode configuration with a carbon brush cathode and Nafion 117 membrane. The fuel cell with a plain CC anode showed no power generation (Fig. 11e), while the Ni-MOF/CC anode generated power, with a peak output of 5.5 mW/cm^2 at 1 M urea (Fig. 11f). Performance decreased at higher urea concentrations due to increased crossover effects. Fig. 11g-h presents the EIS results for cells using carbon cloth (CC) and Ni-MOF/CC anodes. The data indicates that the Ni-MOF/CC anode exhibits better charge and mass transfer capabilities, as evidenced by the smaller semi-circle radius at medium and low frequencies compared to the CC anode [164].

In another study, *Ravipati et al.* synthesized a Ni-MOF using a one-pot solvothermal method as a bifunctional electrocatalyst for DUFCs. The Ni-MOF/NF electrode showed enhanced UOR performance in 1 M KOH with varying urea concentrations. Fig. 11i shows the CV curves of Ni-MOF/NF with and without urea, revealing its better performance in urea electro-oxidation compared to bare Ni foam. As urea concentration increased, the current density also rose, as seen in Fig. 11j, with a peak current of 188 mA cm^{-2} at 50 mM urea. Fig. 11k demonstrates the Tafel slope of 113 mV dec^{-1} for Ni-MOF/NF, indicating superior catalytic kinetics for UOR over OER, highlighting its promising electrocatalytic activity. Furthermore, Fig. 11l shows CP results for the Ni-MOF/NF electrocatalyst, highlighting its stability in 1 M KOH with 50 mM urea for 20,000 s at 1.56 V (vs RHE). The catalyst retained 71.2% of its capacity, demonstrating excellent stability during UOR. The stability in DUFC was slightly lower due to surface fouling, which can be mitigated with mechanical stirring. Additionally, Fig. 11m shows the CV analysis for Ni-MOF/NF in simulated urine with 0.05 M urea, achieving a current density of 494 mA cm^{-2}. This performance confirms the electrocatalyst's potential for DUFC applications [165].

DUFCs present a promising approach for clean energy production and environmental sustainability by converting urea into electricity. The integration of MOFs as electrocatalysts significantly enhances the efficiency and stability of DUFCs, offering improved reaction kinetics and better charge transfer. MOFs, with their tunable properties and high surface areas, address key challenges such as sluggish reaction rates and low performance at higher fuel concentrations, making DUFCs more practical for real-world applications. These advancements highlight the potential of DUFCs in providing a cost-effective, eco-friendly alternative for energy generation from waste materials.

3.1.4. Biological fuel cells

Biological fuel cells harness the power of biological catalysts, such as microorganisms or enzymes, to convert chemical energy from organic materials into electrical energy. Two key types of biological fuel cells are microbial fuel cells (MFCs) and enzymatic biofuel cells (EBFCs), both of which involve the ORR at the cathode. In MFCs, microorganisms metabolize organic substrates at the anode, generating electrons that flow through an external circuit to the cathode, where ORR takes place. The efficiency of this reaction, influenced by the electrocatalysts at the cathode, directly impacts the cells performance. In EBFCs, enzymes catalyze both the oxidation of fuels at the anode and ORR at the cathode, where oxygen is reduced to water or hydrogen peroxide. Here, we will discuss two key types of biological fuel cells such as MFCs and EBFCs in details.

MFCs offer a promising solution to two major global challenges: the energy crisis and water pollution [166]. These cells operate based on bioelectrochemistry, converting waste organic matter into electricity through the anaerobic respiration process of electroactive bacteria (EAB). At the anode, EABs oxidize organic material from wastewater, releasing electrons, protons, and carbon dioxide [167,168]. The electrons flow through an external circuit to the cathode, where the ORR occurs. The cathode features two potential ORR pathways: the four-electron pathway, which reduces oxygen to water with a higher voltage of 1.229 V, and the two-electron pathway, which produces hydrogen peroxide with a lower voltage of 0.695 V. The PEM allows protons to pass from the anode to the cathode, completing the circuit (Fig. 12a) [169]. The process not only generates electricity but also treats wastewater in an environmentally friendly manner, highlighting the role of MFCs in sustainable energy production and waste management. While MFCs have shown promise in generating green energy, their widespread use is hindered by economic challenges and lower power density compared to other energy sources [170]. Key factors influencing MFC performance include electrode materials, electrolyte composition, microbial species, membrane structure, electron acceptors, and cathode catalysts [171]. Additionally, the slow kinetics of the ORR at the cathode is a major limiting factor [172]. MOFs have the potential to address these challenges by providing highly efficient, tunable catalysts for ORR, improving electrode materials, enhancing electron transfer, and boosting power density in MFCs. For instance, *Zarenezhad et al.* synthesized metalloporphyrin MOF (PCN−600) with 1D channels and a micro/-mesoporous structure, using preassembled [$Fe_3O(OOCCH_3)_6$] building blocks, as a new electrocatalyst for the ORR in MFCs (Fig. 12b). Electrochemical tests showed that PCN−600 outperformed bare graphite electrodes with higher onset and half-wave potentials and faster electron transfer rates. PCN−600 increased power density by 52.72% (179.43 mW m^{-2}) compared to the control (MFC-Ctrl, 88.41 mW m^{-2}) and improved COD removal efficiency to 82.58%, compared to 59.87% in MFC-Ctrl (Fig. 12c-d). The N and M−N structure of PCN−600 enhanced ORR performance, boosting bioelectricity generation in MFCs [173]. Furthermore, *Noori et al.* synthesized amine-functionalized single (Zr) and bimetallic (Zr, Ni) MOFs, NH_2-UiO−66(Zr) and NH_2-UiO−66 (Zr/Ni), and tested them as cathode catalysts for enhancing the ORR in MFCs. Electrochemical tests showed NH_2-UiO−66(Zr/Ni) outperformed both NH_2-UiO−66(Zr) and 10% Pt-C catalysts, exhibiting higher ORR peak current, lower charge transfer resistance, and higher diffusion coefficient. MFC testing demonstrated that NH_2-UiO−66(Zr/Ni) achieved a power density of 0.8 W/m^2 and a coulombic efficiency of 75.4%, outperforming the Pt-C catalyzed MFC [174]. The study suggests NH_2-UiO−66(Zr/Ni) as an efficient ORR catalyst for large-scale MFC applications.

EBFCs convert biological energy into electricity using enzyme-catalyzed redox reactions, making them ideal for sustainable energy. As shown in Fig. 12e, at the anode, enzyme 2 oxidizes the fuel, releasing e^- and H^+. The electrons travel through an external circuit, generating electricity, while the protons move through the membrane toward the cathode. At the cathode, enzyme 1 catalyzes the reduction of O_2, forming water [175]. The process results in the continuous generation of power, making EBFCs suitable for applications like implantable devices due to their miniaturized and eco-friendly nature. However, challenges such as low power output, enzyme stability, and slow electron transfer hinder their efficiency. MOFs can address these issues by enhancing enzyme stability, improving electron transfer, and acting as efficient catalysts, thus boosting the overall performance of EBFCs. For instance, *Li et al.* developed a self-powered biosensor using a biofuel cell as both the power source and sensing system. The successfully encapsulated laccase (LAC) in zeolitic imidazolate framework−8 (ZIF−8) and combined it with a bacterial cellulose (BC)/carboxylated multi-walled carbon nanotubes (c-MWCNTs) skeleton to create a highly flexible electrode (Fig. 12f). In shown in Fig. 12g, a pair of redox peaks was observed at the BC/c-MWCNTs/ZIF−8/LAC electrode in 0.05 mM ABTS solution, confirming direct electrochemistry, with the redox peaks matching previous LAC reports. The BC/c-MWCNTs/ZIF−8@LAC electrode showed higher redox peak currents due to a higher LAC content promoting electron transfer. The CV scans from 50 to 300 mV/s demonstrated a linear relationship between current and scanning rate, confirming bioreceptor diffusion control behavior (Fig. 12h). Fig. 12i shows the single-EBFC generating a voltage signal upon BPA addition, with BC/c-MWCNTs/ZIF−8@LAC acting as both anode and cathode. Finally, Fig. 12j confirms that LAC is the sole contributor to voltage generation, as the non-LAC electrode did not generate any voltage

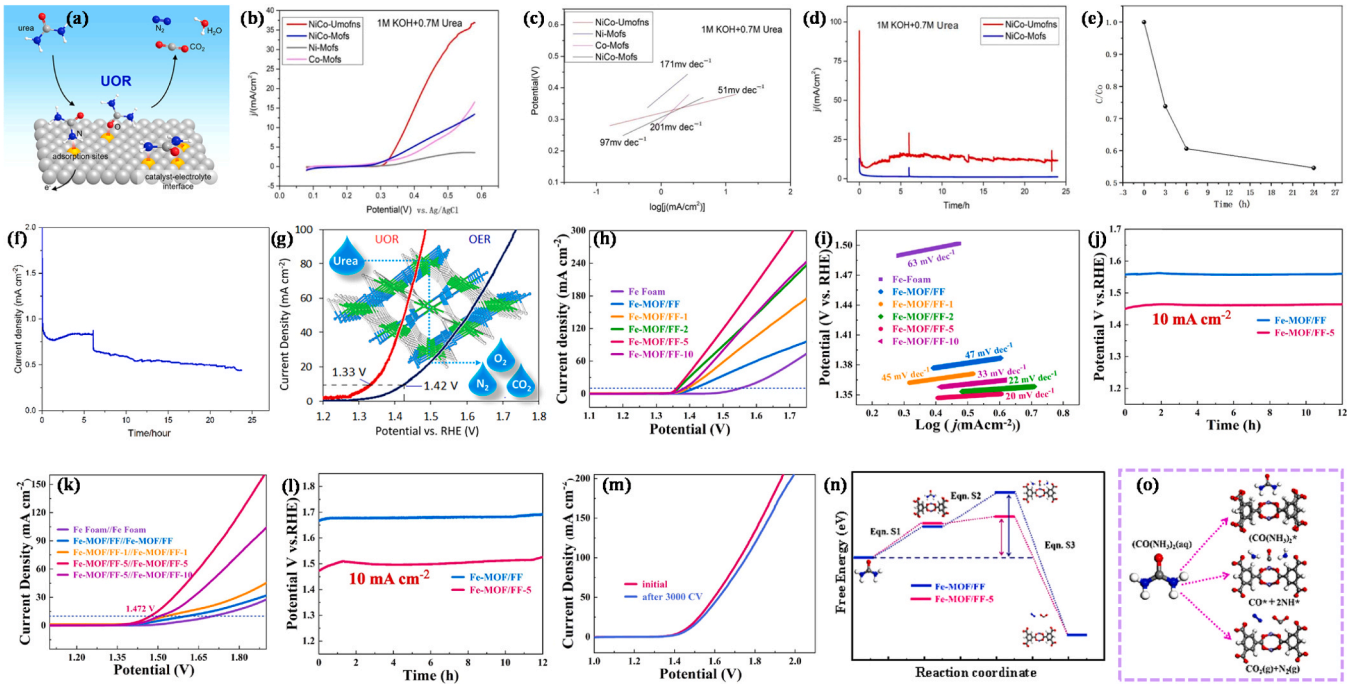

Fig. 13. (a) Schematic illustration of the UOR at the catalyst-electrolyte interface, showing urea adsorption and the formation of N_2, CO_2, and H_2O. Copyright 2022 Elsevier. (b) LSV curves at 10 mV/s and 5 mV/s. (c) Corresponding Tafel slope. (d) I-t curves at a constant potential of 0.5 V. (e) Graph illustrating the change in urea concentration (C) relative to the initial concentration (C_0) over a 24-h period. (f) Current density variation during extended urea electrolysis. (Under CC license). (g) LSV curve showing the UOR and OER performance of $Ni_{0.15}Co_{0.85}$-MOF. Copyright © 2024 American Chemical Society. Urea electrolysis performance: (h) LSV curves and (i) corresponding Tafel slope analysis. (j) CP measurements for Fe-MOF/FF and Fe-MOF/FF−5. (k) Overall urea electrolysis LSV curves. (l) CP curves for extended testing. (m) Stability test after 3000 CV cycles. All measurements were conducted in a 1 M KOH electrolyte with 0.33 M urea, and IR compensation was applied to correct the data. (n) UOR Gibbs free energy diagram. (o) A schematic representation of the urea oxidation electrolysis process. Copyright 2023 Elsevier. (a) Reproduced with permission from ref [179]. (b-f) Reproduced with permission from ref [186]. (g) Reproduced with permission from ref [185]. (h-o) Reproduced with permission from ref [187].

[176].

Both MFCs and EBFCs hold significant promise for sustainable energy production and waste management. The efficiency of these cells, particularly the ORR at the cathode, plays a crucial role in their performance. The integration of MOFs has emerged as a key advancement in addressing some of the challenges faced by these systems, such as low power output and slow electron transfer. MOFs enhance the ORR by improving catalytic efficiency, electron transfer, and enzyme stability. These advancements open up new possibilities for high-performance biofuel cells, especially in small-scale and implantable applications. Overall, the combination of MOFs and biological catalysts offers an exciting direction for the future development of green energy solutions.

3.2. *Urea electrolysis: dual HER-UOR systems*

Urea electrolysis couples the HER at the cathode with the UOR at the anode, enabling simultaneous hydrogen production and wastewater remediation [177,178]. The UOR in alkaline conditions generates non-toxic products like N_2, CO_2, and H_2O ($CO(NH_2)_{2(aq)} + 6OH^- \rightarrow N_{2\,(g)} + 5\,H_2O_{(l)} + CO_{2\,(g)} + 6e^-$) making it a promising strategy for wastewater treatment and clean energy production. As shown in Fig. 13a urea adsorbs onto the catalyst surface, leading to its oxidation. In this process, urea breaks down into CO_2, N_2, and H_2O, with the release of e^-, which can be used to generate electrical energy. The adsorption sites on the catalyst are crucial in facilitating the UOR, allowing the urea molecule to interact with the catalyst surface and undergo the oxidation process. The mechanism occurs at the catalyst-electrolyte interface, making it efficient for clean energy production and wastewater treatment [179]. By lowering the anodic thermodynamic potential from 1.23 V for water oxidation to 0.37 V vs. SHE for UOR, the dual HER-UOR system reduces overall energy consumption, making it a cost-effective and efficient platform for hydrogen generation in urea-assisted water splitting systems [180,181]. In this section, we will discuss urea electrolysis for hydrogen production and dual HER-UOR systems in detail.

3.2.1. *Urea electrolysis for hydrogen production*

The UOR offers a promising alternative to water splitting for hydrogen production, requiring a lower potential than the OER, making it an energy-efficient method for hydrogen generation from wastewater or industrial effluents. Both electrochemical water splitting and urea oxidation are increasingly recognized for their high hydrogen yield and purity [182,183]. However, the 6-electron transfer involved in UOR leads to slow reaction kinetics and high overpotentials, limiting its overall efficiency [184]. MOFs, with their versatile material morphologies, large surface areas, and well-defined pore structures, can address these limitations by enhancing the reaction kinetics, lowering overpotentials, and improving electrocatalytic efficiency [185]. For instance, *Yu et al.* synthesized MOFs (NiCo-UMOFs) using ultrasound and hydrothermal methods to evaluate their activity toward the UOR. Electrochemical tests revealed that NiCo-UMOFs exhibited the best performance, with an onset potential of 0.32 V (vs. Ag/AgCl) and a Tafel slope of 51 mV dec^{-1}, and a current density of 13 mA cm^{-2} at 0.5 V in a 1 M KOH electrolyte with 0.7 M urea (Fig. 13b-c). The stability of NiCo-UMOFs and NiCo-MOFs over 24 h showed current density fluctuations due to bubble formation, but both materials demonstrated good stability, with NiCo-UMOFs achieving a higher current density of 13 mA cm^{-2} and superior catalytic performance toward UOR (Fig. 13d). NiCo-UMOFs, prepared by ultrasound, were used as the anode catalyst on a carbon fiber electrode for urea degradation. In Fig. 13e, the urea concentration dropped from 50 mg/L to 27.6 mg/L after 24 h, achieving 45.4% removal. Fig. 13f shows the current density decreasing from 1.9 mA cm^{-2} to 0.4 mA cm^{-2} due to concentration polarization [186].

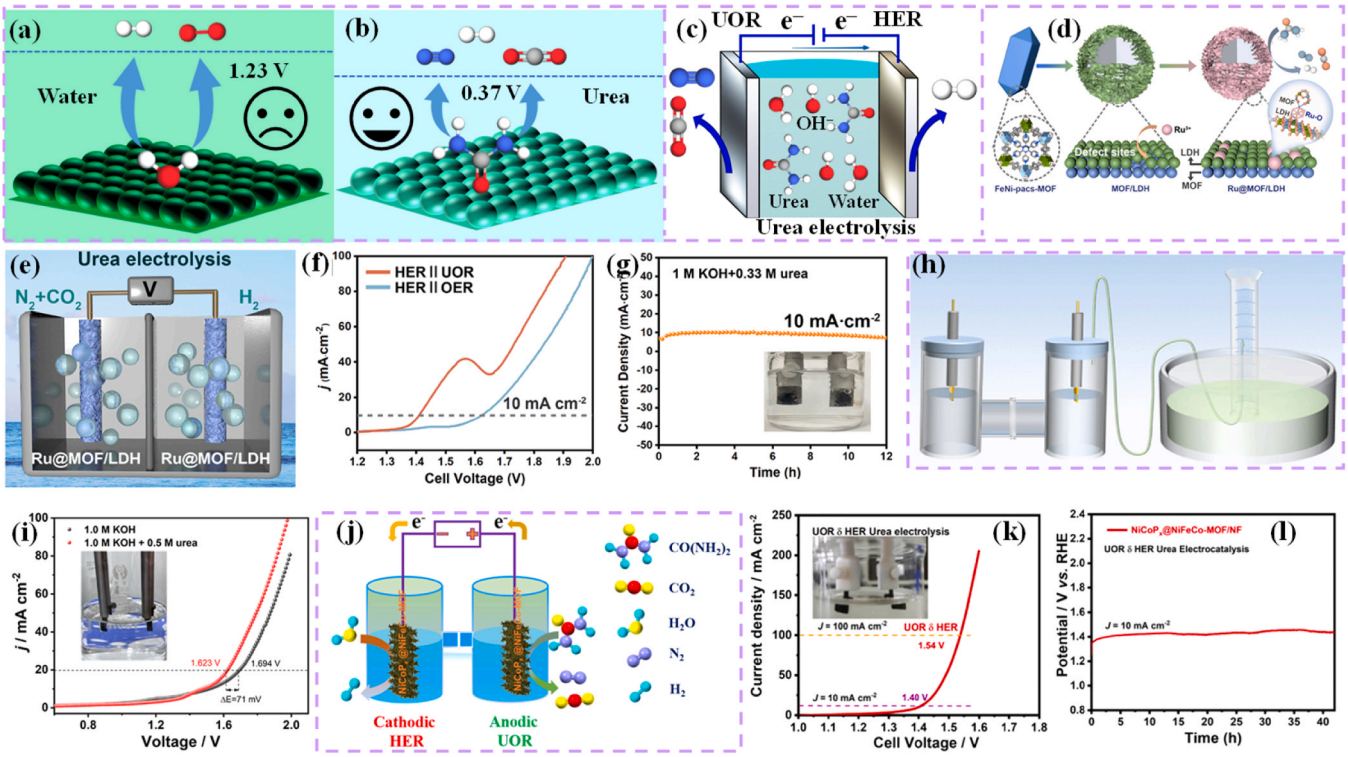

Fig. 14. Schematic illustration of the electrolysis processes of (a) OER (1.23 V) and (b) UOR (0.37 V), highlighting the reduced voltage required for UOR. (c) Schematic of a hybrid electrolyzer for urea electrolysis, illustrating the UOR at the anode and HER at the cathode (d) Schematic of the rational design of Ru@MOF/LDH electrocatalysts for urea electrolysis. (e) Schematic of urea electrolysis and (f) LSV curves of Ru@MOF/LDH as both anode and cathode catalysts. (g) *i-t* test of Ru@MOF/LDH in 1 M KOH + 0.33 M urea for urea electrolysis. Copyright 2025 Elsevier. (h-i) The LSV curves show the overall water splitting performance of NiCoRu−12 in 1.0 M KOH with and without 0.5 M urea, along with a schematic of the water splitting-H_2 gas collection setup. Copyright 2025 Elsevier. (j) Schematic of a hybrid electrolyzer. (k) LSV curve of the NiCoPx@NiFeCo-MOF/NF electrode for urea electrolysis and (l) long-term CP measurement at 10 mA cm^{-2}. Copyright 2022 Elsevier.
(d-g) Reproduced with the permission from ref [191]. (h-i) Reproduced with the permission from ref [192]. (j-l) Reproduced with the permission from ref [193].

Furthermore, *Sanati et al.* synthesized Ni-Co MOFs for UOR, offering an efficient, noble-metal-free solution for hydrogen production and wastewater treatment. The $Ni_{0.15}Co_{0.85}$-MOF exhibited excellent UOR performance with a low overpotential of 1.33 V, TOF of 0.47 s^{-1}, and Tafel slope of 125 mV dec^{-1}, along with outstanding stability over 72 h. It also showed an overpotential of 1.42 V for OER (Fig. 13g). The enhanced performance was attributed to the synergistic effect between Ni and Co, high porosity, and abundant active sites, improving the reaction rate and charge transfer [185]. In another study, *Xu et al.* developed an Fe-MOF electrocatalyst on Fe foam (FF) using hydrothermal synthesis and plasma technology. Plasma treatment tailored the surface morphology and electronic structure, enhancing performance for urea oxidation. The catalyst achieved excellent activity of 1.472 V for urea electrolysis at 10 mA cm^{-2} with 20 mV dec^{-1} (Fig. 13h-i). Additionally, i-t measurements showed that the catalyst-maintained stability for over 12 h of continuous testing, with negligible changes in overpotential (Fig. 13j). Fig. 13k shows the UOR overpotential of 1.472 V, lower than that of the Fe-MOF/FF (+/-) cell at 1.59 V. Furthermore, Fig. 13l, demonstrates stable performance for over 12 h at 10 mA cm^{-2}, with no significant change in overpotential. After 3000 CV cycles, the LSV curve in Fig. 13m remained almost identical to the initial curve, highlighting the exceptional durability of Fe-MOF/FF−5(+/-) for urea electrolysis. For the UOR, the adsorption of urea molecules on the electrocatalyst surface and the dissociation of key intermediates (CO* and NH*) are crucial steps. Fe-MOF/FF−5 demonstrates higher catalytic activity compared to Fe-MOF/FF, as it requires a lower free energy of 2.41 eV to dissociate the adsorbed $CO(NH_3)_2$* into CO* and NH* intermediates, whereas Fe-MOF/FF requires 3.81 eV (as shown in Fig. 13n-o) [187]. This suggests that plasma treatment significantly promotes the desorption of CO* and NH* intermediates.

The enhanced UOR performance of MOF-based catalysts is directly governed by their structural features, which effectively address the sluggish 6-electron transfer kinetics and high energy barriers of key intermediates. As discussed in Section 2, the rate-determining steps in UOR typically involve urea adsorption and the dehydrogenation/decomposition of *$NHCONH_2$-derived intermediates. In NiCo-UMOFs and $Ni_{0.15}Co_{0.85}$-MOF, the bimetallic Ni-Co synergy optimizes the electronic structure, increases active site density, and lowers the adsorption energy of urea, resulting in low onset potential, small Tafel slope, and high current density. The abundant porosity of these MOFs further facilitates urea diffusion and product removal (N_2, CO_2), mitigating concentration polarization. In the plasma-treated Fe-MOF/FF−5, surface modification and electronic tuning significantly reduce the free energy barrier for dissociation of the adsorbed urea intermediate, promoting faster desorption of CO* and NH* species. These structural advantages bimetallic modulation, tailored porosity, and defect/electronic engineering collectively translate into lower overpotentials, excellent stability, and efficient simultaneous hydrogen production and wastewater remediation.

As summarized in Table 2.2, the development of MOF-based electrocatalysts for UOR highlights significant progress in enhancing both catalytic efficiency and stability for hydrogen production. Through synergistic metal centers, porosity engineering, and post-synthetic treatments such as plasma activation, these materials offer exciting prospects for energy-efficient hydrogen production coupled with environmental remediation.

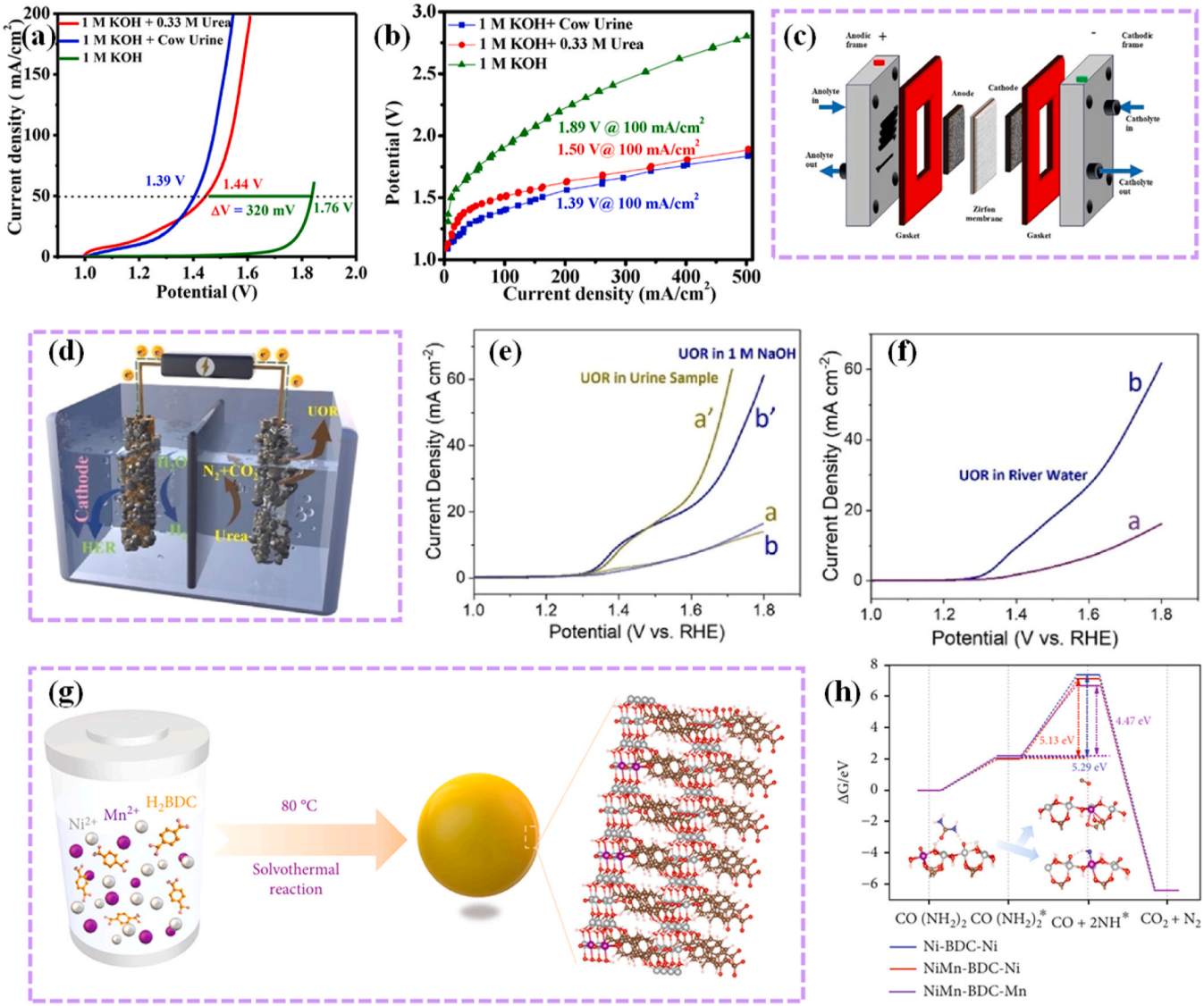

Fig. 15. (a) Linear polarization curves for the two-electrode configuration CoPBO/Co-MOF@NF $^{(+)}$ || $^{(-)}$ CoPBO/Co-MOF@NF in various electrolytes: 1 M KOH + 0.33 M urea, 1 M KOH + cow urine, and 1 M KOH. (b) Linear polarization curves of CoPBO/Co-MOF@NF electrodes in a two-electrode system, tested in different electrolytes (1 M KOH + 0.33 M urea, 1 M KOH + cow urine, and 1 M KOH) within an advanced alkaline electrolyzer. (c) Illustration of an advanced alkaline electrolyzer featuring a zero-gap configuration. Copyright 2025 Elsevier. (d) Schematic illustration of a two-electrode electrolyzer. (e) LSV curves of W@Mo-Cu-MOF-MOCC in human urine with 0.1 M urea (curve a′) and in 1.0 M NaOH + 0.1 M urea (curve b′), along with control experiments without urea (curves a and b, respectively). (f) LSV curves in river water without (curve a) and with 0.1 M urea (curve b). Copyright 2025 Elsevier. (g) Schematic of preparation method of $NiMn_{0.14}$-BDC. (h) Free energy profile of $NiMn_{0.14}$-BDC. Creative Commons Attribution License 4.0 (CC BY 4.0). Copyright © 2022. Exclusive licensee Science and Technology Review Publishing House.
(a-c) Reproduced with permission from ref [202]. (d-f) Reproduced with permission from ref [203]. (g-h) Reproduced with permission from ref [204].

3.2.2. *Dual HER-UOR systems*

Hybrid electrolyzers that combine the UOR with the HER provide an innovative and energy-efficient solution for sustainable hydrogen production. By replacing the conventional OER with UOR, which has a lower thermodynamic potential (0.37 V), the overall energy consumption in the hydrogen production process is significantly reduced (Fig. 14a-b) [178,188]. This approach not only improves energy efficiency but also utilizes urea, a widely available pollutant, as a feedstock for hydrogen generation. Fig. 14c illustrates the urea electrolysis process, where UOR occurs at the anode and HER takes place at the cathode. UOR is thermodynamically favorable potential and its harmless byproduct N_2 make it an eco-friendly alternative to traditional electrolysis methods. Despite the advantages, UOR is complex six-electron transfer mechanism and slow kinetics pose challenges in developing effective catalysts [189,190]. MOFs can address these challenges by providing efficient catalysts with tunable properties that enhance the reaction kinetics and improve the overall performance of hybrid electrolyzers. For instance, *Huo et al.* developed Ru clusters anchored on a MOF/LDH heterostructure using an interface-induced strategy (Fig. 14d). The unique structure, formed by hydrolyzing the MOF precursor, provided abundant sites for Ru confinement, resulting in monodispersed Ru clusters and Ru-O-M bonds at the heterointerface. The Ru@MOF/LDH exhibited excellent bifunctional activity for HER and UOR in alkaline media, achieving ultra-low overpotentials of 84.7 mV for HER and 1.44 V for UOR. Furthermore, the performance of urea electrolysis was tested in a two-electrode alkaline electrolyzer, using the samples as the anode and cathode in a 1 M KOH electrolyte with 0.33 M urea, achieving efficient urea-assisted water splitting at 1.4 V (Fig. 14e-f). The *i-t* test showed excellent durability for urea-assisted water splitting (Fig. 14g) [191]. Furthermore, *Huang et al.* developed

highly effective NiCoRu-X catalysts by introducing Ru into reduced dual MOFs through a mild chemical reduction, preserving multi-hetero-interfaces. The catalysts showed strong UOR activity, with the optimal catalyst performing better in HER. DFT calculations revealed that the hetero-interface promotes dynamic Ni^{3+} species like NiOOH, enhancing UOR. The NiCoRu−12 catalysts demonstrated high electrocatalytic activity and stability for both HER and UOR in 1 M KOH with 0.5 M urea. In a two-electrode system with NiCoRu−12 as both the anode and cathode, the cell required only 1.623 V to achieve 20 mA cm^{-2} in urea-assisted water splitting, compared to 1.694 V in a urea-free solution, indicating improved efficiency with urea. CP showed a 15.8% decay in current after 33 h, stabilizing at equilibrium. The faradaic efficiency in urea-assisted water splitting reached 98.5% at 2.0 V, surpassing traditional water splitting (92.9%) (Fig. 14h-i) [192]. Additionally, *Chen et al.* developed bimetallic $NiCoP_x$@NiFeCo-MOF/NF catalysts for urea-assisted wastewater splitting, combining $NiCoP_x$ nanowire arrays with ultrathin NiFeCo-MOF nanosheets. The core-shell hybrids were prepared through hydrothermal and phosphorization methods. The $NiCoP_x$@NiFeCo-MOF/NF electrode exhibited excellent bifunctional electrocatalytic activity, requiring only 44 mV for HER and 1.37 V for UOR at 100 mA cm^{-2} in 1.0 M KOH + 0.5 M urea. The 3D hierarchical structure, synergistic effects, and enhanced electron transfer contributed to its outstanding performance. DFT calculations revealed that NiFeCo-MOF optimized COO* adsorption on Ni sites, promoting UOR. Encouraged by the excellent UOR and HER performance, a two-electrode urea-assisted water splitting cell was assembled using the $NiCoP_x$@NiFeCo-MOF/NF electrode as both anode and cathode (Fig. 14j). The cell achieved 10 mA cm^{-2} at 1.40 V and 100 mA cm^{-2} at 1.54 V. Long-term stability tests showed steady performance for over 42 h at 10 mA cm^{-2} (Fig. 14k-l) [193]. The hybrid electrolyzers combining UOR and HER provide an efficient and sustainable approach to hydrogen production by using urea, a readily available pollutant, as a feedstock. Despite challenges like slow UOR kinetics, recent advancements in electrocatalyst design have significantly improved efficiency and stability. These developments enhance the performance of urea-assisted water splitting, paving the way for more sustainable hydrogen production in clean energy applications.

3.2.3. *Wastewater treatment*

Electrochemical UOR is an effective method for degrading urea-based pollutants found in

agricultural and industrial wastewater [194–196]. Urea, commonly used in fertilizers, is a major nitrogenous pollutant that can lead to environmental hazards like eutrophication if not properly treated. The electrochemical UOR process offers a sustainable solution by facilitating the oxidation of urea into non-toxic products like N_2, CO_2, and H_2O, while also generating clean energy [197,198]. This makes it an attractive choice for wastewater treatment, especially in areas dealing with high concentrations of urea from industrial runoff or agricultural activities. Furthermore, urine, which contains high amounts of urea, is also a significant contributor to wastewater [199]. With millions of liters of urine being produced daily by both humans and animals, efficient treatment technologies are essential to prevent contamination and pollution [200,201]. MOFs have emerged as a promising solution for improving the efficiency of electrochemical reactions, including urea oxidation. These materials are made up of metal ions or clusters coordinated to organic ligands, forming highly porous structures that offer exceptional surface area and electrocatalytic properties [158]. The ability to tune their structure and chemical composition allows MOFs to enhance reaction rates, improve electron transfer, and increase the active sites for catalytic processes, making them an ideal choice for UOR. For instance, *Bhabal et al.* synthesized a CoPBO/Co-MOF composite electrocatalyst over NF using a solvothermal method and chemical reduction for UOR. The CoPBO/Co-MOF@NF catalyst exhibited excellent bifunctional activity with low potentials of + 1.32 V for UOR and −0.095 V for HER at 100 mA cm^{-2} in 1 M KOH + 0.33 M urea. Under industrial conditions (6 M KOH), the required potential for UOR decreased to 1.14 V, achieving a high current density of 1 A cm^{-2} at 1.35 V, below the thermoneutral voltage for water splitting (Fig. 15a). Electrochemical analysis showed that the composite efficiently combines CoPBO strong OH^- adsorption with Co-MOF urea adsorption, improving UOR performance. To further validate its performance, the catalyst was tested in a two-electrode system using fresh cow urine mixed with 1 M KOH, where salts precipitated but were not filtered. Polarization curves in 1 M KOH with and without urea or cow urine were recorded. The introduction of urea reduced the cell voltage by 320 mV, while cow urine reduced it by 370 mV. At 50 mA cm^{-2}, the cell voltage dropped to 1.44 V with urea and 1.39 V with cow urine, and at 100 mA cm^{-2}, it was 1.52 V for urea and 1.47 V for cow urine. After testing with cow urine in a two-electrode system, the same setup was used in an advanced alkaline electrolyzer with a zero-gap assembly, where CoPBO/Co-MOF@NF (5 cm^2) served as both the anode and cathode, and a Zirfon membrane acted as the separator. Polarization curves were recorded in three different anolytes: 1 M KOH + 0.33 M urea, 1 M KOH + cow urine, and 1 M KOH (Fig. 15b-c). The cow urine was filtered to remove solid precipitates before testing. CoPBO/Co-MOF@NF demonstrated superior performance in cow urine, requiring only 1.39 V to reach 100 mA cm^{-2}, which is lower than the 1.50 V needed for urea and 1.89 V for pure KOH. At higher current densities (0.5 A cm^{-2}), the voltage remained low in both urea and urine solutions (1.89 V and 1.83 V, respectively), significantly lower than the 2.8 V required for water oxidation [202]. Furthermore, *Zheng et al.* developed a W@Mo-Cu MOF-MOCC as a nickel free and noble-metal-free catalyst for the UOR. The catalyst delivered 10.0 mA cm^{-2} at 1.38 V, with a Tafel slope of 77.8 mV dec^{-1}, outperforming other prepared catalysts. Its improved activity was attributed to W-induced lattice modulation, abundant active sites from the globular morphology, and strong W-Mo-Cu interfacial synergy. In practical tests (Fig. 15d), the W@Mo-Cu-MOF-MOCC catalyst required only 1.35 V (vs. RHE) to achieve 10 mA cm^{-2} in human urine with 0.1 M urea (Fig. 15e, curve a′), matching the performance of 1 M KOH with 0.1 M urea (curve b′). An electrolysis cell using urine as the electrolyte operated at 1.35 V, > 200 mV lower than the urea-free system (curves a/b). The catalyst showed stability in 1.0 M NaOH, highlighting its potential for energy and wastewater treatment. Seawater's impact was assessed with 1.0 M NaOH + seawater (Fig. 15f, curve a) and 1.0 M NaOH + seawater + 0.1 M urea (curve b). The catalyst achieved 10 mA cm^{-2} at 1.38 V, demonstrating resilience to $Mg(OH)_2$ and $Ca(OH)_2$ formation, emphasizing the advantages of seawater as an electrolyte [203]. Considering the wide availability of seawater and the increasing shortage of freshwater, this system provides a promising and sustainable approach for treating urea-rich wastewater. Additionally, *Xu et al.* reported a Ni/Mn-based MOF electrocatalyst, $NiMn_{0.14}$-BDC synthesized via a one-step solvothermal method for efficient urea oxidation and wastewater treatment (Fig. 15g). The catalyst achieved 10 mA cm^{-2} at a low potential of 1.317 V and delivered a TOF of 0.15 s^{-1} at 1.4 V, resulting in 81.87% urea degradation in 0.33 M urea solution. Experimental and theoretical results showed that Ni and Mn sites work synergistically, where Mn incorporation lowers the urea adsorption barrier on Ni sites and facilitates key intermediate formation (Fig. 15h) [204]. This study highlights binary active-site engineering in MOFs as an effective strategy for improving UOR kinetics and urea-rich wastewater degradation.

MOF-based electrocatalysts offer a viable and sustainable route for treating urea-rich wastewater via the UOR. The ability to engineer bimetallic sites, tune electronic structures, and create robust interfaces allows these materials to perform efficiently even in complex real-world matrices such as urine and seawater. Key advantages include lowered operating potentials, enhanced degradation efficiencies, and tolerance to common impurities. The demonstrated compatibility with scalable electrolyzer configurations further supports the practical deployment of MOF-mediated UOR for simultaneous pollutant abatement and energy

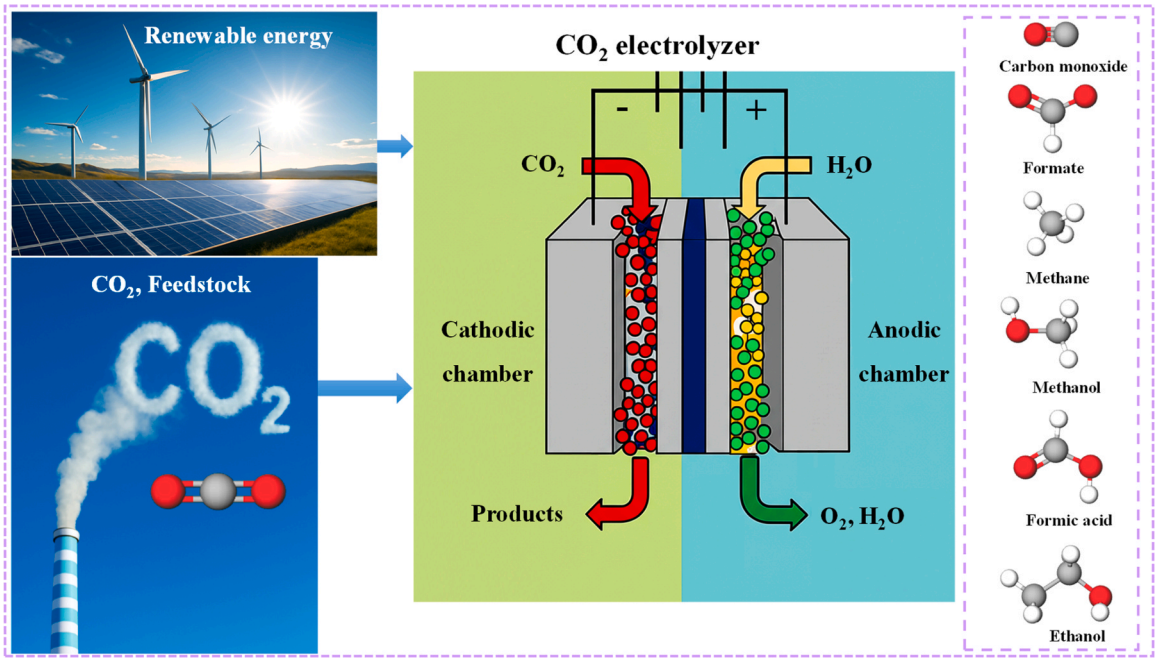

Fig. 16. CO_2 electrolyzer powered by renewable energy, converting CO_2 into value-added products.

recovery. Continued development in catalyst stability, selective degradation, and process integration will be essential to translate these

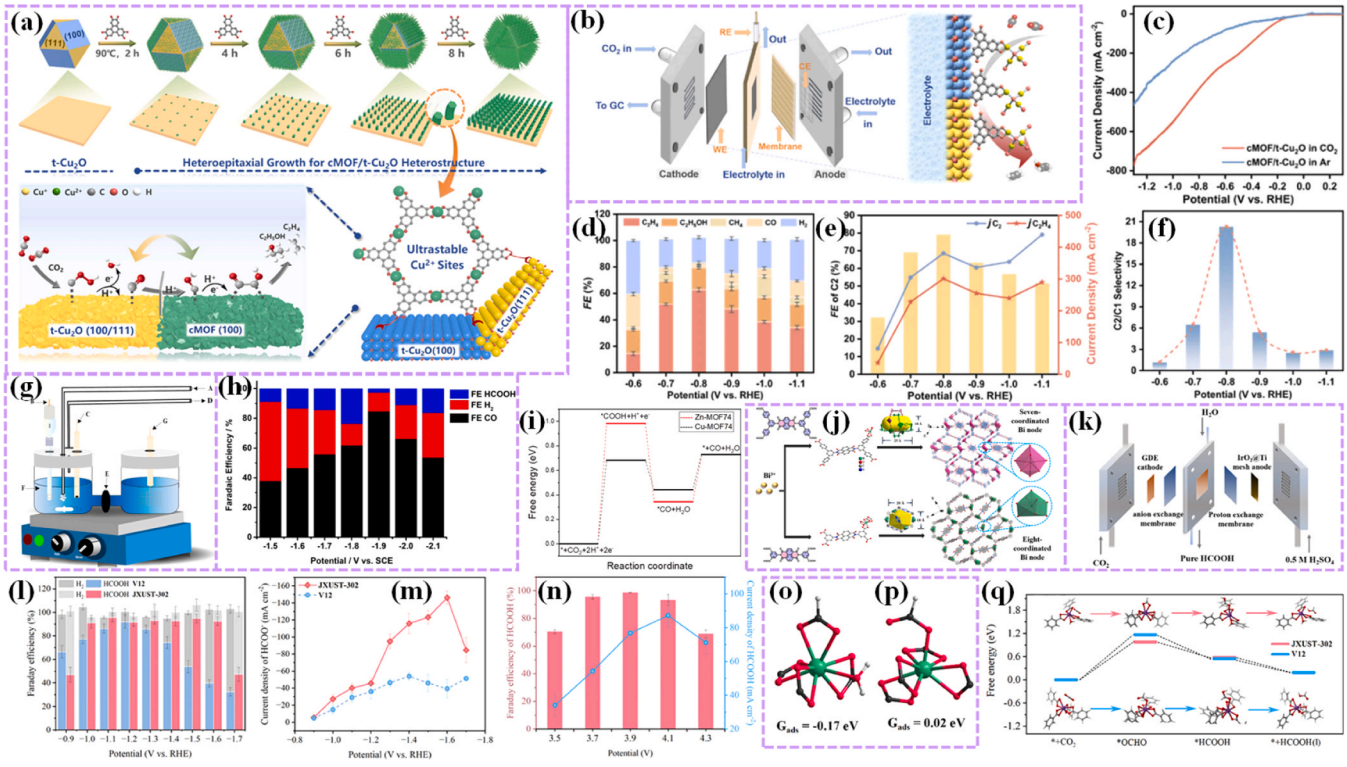

Fig. 17. (a) The c-MOF/t-Cu_2O heterostructure is formed through *in-situ* heteroepitaxial growth, which helps prevent electron accumulation and promotes efficient conversion at the highly charged Cu sites, enhancing the CO_2RR performance. Electrocatalytic CO_2RR performance in a flow cell: (b) Flow cell reactor schematic and lattice facet-junction regions, (c) LSV curves under Ar- and CO_2-saturation, (d) FE at varying potentials, (e) FE for C_2 products and current density for C_2 and C_2H_4, (f) C_2/C_1 ratios at different potentials. Copyright 2025 Elsevier. (g) A schematic illustration of the electrochemical process in H-type cell systems. (h) FE for the CO, H_2, and HCOOH products generated by the Cu-MOF74 catalyst at different potentials. (i) Free energy profile of the CO_2RR for Cu-MOF74 and Zn-MOF74. Copyright 2021 Elsevier. (j) A diagram depicting the synthesis process and structural configurations of JXUST−302 and V12. (k) Schematic of the MEA-SSE device for CO_2RR performance. (l) Faradaic efficiency and (m) current density of $HCOO^-$ (j_{HCOO^-}) for JXUST−302 and V12. (n) Faradaic efficiency of HCOOH (FE_{HCOOH}) and current density of HCOOH (j_{HCOOH}). (o-p) Absorption configurations of *OCHO on the Bi site of JXUST−302 and V12. (q) Schematic representation of the reaction mechanism and the free energy associated with CO_2 reduction to formate for JXUST−302 and V12. Copyright 2025 © Wiley-VCH.
(a-f) Reproduced with permission from ref [221]. (g-i) Reproduced with permission from ref [222]. (j-q) Reproduced with permission from ref [223].

laboratory advances into full-scale wastewater treatment systems.

3.3. CO_2 reduction: selectivity and power-to-X opportunities

Beyond the direct production of fuels, CO_2RR also plays a significant role in several broader applications. CO_2 electrolyzers use renewable electricity to convert CO_2 into fuels and chemicals, such as carbon monoxide, methanol, and formate [205]. In the field of synthetic fuels and chemicals, CO_2RR is crucial for carbon-neutral fuel production, enabling the electrochemical conversion of CO_2 into valuable hydrocarbons or alcohols [206,207]. Additionally, integrated with direct air capture (DAC), CO_2RR facilitates carbon capture and utilization (CCU), helping to convert captured CO_2 into syngas for processes like Fischer-Tropsch synthesis [208–210]. CO_2RR also mimics natural photosynthesis in artificial photosynthesis systems, utilizing renewable energy to generate hydrocarbons. Notably, direct CO_2-to-methanol or CO_2-to-ethanol conversion provides a sustainable alternative to fossil-derived fuels. In this section, we will delve into various CO_2 reduction technologies, including CO_2 electrolyzers, synthetic fuels and chemicals (methanol and ethanol production), CCU, artificial photosynthesis and green hydrogen with carbon utilization.

3.3.1. CO_2 electrolyzers

CO_2 electrolyzers are electrochemical devices designed to convert CO_2 into valuable chemicals and fuels using renewable electricity. By applying an electric current, CO_2 is reduced at the cathode, where it can be transformed into a variety of products such as carbon monoxide, methane, formic acid, and alcohols [211,212]. The CO_2 electrolyzer process helps mitigate CO_2 emissions while also providing a sustainable route for producing carbon-neutral fuels, contributing to a circular carbon economy [213]. As Fig. 16 shows, the CO_2 electrolysis process, which converts CO_2 into valuable products using renewable energy. At the top, it shows the role of renewable energy sources, such as wind and solar power, which supply the electricity needed for the electrolysis process. CO_2 from industrial emissions serves as the feedstock for the reaction [214,215]. The CO_2 is introduced into the cathodic chamber of the electrolyzer, where it undergoes reduction, facilitated by the input of electrons. In this chamber, CO_2 reacts with H^+, and the reduction process produces various carbon-based products, such as CH_4, CH_3OH, $HCOO^-$, CO, and C_2H_5OH. The products are directed out of the electrolyzer through an output for conversion and utilization. On the other side of the system, the anodic chamber, water undergoes oxidation, producing O_2 and H^+, which are essential for maintaining the electrochemical balance of the system [216]. This process not only helps mitigate CO_2 emissions by transforming them into useful chemicals but also enables the integration of renewable energy into sustainable fuel production, offering a cleaner alternative to traditional fossil fuels.

CO_2 is a chemically inert molecule, making the CO_2 challenging due to its high-energy barrier and slow reaction kinetics [217,218]. Additionally, side reactions like hydrogen production can lead to low product selectivity. Over the past decades, various catalysts have been developed for CO_2RR, including metal alloys, metal oxides, nitrogen-doped carbon catalysts, and MOFs. Among these, MOFs are particularly promising due to their porous crystalline structure, large surface area, and high porosity, which enhance CO_2 adsorption and facilitate diffusion to catalytic sites [219]. Moreover, the metal sites and functional groups in MOFs can be easily modified, making them ideal for tailoring catalysts to specific products and improving catalytic efficiency [220]. For instance, *Meng et al.* reported the use of ultra-stable Cu^{2+} sites in a c-MOF/t-Cu_2O heterostructure, synthesized using a combination of wet chemical reduction and solvothermal methods, to enhance CO_2RR selectivity and stability towards C_2 products (Fig. 17a). The c-MOFs strong electron-accepting properties help evacuate accumulated electrons, protecting the highly charged Cu^{2+} sites at the c-MOF/t-Cu_2O interface. The Cu^{2+} sites promote a more favorable hydrogenation pathway, as confirmed by *in-situ* spectra and theoretical calculations. Furthermore, cMOF/t-Cu_2O was tested in a flow-cell with 1 M KOH electrolyte and a constant CO_2 flow of 30 mL/min (Fig. 17b). As shown in Fig. 17c, it exhibited higher current densities under CO_2 compared to Ar, indicating favorable CO_2RR kinetics. At −0.8 V vs. RHE, cMOF/t-Cu_2O achieved a maximum C_2 Faradaic efficiency (FE) of 79.3% (C_2H_4 FE of 62.7% and C_2H_5OH FE of 16.6%) with a current density of 440 mA cm^{-2} and ultra-long stability over 40 h (Fig. 17d-e). It also showed a high C_2/C_1 selectivity of 20.3, highlighting excellent product selectivity (Fig. 17f). DFT calculations confirmed that the Cu^{2+}-Cu^+ interfaces in the cMOF/t-Cu_2O heterostructure facilitate more favorable CO formation and C-C coupling, with lower energy barriers for *CO formation and *COH to COCOH conversion, promoting efficient CO_2RR with improved stability [221]. Furthermore, *Phuc et al.* synthesized Cu- and Zn-MOF74 using nitrate salts of Cu and Zn with 2,5-dihydroxyterephtalic acid via a solvothermal method. The electrocatalytic activity of Cu-MOF74 and Zn-MOF74 was evaluated using LSV in a CO_2-saturated 0.1 M $KHCO_3$ solution with a scan rate of 20 mV/s. The experiments were conducted in an H-type cell (Fig. 17g), with CO_2 bubbled into the cathode compartment for 30 min and a Nafion 115 membrane separating the two compartments, where the cathode contained a glassy carbon electrode and the anode a Pt mesh counter electrode. The FE for CO production on Cu-MOF74 and Zn-MOF74 were measured at various potentials, with Cu-MOF74 achieving a maximum FE of 85% at −1.9 V vs. SCE, which is about twice that of Zn-MOF74 (~45%) (Fig. 17h). Additionally, formic acid was detected in the liquid products after a 6-h chronoamperometry test. DFT calculations were performed, as shown in Fig. 17i, the *COOH formation was identified as the rate-limiting step, with Cu-MOF74 showing a lower energy barrier and better catalytic performance compared to Zn-MOF74 [222]. Additionally, *Wu et al.* developed a new Bi-MOF (JXUST−302) with seven-coordinated Bi nodes using hydrothermal method (Fig. 17j). JXUST−302 and V12 were evaluated for CO_2 reduction in a flow-cell, showing that JXUST−302 outperforms V12 in CO_2RR with a higher current density and Faradaic efficiency for formate production (Fig. 17k-l). JXUST−302 achieved a maximum FE of 95.5% for formate at −1.1 V with a current density of 146.2 mA cm^{-2}, nearly three times higher than V12. In contrast, JXUST−302 maintained a FE over 90% across a wide potential window of 700 mV, whereas V12 only reached this efficiency at −1.2 V. Additionally, using a MEA-SSE device, JXUST−302 demonstrated a high FE of 98.8% for formic acid production (Fig. 17m-n), maintaining over 90% FE for 12 h with a current density of 85.0 mA cm^{-2}, confirming its stability and potential for long-term use. DFT calculations were used to investigate the effect of coordination number on CO_2RR performance. JXUST−302, with a lower coordination number, showed a more favorable interaction with the *OCHO intermediate compared to V12, as indicated by the absorption energy results (Fig. 17o-p). The lower coordination number shifted the p-band center closer to the Fermi level, enhancing O-Bi binding and promoting CO_2 reduction to HCOOH by lowering the Gibbs free energy barrier (Fig. 17q) [223]. These findings highlight the importance of coordination number in optimizing catalyst performance for CO_2RR, providing insights for developing more efficient catalysts.

The catalytic performance of MOF-based materials in CO_2 electrolyzers is governed by the interplay among metal-node coordination, electronic structure, and the local microenvironment, which together dictate intermediate adsorption and reaction pathways. As discussed in Section 2, the selectivity and efficiency of CO_2RR depend critically on the binding strength of key intermediates such as *COOH, *CO, and *OCHO. In the c-MOF/t-Cu_2O heterostructure, the strong electron-accepting ability of the c-MOF stabilizes Cu^{2+} sites at the interface, lowering energy barriers for *CO formation and subsequent C-C coupling, resulting in high C_2 Faradaic efficiency and excellent stability at industrial-level current densities. In Cu-MOF74, the Cu nodes exhibit a lower energy barrier for *COOH formation compared to Zn-MOF74, leading to superior CO selectivity. Similarly, in Bi-MOF JXUST−302, the lower coordination number of Bi centers shifts the p-band center closer to the Fermi level, strengthening *OCHO adsorption and

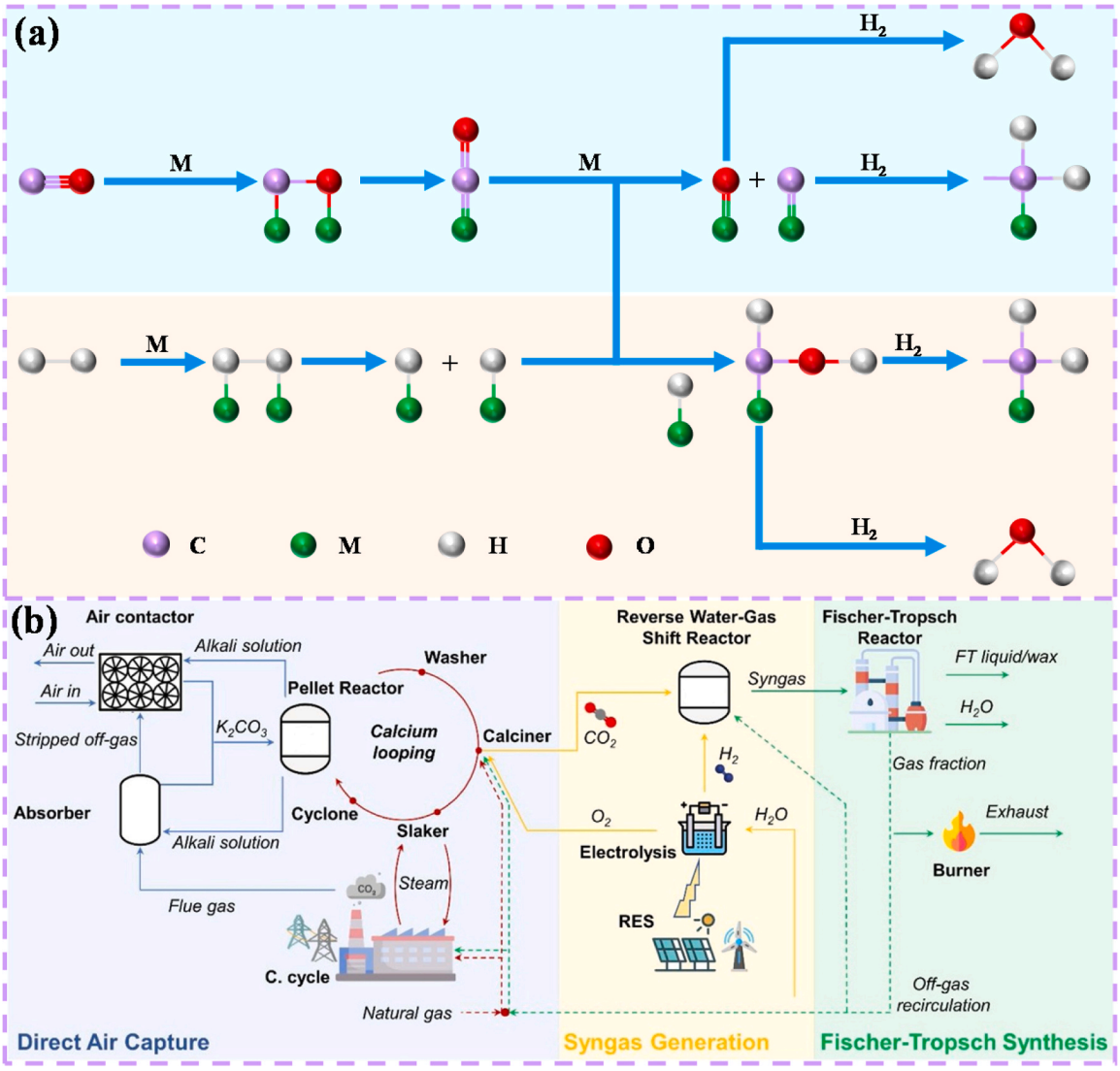

Fig. 18. (a) Carbide mechanism in the FT synthesis. (b) Schematic illustration of DAC integrated with syngas generation and FT synthesis for sustainable fuel production. Reproduced with permission from ref [208]. (Under CC license).

achieving remarkable formate selectivity with good stability in MEA devices. These examples demonstrate how precise control over metal node coordination, heterostructure interfaces, and electronic modulation in MOFs effectively bridges the mechanistic insights with high activity, selectivity, and stability observed in practical CO_2 electrolyzers.

CO_2 electrolyzers utilizing MOF-based catalysts show great promise for advancing CO_2 reduction technologies (Table 2.3). By converting CO_2 into valuable products such as CO, methane, formic acid, and alcohols using renewable electricity, these systems support both climate change mitigation and the development of a circular carbon economy. Continued efforts to optimize catalyst coordination environment, electronic structure, and device integration will be key to realizing large-scale implementation.

3.3.2. *Carbon capture & utilization (CCU)*

CCU and DAC have emerged as vital strategies in addressing climate change [224,225]. CCU involves capturing CO_2 from industrial sources or directly from the atmosphere through DAC technologies. Integrating CO_2RR with DAC not only aids in reducing atmospheric CO_2 levels but also contributes to a circular carbon economy by producing carbon-neutral fuels. The captured CO_2 is utilized for various processes, including CO_2RR, which convert CO_2 into valuable products such as syngas (a mixture of hydrogen and carbon monoxide). Syngas plays a crucial role in *Fischer-Tropsch* (FT) synthesis, where it is used to produce synthetic fuels, such as liquid hydrocarbons, offering a sustainable alternative to fossil fuels. The FT synthesis process has been extensively studied, with significant contributions from researcher like *B.H. Davis* [226,227]. The complex reaction network of FT synthesis involves the formation of carbon-carbon bonds, hydrogenation of CO, and the subsequent production of hydrocarbons. Several mechanisms have been proposed to explain the synthesis, including the carbide mechanism, CO insertion, and the hydroxycarbene mechanism. In the carbide mechanism (Fig. 18a), CO adsorbs onto the catalyst surface, initiating the FT reaction by forming metal carbide (M-C) species. The CO molecule dissociates into carbon and oxygen, and surface hydrogen reacts with the carbon to form C_1 intermediates. These intermediates are hydrogenated to methylene (CH_2) species, which removes the oxygen as water. The enol mechanism suggests the formation of enol groups from CO and hydrogen, which are hydrogenated to form methyl groups and eliminate oxygen as water. Propagation and chain termination steps occur afterward, with the final product distribution depending on the temperature. Higher temperatures favor the carbide mechanism, while lower temperatures promote the formation of enol groups [228]. As shown in Fig. 18b the integration of DAC with FT synthesis for sustainable fuel

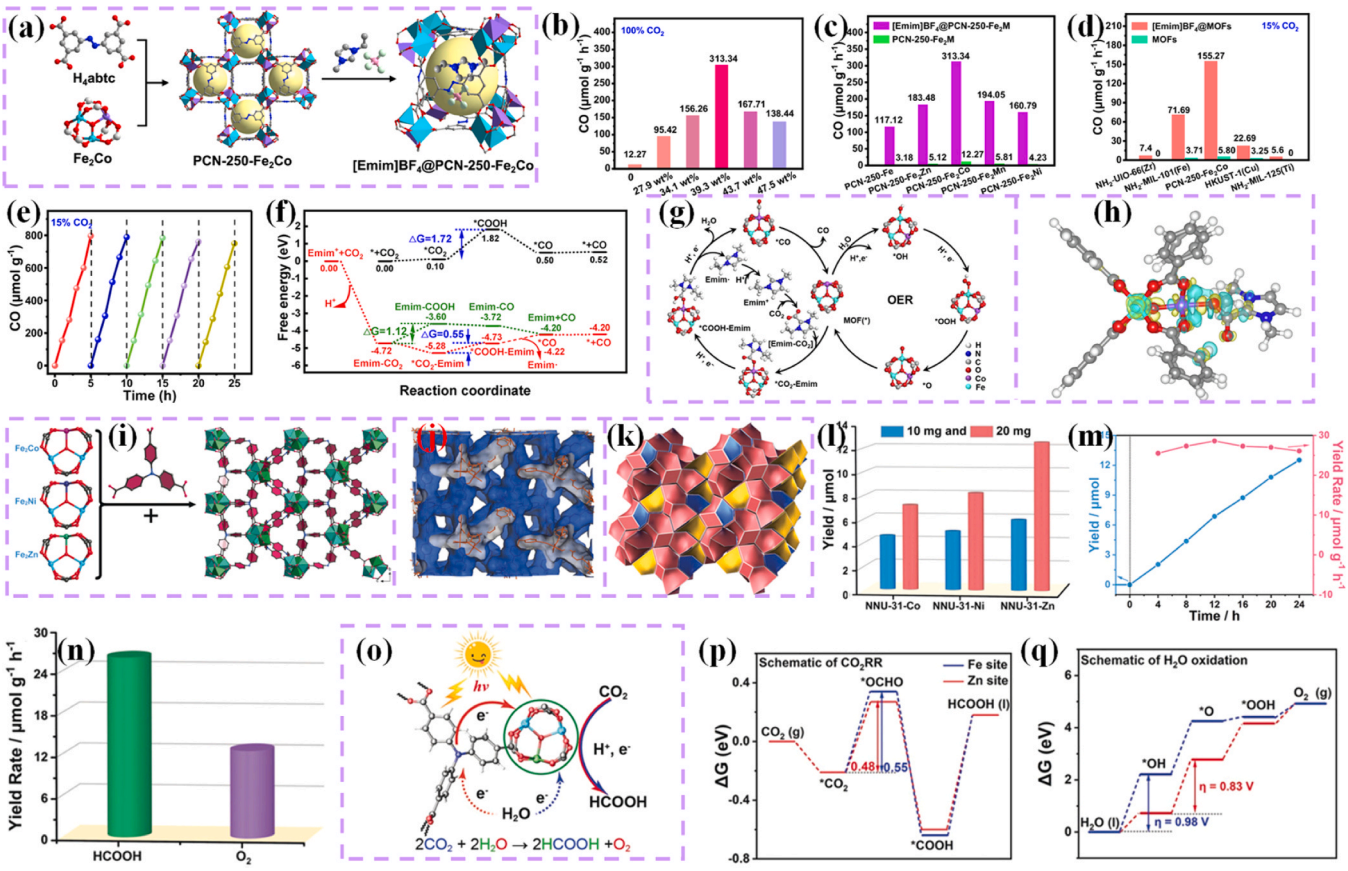

Fig. 19. (a) Fabrication method of [Emim]BF_4@PCN−250-Fe_2M. (b) Photocatalytic performance of PCN−250-Fe_2Co with varying [Emim]BF_4 loadings. (c) Performance of PCN−250-Fe_2M and [Emim]BF_4@PCN−250-Fe_2M. (d) CO_2 reduction performance under diluted CO_2 (15% CO_2, 85% N_2). (e) Stability of [Emim]BF_4(39.3 wt%)@PCN−250-Fe_2Co under diluted CO_2 atmosphere. (f) Free energy profiles of PCN−250-Fe_2Co, Emim + , and [Emim]BF_4@PCN−250-Fe_2Co during photocatalytic CO_2 reduction to CO. (g) Schematic of the photocatalytic CO_2 reduction and H_2O oxidation mechanism. (h) Differential charge density of *CO_2-Emim, with yellow and blue contours showing charge accumulation and depletion, respectively. (Under CC license). (i) 3D structure of NNU−31-M with Fe_2M clusters and TCA. (j) Simulated 3D channel diagram of NNU−31-Zn. (k) Tiling arrangement of NNU−31-Zn. (l) HCOOH yield from NNU−31-M after 24 h with catalyst weights of 10 or 20 mg. (m) Amount (blue) and production rate (orange) of HCOOH over time under visible light irradiation on NNU−31-Zn. (n) Production rates of HCOOH and O_2 using NNU−31-Zn. (o) Mechanism of CO_2 reduction and water oxidation using NNU−31-M. (p) Free energy profile for the CO_2 reduction pathway. (q) Free energy profile for the water oxidation reaction pathway. Copyright 2020 © Wiley-VCH.
(a-h) Reproduced with permission from ref [238]. (i-q) Reproduced with permission from ref [239].

production. It shows the process of CO_2 capture via an absorber, followed by syngas generation through reverse water-gas shift (RWGS) and electrolysis. The generated syngas is then used in a FT reactor to produce FT liquid/wax, completing the process of converting CO_2 and renewable energy sources into synthetic fuels [208]. However, challenges remain in scaling up these processes, particularly with regards to energy efficiency, costs, and the need for improved catalysts. MOFs offer significant advantages as catalysts or catalyst supports, due to their tunable metal sites, high surface area, and porous structure, which facilitate the production of syngas from CO_2. For instance, *Davoodian et al.* evaluated FT synthesis using a cobalt catalyst supported on UiO−66. The Co@UiO−66 catalyst exhibited higher cobalt reducibility due to stronger interactions between cobalt and zirconium atoms, compared to the Co/Zr/SBA−15 catalyst. After 20 h on stream, Co@UiO−66 exhibited a CO conversion rate of 61.6% with a lower olefin-to-paraffin ratio of 0.17, and selectivity towards hydrocarbons was as follows: CH_4 (21.4%), C_2-C_4 (20.8%), C_5-C_{12} (38.2%), C_{13}-C_{19} (12.7%), and C_{20+} (6.9%). In contrast, Co/Zr/SBA−15 showed a CO conversion of 56.2%, a higher olefin-to-paraffin ratio of 0.22, with the following hydrocarbon selectivity: CH_4 (24.9%), C_2-C_4 (18.7%), C_5-C_{12} (35.6%), C_{13}-C_{19} (12.9%), and C_{20+} (8.0%) [229].

While the integration of CO_2RR with DAC presents promising potential for sustainable fuel production through FT synthesis, there remains a significant challenge in scaling these processes efficiently. Currently, MOFs have shown great promise as catalysts, but there is only one study to date on MOFs-based FT synthesis, highlighting the need for further research to optimize these catalysts and expand their applicability in industrial-scale processes.

3.3.3. *Artificial photosynthesis*

Artificial photosynthesis replicates natural photosynthesis to convert sunlight, water, and CO_2 into valuable chemicals and fuels using renewable energy sources like solar power [230,231]. CO_2RR are central to this process, capturing CO_2 from the atmosphere and converting it into hydrocarbons, alcohols, and other chemicals. This method offers a sustainable, carbon-neutral solution for producing fuels while mitigating climate change by reducing atmospheric CO_2 levels. While many semiconductor photocatalysts show high activity in pure CO_2, their efficiency significantly drops under diluted CO_2 conditions, mainly due to slow CO_2 adsorption, which hinders overall reaction kinetics [232,233]. Therefore, developing robust artificial photosynthetic systems capable of enriching diluted CO_2 and enabling in situ reduction is crucial for practical implementation. MOFs are crystalline materials made of organic ligands and metal nodes, offering significant potential in artificial photosynthesis due to their high surface area, structural flexibility, customizable light absorption, and abundant metal sites [234,235].

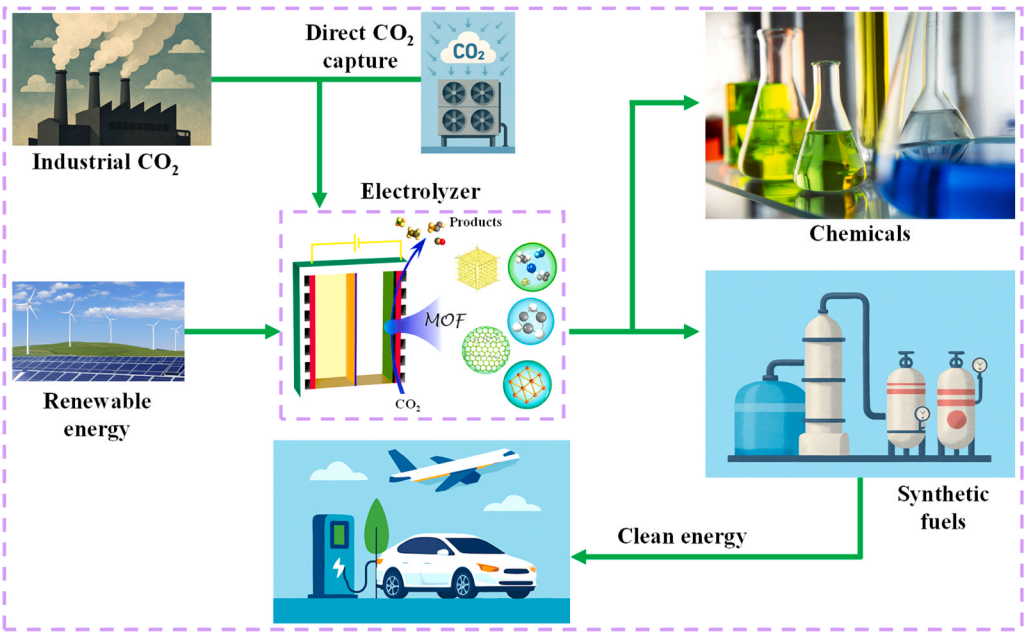

Fig. 20. A schematic illustration of the process of CO_2 reduction for synthetic fuels and chemicals production, where industrial CO_2 emissions are captured and fed into a CO_2 electrolyzer powered by renewable energy. The process, facilitated by MOFs, converts CO_2 into valuable products such as hydrocarbons and alcohols, which are further used in the production of synthetic fuels, clean energy, and chemicals.

Additionally, their porous nature allows for easy incorporation of guest species, enhancing functionality through post-synthetic modifications. In artificial photosynthesis, the organic ligands typically absorb light, while the metal clusters serve as sites for reduction and oxidation reactions [236,237]. For instance, *Wang et al.* developed a new type of host-guest photocatalysts by combining CO_2-enriching ionic liquids (ILs) with photoactive metal-organic frameworks (PCN−250-Fe_2M, M = Fe, Co, Ni, Zn, Mn) using solvothermal method for efficient CO_2 reduction in gas-solid phase (Fig. 19a). The photocatalytic CO_2 reduction performance of [Emim]BF_4@PCN−250-Fe_2Co was evaluated under visible light without the need for additional photosensitizers or promoters. As shown in Fig. 19b, the catalyst with 39.3 wt% [Emim]BF_4 exhibited a CO production rate of 313.34 μmol g^{-1} h^{-1} under pure CO_2, which is approximately 25 times higher than the activity of pristine PCN−250-Fe_2Co. Under diluted CO_2 (15%), it achieved 153.42 μmol g^{-1} h^{-1} , significantly outperforming the pure MOF. The increased photocatalytic activity was attributed to the enhanced CO_2 enrichment by [Emim]BF_4, improving CO_2 adsorption capacity (Fig. 19c-d). Additionally, as shown in Fig. 19e, the catalyst maintained stable performance after five consecutive photocatalytic cycles in both pure and diluted CO_2, with no degradation in structure or morphology. The free energy profiles of the CO_2-to-CO reaction for PCN−250-Fe_2Co, Emim + , and [Emim]BF_4@PCN−250-Fe_2Co (Fig. 19f-g) show that CO_2 adsorbs on Fe_2Co with a ΔG of 0.10 eV. Emim + enhances CO_2 enrichment, forming a bent structure (∠O-C-O = 133.19°), which facilitates CO_2 transfer to Co^{2+} active sites (Fig. 19h). The synergistic effect between Co^{2+} and Emim promotes proton-coupled electron transfer, lowering the RDS energy for *COOH-Emim formation to 0.55 eV, compared to 1.72 eV for PCN−250-Fe_2Co. Finally, *COOH is converted to CO with a minimal energy barrier of 0.02 eV. Fe^{3+} sites also facilitate H_2O oxidation with an RDS of 1.91 eV, completing the artificial photosynthesis reaction [238]. Theoretical studies confirm the experimental observations, showing that the synergistic effect between Co^{2+} and Emim + sites optimize the reaction kinetics, thereby lowering the energy barriers and facilitating efficient CO_2-to-CO conversion. Furthermore, *Dong et al.* developed a series of stable heterometallic Fe_2M cluster-based MOF photocatalysts (NNU−31-M, M = Co, Ni, Zn) using solvothermal method, that enable the overall conversion of CO_2 and H_2O into HCOOH and O_2 without the need for sacrificial agents or photosensitizers (Fig. 19i-k). The visible-light photocatalytic CO_2RR was carried out under pure CO_2 in aqueous solution without additional photosensitizers or sacrificial agents. As shown in Fig. 19l, NNU−31-Zn exhibited the highest HCOOH yield of 12.51 mmol after 24 h of irradiation, outperforming NNU−31-Co (7.17 mmol) and NNU−31-Ni (8.22 mmol). The yield of HCOOH increased almost linearly with irradiation time, as shown in Fig. 19m. Notably, NNU−31-Zn achieved the highest HCOOH yield of 26.3 mmol g^{-1} h^{-1} with nearly 100% selectivity. The O_2 production from the reaction was also detected, and the HCOOH/O_2 ratio was close to 2:1, as shown in Fig. 19n, indicating high selectivity towards HCOOH. DFT and TDDFT methods were employed to study the photoexcitation and catalytic reaction mechanisms. As shown in Fig. 19o, the light absorption efficiency of NNU−31-Zn was significantly better than NNU−31-Ni, with a broad absorption spectrum between 550 and 650 nm, which enhances photocatalytic performance. The free energy calculations for CO_2RR on NNU−31-Zn revealed that the RDS is the hydrogenation from *CO_2 to *OCOH, with a lower energy barrier on the Zn site compared to the Fe site, as shown in Fig. 19p. For water oxidation, the Fe sites were found to have a 2.06 eV energy barrier for the dissociation of *OH to *O, which is the potential-determining step in the process (Fig. 19q). The calculated overpotential for OER was found to be 0.83 V [239]. The developed heterometallic Fe_2M cluster-based MOFs, particularly NNU−31-Zn, demonstrate excellent photocatalytic CO_2 reduction performance and high selectivity towards HCOOH, with theoretical calculations supporting the observed enhanced efficiency and reaction mechanisms. In another study, *Lan et al.* developed a metal–organic framework-based artificial enzyme (MOZ) by integrating active metal centers, proximal amino acids, and cofactors into a tunable MOF monolayer. They designed two libraries of MOZs for photocatalytic CO_2 reduction and water oxidation reactions, optimizing the activity and selectivity by tuning the incorporated amino acids. By combining the optimized MOZs, they achieved complete artificial photosynthesis for the reaction $(1 + n)\ CO_2 + 2\ H_2O \rightarrow CH_4 + nCO + (2 + n/_2)O_2$ [240].

The above studies show significant progress in developing artificial photosynthesis systems, particularly through the integration of MOFs and CO_2-enriching ionic liquids. These systems have demonstrated

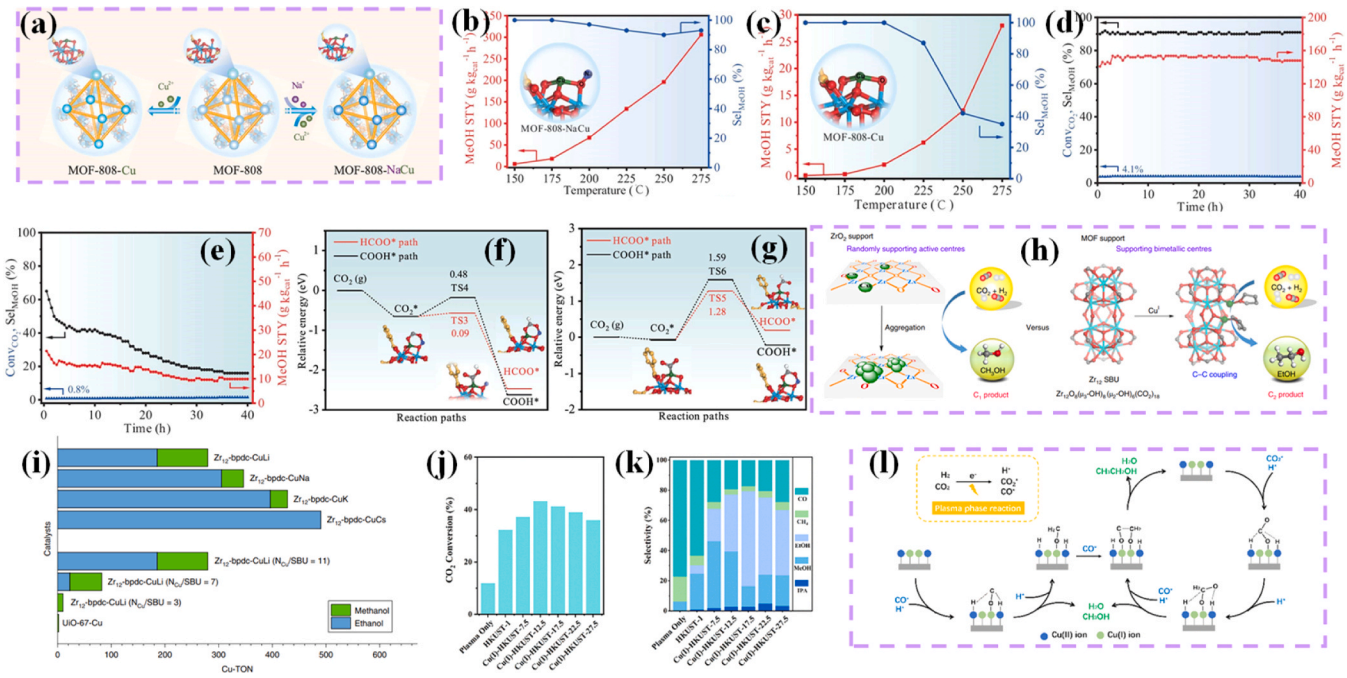

Fig. 21. (a) An illustration depicts the creation of single-atom Cu sites in MOF−808, with or without an Na^+-decorated microenvironment. The catalytic performance for CO_2 hydrogenation was evaluated over MOF−808-Cu and MOF−808-NaCu at temperatures ranging from 150°C to 275°C, with a CO_2/H_2 volume ratio of 1/3 and a pressure of 3.5 MPa. Methanol STY and selectivity are shown in (b) for MOF−808-Cu and (c) for MOF−808-NaCu. For catalyst stability, tests were conducted for 40 h at 250°C with the same CO_2/H_2 ratio and pressure, showing the performance of (d) MOF−808-NaCu and (e) MOF−808-Cu. Energy profiles for CO_2 hydrogenation paths are shown for (f) MOF−808-NaCu and (g) MOF−808-Cu, including the structures of intermediate geometries in the inset. The atoms are color-coded as follows: blue for Zr, red for O, white for H, gray for C of CO_2, and purple for Na. (h) A schematic illustrates Cu supported on ZrO_2 for CO_2 hydrogenation to methanol and bimetallic Cu sites on Zr_{12}-SBUs in a MOF for producing C_2 + oxygenates. Catalytic performance in CO_2 hydrogenation: (i) Turnover numbers (TONs) for alcohols produced on various catalysts, expressed as the number of alcohol molecules formed per copper atom in 10 h. Copyright © 2019 Springer Nature. (j-k) The CO_2 conversion and selectivity in NTP-assisted CO_2 hydrogenation were tested over various catalysts under the following conditions: 35°C, atmospheric pressure, a space velocity of 3.53 min^{-1}, H_2/CO_2 flow ratio of 3:1, 0.5 g catalyst, 30 V input voltage, and a 2-h reaction time. (l) A schematic illustration of the synthesis mechanism of ethanol on the Cu(I)-HKUST-n catalyst with plasma assistance. Copyright 2023 Royal Society of Chemistry.
(a-g) Reproduced with permission from ref [253]. (h-i) Reproduced with permission from ref [260]. (j-l) Reproduced with permission from ref [261].

considerable potential for photocatalytic CO_2 reduction, providing a sustainable pathway for converting CO_2 into valuable fuels and chemicals. Despite challenges such as slow CO_2 adsorption and the need for optimized catalysts under diluted CO_2 conditions. These developments mark substantial progress toward scalable artificial photosynthetic systems, offering a promising pathway for sustainable CO_2 conversion and the generation of carbon-neutral fuels. However, challenges remain in optimizing these systems for industrial-scale applications, with continued research needed to further enhance efficiency, reduce costs, and improve catalyst stability.

3.3.4. *Synthetic fuels & chemicals*

As explained earlier in the CO_2 electrolyzer section, the electrochemical reduction of CO_2 enables the production of synthetic fuels like hydrocarbons and alcohols. These fuels are termed "synthetic" because they are manufactured rather than extracted, and they offer a carbon-neutral pathway when powered by renewable electricity. The CO_2 reduction process is central to synthetic fuel and chemical production, which is key to CO_2RR for carbon-neutral fuel generation [241–243]. As shown in Fig. 20 initially, industrial CO_2 emissions are captured using direct CO_2 capture technologies, a crucial first step in reducing atmospheric CO_2 levels. This captured CO_2 is then directed into a CO_2 electrolyzer, where it undergoes an electrochemical reduction process [244]. Renewable energy, sourced from wind and solar power, drives this reaction, ensuring the process is sustainable and carbon-neutral [245]. MOFs, which act as highly efficient catalysts in the electrolyzer, enable the reduction of CO_2 into valuable products like hydrocarbons, alcohols, and other chemicals. These products are then directed into the production of synthetic fuels and chemicals, providing an alternative to fossil-derived fuels and offering the potential for cleaner, more sustainable energy sources. The resulting products can be used in clean energy applications, such as electric vehicles and aircraft, or as chemical feedstocks [246,247]. By integrating these technologies, this process exemplifies a circular carbon economy where CO_2 is continuously recycled into useful products, mitigating the harmful effects of carbon emissions while fostering a sustainable future. This highlights the immense potential of CO_2RR in addressing the challenges of climate change and energy production.

3.3.4.1. Methanol & ethanol production. CO_2 is a major contributor to the greenhouse effect, prompting efforts to convert it into useful chemicals and fuels through hydrogenation [248]. Copper-based catalysts, like $Cu/ZnO/Al_2O_3$, are commonly used, but face challenges in achieving high CO_2 conversion and methanol selectivity under harsh conditions [249–251]. The effectiveness of Cu-based catalysts depends on the nature of Cu species, with electron-deficient Cu sites ($Cu^{\delta+}$) promoting methanol production, while Cu nanoparticles (NPs) tend to favor CO production [252]. Elevated temperatures accelerate reaction kinetics but lower methanol selectivity due to competing reaction pathways. Therefore, creating stable $Cu^{\delta+}$ support interfaces is essential for efficient CO_2 hydrogenation with high methanol selectivity. For example, *Ling et al.* developed a MOF-based catalyst, MOF−808-NaCu, where single-atom Cu sites are stabilized by Na^+ ions (Fig. 21a). The CO_2 hydrogenation was conducted over MOF−808-Cu and MOF−808-NaCu catalysts at temperatures between 150 and 275°C, showing that Na^+ decoration significantly enhances performance. MOF−808-NaCu achieved a peak methanol space-time yield (STY; grams of methanol per

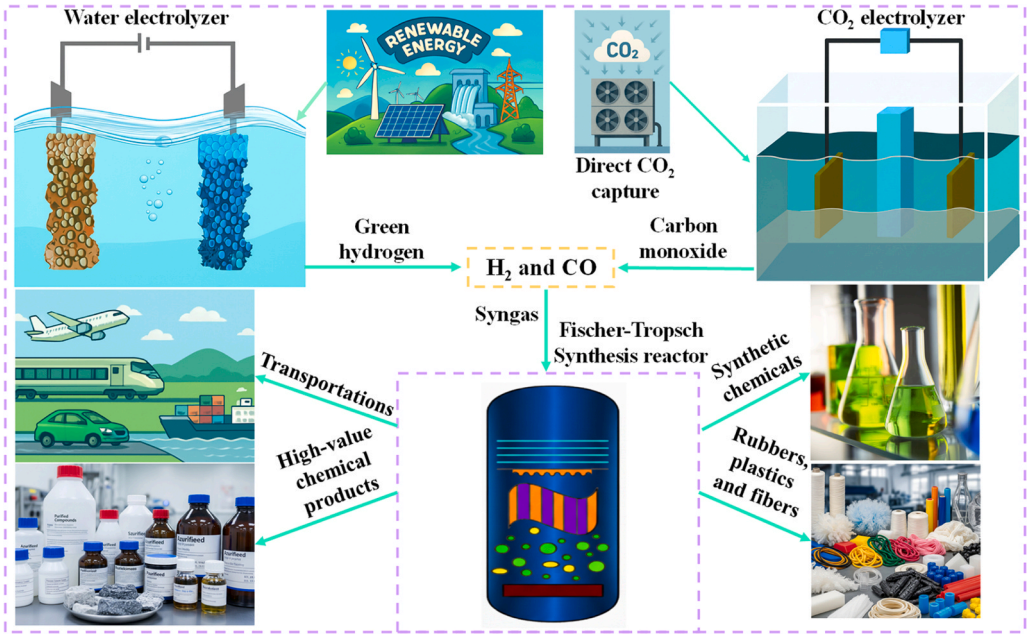

Fig. 22. Schematic of green hydrogen and carbon utilization for power-to-X (PtX) technologies, where renewable electricity drives water electrolysis (HER) and CO_2RR to produce syngas, which is then converted into synthetic fuels, chemicals, and materials through Fischer-Tropsch synthesis.

kilogram of catalyst per hour, $g \cdot kg_{cat}^{-1} \cdot h^{-1}$) of 306 $g \cdot kg_{cat}^{-1} \cdot h^{-1}$ at 275°C (Figs. 21b), 10.9 times higher than MOF−808-Cu (28 $g \cdot kg_{cat}^{-1} \cdot h^{-1}$) (Fig. 21c). At elevated temperatures, MOF−808-NaCu maintained > 93% methanol selectivity, unlike MOF−808-Cu, which shifted to CO production with reduced selectivity (35%) at 275°C. Moreover, MOF−808-NaCu showed excellent stability with nearly unchanged performance after 40 h at 250°C, with 91% methanol selectivity (Fig. 21d), whereas MOF−808-Cu performance degraded (Fig. 21e). These results highlight the critical role of Na^+ in stabilizing Cu sites for improved activity, selectivity, and stability. Additionally, DFT calculations confirm that the formate-mediated pathway, involving the HCOO* intermediate, is the preferred mechanism for CO_2 hydrogenation over both MOF−808-Cu and MOF−808-NaCu with single-atom Cu sites. MOF−808-NaCu exhibits a significantly lower energy barrier (0.09 eV, Fig. 21f) compared to MOF−808-Cu (1.28 eV, Fig. 21g), explaining its superior methanol production at lower temperatures [253]. As temperature increases, Cu nanoparticles form in MOF−808-Cu, slightly raising the energy barrier for the HCOO* formation (3.29 eV), supporting the coexistence of both pathways at higher temperatures.

Furthermore, the hydrogenation of CO_2 to ethanol is a promising but challenging process due to the need to form C-C bonds while preserving C-O bonds [254]. Ethanol from CO_2 has higher energy density than methanol, making it an attractive fuel or fuel additive [255,256]. However, low selectivity for ethanol in CO_2 hydrogenation remains a major hurdle. Copper-based catalysts are effective for methanol production but show low selectivity for C_{2+} oxygenates like ethanol [257]. Modifying copper nanoparticles to introduce Cu^I sites or using alkali metals can improve ethanol selectivity [258]. MOFs with metal clusters, like Zr-MOFs, offer a tunable platform for designing single-site catalysts, potentially enhancing Cu-based catalysts for CO_2-to-ethanol conversion [259]. For instance, *An et al.* report the use of cooperative Cu^I sites on a Zr_{12} cluster within a MOF for selective CO_2 hydrogenation to ethanol. By incorporating an alkali cation, Cs^+, the catalyst activates hydrogen via bimetallic oxidative addition, promoting C-C coupling to produce ethanol (Fig. 21h). The Cs^+-modified MOF catalyst achieved > 99% ethanol selectivity with a turnover number of 4080 in supercritical CO_2 at 85°C, and 490 at 100°C with CO_2/H_2 (1/3) (Fig. 21i) [260]. This study demonstrates the potential of MOFs as tunable platforms for designing earth-abundant metal catalysts for CO_2 conversion. Furthermore, *Zou et al.* demonstrate a novel approach to CO_2 hydrogenation, using non-thermal plasma to activate CO_2 at ambient conditions and a Cu(I)-MOF catalyst for selective ethanol production. The Cu(I)-HKUST−17.5 catalyst achieved 41.2% CO_2 conversion and 62.9% ethanol selectivity (Fig. 21j-k). Control experiments revealed that Cu(I) sites are crucial for C–C coupling and ethanol synthesis. *DRIFTS* analysis suggests a synergistic catalytic mechanism between non-thermal plasma and Cu(I)/Cu(II) sites (Fig. 21l) [261]. The study highlights the potential of non-thermal plasma-assisted catalysis for CO_2-to-ethanol conversion under mild conditions.

The direct hydrogenation of CO_2 to methanol and ethanol offers a sustainable route to reduce CO_2 emissions. The development of catalysts, such as MOF-based Cu and Cu^I sites, significantly enhances CO_2 conversion and selectivity for both methanol and ethanol. The incorporation of alkali metals and the use of non-thermal plasma activation further optimize the reaction, enabling ethanol production under mild conditions. Overall, these advances in catalyst design and reaction engineering highlight the significant progress made toward more efficient and selective CO_2 conversion processes, paving the way for sustainable fuel production and reduced greenhouse gas emissions.

3.3.5. *Green hydrogen & carbon utilization*

The process of green hydrogen and carbon utilization is central to enabling PtX technologies, where renewable electricity is harnessed to convert water and CO_2 into synthetic fuels and valuable chemicals, as illustrated in Fig. 22 [262–264]. This innovative approach begins with the HER, a crucial component of water electrolysis, where renewable energy sources, such as solar or wind, drive the electrolyzer to split water into green H_2 and O_2. Green H_2, produced in this manner, serves as a clean energy carrier for various decarbonization efforts, particularly in transportation. Simultaneously, the CO_2RR captures CO_2 either directly from the atmosphere or from industrial emissions. The CO_2RR process enables the conversion of CO_2 into CO, a key building block for the synthesis of fuels and chemicals. These two processes HER and CO_2RR converge to produce syngas (a mixture of hydrogen and carbon monoxide), which is then utilized in advanced chemical synthesis [265–267]. The syngas is fed into a FT synthesis reactor, where it undergoes conversion into synthetic hydrocarbons such as liquid fuels (diesel, gasoline), waxes, and chemicals. These synthetic fuels provide a

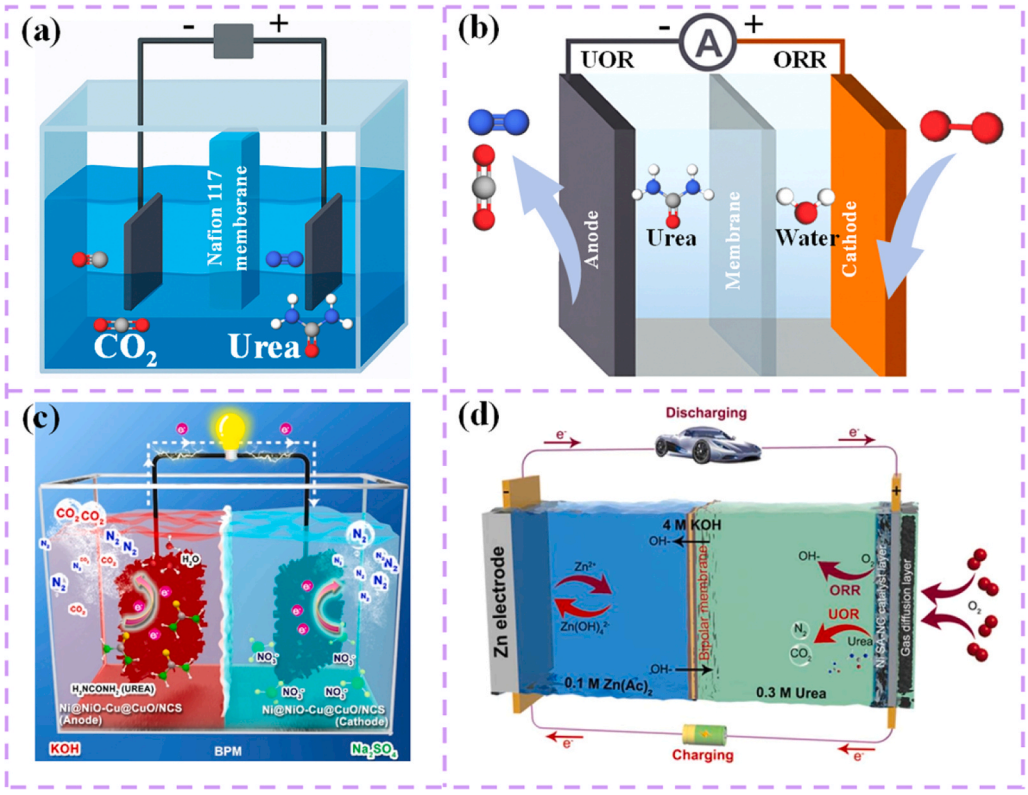

Fig. 23. (a) Schematic diagram of a urea-assisted CO_2 electrochemical cell, illustrating the Nafion 117 membrane separating the anode and cathode compartments, where urea and CO_2 are oxidized and reduced, respectively. (b) Illustration of the UOR at the anode and ORR at the cathode in a urea-based fuel cell with a membrane for ion transport, showing the flow of urea and water in the system. (c) Schematic illustration of a UOR and NRR system, utilizing Ni@NiO-Cu@CuO/NCS catalysts at the anode and cathode. The UOR at the anode involves the oxidation of urea to produce CO_2 and N_2, while the NRR at the cathode reduces N_2 to NH_3, demonstrating a sustainable platform for nitrogen fixation. The bipolar membrane (BPM) separates the two compartments, with KOH and Na_2SO_4 electrolytes supporting the reactions. Copyright 2021 Elsevier. (d) Schematic illustration of a urea-assisted ZABs system, showcasing the Zn electrode and urea solution in both charging and discharging modes. The bipolar membrane, where OH^- ions are transferred across, enabling ORR and UOR at the respective electrodes. The system utilizes Ni-SANC catalysts at the cathode and gas diffusion layers for enhanced efficiency, powering an electric vehicle during discharge and regenerating energy during charge. Copyright 2022 Elsevier.
(c) Reproduced with the permission from ref [276]. (d) Reproduced with the permission from ref [277].

sustainable alternative to traditional fossil fuels for transportation and other sectors, helping to reduce carbon footprints. In addition to fuels, the FT process allows the production of high-value chemicals, which are essential for industries like pharmaceuticals and agriculture, while also enabling the creation of rubbers, plastics, and fibers for use in various consumer goods and manufacturing [268,269]. By utilizing HER and CO_2RR in PtX technologies, the system effectively turns renewable electricity into a cycle of sustainable production, reducing greenhouse gases and generating valuable resources, including fuels and materials, thereby contributing significantly to industrial decarbonization and the circular economy.

3.4. Hybrid and multi-functional fuel cells

Hybrid and multi-functional fuel cells, integrating reactions like UOR, ORR, and CO_2RR, represent an innovative approach to co-generation electrochemical devices [270–272]. These devices can simultaneously generate energy and remediate pollutants, addressing both environmental and energy needs. In UOR and CO_2RR coupled systems, urea is oxidized at the anode, generating electrons and byproducts like CO_2 and N_2, while CO_2RR at the cathode reduces carbon dioxide into useful fuels like formate or carbon monoxide, facilitating both waste conversion and energy production (Fig. 23a) [273]. Furthermore, UOR and ORR involves using urea as a fuel source at the anode, while ORR at the cathode reduces oxygen, enabling low-voltage power generation and providing an efficient alternative to conventional fuel cells (Fig. 23b) [274,275]. Moreover, the UOR and nitrogen reduction reaction (NRR) coupling utilizes urea to provide nitrogen for green ammonia synthesis, offering a cleaner route to industrial applications (Fig. 23c) [276]. Additionally, urea-assisted ZABs combine the oxidation of urea with the air cathode's oxygen reduction reaction, resulting in a system that not only generates power but also removes urea pollutants from wastewater (Fig. 23d) [277]. Despite the promising potential of these systems, no literature has reported their integration with MOFs, which could offer unique structural and catalytic benefits, such as enhanced surface area, tunable porosity, and robust stability for these electrochemical reactions. Thus, incorporating MOFs could be a key step in advancing these multi-functional devices for practical applications in energy and environmental remediation.

4. From Lab to market: deployment challenges and mitigation strategies

The transition of MOFs from laboratory research to commercial electrocatalytic applications requires addressing interconnected challenges spanning technoeconomics, sustainability, and engineering design. Although MOFs have captivated researchers for over 25 years, only a few have successfully transitioned to commercial markets, underscoring the gap between academic promise and practical deployment. Despite their exceptional tunability and catalytic efficiency at the lab scale, large-scale deployment faces barriers linked to synthesis cost, manufacturing scalability, and reliable supply chains. Equally important

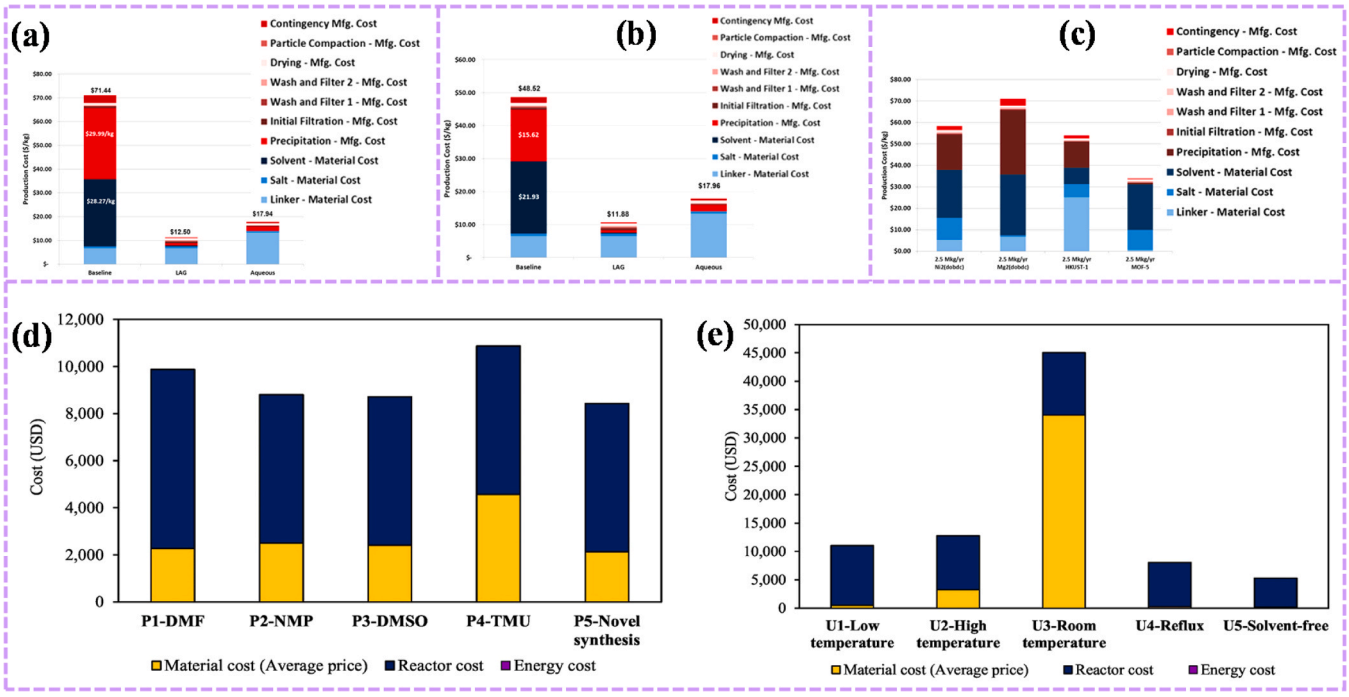

Fig. 24. (a) The baseline total cost for producing 2.5 million kg/year of four MOFs using solvothermal synthesis is broken down into material costs (solvents, metal salts, and linker) shown in blue, and manufacturing costs for each step, represented in red. (b) The detailed cost breakdown for synthesizing Mg_2(dobdc) using baseline industrial-scale solvothermal, LAG, and aqueous synthesis methods, with reported yields of 69%, 69%, and 92%, respectively, is provided. (c) The detailed cost breakdown for synthesizing Mg_2(dobdc) using baseline industrial-scale solvothermal, LAG, and aqueous synthesis methods at 92% yield is shown. Aqueous linker costs are higher than those of the LAG and baseline methods due to the higher salt-to-linker ratios used in the aqueous method. Copyright © 2017 American Chemical Society. TEA of the production routes for (d) PIM−1 and (e) UiO−66-NH_2. Copyright 2023 Elsevier.
(a-c) Reproduced with permission from ref [281]. (d-e) Reproduced with permission from ref [282].

are sustainability considerations, including life-cycle impacts, recyclability, and the development of greener synthesis routes. To bridge these gaps, several strategies have been proposed, including MOF-based hybrids, post-synthetic modifications (PSM), as well as advanced composite systems such as POM@MOF and COF@MOF heterostructures. In this section, we will discuss these aspects in details.

4.1. Technoeconomic assessment (TEA): cost, scalability, and supply chain

Deploying MOFs for electrocatalysis from lab to market involves navigating complex technoeconomic challenges related to cost, scalability, and supply chain logistics. The technoeconomic barriers to large-scale deployment of MOFs in electrocatalysis are strongly influenced by both production and market dynamics. High synthesis costs remain a major challenge, as MOFs have expensive organic linkers, metal salts, and energy-intensive solvothermal processes [278–280]. For example, *Santis et al.* conducted a technoeconomic assessment (TEA) to assess the cost drivers for large-scale production of MOFs for natural gas and hydrogen storage in light-duty vehicles. The analysis focused on four MOFs: Ni-MOF−74, Mg-MOF−74, MOF−5, and HKUST−1, with different metal centers and linkers. Cost analysis for the four MOFs (Ni_2(dobdc), Mg_2(dobdc), MOF−5, and HKUST−1) using solvothermal synthesis revealed that solvent costs dominate material costs, with HKUST−1 being an exception due to the high price of its linker. Material costs contributed more to the total production cost than manufacturing costs, with potential savings from manufacturing the linker for HKUST−1 in-house (Fig. 24a). As shown in Fig. 24b compares the cost breakdown for three industrial-scale synthesis methods applied to Mg_2(dobdc), showing material and manufacturing costs for each method. The linker cost is $6.74/kg for both the baseline and LAG methods, while aqueous synthesis has a higher linker cost of $13.28/kg, which could be reduced by up to 33%. Solvent costs are significantly lower in LAG ($27.87/kg reduction) and eliminated in aqueous synthesis ($28.27/kg reduction). Both LAG and aqueous methods also reduce manufacturing costs by lowering reactor volume and operation times, with cost reductions of $31.92/kg and $31.52/kg, respectively. Yields above 90% have been demonstrated in previous studies, and it is expected that future MOFs will reach similar levels when fully optimized. To account for this, the MOF cost analysis was repeated at 92% yield for all four MOFs and three synthesis routes, eliminating yield-based differences. Fig. 24c shows that both the baseline and LAG methods have reduced costs at 92% yield [281]. While material costs (linker and metal salt) decrease slightly due to higher yield, manufacturing costs see more significant reductions, driven by lower capital expenditures for the same production rate. Furthermore, *Goh et al.* conducted a TEA using a cradle-to-gate approach to evaluate the production of PIM−1 polymer and UiO−66-NH_2 filler for mixed matrix membranes. The study focused on five different synthesis routes. The results revealed that the P5-Novel synthesis for PIM−1 and the U5-Solvent-free synthesis for UiO−66-NH_2 were the most economically viable, demonstrating significant cost reductions. The economic viability of different production routes for PIM−1 and UiO−66-NH_2, with production costs being the main metric. The highest material cost was found in the PIM−1 route using TMU as a solvent (USD 9642/kg), which contributed significantly to the overall cost, though reactor costs were similar across all routes. Surprisingly, the room-temperature synthesis of UiO−66-NH_2 (U3-Room temperature) had the highest production cost at USD 29,521/kg, mainly due to the use of an acid modulator and washing solvent. In contrast, the most cost-effective methods were the P5-Novel synthesis for PIM−1 and the U5-Solvent-free route for UiO−66-NH_2. The estimated production costs for PIM−1 and UiO−66-NH_2 were USD 7780/kg and USD 5252/kg, respectively (Fig. 24d-e). The lower cost of PIM−1 using the P5-Novel

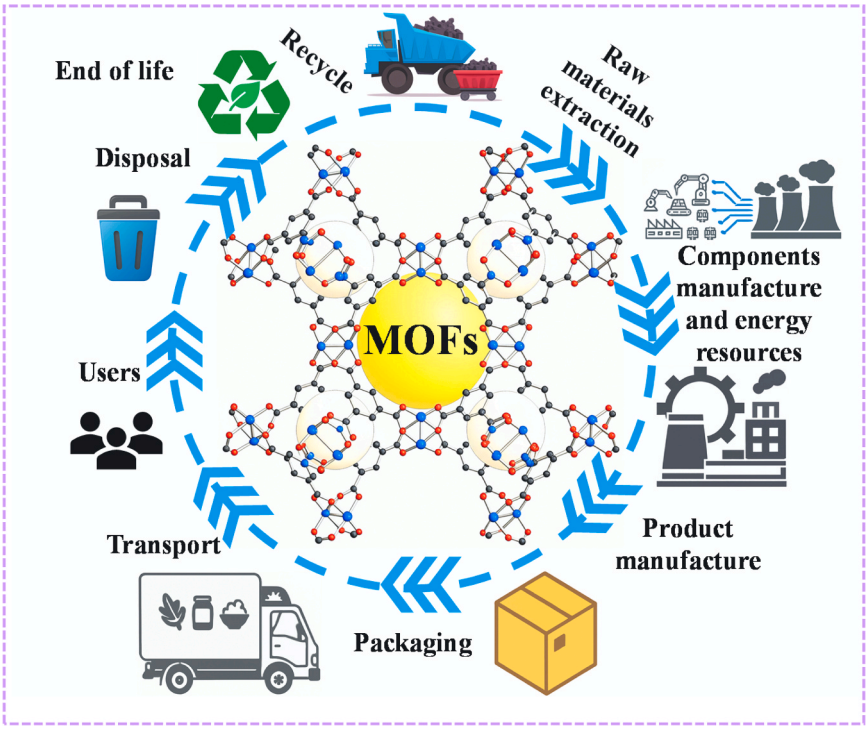

Fig. 25. A lifecycle diagram for a generic product.

route is attributed to the use of a cheaper chloro-analogue of TFTPN, while the solvent-free UiO−66-NH_2 production reduces solvent costs, resulting in a more economical production process [282]. These findings suggest that reducing solvent use or replacing it with greener alternatives can substantially lower both environmental impact and production costs, providing a foundation for developing more sustainable materials.

Scaling production also entails substantial capital expenditure for reactors, purification units, and other specialized equipment, with cost estimates carrying significant uncertainty for early-stage technologies [283]. Operating expenditure further adds to the economic burden, encompassing energy consumption, labor, and waste treatment, along with electrode fabrication and device integration, which require precise engineering. Finally, market price sensitivity poses a competitive hurdle: MOFs must reach cost parity or demonstrate superior performance compared to established catalysts such as platinum or other non-precious metal alternatives to gain traction in electrocatalytic applications [284,285]. Scaling up MOF-based electrocatalysts from the laboratory to industrial applications faces several critical hurdles. Lab-scale synthesis is typically performed in batch processes, which are inefficient for large-scale production, making the transition to continuous reactor systems necessary to ensure both scalability and consistent product quality. Beyond synthesis, material stability poses a major concern, as many MOFs degrade or lose catalytic activity under harsh electrochemical environments such as strongly acidic or alkaline electrolytes [216,286,287]. Even when stability is addressed, performance variability remains a challenge, since properties like high surface area and catalytic activity observed at the lab scale are difficult to replicate at scale due to variations in crystal size, defect density, and impurities. Finally, integration into functional devices including fuel cells, electrolyzers, and other electrochemical platforms requires scalable, standardized methods for coating, deposition, and electrode assembly, which are still underdeveloped [288].

The large-scale deployment of MOFs for electrocatalysis is also constrained by supply chain and market-related challenges. The availability of raw materials is a key concern, as specialized organic linkers and high-purity metal salts are often sourced from a limited number of suppliers, creating vulnerabilities to global disruptions such as geopolitical instability or pandemics. Logistics further complicate commercialization, since many MOFs are moisture-sensitive or thermally unstable, necessitating controlled storage and transportation that increase overall costs. In addition, waste management from synthesis particularly solvent residues and unreacted precursors requires costly treatment or recycling, adding to both operational expenses and the environmental footprint. Finally, limited industrial familiarity with MOFs in electrocatalytic applications hinders market adoption, as potential end-users such as fuel cell or electrolyzer manufacturers may hesitate to integrate MOFs without demonstrated long-term reliability and proven performance at scale. Deploying MOFs for electrocatalysis requires addressing high synthesis costs, scalability bottlenecks, and supply chain vulnerabilities. Recent TEAs highlight the need for significant cost reductions and performance improvements to compete with existing catalysts. By leveraging process intensification, learning curves, and industry collaboration, MOFs can transition from lab to market, supporting applications in sustainable energy.

4.2. Sustainability considerations: life cycle, recyclability, and green synthesis

Sustainability is a critical factor in deploying MOFs for electrocatalysis. From an industrial perspective, it is vital to assess the environmental impacts of MOF synthesis and production by comparing various methods for their sustainability [289–291]. Life cycle assessment (LCA) is an essential management tool for this purpose, providing a comprehensive evaluation of the impacts associated with a product or process across its entire lifecycle, from raw material extraction to end-of-life disposal (Fig. 25) [292–294]. The concept of sustainability, as defined by the United Nations Brundtland Report, is "development that meets the needs of the present without compromising the ability of future generations to meet their own needs," highlighting the need for a holistic approach [295,296].

Traditional MOF synthesis methods often involve hazardous solvents, high energy consumption, and significant environmental footprints [291,297]. LCAs reveal that MOF synthesis typically carries substantial environmental burdens, with solvent-intensive processes

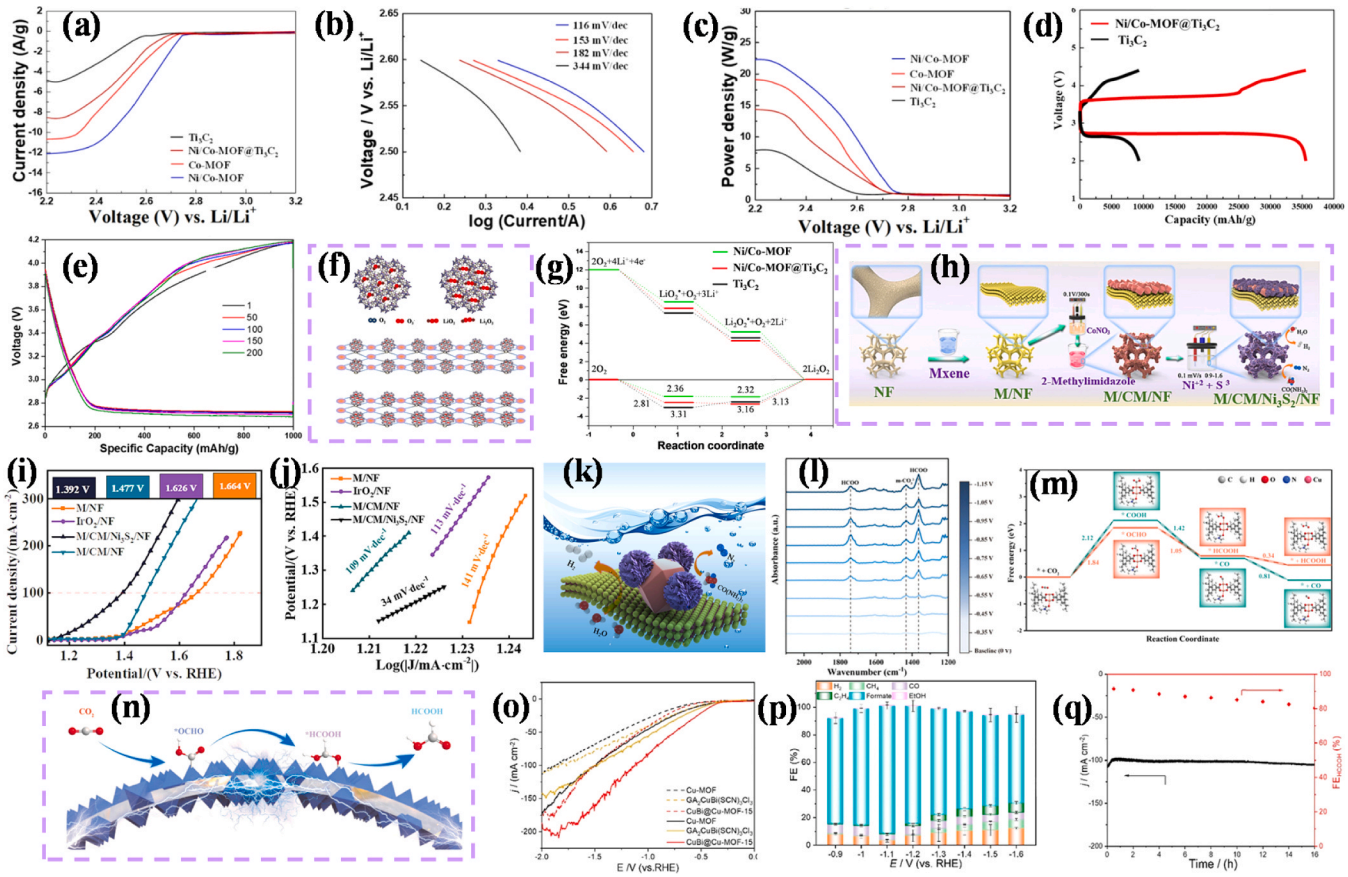

Fig. 26. The ORR analysis of the prepared materials. (a) ORR polarization curves, (b) Tafel plots, and (c) power density curves for Ni/Co-MOF@Ti_3C_2. (d) Initial discharge–charge curves of the Ti_3C_2 membrane and Ni/Co-MOF/Ti_3C_2 membrane at a current of 1000 mA/g. (e) Final discharge/charge voltages of the Li–O_2 batteries. (f-g) The energy diagrams for the ORR and OER processes were calculated. (Under CC license). (h) Synthesis process of M/CM/Ni_3S_2/NF. (i) UOR LSV curves and (j) Tafel slope of M/CM/Ni_3S_2/NF and other prepared catalysts. (k) Catalytic process of M/CM/Ni_3S_2/NF. Copyright 2023 Elsevier (l) *In-situ* infrared spectroscopy at different potentials. (m) Diagram showing the calculated free energy changes for CO_2 reduction to HCOOH and CO. (n) Schematic representation of the CO_2 reduction process. Copyright 2023 © Wiley-VCH. (o) LSV curves of different samples in electrolytes saturated with N_2 (dashed) and CO_2 (solid). (p) FEs of CuBi@Cu-MOF−15 at various applied potentials. (q) Long-term stability test of CuBi@Cu-MOF−15 at −1.1 V vs RHE. Copyright © 2024 American Chemical Society. (a-g) Reproduced with permission from ref [312]. (h-k) Reproduced with permission from ref [313]. (l-n) Reproduced with permission from ref [314]. (o-q) Reproduced with permission from ref [315].

dominating impacts such as global warming potential (GWP), ecotoxicity, and resource depletion [298,299]. In electrocatalysis, improper management of end-of-life disposal increases ecotoxicity risks, potentially offsetting the sustainability gains of green hydrogen production. Furthermore, recyclability remains limited, as many MOFs degrade under harsh conditions, and the use of traditional petrochemical-derived linkers hinders circularity. Waste streams from unreacted solvents also increase treatment costs and environmental burdens. Additionally, conventional synthesis methods often rely on hazardous solvents and high-temperature conditions, leading to high cumulative energy demand (CED) and safety risks [300,301].

LCA serves as a powerful tool for eco-design, identifying high-impact stages in the MOF synthesis process and guiding the development of greener alternatives. For instance, solvent-free methods such as reactive extrusion for ZIF−67 significantly reduce environmental impacts by several orders of magnitude compared to solvothermal routes. For example, *Grande et al.* demonstrated the use of four different synthesis recipes for CPO−27-Ni MOF, including a novel method that exclusively uses water as the solvent. A cradle-to-gate LCA revealed that removing organic solvents from the synthesis process could reduce CO_2 emissions by two orders of magnitude and decrease freshwater toxicity and resource depletion by one order of magnitude. This approach serves as an effective initial screening tool to assess the environmental performance of novel materials and to identify potential solvent recycling strategies or alternative solvents that can minimize the environmental footprint [302]. Furthermore, *Hernandez et al.* investigate the sustainability of MOF technology, focusing on industrial production of ZIF−67 using cradle-to-gate LCA. The study compares four synthesis routes, including the traditional solvothermal method and a novel reactive extrusion technique. The findings demonstrate that reactive extrusion reduces environmental and health impacts by 3–5 orders of magnitude compared to solvothermal synthesis. The LCA highlighted ecotoxicity and global warming as major concerns, with ammonia presence being a significant contributor to the overall environmental burden. The study also stresses the importance of accounting for error sources in LCA models and suggests further improvements for more accurate assessments [303]. The study lays the groundwork for evaluating the sustainability of MOF production and can be extended to other materials to tackle broader environmental and energy challenges.

In electrocatalysis, integrating LCA with performance metrics enables the selection of MOFs like UiO−66 derivatives, where aqueous synthesis reduces energy demand without compromising stability [304,305]. Recyclability can be enhanced through the use of circular precursors and waste-derived MOFs, such as MIL−53(Al) synthesized from PET bottles [306–308]. Strategies like solvent recovery and framework regeneration can also improve recyclability. Green synthesis routes, including solvent-free, microwave-assisted, and mechanochemical methods, further reduce reaction times, energy use, and emissions.

Incorporating these green synthesis strategies can reduce the environmental impacts of MOF production by 50–90%, making them more viable for electrocatalytic applications in sustainable energy systems [309].

The sustainability of MOFs in electrocatalysis is a multifaceted challenge that requires careful evaluation and optimization of synthesis methods. By incorporating LCA, it is possible to identify the most environmentally responsible approaches, minimize negative impacts, and move toward more sustainable production processes. The use of green synthesis techniques, solvent-free methods, and improved recyclability options offer promising pathways to reduce energy consumption, hazardous waste, and environmental burdens. As MOF technology continues to evolve, further research and innovation in both synthesis methods and material properties are essential for advancing the integration of MOFs into sustainable energy systems, making them viable for widespread industrial application while supporting a circular economy.

4.3. Mitigation strategies: MOF hybrids and post-synthetic modifications

To overcome deployment challenges like poor conductivity, instability, and limited active sites in MOFs for electrocatalysis, advanced mitigation strategies include creating MOF hybrids, PSM, as well as integrating MOFs with POMs and COFs. These approaches enhance electrocatalytic performance in reactions like ORR, UOR and CO_2RR. Below, we will explain these mitigation strategies in details.

4.3.1. MOF hybrids

MOF hybrids for electrocatalysis are materials formed by integrating MOFs with other functional materials like carbon-based, graphene, or MXenes [310,311]. These hybrids synergistically combine the high porosity and abundant active sites of MOFs with the superior electrical conductivity and stability of the secondary component. For instance, *Liu et al.* addressed the challenges of sluggish ORR and the accumulation of Li_2O_2 in lithium-oxygen (Li-O_2) batteries by developing a Ni/Co-MOF@MXene hybrid cathode. This free-standing, flexible membrane was synthesized using a layer-by-layer assembly method, combining the conductive, mechanical, and structural advantages of Ti_3C_2 MXene with the catalytic properties of Ni/Co-MOF. The electrocatalytic activity of various materials for ORR was tested in an O_2-saturated 1 M LiTFSI electrolyte at a scan rate of 5 mV/s and an electrode rotation speed of 900 rpm. Fig. 26a shows that Ni/Co-MOF@Ti_3C_2 had the highest half-wave potential (2.46 V), outperforming Ti_3C_2 (2.41 V) and even the commercial Pt/C catalyst. This enhanced performance is due to the synergistic effect of Ti_3C_2 and the Co-N-C catalyst in Ni/Co-MOF, providing more active sites. Fig. 26b shows that Ni/Co-MOF@Ti_3C_2 (182 mV dec^{-1}) had a lower Tafel slope than Ti_3C_2 (344 mV dec^{-1}), indicating faster ORR kinetics. Fig. 26c further confirms Ni/Co-MOF@Ti_3C_2 superior performance, showing higher onset potential and peak current density than Ti_3C_2. Li-O_2 batteries with Ti_3C_2 and Ni/Co-MOF@Ti_3C_2 (10 μm thick) cathodes showed significant performance differences. Fig. 26d reveals that the Ni/Co-MOF@Ti_3C_2 cathode achieved a high capacity of 36,125 mAh/g, far exceeding Ti_3C_2 8856 mAh/g. Furthermore, Fig. 26e shows stable charge-discharge cycles for Ni/Co-MOF@Ti_3C_2 at 1000 mAh/g. Rate tests demonstrate that Ni/Co-MOF@Ti_3C_2 maintains superior performance up to 1 C, while Ti_3C_2 fails at 0.5 C. This indicates better Li^+, O_2, and electron transfer with Ni/Co-MOF@Ti_3C_2, enhancing Li_2O_2 processing. DFT simulations optimized the adsorption of LiO_2 and Li_2O_2 on Ni/Co-MOF@Ti_3C_2, showing strong coordination between Li atoms and Ni/Co sites (Fig. 26f-g). The LiO_2 Li atom coordinates with Ni or Co, while the O atoms interact with Ni, Co, and Ti, promoting Li_2O_2 formation and decomposition, boosting battery stability. Ni/Co-MOF exhibited the lowest overpotential (2.38 V) compared to Ni/Co-MOF@Ti_3C_2 and Ti_3C_2. The Gibbs free energies for Ni/Co-MOF, Ni/Co-MOF@ Ti_3C_2, and Ti_3C_2 were 2.36 eV, 2.81 eV, and 3.31 eV, respectively. Ni sites serve as primary active sites, with Co sites contributing when Ni sites are saturated [312]. The combination of Ni, Co, and Ti reduces overpotential, enhancing catalytic activity and cycle stability, while Ti_3C_2 may improve performance by providing additional electron channels.

Furthermore, *Wang et al.* developed a bifunctional catalyst for the UOR by electrodepositing Ni_3S_2 species onto a CoMOF on MXene (Fig. 26h). The resulting M/CM/Ni_3S_2/NF catalyst exhibited excellent electrocatalytic performance for UOR, requiring an overpotential of 1.392 V to achieve 100 mA cm^{-2} and a Tafel slope of 34 mV dec^{-1} (Fig. 26i-k). The catalyst further demonstrated excellent 25 h stability at 50 mA cm^{-2}. DFT calculations indicated that the coupling of MXene, CoMOF, and Ni_3S_2 optimizes the free energy of urea adsorption, enhancing the catalyst performance [313].

MOFs hybrid materials have emerged as promising catalysts for the electrocatalytic CO_2RR. For instance, *Liu et al.* developed a dual- MOF copper-based catalytic electrode via *in situ* synthesis on a foamed copper substrate for efficient electrocatalytic CO_2 reduction. The MOF-on-MOF structure prevents H_2 and CO formation, enhancing HCOOH selectivity. By replacing expensive and fragile GDEs with durable poly(tetrafluoroethylene) (PTFE), the reactor design improves stability, durability, and electrode replaceability. The optimized reactor achieved a Faradaic efficiency of 89.2% in neutral medium and a current density of 26.1 mA cm^{-2} in the flow cell, matching GDE performance while ensuring long-term stability. PTFE enhances the gas channels service life and supports effective catalysis. *In-situ* FTIR spectra (Fig. 26l) revealed a peak at 1363 cm^{-1}, corresponding to formic acid species ($HCOO^-$), which peaked at −0.95 V. The 1743 cm^{-1} peak was observed only in Bi@$Cu_{1/2}$, indicating dual pathways for formic acid generation. The structure improved HCOOH selectivity by inhibiting side reactions. DFT calculations showed CO_2 adsorbs as *OCHO, favoring HCOOH formation over CO. In 0.5 m $KHCO_3$, Bi@$Cu_{1/2}$ enhanced CO_2 reduction while suppressing H^+ reduction, promoting HCOOH generation (Fig. 26m-n) [314]. Additionally, *Wang et al.* developed Cu-MOF and CuBi double-perovskite composite catalysts for CO_2 electrochemical reduction to HCOOH. The CO_2RR performance of CuBi@Cu-MOF-X (X = 5, 10, 15, 20) catalysts was evaluated in a 1 M KOH electrolyte using a flow-cell device. The main product was liquid-phase HCOOH, with minor gas products. LSV results showed that CuBi@Cu-MOF−15 had the highest current density and most efficient CO_2RR (Fig. 26o). Tafel slopes were lowest for CuBi@Cu-MOF−15 (38.7 mV dec^{-1}), indicating optimal electrocatalytic kinetics. Product distribution revealed a maximum FE_{HCOOH} of 93% at −1.1 V (Fig. 26p). Controlled potential electrolysis confirmed that CuBi@Cu-MOF−15 achieved 93% FE_{HCOOH} at −1.1 V, outperforming other catalysts. The CuBi@Cu-MOF−15 catalyst demonstrated excellent CO_2RR performance for HCOOH production across a wide potential range (−0.9 to −1.6 V vs RHE), especially for high HCOOH generation rates. Additionally, after 16 h of continuous reaction, the FE of HCOOH and current density showed only slight degradation, highlighting its strong durability (Fig. 26q) [315].

MOF hybrid materials offer significant advantages in electrocatalysis due to their high surface areas, tunable structures, and abundant active sites. By combining MOFs with other functional materials, such as conductive carbon-based materials or MXenes, these hybrids enhance electrical conductivity, stability, and overall catalytic performance. The synergistic effects of the combined components improve the efficiency of various electrochemical reactions, including CO_2 reduction, UOR, and oxygen reduction, while also addressing challenges like poor conductivity and limited active sites. The versatility of MOF hybrids makes them promising candidates for advancing energy conversion and storage technologies, offering pathways to more efficient and durable electrocatalysts for a range of applications.

4.3.2. Post-synthetic modifications

PSM of MOFs are a powerful strategy to fine-tune the properties of these materials for specific applications, particularly in electrocatalysis. MOFs are inherently versatile due to their tunable structure, high

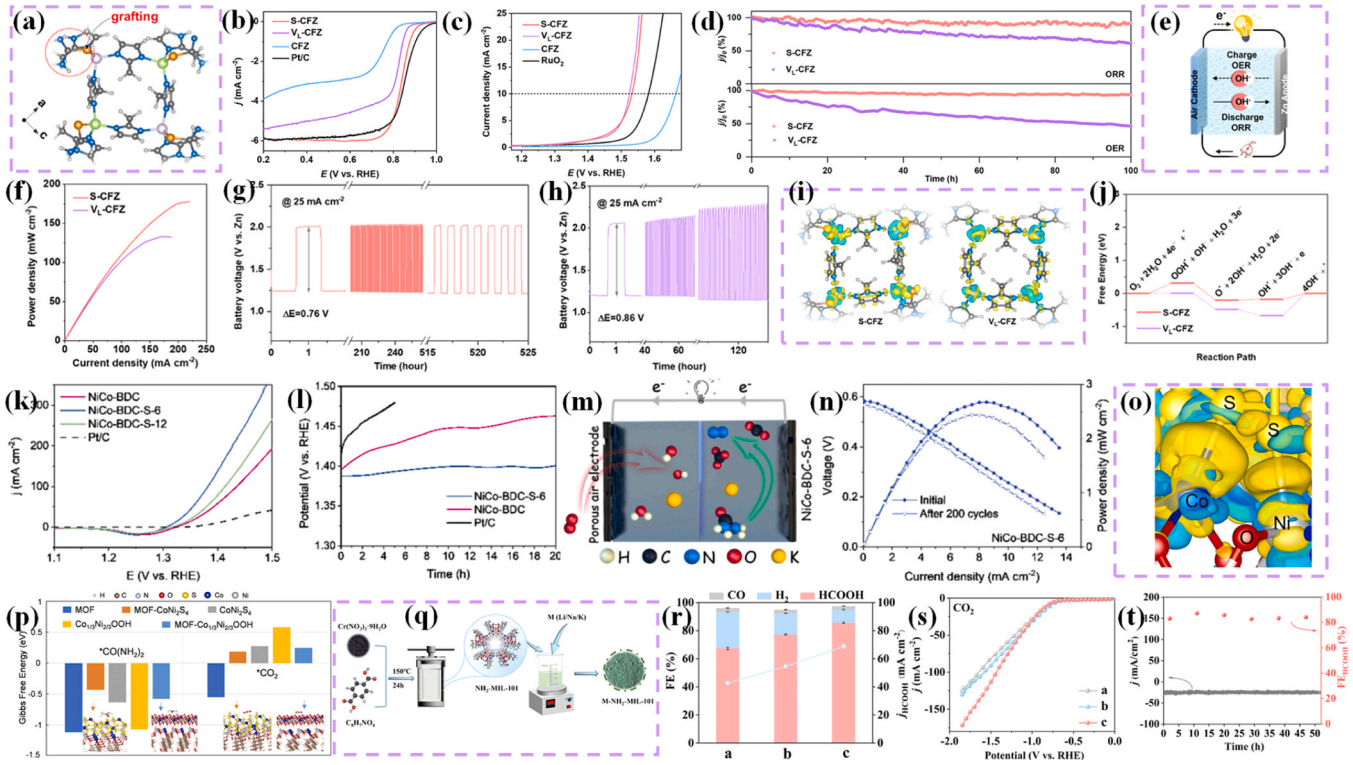

Fig. 27. (a) A schematic illustrating the grafting of S-based groups onto VL-CFZ. The electrochemical performance in a half-cell at 25 °C: (b) ORR LSV, (c) OER LSV curves, and (d) chronoamperometric response for ORR and OER at a constant overpotential. Performance evaluation of ZAB: (e) Schematic of the ZAB configuration, (f) power density plots for S-CFZ and VL-CFZ electrodes, and (g-h) galvanostatic cycling stability of ZABs with the S-CFZ electrode. (i) The charge density distribution and (j) Gibbs free energy diagrams for ORR and OER of S-CFZ and VL-CFZ. Copyright © 2022 American Chemical Society. (k) LSV curves in 1 M KOH with 0.33 M urea at a scan rate of 5 mV s^{-1}. (l) CP curves in 1 M KOH with 0.33 M urea at a constant current density of 20 mA cm^{-2}. (m) Schematic of a urea fuel cell configuration. (n) Polarization and power density curves before and after CV cycles for urea fuel cells using Pt/C as the cathode and NiCo-BDC-S−6 as the anode catalyst. (o) Enlarged differential charge density distribution of the MOF-$CoNi_2S_4$ heterostructure, with yellow and blue representing positive and negative electron densities, respectively, at an iso-surface value of 0.0015. (p) Free energy diagram for the adsorption of urea and CO_2 molecules during the UOR process. Copyright 2022 Elsevier. (q) Schematic of the synthesis process for M-NH_2-MIL−101. (r) FE and partial current densities of HCOOH at −1.3 V vs RHE using CO_2-saturated 0.5 M $NaHCO_3$ as the electrolyte in an H-type electrolytic cell. (s) LSV curves under CO_2 atmosphere for Bi, Bi-NH_2-MIL−101, and Bi−0.1 K-NH_2-MIL−101 at a scan rate of 100 mV s^{-1}. (t) CO_2RR stability test of Bi−0.1 K-NH_2-MIL−101 at −1.0 V vs RHE in an H-type electrolytic cell. Copyright 2025 Elsevier.
(a-j) Reproduced with permission from ref [319]. (k-p) Reproduced with permission from ref [320]. (q-t) Reproduced with permission from ref [321].

surface area, and ability to host a wide variety of functional groups. However, their catalytic activity can often be limited by factors such as low conductivity, poor stability, or insufficient active sites for specific reactions. To address these challenges, PSMs such as metal doping, functionalization with ligands, and integration with conductive materials have emerged as key techniques to enhance the catalytic performance of MOFs [316–318]. These modifications allow for precise control over the electronic properties, active sites, and stability of MOFs, making them highly efficient for important electrocatalytic reactions. For instance, *Jiang et al.* proposed a linker compensation strategy to modify the intermediate adsorption energy on the Co-Fe zeolitic imidazolate framework (CFZ), enhancing its catalytic performance. A Co^{2+} center coordinated with imidazole ligands forms monoclinic zeolitic imidazolate frameworks, while Fe incorporation generates linker vacancies (VL) in VL-CFZ, improving conductivity and creating mesopores. These vacancies are compensated by grafting S-containing groups through S-Co/Fe coordination via a low-temperature hydrothermal reaction with thiourea (Fig. 27a). VL-CFZ showed improved ORR and OER performance compared to CFZ, with a half-wave potential of 0.82 V for ORR and 1.52 V at 10 mA cm^{-2} for OER. S-CFZ further enhanced ORR with a half-wave potential of 0.85 V and higher current density, rivaling Pt/C (Fig. 27b). It also outperformed RuO_2 in OER activity (Fig. 27c) and showed excellent stability with 91% retention for ORR and 93% for OER over 100 h (Fig. 27d), demonstrating its high bifunctionality. Building on its strong electrocatalytic performance and stability in alkaline solutions, S-CFZ was tested as an air cathode for ZAB under ambient conditions (Fig. 27e). S-CFZ demonstrated promising performance as an air cathode for ZABs, with a peak power density of 178 mW cm^{-2}, surpassing VL-CFZ at 130 mW cm^{-2} (Fig. 27f). The initial discharge-charge voltage gap for S-CFZ was 0.76 V, showing 61.9% energy efficiency (Fig. 27g). After 500 h of cycling at 25 mA cm^{-2}, it showed negligible fading, outperforming other catalysts. Even at a current density of 35 mA cm^{-2}, the charge-discharge voltage gap showed a minimal fading rate of less than 0.01% per hour over 160 h of operation. (Fig. 27h). DFT calculations were performed to explain the enhanced bifunctional activity of S-CFZ. The charge density differences in Fig. 27i show electron redistribution due to isothiourea grafting, which leads to electron delocalization in S-CFZ. This is supported by a higher Bader charge, indicating stronger electron withdrawal from the S-containing groups. This adjustment improves the adsorption-desorption behavior of oxygen intermediates, enhancing ORR/OER performance. As shown in Fig. 27j, S compensation optimizes OH* adsorption, reducing the energy barrier for OH^- formation and improving ORR activity compared to the uncompensated VL-CFZ [319].

Furthermore, *Ao et al.* developed a hierarchical structure by partially sulfurizing a pre-synthesized 2D MOF (NiCo-BDC), where nickel and cobalt are coordinated with benzenedicarboxylic acid ligands. The sulfurization process was controlled by adjusting the reaction time, creating several samples with varying sulfur content (denoted as NiCo-BDC-S-T). This partial sulfurization maintained the MOF's porous

Table 1
Comparison of MOF hybridization and PSM strategies for electrocatalysis.

Aspect	MOF Hybridization	Post-Synthetic Modification (PSM)
Engineering approach	Integration of a secondary functional phase (e.g., carbon, MXene, metal sulfides)	Chemical tailoring of a pre-formed MOF (ligand grafting, metal doping, sulfurization)
Active site regulation	Creates emergent active sites at heterointerfaces	Precise modification of existing metal nodes and coordination sphere
Electronic structure tuning	Long-range charge redistribution and enhanced conductivity via interfacial electron transfer	Localized tuning of D-band center and charge density around active centers
Stability mechanism	External protection through mechanical scaffolding and encapsulation	Internal reinforcement by defect healing and protective shell formation
Mass transport & conductivity	Excellent (benefitted by conductive networks and hierarchical pores)	Moderate (limited by intrinsic MOF conductivity)
Advantages	High current density, mechanical robustness, synergistic interfacial effects	Atomic-level precision, high selectivity, optimized intermediate adsorption
Limitations	Less control over local coordination chemistry	Limited improvement in bulk conductivity
Best suited for	High-rate reactions	Reactions requiring high selectivity and fine-tuned binding energies
Industrial relevance	Higher potential for scale-up due to improved conductivity, mechanical stability, and compatibility with large-area electrodes; easier integration into practical devices.	Excellent for high-value, selective processes but may face challenges in cost-effective large-scale synthesis and conductivity.

structure and active sites while forming a highly conductive $CoNi_2S_4$ layer on the surface, which improved electron transport and redistribution. The optimal NiCo-BDC-S−6 exhibited excellent catalytic performance for UOR, with a driving potential of 1.326 V at 10 mA cm^{-2}, surpassing many state-of-the-art UOR catalysts (Fig. 27k). As shown in Fig. 27l, chronopotentiometric tests at 20 mA cm^{-2} revealed that NiCo-BDC-S−6 maintained stable UOR activity for over 20 h, highlighting the improved durability from partial sulfurization compared to pristine NiCo-BDC and Pt/C. Additionally, the urea fuel cell achieves a maximum power density of 2.68 mW cm^{-2}, significantly outperforming a Pt/C-based anode catalyst (0.78 mW cm^{-2}) (Fig. 27m-n). Spin-polarized DFT calculations revealed that the MOF-$CoNi_2S_4$ heterostructure significantly improves electrical conductivity and electron transport, which is beneficial for electrocatalysis. As shown in Fig. 40o, electron transfer occurs from Ni and Co atoms to adjacent S atoms. Gibbs free energy calculations (Fig. 27p) show that the MOF-$CoNi_2S_4$ heterostructure provides optimal adsorption for UOR while enabling favorable CO_2 desorption, making it ideal for the UOR process [320].

Additionally, *Zhang et al.* developed alkali metal ion-doped M-NH_2-MIL−101 (M = Li, Na, K) adsorbents via post-modification to enhance CO_2 capture and cycling stability (Fig. 27q). The doping of alkali metal cations, especially 0.1 M K^+ (denoted as 0.1 K-NH_2-MIL−101), significantly increased CO_2 adsorption capacity (8.2 mmol g^{-1} at 298 K), about 3.2 times higher than NH_2-MIL−101, with excellent cyclic stability. The CO_2 adsorption and conversion properties of the 0.1 K-NH_2-MIL−101 adsorbent combined with a Bi catalyst were investigated. As shown in Fig. 27r, the FE for HCOOH was 77% for Bi-NH_2-MIL−101 and 87% for Bi−0.1 K-NH_2-MIL−101, significantly improving upon pure Bi 67%. The partial current density for HCOOH in Bi−0.1 K-NH_2-MIL−101 at −1.3 V vs RHE was 1.3 and 1.6 times higher than that of pure Bi and Bi-NH_2-MIL−101, respectively, indicating better CO_2 adsorption and reaction (Fig. 27s). In long-term stability tests (Fig. 27t), Bi−0.1 K-NH_2-MIL−101 maintained an HCOOH FE above 80% for 52 h, outperforming other Bi-based electrocatalysts [321].

The PSMs explored in these studies significantly enhance the performance and stability of MOFs for electrocatalysis. The introduction of functional groups and modifications like sulfurization and alkali metal doping improves conductivity, active site availability, and overall catalytic efficiency. These modifications not only optimize the adsorption-desorption behavior of key intermediates but also enable better electron transfer, leading to improved electrocatalytic activity. Furthermore, the long-term stability of these modified MOFs, as demonstrated by several tests, confirms their potential for practical applications, particularly in energy conversion and CO_2 reduction processes. These advancements underscore the importance of tailoring MOFs through post-synthetic modifications to address specific challenges in electrocatalysis and enhance their applicability in real-world applications.

4.3.3. *Mechanistic comparison of MOF hybridization and PSM*

The electrocatalytic performance of MOF-based materials in this section stems from two complementary but mechanistically distinct engineering philosophies. MOF hybridization integrates a secondary functional phase during or after framework assembly, whereas PSM chemically tailors a pre-formed MOF. Their mechanistic roles in regulating active sites, electronic structure, and stability can be compared directly using the ORR, UOR, and CO_2RR examples discussed above.

Active-site creation and regulation: Hybridization primarily generates active sites at the heterointerface (Table 1). In Ni/Co-MOF@Ti_3C_2, synergistic Co-N-C motifs coupled with Ti sites enhance ORR performance. Similarly, the M/CM/Ni_3S_2/NF and Bi@Cu MOF-on-MOF systems create multi-component interfaces that enable efficient urea oxidation and selective formate production, respectively. In contrast, PSM modifies the coordination environment of existing nodes with molecular precision. Linker compensation in S-CFZ, partial sulfurization in NiCo-BDC-S-T, and K^+ doping in NH_2-MIL−101 exemplify how PSM targets vacancies, ligands, or pore environments to create or optimize active sites without changing the overall topology.

Electronic structure tuning: Hybridization facilitates long-range charge redistribution and conductivity enhancement through interfacial electron transfer. DFT studies on Ni/Co-MOF@Ti_3C_2 and Bi@Cu systems show optimized adsorption energies of key intermediates (*OOH, *CO, *OCHO) via D-band center modulation at the interface. PSM, conversely, enables localized electronic tuning. Sulfur grafting in S-CFZ and partial sulfurization in NiCo-BDC-S-T induce electron withdrawal/delocalization around metal centers, while alkali-metal doping primarily modulates the local reactant concentration rather than the intrinsic electronic states of the framework.

Stability enhancement: Hybridization improves stability through external protection and mechanical reinforcement (e.g., Ti_3C_2 nanosheets or PTFE matrix). PSM strengthens the MOF internally by saturating defect sites (S-CFZ) or forming protective shells (NiCo-BDC-S-T), thereby suppressing framework dissolution.

In summary, hybridization excels at creating robust, conductive composites with emergent interfacial synergies, making it particularly effective for high-current-density applications. PSM offers atomic-level precision for optimizing intermediate binding and intrinsic framework stability. The most effective electrocatalysts often integrate both strategies PSM for precise active-site engineering and hybridization for enhanced charge transport and durability.

4.3.4. *POMs@MOFs*

Polyoxometalates (POMs) are anionic metal-oxygen clusters with reversible multielectron redox behavior, making them attractive for electrocatalysis [322,323]. However, their low conductivity and instability limit practical use. Encapsulating POMs within MOFs creates POM@MOF composites that combine the redox richness of POMs with the high surface area and structural regularity of MOFs [324]. The MOF scaffold prevents POM aggregation, reduces leaching, and modulates electronic structure via host-guest interactions. Consequently, these composites enhance performance across key reactions: for ORR, they

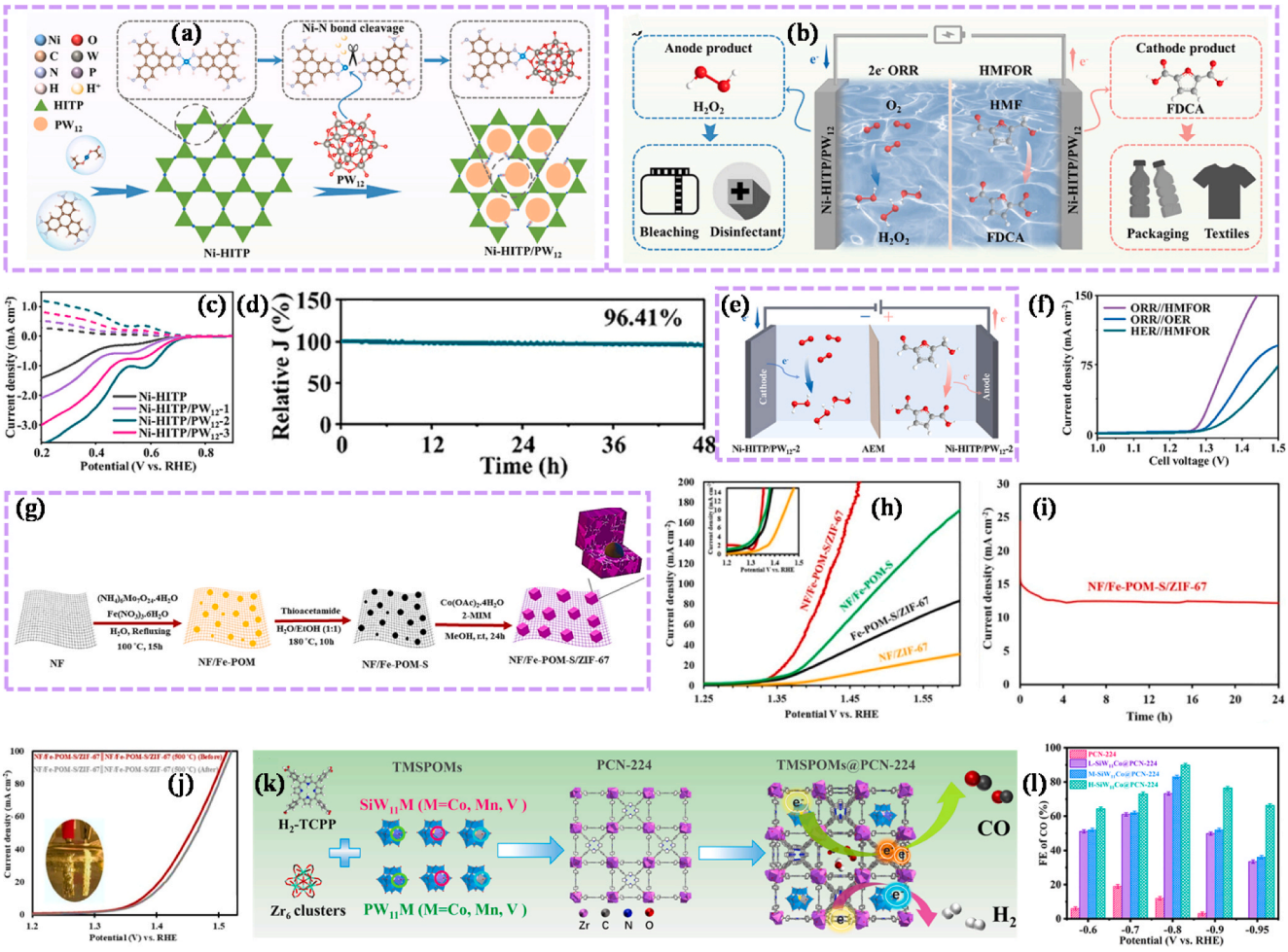

Fig. 28. Schematic illustration of (a) the preparation route for Ni-HITP/PW_{12}, and (b) the two-electrode setup combining anodic two-electron ORR with cathodic HMFOR, along with possible uses of the resulting high-value products. (c) LSV curves of Ni-HITP/PW_{12}−2 and other prepared catalysts. (d) CP stability test and FE of Ni-HITP/PW_{12}−2. (e) Schematic of two-electrode system. (f) LSV curves of various systems. Copyright 2025 © Wiley-VCH. (g) Schematic illustration of preparation method of NF/Fe-POM-S/ZIF−67. (h) UOR LSV curves of prepared catalysts. (i) CP test of NF/Fe-POM-S/ZIF−67. (j) In-two electrode system LSV curves before and after 1000 CV cycles. Copyright 2025 Elsevier. (k) Synthesis process and (l) FE of SiW_{11}Co@PCN−224. Copyright © 2024 American Chemical Society. (a-f) Reproduced with permission from ref [327]. (g-j) Reproduced with permission from ref [328].(k-l) Reproduced with permission from ref [329].

enable efficient two- or four-electron pathways; for UOR, multielectron transfer accelerates the sluggish six-electron urea oxidation; and for CO_2RR, tunable redox states stabilize intermediates like *COOH and improve product selectivity [325,326]. For instance, *Bao et al.* developed a bifunctional electrocatalyst, Ni-HITP/PW_{12}, using a ligand replacement strategy to synthesize highly ordered conductive MOF (Fig. 28a). The catalyst, featuring Ni-O-W bonds, modulates the electronic structure of both Ni and W sites, enhancing cathodic 2e⁻ ORR for H_2O_2 production and anodic HMFOR for FDCA oxidation (Fig. 28b). Ni-HITP/PW_{12}−2 demonstrated the highest current density in ORR tests (Fig. 28c), indicating its superior O_2 adsorption and activation capabilities. Its onset potential was measured at 0.60 V vs. RHE at 1 mA cm^{-2}. Moreover, the catalyst exhibited outstanding stability, maintaining its performance for 48 h along with 96.41% FE (Fig. 28d). In the ORR//HMFOR coupled system (Fig. 28e), the Ni-HITP/PW_{12}−2 composite achieved a H_2O_2 production rate of 9.51 mol $gcat^{-1}$ h^{-1} and 96.8% FDCA yield at 100 mA cm^{-2} with a cell voltage of 1.38 V (Fig. 28f), significantly outperforming traditional ORR/OER systems [327]. In addition to ORR, POM-MOF composites have also shown promise for UOR. For instance, *Naghshbandi et al.* developed a sulfur-doped iron polyoxometalate/ZIF−67 catalyst on nickel foam (NF/Fe-POM-S/ZIF−67) for urea oxidation, synthesized using a solvothermal method (Fig. 28g). The catalyst achieved 10 mA cm^{-2} at 1.33 V in 1.0 M KOH with 0.5 M urea (Fig. 28h). It demonstrated excellent stability, maintaining its activity for over 48 h at a current density of 100 mA cm^{-2} (Fig. 28i). Overall urea electrolysis required 1.38 V at 10 mA cm^{-2} (Fig. 28j) [328]. The versatility of POM-MOF hybrids extend to CO_2RR, where tuning the redox properties of encapsulated POMs can stabilize key intermediates. For example, *Zhang et al.* developed TMSPOMs@PCN−224 composites by encapsulating transition metal-doped polyoxometalates (TMSPOMs) within a porphyrin-based PCN−224 framework to enhance the electron density at active sites for CO_2RR (Fig. 28k). The cobalt-substituted SiW_{11}Co@PCN−224, exhibited a FE for CO production (FE_{CO}) of 89.9%, significantly higher than the 12.1% FE_{CO} of PCN−224 (Fig. 28l). The electrocatalytic activity was optimized by fine-tuning POM loading, and the catalyst demonstrated excellent stability over 20 h. Comparative analysis of the composites, supported by DFT calculations, revealed that the negative charge of the polyanions facilitates electron transfer, enhancing overall performance [329].

POM@MOF composites illustrate how host-guest chemistry can transform two individually limited components into a synergistic electrocatalytic platform. Above studies confirm that the same design principle confining redox-active POMs within porous, conductive MOF scaffolds effectively addresses longstanding challenges of conductivity, stability, and active-site accessibility. Further gains can be expected

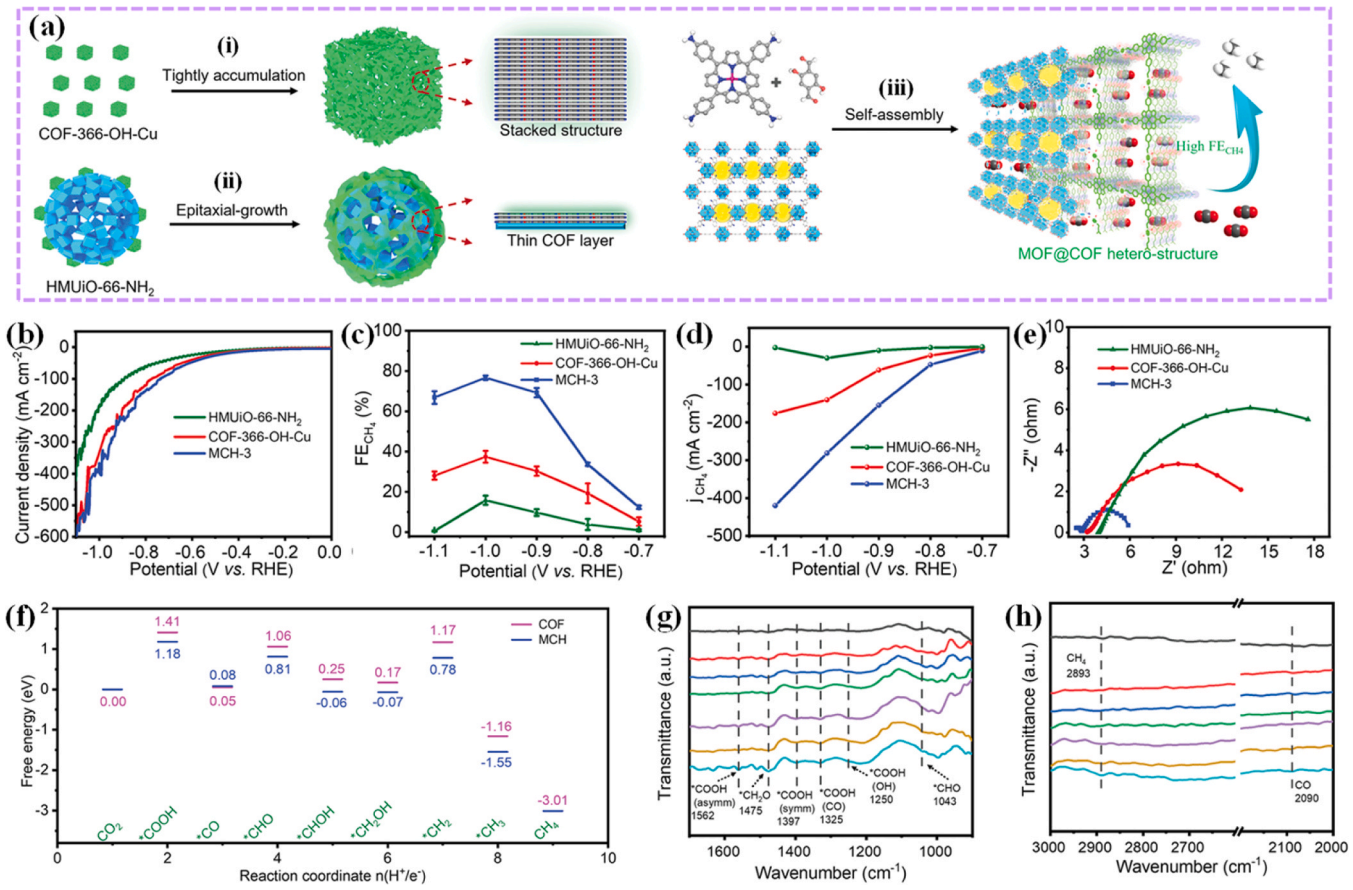

Fig. 29. (a) Schematic showing the synthesis and key benefits of honeycomb-like MOF@COF heterostructures for electrocatalytic CO_2RR. Electrocatalytic CO_2RR performance of HMUiO-66-NH_2, COF-366-OH-Cu, and MCH-3. (b) LSV curves. (c) FE for CH_4 across various potential (d) Partial current density for CH_4. (e) Nyquist plots. Mechanistic insights into CO_2RR on MCH-3. (f) Free energy profiles for the CO_2-to-CH_4 pathway on COF and MCH-3. *In-situ* ATR-FTIR spectra of MCH-3 during CO_2RR in the range of (g) 1700–900 cm^{-1} and (h) 3000–2000 cm^{-1}. Reproduced with permission from ref [334]. Copyright 2022 © Wiley-VCH.

from integrating machine learning to predict optimal POM-MOF pairings, developing scalable synthetic routes, and exploring POM@MOF films in membrane electrode assemblies. Such advances will be critical to moving these composites from laboratory demonstrations to practical energy and environmental devices.

4.3.5. *COFs@MOFs*

Covalent organic frameworks (COFs) are crystalline porous polymers with strong covalent bonds, offering stability, porosity, and tunable electronic properties [330,331]. Intact COF@MOF heterostructures (non-pyrolyzed) combine the high surface area and abundant metal nodes of MOFs with the conductive, ordered channels of COFs, preserving both molecular architectures [332,333]. This synergy benefits electrocatalytic reactions requiring efficient mass transport and stable interfaces. However, their application remains largely unexplored. To date, literature on intact COF@MOF systems for the ORR is extremely limited (mostly involving pyrolyzed derivatives), and no such system has been reported for the UOR, leaving a clear research gap. In contrast to the scarce reports for ORR and UOR, the potential of intact COF@MOF heterostructures has been successfully demonstrated for the electrocatalytic CO_2RR. For example, *Yang et al.* synthesized a series of honeycomb-like porous crystalline hetero-electrocatalysts (MCH-X, X = 1–4) via an epitaxial growth method (Fig. 29a). These structures combine a porous MOF template with an ultrathin COF coating, creating abundant open channels and fully exposed active sites. This architecture enables efficient CO_2 adsorption, activation, and subsequent conversion to CH_4. LSV curves show that at −1.0 V, MCH-3 achieves a current density of −398.1 mA cm^{-2} (Fig. 29b). For MCH-3, a FE_{CH4} of 76.7% is achieved at −1.0 V with a minor FE_{CH2} of 3.3% (Fig. 29c). Notably, FE_{CH4} of MCH-3 remains ≈ 70% across −0.9 to −1.1 V. Partial CH_4 current densities at −1.0 V are −29.8, −140.3, and −281.2 mA cm^{-2} for HMUiO-66-NH_2, COF-366-OH-Cu, and MCH-3, respectively, with MCH-3 delivering roughly twice that of the COF alone (Fig. 29d). EIS further reveals that MCH-3 exhibits superior charge transfer kinetics at −1.0 V (Fig. 29e). DFT calculations (Fig. 29f) reveal that the rate-determining step for CO_2-to-CH_4 conversion is *COOH formation (ΔG = 1.18 eV for MCH−3). This free energy barrier is lower than that of COF−366-OH-Cu, indicating that the MOF component stabilizes key intermediates. *In-situ* ATR-FTIR spectra (Fig. 29g-h) confirm the presence of *COOH, *CHO, *CH_2O, and *CO intermediates along the reaction pathway [334]. This study demonstrates that intact COF@MOF heterostructures with a honeycomb-like morphology can effectively integrate the respective strengths of both frameworks, achieving high activity, selectivity, and stability for CO_2-to-CH_4 conversion, thereby validating the promise of this material class for electrocatalytic CO_2RR.

Intact COF@MOF heterostructures represent an emerging class of electrocatalytic materials that combine the structural stability and ordered porosity of COFs with the high density of accessible metal nodes from MOFs. To date, the only successful demonstration of such intact heterostructures in electrocatalysis is for the CO_2RR, where honeycomb-like architectures have achieved high current density, FE, and product selectivity. In contrast, no intact COF@MOF system has been reported for the ORR, nor for the UOR. This complete absence for ORR and UOR highlights substantial research opportunities. Future efforts should focus on expanding synthetic strategies to create stable COF@MOF interfaces, exploring their performance for these challenging

Table 2
MOFs based materials in electrocatalysis.

Table 2.1. MOFs based electro-catalysts for ORR

Catalysts	Synthesis method	Electrolyte	Specific capacity (mA h g^{-1})	Onset Overpotential (V)	Tafel slope (mV dec^{-1})	Diffusion Limiting (mA/ cm^{-2})	Peak Power Density (mW cm^{-2})	Voltage Plateau (V)	Ref.
Co_4-Co-MOF	Solvothermal	0.1 M KOH	825	-	49.5	-	230	1.49	[335]
CoNi-MOF/rGO	Solvothermal	0.1 M KOH at 1600 rpm	711	0.88	67	5.35	97	1.31	[142]
b-CZIF−67/MXene	Solvothermal	O_2 saturated 0.5 M H_2SO_4	-	0.91	73	5.56	-	-	[336]
b-CZIF−67/MXene	Solvothermal	0.1 M KOH	-	0.93	68.5	5.90	-	1.49	[336]
Co_3O_4/Ni-Co-HITP	Solvothermal	O_2.saturated 0.1 M KOH	-	0.77	60	4.6	143.1	1.45	[337]
Co_3HITP_2	Solvothermal	0.1 M KOH solution at 1600 rpm	784	0.79	89	5.52	164	-	[338]
HCF-MOF	Solvothermal	Alkaline polycrylate, hydrogel	-	0.82	-	-	113.5	1.38	[339]
Mn/Fe/HIB-MOF	Reduction	FBN membrane	769	0.88	36	-	194	1.48	[144]
Fe/Ni-BTC	Solvothermal	6 M KOH	775	0.96	-	-	182	1.55	[340]
$Ni_{5.7}Ru_{0.3}(HHTP)_3(H_2O)_x$	Hydrothermal	Solid State	654	0.68	64	-	98.3	1.332	[341]
CuCo-HITP	Solvothermal	0.1 M KOH	-	0.79	96.4	-	-	-	[342]
CuCo-HITP	Solvothermal	0.1 M PBS	-	0.72	319.3	-	-	-	[342]
Cu-MOF@Fe-MOF	hydrothermal	0.1 M KOH	-	-	48.5	-	231.2	-	[343]
CoNi/Co_2P@PCN−0.1 P	Defect-mediated epitaxial growth	0.1 M KOH	794.7	0.91	40.7	-	176.5	-	[344]
Ru@FeZn-HNC/CNFs	electrospinning	0.1 M KOH	810.2	-	99.9	6.15	175	1.48	[345]
mZIF/Bamb-C	Biomass assisted assembly + carbonization	0.1 M KOH	-	0.94	241	-	-	-	[346]
ZnCo-ZIFs	Solvothermal	0.1 M KOH	-	0.6	73.9	-	-	-	[347]
La-MOF/MXene	Solvothermal	0.1 M KOH	-	0.84	82	-	-	-	[348]
NiCoFeMn-MOF	Electrodeposition	0.1 M NaOH	800	0.81	61	-	-	-	[349]

Table 2.2. MOFs based electro-catalysts for UOR

Catalyst	**Synthesis method**	**Electrolyte**	**ECSA cm^2**	**mA cm^{-2}/ mV**	**Tafel slope**	**TOF**	**mA cm^{-2}/cell voltage**	**Stability (h)**	**Ref.**
FeNi-MOF NSs	Solvothermal	1.0 M KOH + 0.33 M Urea	-	10/131	28	-	10/1.361	10	[350]
Fe-MOF/FF−5	Solvothermal + Plasma irradiation	1.0 M KOH + 0.33 M Urea	-	10/1.362 V	20	-	10/1.472	12	[187]
NH_2–NiCoFe-MIL−101	Solvothermal	1.0 M KOH + 0.33 M Urea	-	100/1.56 V	48	-	100/1.56	80	[351]
$Ni_{0.15}Co_{0.85}$-MOF	Solvothermal	1.0 M KOH + 0.33 M Urea	-	10/1.33 V	125	0.47	-	72	[185]
Ni-DMAP−2/NF	Solvothermal	1.0 M KOH + 0.5 M Urea	-	100/1.30 V	23	-	10/1.35	10	[352]
NiMnCo-MOF	Solvothermal	1.0 M KOH + 0.33 M Urea	-	10/1.29 V	46	-	100/1.63	24	[353]
Ru-NiFe-③/NF	Solvothermal	1.0 M KOH + 0.33 M Urea	-	100/1.37 V	43.8	-	100/1.63	20	[354]
Ni-MOF−0.5	hydrothermal	1.0 M KOH + 0.5 M Urea	-	10/1.38 V	52		10/1.52	2	[355]
NiCoPx@NiFeCo-MOF	Solvothermal	1.0 M KOH + 0.5 M Urea		100/1.37 V	144.2		10/1.40	45	[193]
Co-MOF (CoS_x/Co-MOF)	Solvothermal	1.0 M KOH + 0.5 M Urea		10/1.315 V	50		10/1.48	10	[356]
RuNi-MOF@NMO	Solvothermal	1.0 M KOH + 0.33 M Urea	-	10/120	-	-	10/1.28	200	[357]
NC-FNCP	Solvothermal	1.0 M KOH + 0.5 M Urea	-	10/1.37 V	35.79	-	10/1.52	20	[358]
Ru@MOF/LDH	*in-situ* reduction	1.0 M KOH + 0.33 M Urea	31.1	50/1.38 V	72.3	-	10/1.44	12	[359]
$NiCoFe(OH)_x$/NF	Electrodeposition	1.0 M KOH + 0.5 M Urea	-	10/1.24 V	46.13	-	10/1.58	100	[360]
MIM@$Fe_{0.1}$-CoNi CH/NF	Solvothermal	1.0 M KOH + 0.5 M Urea	-	10/1.31 V	48.84	-	10/1.36	160	[361]
NiFe-MIL−53-NH_2	Solvothermal	1.0 M KOH + 0.33 M Urea	-	10/1.398 V	14	0.16	10/1.56	20	[362]
MoO_2/Ni-MOF/rGO	Hydrothermal	1.0 M KOH + 0.33 M Urea	-	10/1.32 V	31	-	-	-	[363]
$Zn_{0.33}V_{0.66}$-MOF/NF	Hydrothermal	1.0 M KOH + 0.33 M Urea	-	10/1.37 V	122		-	70	[364]
50TEA@Ni-TDA/NF	Solvothermal	1.0 M KOH + 0.33 M Urea	-	10/1.277	-	-	50/ 1.709	100	[365]
NiCo-MOF-DFc	Solvothermal	1.0 M KOH + 0.33 M Urea	-	100/1.408	34.7	-	1000/1.83	100	[366]

(*continued on next page*)

Table 2 (*continued*)

Table 2.2. MOFs based electro-catalysts for UOR

Catalyst	Synthesis method	Electrolyte	ECSA cm^2	mA cm^{-2}/ mV	Tafel slope	TOF	mA cm^{-2}/cell voltage	Stability (h)	Ref.
Ce-Ni-BDC	Solvothermal	1.0 M KOH + 0.5 M Urea	-	100/1.32	44.33	-	-	20	[367]
NM MOF/NMC $LDH_{0.005}$	Solvothermal	1.0 M KOH + 0.33 M Urea	-	100/1.42	-	-	10/1.65	24	[368]
Cd (II)-BPFA-MOF/NF	Solvothermal	1.0 M KOH + 0.33 M Urea	-	10/1.59	-	-	10/1.54	100	[369]

Table 2.3. MOFs based electrocatalysts for CO_2RR

Catalyst	Synthesis method	Electrolyte	*j* (mA cm^{-2})	Products	FE (%)	Potential (V)	TOF	Ref.
C-FePc$(CN)_8$/ZIF	Pyrolysis	0.5 M $KHCO_3$	5	CO	94	−0.46	0.13 s^{-1}	[370]
PPy@MOF−545-Co	*In-situ* polymerization	0.5 M $KHCO_3$	13	CO	98	−0.8	-	[371]
ZIF−8@PPy	*In-situ* electrochemically polymerization	0.25 M K_2SO_4	18	CO	96	−1.1	-	[372]
Cu_6MePz	Solvothermal	1 M KOH	400	CH_4	66.40	−1.0	-	[373]
$Cu_2O_{(OL-MH)}$/Ppy	Oxidative polymerization	0.5 M $KHCO_3$	0.223	CH_3OH	93	−0.85	-	[374]
MOF-based LNCCs	Electrochemical reduction	0.5 M $KHCO_3$	10.6	C_2H_5OH	82.5	−1.0	0.656 s^{-1}	[375]
CuSn-HAB	Solvothermal	1 M KOH	68	C_2H_5OH	56	−0.57	0.0601 s^{-1}	[376]
HKUST−1	Electrochemical reduction	0.1 M $KHCO_3$	-	CH_3OH C_2H_5OH HCOOH	45.2–71.2	0.1–0.7	-	[377]
HKUST−1(Cu,M_D)	Solventless Synthesis	0.5 M $KHCO_3$	20	CH_3OH and C_2H_5OH	47.2	-	-	[378]
Cu-MOF/GO	Solvothermal	0.1 M TBAB/DMF	-	HCOOH	58	−0.6	-	[379]
PCN−222(Cu)/C	Solvothermal	0.5 M $KHCO_3$	3.2	HCOOH	44.3	−0.7–0.9	-	[380]
MOF-derived $Bi_2O_2CO_3$	In situ transformation	0.5 M $KHCO_3$	12.7	$HCOO^-$	96.1	−0.669	-	[381]
Bi-MOF	Solvothermal	1 M KOH 1 M $KHCO_3$	150	HCOOH	92.0 80.0	−0.64 −1.1	-	[382]
Bi-FDCA	Solvothermal mixing	0.1 M $KHCO_3$	19.6	HCOOH	95.1	−1.2	-	[383]
Cu_2-(CuTCPP)	Solvothermal	1 M H_2O and 0.5 M $EMIMBF_4/CH_3CN$	4.5	$HCOO^-$	68.4	−1.55	2037 h^{-1}	[384]
Sn-N6-MOF	Pyrolysis	0.5 M $KHCO_3$	23	HCOOH	85	−1.23	-	[385]
MIL−53 (AL)	Solvothermal	0.05 M K_2CO_3	-	HCOOH and CO	40	−0.9~−1.1	-	[386]
MOF−808 (Zr)	MOF-confined reduction	0.1 M $KHCO_3$	~7	$HCOO^-$	> 99	−0.25	-	[387]
Pb-MOF	Electroreduction	0.1 M $KHCO_3$	1.9	HCOOH	96.8	−0.88	-	[388]
$MF\text{-}cMOF_{Q1.28/t5}$	Microfluidic printing	0.1 mM $KHCO_3$-KCl	383	CH_4	79.6	-	-	[389]
Cu-NH_2BDC	modulator-assisted synthesis	0.1 M $KHCO_3$	53	CH_4	63.5	−0.22	-	[390]
Cu_2O@PCN−223	In-situ Synthesis	0.1 M $KHCO_3$	22.81, 14.98 and 10.38	CH_4, C_2H_4, CO	87.4	-	-	[391]
CuO/Cu-MOF (HKUST−1)	Hydrothermal	0.1 M $KHCO_3$	~80	CH_4, C_2H_4	69	-	-	[392]

multielectron reactions, and systematically correlating heterostructure architecture with electrocatalytic metrics. Addressing these gaps will be key to unlocking the full potential of this promising material class for sustainable energy conversion Table 2.

5. Conclusion and future outlook

This review has systematically highlighted the transformative journey of MOFs from their foundational tunability to their emerging role in practical electrochemical devices for the ORR, UOR, and CO_2RR reactions. By integrating fundamental mechanistic insights from DFT with critical performance analysis in real-world systems from fuel cells and metal-air batteries to urea electrolyzers and CO_2 converters, we have established a clear structure-property-application relationship for MOF-based electrocatalysts. The unparalleled modularity of MOFs allows for the precise engineering of active sites and pore environments, offering a powerful pathway to circumvent the limitations of traditional noble-metal catalysts.

However, the transition of promising MOF electrocatalysts to practical technologies faces a series of significant deployment challenges, which include:

1. **Chemical and electrochemical stability of MOFs: Overcoming degradation challenges**

The practical deployment of MOF-based electrocatalysts is fundamentally constrained by their chemical and electrochemical stability under harsh operational conditions, such as extreme pH or sustained applied potentials. Framework degradation, active site leaching, or structural collapse can lead to rapid performance decay. To engineer resilience, research is pivoting from common transition metals toward frameworks constructed from high-valent metal clusters (e.g., Zr^{4+}, Ti^{4+}, Cr^{3+}), which form stronger metal-linker bonds (Fig. 30). Parallel strategies include developing covalent organic frameworks (COFs) and exploring PSM to cross-link ligands or introduce hydrophobic groups, thereby shielding the internal structure from corrosive electrolytes.

2. **Navigating the activity-selectivity-stability trade-off**

Beyond basic stability, a more sophisticated challenge lies in breaking the fundamental scaling relationships that intrinsically link activity, selectivity, and stability, often forcing a compromise. Innovative active site design is key to circumventing these limitations. Promising pathways involve engineering multi-metallic sites or high-entropy MOF (HE-MOF) platforms, where synergistic interactions between adjacent, dissimilar metals can create unique adsorption energies for key intermediates. Complementarily, precise engineering of the secondary coordination sphere by installing functional groups within the MOF pores allows control over the local microenvironment (e.g., pH, water concentration), thereby steering

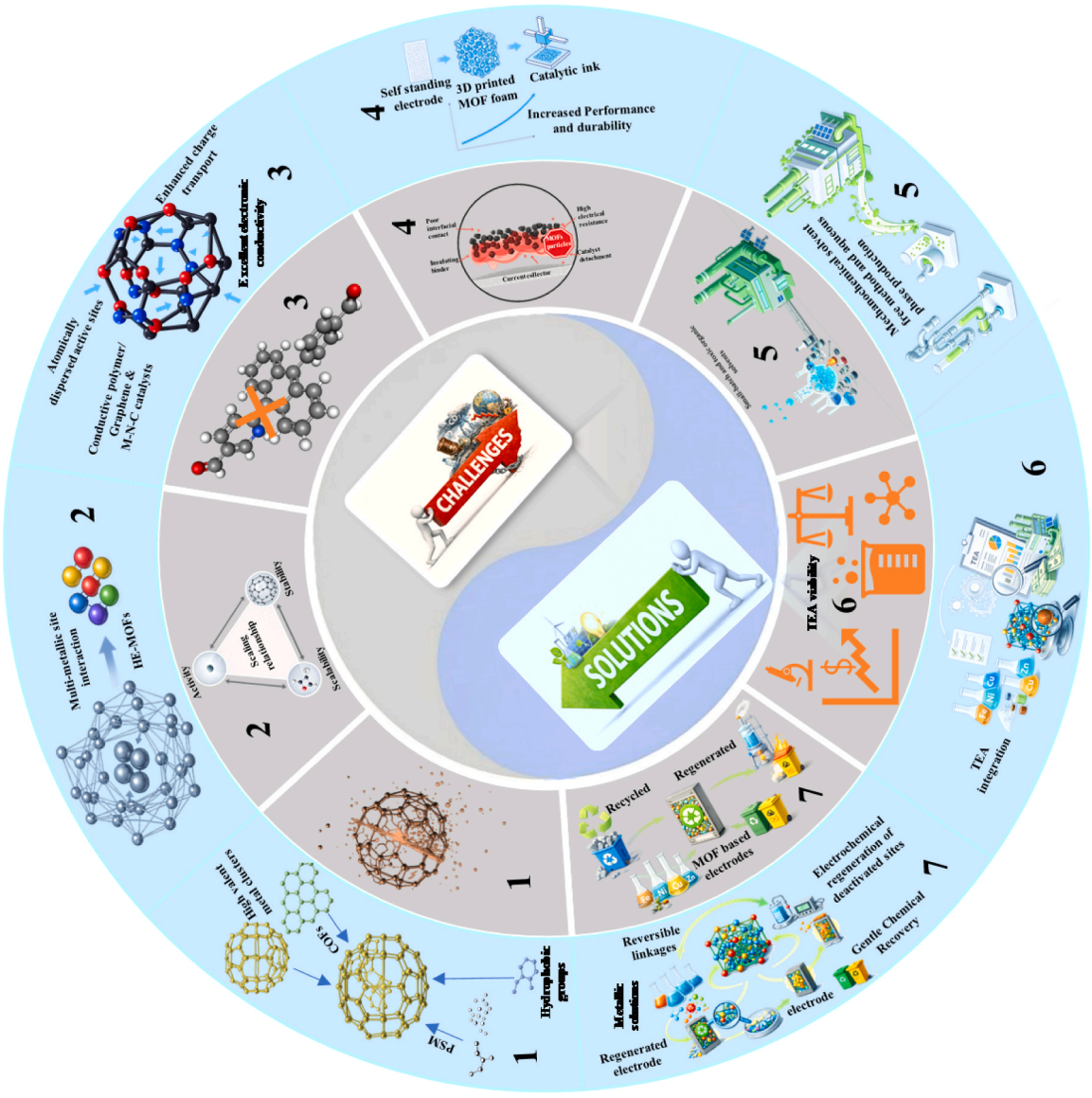

Fig. 30. Overview of key challenges (highlighted in gray) and corresponding solutions (highlighted in blue) for MOF-based electrocatalysts in ORR, UOR, and CO_2RR applications.

complex reaction pathways, such as selective CO_2 reduction toward valuable multi-carbon (C_2^+) products.

3. **Overcoming intrinsic conductivity limitations**

The typically insulating or semiconducting nature of pristine MOFs severely limits charge transport, creating a bottleneck for high-current-density applications. The most viable mitigation strategy is the deliberate construction of MOF-based conductive composites and hybrids. Integrating MOFs with conductive matrices like carbon nanotubes, graphene, or conductive polymers creates essential percolation networks. Alternatively, using MOFs as sacrificial templates or precursors to synthesize MOF-derived porous carbons or metal-nitrogen-carbon (M-N-C) catalysts preserves the desirable, atomically dispersed active sites while endowing the material with excellent electronic conductivity.

4. **Device integration and interfacial engineering**

A critical translational hurdle is moving from high-performance catalyst powders to efficient, durable electrodes. Poor interfacial contact between MOF particles, insulating binders, and current collectors leads to high electrical resistance, catalyst detachment, and ultimately device failure. Next-generation integration focuses on advanced fabrication techniques. This includes developing binder-free, self-standing MOF electrodes (e.g., thin films, foams) and employing additive manufacturing (3D printing) for precise architectural control. Techniques like inkjet printing of catalytic inks or direct electrodeposition of MOF layers onto substrates promise to create robust, well-adhered interfaces with optimal catalyst utilization and mass transport.

5. **Pathways to scalable and sustainable synthesis**

For industrial relevance, MOF synthesis must transition from bespoke, small-batch laboratory methods to scalable, cost-effective, and environmentally benign processes. Conventional solvothermal routes often involve toxic organic solvents, high energy input, and low space-time yields. The field is increasingly adopting green chemistry principles, exemplified by mechanochemical (solvent-free) synthesis, aqueous-phase production, and continuous flow chemistry. Flow synthesis, in particular, offers superior control over particle size and morphology while enabling high-throughput, reproducible manufacturing essential for commercialization.

6. **Ensuring techno-economic viability**

The economic feasibility of MOF-based devices cannot be an

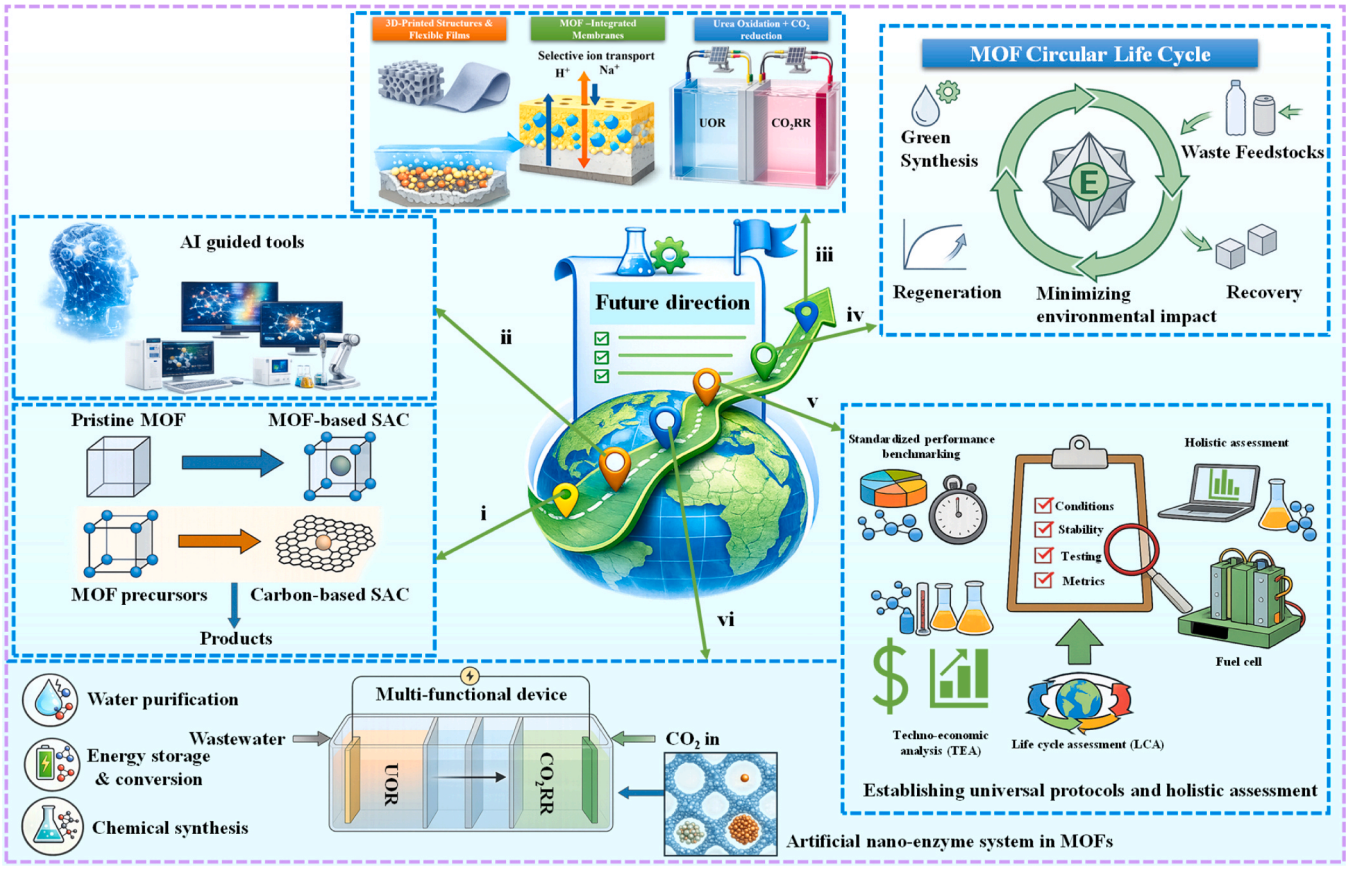

Fig. 31. Future roadmap.

afterthought. Costs associated with specialized organic linkers or scarce precious metals can be prohibitive at scale. A foundational strategy is the prioritization of MOFs constructed from earth-abundant elements (e.g., Fe, Ni, Cu, Zn) and simple, commodity-scale organic linkers. Crucially, TEA must be integrated early in the research and development cycle. This analytical framework guides material selection and process design by modeling costs at scale, ensuring research targets are aligned with realistic economic thresholds for the intended application.

7. **Embracing circularity and end-of-life management**

A truly sustainable technology requires a plan for its full lifecycle, including end-of-life management. Currently, strategies for the recycling, regeneration, or safe disposal of spent MOF-based electrodes are underdeveloped. Future material design must incorporate circular economy principles, such as engineering reversible linkages that allow for the gentle chemical recovery of metal nodes and organic linkers. Furthermore, research into the electrochemical regeneration of deactivated active sites or the upcycling of spent electrodes into new functional materials (e.g., for catalysis or sensing) is vital for minimizing waste and closing the material loop.

To accelerate the transition of MOF electrocatalysts from laboratory breakthroughs to industrial technology pillars, focused efforts must address the following interconnected frontiers:

i. **Rational design of MOF-based single-atom catalysts (SACs):** A primary frontier is the atomic-level precision engineering of MOF-based SACs. This involves two main strategies: using pristine MOFs as hosts to immobilize and isolate single metal atoms, and employing MOFs as sacrificial templates to derive carbon-based SACs with atomically dispersed metal sites. The core challenge and opportunity lie in the precise control of the single-atom site micro-environment managing its coordination number, neighboring heteroatom dopants (e.g., N, S, P), and local electronic structure. By combining MOF tunability with SAC maximum atom-utilization efficiency, researchers can target electrocatalysts with unprecedented activity and selectivity, particularly for complex multi-electron reactions like CO_2 reduction to specific C_2^+ products.

ii. **AI-guided discovery and autonomous synthesis:** Overcoming the vast MOF design space requires a paradigm shift from trial-and-error to a closed-loop, AI-accelerated workflow. Machine learning (ML) models must be integrated to predict novel structures, simulate properties, and optimize synthesis parameters for target reactions like ORR, UOR, and CO_2RR (Fig. 31). The next step is coupling these computational insights with high-throughput automated laboratories that can execute synthesis and preliminary characterization, creating a rapid feedback cycle. This approach is essential for the efficient exploration of complex material classes like high-entropy MOFs and bespoke SACs.

iii. **Next-generation electrode and device architectures:** The focus must expand from catalyst powder to integrated systems. Key directions include: (a) Advanced electrode engineering through additive manufacturing of 3D-printed structures and flexible films to optimize catalyst utilization and mass transport; (b) Membrane and interface engineering by designing MOF-incorporated membranes for selective ion transport and minimizing interfacial resistance; and (c) Developing hybrid multifunctional systems that intelligently couple reactions, such as integrating urea oxidation for wastewater remediation with CO_2 reduction for synchronous environmental and energy benefits.

iv. **Advancing circular economy and sustainable life cycles:** Sustainability must be a design criterion from the outset.

Research should prioritize "green-by-design" synthesis using water or mechanochemical methods, and explore using waste streams (e.g., plastic bottles, metal cans) as feedstocks for linker and metal source recovery. Equally crucial is developing efficient recycling and upcycling protocols for spent MOF electrodes. This involves designing MOFs with cleavable linkages for gentle recovery of valuable components and investigating pathways to regenerate catalytic activity or transform spent materials into new functional products.

v. **Establishing universal protocols and holistic assessment:** To enable meaningful progress comparison and guide industrial translation, the community must converge on standardized performance benchmarking protocols. These should define minimum stability thresholds (e.g., >1000 h for fuel cells), consistent testing conditions, and uniform reporting metrics. Furthermore, TEA and LCA must be integrated early in the research cycle to evaluate not just catalytic metrics but also cost viability and environmental impact, ensuring promising lab materials have a realistic path to market.

vi. **Designing bio-inspired, multi-functional integrated systems:** The ultimate ambition is to create complex, adaptive systems. Inspired by biological enzymes, future work should explore "artificial nano-enzyme" systems within MOFs, where multiple cooperative active sites work in concert. This vision extends to fully integrated, multi-functional devices that couple processes like UOR-driven wastewater purification with CO_2RR, achieving simultaneous remediation, energy storage, and chemical synthesis in a single, efficient platform.

vii. **Pioneering fundamental hypotheses:** The field must test new paradigms to break existing limitations. Can dynamic or "soft" MOFs that adapt under operation offer superior stability or selectivity? Can high-entropy MOF platforms create synergistic sites that definitively break scaling relationships for complex reactions like CO_2-to-C_2^+ conversion? How can we design MOF-electrolyte interfaces to control the local microenvironment and dramatically boost selectivity?

The exceptional promise of MOFs in electrocatalysis will only be realized through a fundamental paradigm shift: from a primary focus on novel synthesis and activity screening to a holistic "design-for-deployment" philosophy. These demands concerted, interdisciplinary efforts that synergize atomic-scale material innovation, robust device engineering, intelligent computational tools, and sustainable life-cycle management. By embracing this integrated approach, MOF-based technologies can transcend their status as compelling laboratory discoveries and evolve into indispensable, practical components of a global clean energy infrastructure, thereby making a direct and significant contribution to achieving a carbon-neutral future.

CRediT authorship contribution statement

Sheraz Muhammad: Conceptualization, Writing draft and Drawing figures; **Hao Sun:** Writing reviewing, Drawing figures and editing of text; **Sana Zahoor:** Writing – reviewing and editing of text; **Sumayya Khan:** Conceptualization and Investigation; **Rahmat Ullah:** Conceptualization; **Biao Fu:** Investigation; **Sana Ullah:** Conceptualization and Investigation; **Tayirjan Taylor Isimjan:** Writing – reviewing and editing; **Shohreh Azizi:** Writing – reviewing and editing and **Xiulin Yang:** Writing – reviewing and editing, Project administration, Supervision.

Declaration of Competing Interest

The authors declare that they have no known competing financial interests or personal relationships that could have appeared to influence the work reported in this paper

Acknowledgements

This work was financially supported by the Guangxi Science and Technology Projects (GUIKE LT2600640010), the Natural Science Foundation of Guangxi Province (2026GXNSFBA00640178), and the National Natural Science Foundation of China (52363028; W2621022; 21965005). I, Sheraz Muhammad, a PhD student at Guangxi Normal University, am also deeply grateful to the China Scholarship Council (CSC) for providing the scholarship that supports my doctoral studies in China.

Data availability

Data will be made available on request.

References

[1] B. Meng, Y. Liu, R. Andrew, M. Zhou, K. Hubacek, J. Xue, G. Peters, Y. Gao, More than half of China's CO_2 emissions are from micro, small and medium-sized enterprises, Appl. Energy 230 (2018) 712–725, https://doi.org/10.1016/j.apenergy.2018.08.107.

[2] H. Xiao, K.-J. Sun, H.-M. Bi, J.-J. Xue, Changes in carbon intensity globally and in countries: Attribution and decomposition analysis, Appl. Energy 235 (2019) 1492–1504, https://doi.org/10.1016/j.apenergy.2018.09.158.

[3] S. Fawzy, A.I. Osman, J. Doran, D.W. Rooney, Strategies for mitigation of climate change: a review, Environ. Chem. Lett. 18 (2020) 2069–2094, https://doi.org/10.1007/s10311-020-01059-w.

[4] J. Tian, L. Yu, R. Xue, S. Zhuang, Y. Shan, Global low-carbon energy transition in the post-COVID-19 era, Appl. Energy 307 (2022) 118205, https://doi.org/10.1016/j.apenergy.2021.118205.

[5] K.K. Jaiswal, C.R. Chowdhury, D. Yadav, R. Verma, S. Dutta, K.S. Jaiswal, SangmeshB, K.S.K. Karuppasamy, Renewable and sustainable clean energy development and impact on social, economic, and environmental health, Energy Nexus 7 (2022) 100118, https://doi.org/10.1016/j.nexus.2022.100118.

[6] Z. Wang, S. Li, Z. Jin, Z. Li, Q. Liu, K. Zhang, Oil and gas pathway to net-zero: review and outlook, Energy Strategy Rev. 45 (2023) 101048, https://doi.org/10.1016/j.esr.2022.101048.

[7] C. Voigt, The power of the Paris Agreement in international climate litigation, RECIEL 32 (2023) 237–249, https://doi.org/10.1111/reel.12514.

[8] S. Shiva Kumar, H. Lim, An overview of water electrolysis technologies for green hydrogen production, Energy Rep. 8 (2022) 13793–13813, https://doi.org/10.1016/j.egyr.2022.10.127.

[9] M. Awad, A. Said, M.H. Saad, A. Farouk, M.M. Mahmoud, M.S. Alshammari, M. L. Alghaythi, S.H.E. Abdel Aleem, A.Y. Abdelaziz, A.I. Omar, A review of water electrolysis for green hydrogen generation considering PV/wind/hybrid/hydropower/geothermal/tidal and wave/biogas energy systems, economic analysis, and its application, Alex. Eng. J. 87 (2024) 213–239, https://doi.org/10.1016/j.aej.2023.12.032.

[10] X. Jiang, L. Ke, K. Zhao, X. Yan, H. Wang, X. Cao, Y. Liu, L. Li, Y. Sun, Z. Wang, D. Dang, N. Yan, Integrating hydrogen utilization in CO_2 electrolysis with reduced energy loss, Nat. Commun. 15 (2024) 1427, https://doi.org/10.1038/s41467-024-45787-x.

[11] M. Liu, X. Xiao, Q. Li, L. Luo, M. Ding, B. Zhang, Y. Li, J. Zou, B. Jiang, Recent progress of electrocatalysts for oxygen reduction in fuel cells, J. Colloid Interface Sci. 607 (2022) 791–815, https://doi.org/10.1016/j.jcis.2021.09.008.

[12] S. Aslam, S. Rani, K. Lal, M. Fatima, T. Hardwick, B. Shirinfar, N. Ahmed, Electrochemical hydrogen production: sustainable hydrogen economy, Green. Chem. 25 (2023) 9543–9573, https://doi.org/10.1039/D3GC02849F.

[13] Q. Hassan, S. Algburi, A.Z. Sameen, H.M. Salman, M. Jaszczur, A review of hybrid renewable energy systems: Solar and wind-powered solutions: Challenges, opportunities, and policy implications, Results Eng. 20 (2023) 101621, https://doi.org/10.1016/j.rineng.2023.101621.

[14] T.-Z. Ang, M. Salem, M. Kamarol, H.S. Das, M.A. Nazari, N. Prabaharan, A comprehensive study of renewable energy sources: Classifications, challenges and suggestions, Energy Strategy Rev. 43 (2022) 100939, https://doi.org/10.1016/j.esr.2022.100939.

[15] A.G. Olabi, K. Elsaid, K. Obaideen, M.A. Abdelkareem, H. Rezk, T. Wilberforce, H. M. Maghrabie, E.T. Sayed, Renewable energy systems: Comparisons, challenges and barriers, sustainability indicators, and the contribution to UN sustainable development goals, Int. J. Thermofluids 20 (2023) 100498, https://doi.org/10.1016/j.ijft.2023.100498.

[16] V. Purohit, A. Datar, Overview of Topics in Electrocatalysis for Sustainability: Reactions, Electrocatalysts, Degradation, and Mitigation, Processes 13 (2025) 2659, https://doi.org/10.3390/pr13082659.

[17] C. Pak, S.G. Kim, H.S. Yang, Y.W. Kim, J.T. Lang, H.-M.J. Chang, O. Kwon, I. V. Zenyuk, Pathways to Low-Iridium Loading in Proton Exchange Membrane Water Electrolyzer Anodes: From Catalyst Design to Catalyst Layer Integration, ACS Appl. Energy Mater. 8 (2025) 11771–11785, https://doi.org/10.1021/acsaem.5c01438.

[18] J. George, S. Thangarasu, A. Jayaram, J. Jesuraj Periyanayagam, Materials for Electrocatalysis: Future Prospects in Energy Conversion, Chem. Rec. 25 (2025) e202400254, https://doi.org/10.1002/tcr.202400254.
[19] H. Wang, Z. Yan, F. Cheng, J. Chen, Advances in Noble Metal Electrocatalysts for Acidic Oxygen Evolution Reaction: Construction of Under-Coordinated Active Sites, Adv. Sci. 11 (2024) 2401652, https://doi.org/10.1002/advs.202401652.
[20] R. Nakatani, T. Irie, S. Das, Q. Fang, Y. Negishi, Converging the Complementary Traits of Metal–Organic Frameworks and Covalent Organic Frameworks, ACS Appl. Mater. Interfaces 17 (2025) 24701–24729, https://doi.org/10.1021/acsami.4c21991.
[21] V.F. Yusuf, N.I. Malek, S.K. Kailasa, Review on Metal–Organic Framework Classification, Synthetic Approaches, and Influencing Factors: Applications in Energy, Drug Delivery, and Wastewater Treatment, ACS Omega 7 (2022) 44507–44531, https://doi.org/10.1021/acsomega.2c05310.
[22] X. Chen, S.M. Argandona, F. Melle, N. Rampal, D. Fairen-Jimenez, Advances in surface functionalization of next-generation metal-organic frameworks for biomedical applications: Design, strategies, and prospects, Chem 10 (2024) 504–543, https://doi.org/10.1016/j.chempr.2023.09.016.
[23] S. Sonowal, R. Prasad, Exploring the recent advancement of MOFs (metal-organic frameworks) in agriculture and food technology, Mater 9 (2025) 101016, https://doi.org/10.1016/j.nxmate.2025.101016.
[24] N.F. Suremann, B.D. McCarthy, W. Gschwind, A. Kumar, B.A. Johnson, L. Hammarström, S. Ott, Molecular Catalysis of Energy Relevance in Metal–Organic Frameworks: From Higher Coordination Sphere to System Effects, Chem. Rev. 123 (2023) 6545–6611, https://doi.org/10.1021/acs.chemrev.2c00587.
[25] Z. Fei, Y. Song, M. Wu, Y. Wu, Y. Chen, D.J. Kang, C. Bian, Y. Qian, MOF-Derived Metal Sulfides and Their Composites: Synthesis and Their Electrochemical Water Splitting, Catalysts 15 (2025) 928, https://doi.org/10.3390/catal15100928.
[26] Y. Qian, Y. Sun, F. Zhang, Y. Song, X. Luo, L. Shen, M. Sohn, H. Shi, D.J. Kang, Controlling the microenvironment by introducing dual metal atoms into ZIF-L to enhance hydrogen evolution activity, Appl. Surf. Sci. 684 (2025) 161791, https://doi.org/10.1016/j.apsusc.2024.161791.
[27] N. Yao, H. Jia, J. Zhu, Z. Shi, H. Cong, J. Ge, W. Luo, Atomically dispersed Ru oxide catalyst with lattice oxygen participation for efficient acidic water oxidation, Chem 9 (2023) 1882–1896, https://doi.org/10.1016/j.chempr.2023.03.005.
[28] L. Junlin, Z. Wei, P. Yudi, Z. Yifan, W. Shengchen, W. Qingqing, Z. Wei, L. Suli, D. Zhihui, W. Dingsheng, MOFs-based single/dual-atom catalysts: atomically active sites engineering for efficient CO_2 reduction, Chem. Synth. 5 (2025) 69, https://doi.org/10.20517/cs.2025.12.
[29] J. Xiang, P. Wang, P. Li, M. Zhou, G. Yu, Z. Jin, Inter-Site Distance Effect in Electrocatalysis, Angew. Chem. Int. Ed. 64 (2025) e202500644, https://doi.org/10.1002/anie.202500644.
[30] Y. Zhang, L.-Z. Dong, S. Li, X. Huang, J.-N. Chang, J.-H. Wang, J. Zhou, S.-L. Li, Y.-Q. Lan, Coordination environment dependent selectivity of single-site-Cu enriched crystalline porous catalysts in CO_2 reduction to CH_4, Nat. Commun. 12 (2021) 6390, https://doi.org/10.1038/s41467-021-26724-8.
[31] K. Harrath, Z. Yao, Y.-F. Jiang, Y.-G. Wang, J. Li, Tailoring the Active-Site Spacing of a Single-Atom Catalyst for CH_4-to-CH_3-OH Conversion: The Co_1/UiO-66 MOF as an Exemplary Model, J. Phys. Chem. C. 128 (2024) 5579–5589, https://doi.org/10.1021/acs.jpcc.4c00742.
[32] Y. Qian, F. Zhang, S. Zhao, C. Bian, H. Mao, D.J. Kang, H. Pang, Recent progress of metal-organic framework-derived composites: Synthesis and their energy conversion applications, Nano Energy 111 (2023) 108415, https://doi.org/10.1016/j.nanoen.2023.108415.
[33] N. Sun, S.S.A. Shah, Z. Lin, Y.-Z. Zheng, L. Jiao, H.-L. Jiang, MOF-Based Electrocatalysts: An Overview from the Perspective of Structural Design, Chem. Rev. 125 (2025) 2703–2792, https://doi.org/10.1021/acs.chemrev.4c00664.
[34] Y. Yang, Y. Yang, Y. Liu, S. Zhao, Z. Tang, Metal–Organic Frameworks for Electrocatalysis: Beyond Their Derivatives, Small Sci. 1 (2021) 2100015, https://doi.org/10.1002/smsc.202100015.
[35] C. Li, H. Zhang, M. Liu, F.-F. Lang, J. Pang, X.-H. Bu, Recent progress in metal–organic frameworks (MOFs) for electrocatalysis, Ind. Chem. Mater. 1 (2023) 9–38, https://doi.org/10.1039/D2IM00063F.
[36] Y. Guo, S. Zhao, X. Tang, H. Yi, Research progress on metal-organic framework compounds (MOFs) in electrocatalysis, J. Environ. Sci. 141 (2024) 261–276, https://doi.org/10.1016/j.jes.2023.06.027.
[37] B. He, Q. Zhang, Z. Pan, L. Li, C. Li, Y. Ling, Z. Wang, M. Chen, Z. Wang, Y. Yao, Q. Li, L. Sun, J. Wang, L. Wei, Freestanding Metal–Organic Frameworks and Their Derivatives: An Emerging Platform for Electrochemical Energy Storage and Conversion, Chem. Rev. 122 (2022) 10087–10125, https://doi.org/10.1021/acs.chemrev.1c00978.
[38] Y. Song, Q. Fang, Y. Liang, Y. Wu, B. Tong, Z. Fei, D.J. Kang, Y. Qian, Recent progress of metal-organic frameworks derived carbon-based composites: Synthesis and electrochemical applications, J. Alloy. Compd. 1040 (2025) 183604, https://doi.org/10.1016/j.jallcom.2025.183604.
[39] F. Zhang, Y. Qian, Z. Jin, Z. Fei, J. Zhang, H. Mao, D.J. Kang, H. Pang, Recent advances in MOFs/MXenes composites: Synthesis and their electrochemical energy applications, J. Energy Storage 72 (2023) 108213, https://doi.org/10.1016/j.est.2023.108213.
[40] H.-Y. Tan, J. Wang, S.-C. Lin, T.-R. Kuo, H.M. Chen, Dynamic Coordination Structure Evolutions of Atomically Dispersed Metal Catalysts for Electrocatalytic Reactions, Adv. Mater. Interfaces 10 (2023) 2202050, https://doi.org/10.1002/admi.202202050.
[41] J. Wang, H. Kong, J. Zhang, Y. Hao, Z. Shao, F. Ciucci, Carbon-based electrocatalysts for sustainable energy applications, Prog. Mater. Sci. 116 (2021) 100717, https://doi.org/10.1016/j.pmatsci.2020.100717.
[42] K. Zeng, X. Zheng, C. Li, J. Yan, J.-H. Tian, C. Jin, P. Strasser, R. Yang, Recent Advances in Non-Noble Bifunctional Oxygen Electrocatalysts toward Large-Scale Production, Adv. Funct. Mater. 30 (2020) 2000503, https://doi.org/10.1002/adfm.202000503.
[43] T. Wang, A. Chutia, D.J.L. Brett, P.R. Shearing, G. He, G. Chai, I.P. Parkin, Palladium alloys used as electrocatalysts for the oxygen reduction reaction, Energy Environ. Sci. 14 (2021) 2639–2669, https://doi.org/10.1039/D0EE03915B.
[44] S. Siahrostami, A. Verdaguer-Casadevall, M. Karamad, D. Deiana, P. Malacrida, B. Wickman, M. Escudero-Escribano, E.A. Paoli, R. Frydendal, T.W. Hansen, I. Chorkendorff, I.E.L. Stephens, J. Rossmeisl, Enabling direct H_2O_2 production through rational electrocatalyst design, Nat. Mater. 12 (2013) 1137–1143, https://doi.org/10.1038/nmat3795.
[45] A. Kulkarni, S. Siahrostami, A. Patel, J.K. Nørskov, Understanding Catalytic Activity Trends in the Oxygen Reduction Reaction, Chem. Rev. 118 (2018) 2302–2312, https://doi.org/10.1021/acs.chemrev.7b00488.
[46] H.A. Hansen, J. Rossmeisl, J.K. Nørskov, Surface Pourbaix diagrams and oxygen reduction activity of Pt, Ag and Ni(111) surfaces studied by DFT, Phys. Chem. Chem. Phys. 10 (2008) 3722–3730, https://doi.org/10.1039/B803956A.
[47] W. Xu, Z. Wu, S. Tao, Urea-Based Fuel Cells and Electrocatalysts for Urea Oxidation, Energy Technol. 4 (2016) 1329–1337, https://doi.org/10.1002/ente.201600185.
[48] J. Ge, J. Kuang, Y. Xiao, M. Guan, C. Yang, Recent development of nickel-based catalysts and in situ characterization techniques for mechanism understanding of the urea oxidation reaction, Surf. Interfaces 41 (2023) 103230, https://doi.org/10.1016/j.surfin.2023.103230.
[49] W. Simka, J. Piotrowski, A. Robak, G. Nawrat, Electrochemical treatment of aqueous solutions containing urea, J. Appl. Electrochem. 39 (2009) 1137–1143, https://doi.org/10.1007/s10800-008-9771-4.
[50] J. Wright, A. Michaels, A. Appleby, Electrooxidation of urea at the ruthenium titanium oxide electrode, AIChE J. 32 (1986) 1450–1458, https://doi.org/10.1002/aic.690320906.
[51] D. Zhu, H. Zhang, J. Miao, F. Hu, L. Wang, Y. Tang, M. Qiao, C. Guo, Strategies for designing more efficient electrocatalysts towards the urea oxidation reaction, J. Mater. Chem. A 10 (2022) 3296–3313, https://doi.org/10.1039/D1TA09989B.
[52] J. Gautam, S.-Y. Lee, S.-J. Park, Cutting-Edge Optimization Strategies and In Situ Characterization Techniques for Urea Oxidation Reaction Catalysts: A Comprehensive Review, Adv. Energy Mater. 15 (2025) 2406047, https://doi.org/10.1002/aenm.202406047.
[53] S. Kumar, G.B. Bhanuse, Y.-P. Fu, Phosphide-Based Electrocatalysts for Urea Electrolysis: Recent Trends and Progress, ChemPhysChem 25 (2024) e202300924, https://doi.org/10.1002/cphc.202300924.
[54] J. Li, J. Li, T. Liu, L. Chen, Y. Li, H. Wang, X. Chen, M. Gong, Z.-P. Liu, X. Yang, Deciphering and Suppressing Over-Oxidized Nitrogen in Nickel-Catalyzed Urea Electrolysis, Angew. Chem. Int. Ed. 60 (2021) 26656–26662, https://doi.org/10.1002/anie.202107886.
[55] W. Chen, L. Xu, X. Zhu, Y.-C. Huang, W. Zhou, D. Wang, Y. Zhou, S. Du, Q. Li, C. Xie, L. Tao, C.-L. Dong, J. Liu, Y. Wang, R. Chen, H. Su, C. Chen, Y. Zou, Y. Li, Q. Liu, S. Wang, Unveiling the Electrooxidation of Urea: Intramolecular Coupling of the N−N Bond, Angew. Chem. Int. Ed. 60 (2021) 7297–7307, https://doi.org/10.1002/anie.202015773.
[56] R. Naz, M. Tahir, Recent Developments in Metal-free Materials for Photocatalytic and Electrocatalytic Carbon Dioxide Conversion into Value Added Products, Energy Fuels 39 (2025) 6127–6150, https://doi.org/10.1021/acs.energyfuels.5c00175.
[57] K. Lian, J. Ding, Y. Liu, Q. Liu, Y. Wu, G. Hu, X. Liu, Recent advances in Ni-based catalysts for hybrid CO_2 electrolysis, J. Mater. Chem. A 13 (2025) 14491–14509, https://doi.org/10.1039/D5TA01358E.
[58] A.J. Martín, G.O. Larrazábal, J. Pérez-Ramírez, Towards sustainable fuels and chemicals through the electrochemical reduction of CO_2: lessons from water electrolysis, Green. Chem. 17 (2015) 5114–5130, https://doi.org/10.1039/C5GC01893E.
[59] A. Al Harthi, M.A. Abri, H.A. Younus, R.A. Hajri, Criteria and cutting-edge catalysts for CO_2 electrochemical reduction at the industrial scale, J. CO2 Util. 83 (2024) 102819, https://doi.org/10.1016/j.jcou.2024.102819.
[60] F. Shen, S. Wu, M. Kurniawan, D. Ostheimer, J. Shi, T. Chen, A. Bund, T. Hannappel, J. Liu, P. Zhao, S. Miao, Study on reaction mechanism of CO_2 electro-reduction to CO in organic medium: Revealed by experimental and spectroscopic Investigations, Appl. Surf. Sci. 681 (2025) 161459, https://doi.org/10.1016/j.apsusc.2024.161459.
[61] K.C. Poon, W.Y. Wan, H. Su, H. Sato, A review on recent advances in the electrochemical reduction of CO_2 to CO with nano-electrocatalysts, RSC Adv. 12 (2022) 22703–22721, https://doi.org/10.1039/D2RA03341K.
[62] S. Jin, Z. Hao, K. Zhang, Z. Yan, J. Chen, Advances and Challenges for the Electrochemical Reduction of CO_2 to CO: From Fundamentals to Industrialization, Angew. Chem. Int. Ed. 60 (2021) 20627–20648, https://doi.org/10.1002/anie.202101818.
[63] A. Naikkath, N.G. Mohan, K. Ramanujam, R. Srinivasan, Mechanism of electrochemical carbon dioxide reduction to formate on tin electrode, Chem. Eng. J. 482 (2024) 148972, https://doi.org/10.1016/j.cej.2024.148972.
[64] J. Dong, Y. Liu, J. Pei, H. Li, S. Ji, L. Shi, Y. Zhang, C. Li, C. Tang, J. Liao, S. Xu, H. Zhang, Q. Li, S. Zhao, Continuous electroproduction of formate via CO_2

reduction on local symmetry-broken single-atom catalysts, Nat. Commun. 14 (2023) 6849, https://doi.org/10.1038/s41467-023-42539-1.
[65] N. Han, P. Ding, L. He, Y. Li, Y. Li, Promises of Main Group Metal–Based Nanostructured Materials for Electrochemical CO_2 Reduction to Formate, Adv. Energy Mater. 10 (2020) 1902338, https://doi.org/10.1002/aenm.201902338.
[66] G. Zhang, T. Wang, M. Zhang, L. Li, D. Cheng, S. Zhen, Y. Wang, J. Qin, Z.-J. Zhao, J. Gong, Selective CO_2 electroreduction to methanol via enhanced oxygen bonding, Nat. Commun. 13 (2022) 7768, https://doi.org/10.1038/s41467-022-35450-8.
[67] S. Wang, T. Kou, S.E. Baker, E.B. Duoss, Y. Li, Electrochemical Reduction of CO_2 to Alcohols: Current Understanding, Progress, and Challenges, Adv. Energy Sustain. Res. 3 (2022) 2100131, https://doi.org/10.1002/aesr.202100131.
[68] Z. Wang, Y. Li, Z. Ma, D. Wang, X. Ren, Strategies for overcoming challenges in selective electrochemical CO_2 conversion to ethanol, iScience 27 (2024) 110437, https://doi.org/10.1016/j.isci.2024.110437.
[69] A. Al Harthi, M.A. Abri, H.A. Younus, R.A. Hajri, Criteria and cutting-edge catalysts for CO_2 electrochemical reduction at the industrial scale, J. CO2 Util. 83 (2024) 102819, https://doi.org/10.1016/j.jcou.2024.102819.
[70] M.S. Hussain, S. Ahmed, M. Irshad, S.S. Bibi, M. Asif, F. Sher, M.K. Khan, Recent engineering strategies for enhancing C_2^+ product formation in copper-catalyzed CO_2 electroreduction, Nano Mater. Sci. (2024), https://doi.org/10.1016/j.nanoms.2024.09.001.
[71] Y. Wang, M. Yu, X. Zhang, Y. Gao, J. Liu, X. Zhang, C. Gong, X. Cao, Z. Ju, Y. Peng, Density Functional Theory Study of CO_2 Hydrogenation on Transition-Metal-Doped Cu(211) Surfaces, Molecules 28 (2023) 2852, https://doi.org/10.3390/molecules28062852.
[72] Y. Yang, M.G. White, P. Liu, Theoretical Study of Methanol Synthesis from CO_2 Hydrogenation on Metal-Doped Cu(111) Surfaces, J. Phys. Chem. C. 116 (2012) 248–256, https://doi.org/10.1021/jp208448c.
[73] N. Sikdar, Electrochemical CO_2 Reduction Reaction: Comprehensive Strategic Approaches to Catalyst Design for Selective Liquid Products Formation, Chem. Eur. J. 30 (2024) e202402477, https://doi.org/10.1002/chem.202402477.
[74] Y. Feng, W. An, Z. Wang, Y. Wang, Y. Men, Y. Du, Electrochemical CO_2 Reduction Reaction on M@Cu(211) Bimetallic Single-Atom Surface Alloys: Mechanism, Kinetics, and Catalyst Screening, ACS Sustain. Chem. Eng. 8 (2020) 210–222, https://doi.org/10.1021/acssuschemeng.9b05183.
[75] B. Chang, H. Pang, F. Raziq, S. Wang, K.-W. Huang, J. Ye, H. Zhang, Electrochemical reduction of carbon dioxide to multicarbon (C_2^+) products: challenges and perspectives, Energy Environ. Sci. 16 (2023) 4714–4758, https://doi.org/10.1039/D3EE00964E.
[76] A.A. Peterson, F. Abild-Pedersen, F. Studt, J. Rossmeisl, J.K. Nørskov, How copper catalyzes the electroreduction of carbon dioxide into hydrocarbon fuels, Energy Environ. Sci. 3 (2010) 1311–1315, https://doi.org/10.1039/C0EE00071J.
[77] Q. Xue, X. Qi, K. Li, Y. Zeng, F. Xu, K. Zhang, T. Yang, X. Qi, J. Jiang, DFT Study of CO_2 Reduction Reaction to CH_3OH on Low-Index Cu Surfaces, Catalysts 13 (2023) 722, https://doi.org/10.3390/catal13040722.
[78] O. Ogunbanjo, P. Rodríguez, P. Anderson, MOF electrocatalysts in CO_2 conversion: critical analysis of research trends, challenges and prospects, Mater. Chem. Front. 9 (2025) 1650–1680, https://doi.org/10.1039/D4QM01060D.
[79] H.M.W. Abid, M.P. Balanay, Next-Generation Cu-MOF-based electrocatalysts for CO_2 reduction: Bridging mechanistic insights and rational design, Carbon Capture Sci. Technol. 17 (2025) 100521, https://doi.org/10.1016/j.ccst.2025.100521.
[80] Z. Lin, Z. Han, G.E.P. O'Connell, T. Wan, D. Zhang, Z. Ma, D. Chu, X. Lu, Graphene and MOF Assembly: Enhanced Fabrication and Functional Derivative via MOF Amorphization, Adv. Mater. 36 (2024) 2312797, https://doi.org/10.1002/adma.202312797.
[81] S. Sanati, R.S. Varma, M. Liu, R. Abazari, Non-noble metal–organic frameworks in electrocatalytic urea-assisted hydrogen production and energy-saving regeneration, Energy Environ. Sci. 18 (2025) 7733–7755, https://doi.org/10.1039/D5EE02029H.
[82] J. Liu, T.A. Goetjen, Q. Wang, J.G. Knapp, M.C. Wasson, Y. Yang, Z.H. Syed, M. Delferro, J.M. Notestein, O.K. Farha, J.T. Hupp, MOF-enabled confinement and related effects for chemical catalyst presentation and utilization, Chem. Soc. Rev. 51 (2022) 1045–1097, https://doi.org/10.1039/D1CS00968K.
[83] Z. Zhai, W. Yan, L. Dong, S. Deng, D.P. Wilkinson, X. Wang, L. Zhang, J. Zhang, Catalytically active sites of MOF-derived electrocatalysts: synthesis, characterization, theoretical calculations, and functional mechanisms, J. Mater. Chem. A 9 (2021) 20320–20344, https://doi.org/10.1039/D1TA02896K.
[84] Z. Fan, X. Cui, J. Wei, C. Chen, H. Tang, J. Li, Host-guest interactions promoted formation of Fe-N_4 active site toward efficient oxygen reduction reaction catalysis, J. Colloid Interface Sci. 621 (2022) 195–204, https://doi.org/10.1016/j.jcis.2022.04.059.
[85] C. Liu, X.-D. Zhang, J.-M. Huang, M.-X. Guan, M. Xu, Z.-Y. Gu, Situ Reconstruction of Cu–N Coordinated MOFs to Generate Dispersive Cu/Cu_2O Nanoclusters for Selective Electroreduction of CO_2 to C_2H_4, ACS Catal. 12 (2022) 15230–15240, https://doi.org/10.1021/acscatal.2c04275.
[86] R. Zafar, A. Javaid, M. Imran, S. Latif, M. Naeem Khan, L. Mitu, R. Crețu, Recent advances in catalytic reduction of CO_2 through bismuth based MOFs, J. Saudi Chem. Soc. 28 (2024) 101926, https://doi.org/10.1016/j.jscs.2024.101926.
[87] H. Wang, H. Zou, Y. Liu, Z. Liu, W. Sun, K.A. Lin, T. Li, S. Luo, Ni_2P nanocrystals embedded Ni-MOF nanosheets supported on nickel foam as bifunctional electrocatalyst for urea electrolysis, Sci. Rep. 11 (2021) 21414, https://doi.org/10.1038/s41598-021-00776-8.
[88] C. Li, Y. Ji, Y. Wang, C. Liu, Z. Chen, J. Tang, Y. Hong, X. Li, T. Zheng, Q. Jiang, C. Xia, Applications of Metal–Organic Frameworks and Their Derivatives in Electrochemical CO_2 Reduction, Nano-Micro Lett. 15 (2023) 113, https://doi.org/10.1007/s40820-023-01092-8.
[89] P. Yuan, C.K.T. Wun, T.W.B. Lo, Harnessing Synergistic Cooperation of Neighboring Active Motifs in Heterogeneous Catalysts for Enhanced Catalytic Performance, Adv. Mater. 37 (2025) 2501960, https://doi.org/10.1002/adma.202501960.
[90] M. Liu, Z. Lei, X. Lv, X. Song, L. Zhang, S. Li, T. Sun, L. Li, J. Hui, W. Zhang, S. Y. Wong, X. Li, G.J. Xia, J. Zhang, S. Sun, Enhancing the ORR durability of single atomic Fe-N_4 active sites with implanted SiO_2 nanoparticles as radical and H_2O_2 inhibitors, Nat. Commun. 16 (2025) 10178, https://doi.org/10.1038/s41467-025-65194-0.
[91] Z. Dai, X. Du, X. Zhang, Controlled synthesis of $NiCo_2O_4$@Ni-MOF on Ni foam as efficient electrocatalyst for urea oxidation reaction and oxygen evolution reaction, Int. J. Hydrog. Energy 47 (2022) 17252–17262, https://doi.org/10.1016/j.ijhydene.2022.03.217.
[92] C. Liu, Z. Wu, Y. Li, H. Yu, S. Chen, W. Hong, S. Deng, J. Wang, situ transformation of a Bi-based MOF to a highly active catalyst for CO_2 reduction, New. J. Chem. 48 (2024) 15112–15119, https://doi.org/10.1039/D4NJ02279C.
[93] X. Hu, S. Liu, U. Farooq, Iu Islam, S. Li, X. Zhao, J. Long, X. Wang, Dynamic regulation of Cu-based catalysts for electrocatalytic CO_2 reduction: Design strategies, mechanism analysis, and industrial challenges, Nano Res. 18 (2025) 94907686, https://doi.org/10.26599/NR.2025.94907686.
[94] R. Saha, K. Gupta, C.J. Gómez García, Strategies to Improve Electrical Conductivity in Metal–Organic Frameworks: A Comparative Study, Cryst. Growth Des. 24 (2024) 2235–2265, https://doi.org/10.1021/acs.cgd.3c01162.
[95] E. Momtaz, M. Amoozadeh, A. Zarepour, A. Khosravi, A. Zarrabi, S. Iravani, MXenes and MOFs for electrochemical reduction of carbon dioxide (CO_2), RSC Sustain. 4 (2026) 1731–1759, https://doi.org/10.1039/d5su00740b.
[96] R. Wei, X. Liu, A.B. Ibragimov, J. Gao, Recent strategies to improve the electroactivity of metal–organic frameworks for advanced electrocatalysis, Inf. Funct. Mater. 1 (2024) 181–206, https://doi.org/10.1002/ifm2.19.
[97] G. Potsi, Y.-H.J. Tsai, A. Reese, D. Yoon, J.L. Hitt, A. Kouloumpis, J. Suntivich, D. A. Muller, T.E. Mallouk, E.P. Giannelis, Effects of Mesoporosity and Conductivity of Hierarchically Porous Carbon Supports on the Deposition of Pt Nanoparticles and Their Performance as Electrocatalysts for Oxygen Reduction Reaction in Alkaline Media, ACS Appl. Mater. Interfaces 15 (2023) 33028–33036, https://doi.org/10.1021/acsami.3c01935.
[98] Y. Liu, Y. Zhang, Z. Sun, L. Dai, B. Liu, W. Li, Catalysts with three-dimensional porous structure for electrocatalytic water splitting, Sustain. Mater. Technol. 44 (2025) e01392, https://doi.org/10.1016/j.susmat.2025.e01392.
[99] K.-K. Liu, Z. Meng, Y. Fang, H.-L. Jiang, Conductive MOFs for electrocatalysis and electrochemical sensor, eScience 3 (2023) 100133, https://doi.org/10.1016/j.esci.2023.100133.
[100] T. Liu, W. Yu, H. Au, Y. Hatakeyama, K. Gotoh, T. Kondo, M.-M. Titirici, H. Nishihara, Recent Progress in the Design of Functional Carbon Materials for Energy Storage, ACS Appl. Energy Mater. 8 (2025) 17155–17179, https://doi.org/10.1021/acsaem.5c03095.
[101] Z. Jia, J. Dang, G. Wen, Y. Zhang, Z. Chen, Z. Bai, L. Yang, Constructing Nanocaged Enzymes for Synergistic Catalysis of CO_2 Reduction, Adv. Sci. 10 (2023) 2300752, https://doi.org/10.1002/advs.202300752.
[102] B. Yang, T. Gu, W. Liu, Z. Wu, Pore engineering to improve oxygen transport in cathode oxygen reduction catalysts of proton exchange membrane fuel cells, Nano Res. 18 (2025) 94907684, https://doi.org/10.26599/NR.2025.94907684.
[103] Y. Luo, K. Li, Y. Hu, T. Chen, J. Hu, J. Feng, J. Feng, Boosting the Performance of Low-Platinum Fuel Cells via a Hierarchical and Interconnected Porous Carbon Support, ACS Appl. Mater. Interfaces 16 (2024) 4811–4817, https://doi.org/10.1021/acsami.3c16637.
[104] W. Li, X. Lu, Z. Li, From Ni Sites to System Synergy: Decoding Structural-Mechanism-Performance Relationships in Urea Electrooxidation Catalysts, Adv. Energy Mater. 16 (2026) e04716, https://doi.org/10.1002/aenm.202504716.
[105] H. Chen, X. Liang, Y. Liu, X. Ai, T. Asefa, X. Zou, Active Site Engineering in Porous Electrocatalysts, Adv. Mater. 32 (2020) 2002435, https://doi.org/10.1002/adma.202002435.
[106] X. Li, X.-T. Wu, Q. Xu, Q.-L. Zhu, Hierarchically Ordered Pore Engineering of Metal–Organic Framework-Based Materials for Electrocatalysis, Adv. Mater. 36 (2024) 2401926, https://doi.org/10.1002/adma.202401926.
[107] M. Li, M.N. Idros, Y. Wu, T. Burdyny, S. Garg, X.S. Zhao, G. Wang, T.E. Rufford, The role of electrode wettability in electrochemical reduction of carbon dioxide, J. Mater. Chem. A 9 (2021) 19369–19409, https://doi.org/10.1039/D1TA03636J.
[108] Y. Liao, Y. Chen, L. Li, S. Luo, Y. Qing, C. Tian, H. Xu, J. Zhang, Y. Wu, Ultrafine Homologous Ni_2P–Co_2P Heterostructures via Space-Confined Topological Transformation for Superior Urea Electrolysis, Adv. Funct. Mater. 33 (2023) 2303300, https://doi.org/10.1002/adfm.202303300.
[109] L. Ye, J. Yang, D.-P. Kim, D. Sun, Advances in hydrophobic metal-organic frameworks (MOFs) for photo/electrocatalytic CO_2 reduction, Nano Res. 19 (2026) 94908041, https://doi.org/10.26599/NR.2025.94908041.
[110] J. Zhang, H.B. Yang, D. Zhou, B. Liu, Adsorption Energy in Oxygen Electrocatalysis, Chem. Rev. 122 (2022) 17028–17072, https://doi.org/10.1021/acs.chemrev.1c01003.
[111] Y. Cao, Y. Mou, J. Zhang, R. Zhang, Z. Liang, Porphyrin-based frameworks and derivatives for the oxygen reduction reaction, Mater. Today Catal. 4 (2024) 100044, https://doi.org/10.1016/j.mtcata.2024.100044.
[112] T. Guo, X. Wang, X. Xing, Z. Fu, C. Ma, A.H. Bedane, L. Kong, Enhancing effect of cobalt phthalocyanine dispersion on electrocatalytic reduction of CO2 towards

methanol, Environ. Sci. Pollut. Res. 30 (2023) 122755–122773, https://doi.org/10.1007/s11356-023-30883-0.
[113] H. Sun, L. Chen, L. Xiong, K. Feng, Y. Chen, X. Zhang, X. Yuan, B. Yang, Z. Deng, Y. Liu, M.H. Rümmeli, J. Zhong, Y. Jiao, Y. Peng, Promoting ethylene production over a wide potential window on Cu crystallites induced and stabilized via current shock and charge delocalization, Nat. Commun. 12 (2021) 6823, https://doi.org/10.1038/s41467-021-27169-9.
[114] S. Lu, X. Zheng, Y. Zeng, Q. Hua, X. Wang, Y. Liu, H. Liu, Triphenylamine-Substituted Ni(II) Porphyrins for Urea Electro-oxidation, Inorg. Chem. 63 (2024) 20929–20934, https://doi.org/10.1021/acs.inorgchem.4c03870.
[115] X. Yin, L. Lin, U. Martinez, P. Zelenay, 2,2′-Dipyridylamine as Heterogeneous Organic Molecular Electrocatalyst for Two-Electron Oxygen Reduction Reaction in Acid Media, ACS Appl. Energy Mater. 2 (2019) 7272–7278, https://doi.org/10.1021/acsaem.9b01227.
[116] D.-H. Nam, O. Shekhah, G. Lee, A. Mallick, H. Jiang, F. Li, B. Chen, J. Wicks, M. Eddaoudi, E.H. Sargent, Intermediate Binding Control Using Metal–Organic Frameworks Enhances Electrochemical CO_2 Reduction, J. Am. Chem. Soc. 142 (2020) 21513–21521, https://doi.org/10.1021/jacs.0c10774.
[117] A. Bohan, X. Jin, M. Wang, X. Ma, Y. Wang, L. Zhang, Uncoordinated amino groups of MIL-101 anchoring cobalt porphyrins for highly selective CO_2 electroreduction, J. Colloid Interface Sci. 654 (2024) 830–839, https://doi.org/10.1016/j.jcis.2023.10.089.
[118] H. Zhao, T. Xing, L. Li, X. Geng, K. Guo, C. Sun, W. Zhou, H. Yang, R. Song, B. An, Synthesis of cobalt and nitrogen co-doped carbon nanotubes and its ORR activity as the catalyst used in hydrogen fuel cells, Int. J. Hydrog. Energy 44 (2019) 25180–25187, https://doi.org/10.1016/j.ijhydene.2019.03.271.
[119] J. Duan, Y. He, H. Zhu, G. Qin, W. Wei, Research progress on performance of fuel cell system utilized in vehicle, Int. J. Hydrog. Energy 44 (2019) 5530–5537, https://doi.org/10.1016/j.ijhydene.2018.08.039.
[120] G. Slaughter, T. Kulkarni, Enzymatic glucose biofuel cell and its application, J. Biochips Tissue Chips 5 (2015) 1000111, https://doi.org/10.4172/21530777.1000111.
[121] N.A.A. Qasem, G.A.Q. Abdulrahman, A Recent Comprehensive Review of Fuel Cells: History, Types, and Applications, Int. J. Energy Res. 2024 (2024) 7271748, https://doi.org/10.1155/2024/7271748.
[122] A. Jamil, S. Rafiq, T. Iqbal, H.A.A. Khan, H.M. Khan, B. Azeem, M.Z. Mustafa, A. S. Hanbazazah, Current status and future perspectives of proton exchange membranes for hydrogen fuel cells, Chemosphere 303 (2022) 135204, https://doi.org/10.1016/j.chemosphere.2022.135204.
[123] J. Li, J. Cheng, Y. Zhang, Z. Chen, M. Nasr, M. Farghali, D.W. Rooney, P.-S. Yap, A.I. Osman, Advancements in Solid Oxide Fuel Cell Technology: Bridging Performance Gaps for Enhanced Environmental Sustainability, Adv. Energy Sustain. Res. 5 (2024) 2400132, https://doi.org/10.1002/aesr.202400132.
[124] M.A. Abdelkareem, K. Elsaid, T. Wilberforce, M. Kamil, E.T. Sayed, A. Olabi, Environmental aspects of fuel cells: A review, Sci. Total. Environ. 752 (2021) 141803, https://doi.org/10.1016/j.scitotenv.2020.141803.
[125] E. Antolini, The stability of molten carbonate fuel cell electrodes: A review of recent improvements, Appl. Energy 88 (2011) 4274–4293, https://doi.org/10.1016/j.apenergy.2011.07.009.
[126] Z. Pu, G. Zhang, A. Hassanpour, D. Zheng, S. Wang, S. Liao, Z. Chen, S. Sun, Regenerative fuel cells: Recent progress, challenges, perspectives and their applications for space energy system, Appl. Energy 283 (2021) 116376, https://doi.org/10.1016/j.apenergy.2020.116376.
[127] F. Cai, S. Cai, Z. Tu, Proton exchange membrane fuel cell (PEMFC) operation in high current density (HCD): Problem, progress and perspective, Energy Convers. Manag. 307 (2024) 118348, https://doi.org/10.1016/j.enconman.2024.118348.
[128] M.M. Tellez-Cruz, J. Escorihuela, O. Solorza-Feria, V. Compañ, Proton Exchange Membrane Fuel Cells (PEMFCs): Advances and Challenges, Polymers 13 (2021) 3064, https://doi.org/10.3390/polym13183064.
[129] J. Tao, X. Wang, M. Xu, C. Liu, J. Ge, W. Xing, Non-noble metals as activity sites for ORR catalysts in proton exchange membrane fuel cells (PEMFCs), Ind. Chem. Mater. 1 (2023) 388–409, https://doi.org/10.1039/D3IM00002H.
[130] R. Iqbal, S. Ali, G. Yasin, S. Ibraheem, M. Tabish, M. Hamza, H. Chen, H. Xu, J. Zeng, W. Zhao, A novel 2D $Co_3(HADQ)_2$ metal-organic framework as a highly active and stable electrocatalyst for acidic oxygen reduction, Chem. Eng. J. 430 (2022) 132642, https://doi.org/10.1016/j.cej.2021.132642.
[131] R. Iqbal, S. Ali, A. Saleem, M.K. Majeed, A. Hussain, S. Rauf, A. Rehman Akbar, H. Xu, L. Qiao, W. Zhao, Electrically conductive Pt-MOFs for acidic oxygen reduction: Optimized performance via altering conjugated ligands, Chem. Eng. J. 455 (2023) 140799, https://doi.org/10.1016/j.cej.2022.140799.
[132] J.I. Koo, S.J. Jeong, Improved Technology Readiness Assessment Framework for System-of-Systems From a System Integration Perspective, IEEE Access. 12 (2024) 23827–23853, https://doi.org/10.1109/ACCESS.2024.3362229.
[133] W. Cheng, X.F. Lu, D. Luan, X.W. Lou, NiMn-Based Bimetal–Organic Framework Nanosheets Supported on Multi-Channel Carbon Fibers for Efficient Oxygen Electrocatalysis, Angew. Chem. Int. Ed. 59 (2020) 18234–18239, https://doi.org/10.1002/anie.202008129.
[134] Z. Liang, H. Guo, G. Zhou, K. Guo, B. Wang, H. Lei, W. Zhang, H. Zheng, U.-P. Apfel, R. Cao, Metal–Organic-Framework-Supported Molecular Electrocatalysis for the Oxygen Reduction Reaction, Angew. Chem. Int. Ed. 60 (2021) 8472–8476, https://doi.org/10.1002/anie.202016024.
[135] B. Li, J. Quan, A. Loh, J. Chai, Y. Chen, C. Tan, X. Ge, T.S.A. Hor, Z. Liu, H. Zhang, Y. Zong, A Robust Hybrid Zn-Battery with Ultralong Cycle Life, Nano Lett. 17 (2017) 156–163, https://doi.org/10.1021/acs.nanolett.6b03691.
[136] C.B. Musgrave III, J. Su, P. Xiong, Y. Song, L. Huang, Y. Liu, G. Li, Q. Zhang, Y. Xin, M.M.-J. Li, R.T.K. Kwok, J.W.Y. Lam, B.Z. Tang, W.A. Goddard III, R. Ye, Molecular Strain Accelerates Electron Transfer for Enhanced Oxygen Reduction, J. Am. Chem. Soc. 147 (2025) 3786–3795, https://doi.org/10.1021/jacs.4c16637.
[137] Y. Wang, N. Xu, R. He, L. Peng, D. Cai, J. Qiao, Large-scale defect-engineering tailored tri-doped graphene as a metal-free bifunctional catalyst for superior electrocatalytic oxygen reaction in rechargeable Zn-air battery, Appl. Catal. B Environ. Energy 285 (2021) 119811, https://doi.org/10.1016/j.apcatb.2020.119811.
[138] R. Cheng, Y. Min, H. Li, C. Fu, Electronic structure regulation in the design of low-cost efficient electrocatalysts: From theory to applications, Nano Energy 115 (2023) 108718, https://doi.org/10.1016/j.nanoen.2023.108718.
[139] Z. Luo, J. Xie, J. Cheng, F. Wei, S. Lyu, J. Zhu, X. Shi, X. Yang, B. Wu, Z.J. Xu, Spin-State Manipulation of Atomic Manganese Center by Phosphide-Support Interactions for Enhanced Oxygen Reduction, Adv. Mater. n/a 2504585, https://doi.org/10.1002/adma.202504585.
[140] L. Wang, J. Huang, J. Huang, B. Yao, A. Zhou, Z. Huang, T.T. Isimjan, B. Wang, X. Yang, Promoting oxygen reduction reaction kinetics through manipulating electron redistribution in CoP/Cu_3P@NC for aqueous/flexible Zn–air batteries, Green. Chem. 27 (2025) 2276–2285, https://doi.org/10.1039/D4GC05538A.
[141] L. Wang, X. Hu, H. Li, Z. Huang, J. Huang, T.T. Isimjan, X. Yang, Engineering built-in electric fields in oxygen-deficient $MnO\text{-}CeO_2$@Cs catalysts: enhanced performance and kinetics for the oxygen reduction reaction in aqueous/flexible zinc–air batteries, Green. Chem. 26 (2024) 2011–2020, https://doi.org/10.1039/D3GC04537D.
[142] X. Zheng, Y. Cao, D. Liu, M. Cai, J. Ding, X. Liu, J. Wang, W. Hu, C. Zhong, Bimetallic Metal–Organic-Framework/Reduced Graphene Oxide Composites as Bifunctional Electrocatalysts for Rechargeable Zn–Air Batteries, ACS Appl. Mater. Interfaces 11 (2019) 15662–15669, https://doi.org/10.1021/acsami.9b02859.
[143] Z. Xia, J. Fang, X. Zhang, L. Fan, A.J. Barlow, T. Lin, S. Wang, G.G. Wallace, G. Sun, X. Wang, Pt nanoparticles embedded metal-organic framework nanosheets: A synergistic strategy towards bifunctional oxygen electrocatalysis, Appl. Catal. B Environ. Energy 245 (2019) 389–398, https://doi.org/10.1016/j.apcatb.2018.12.073.
[144] S.S. Shinde, C.H. Lee, J.-Y. Jung, N.K. Wagh, S.-H. Kim, D.-H. Kim, C. Lin, S. U. Lee, J.-H. Lee, Unveiling dual-linkage 3D hexaiminobenzene metal–organic frameworks towards long-lasting advanced reversible Zn–air batteries, Energy Environ. Sci. 12 (2019) 727–738, https://doi.org/10.1039/C8EE02679C.
[145] Y. Zhou, S. Guo, Recent advances in cathode catalyst architecture for lithium–oxygen batteries, eScience 3 (2023) 100123, https://doi.org/10.1016/j.esci.2023.100123.
[146] Z. Chang, J. Xu, X. Zhang, Recent Progress in Electrocatalyst for Li-O_2 Batteries, Adv. Energy Mater. 7 (2017) 1700875, https://doi.org/10.1002/aenm.201700875.
[147] X. Mu, J. Jiang, H. Deng, Y. Qiao, M. Zheng, X. Zhang, P. He, H. Zhou, H_2O self-trapping air cathode of Li–O_2 battery enabling low charge potential operating in dry system, Nano Energy 64 (2019) 103945, https://doi.org/10.1016/j.nanoen.2019.103945.
[148] Z. Peng, S.A. Freunberger, Y. Chen, P.G. Bruce, A Reversible and Higher-Rate Li-O_2 Battery, Science 337 (2012) 563–566, https://doi.org/10.1126/science.1223985.
[149] X. Hu, Z. Zhu, F. Cheng, Z. Tao, J. Chen, Micro-nano structured Ni-MOFs as high-performance cathode catalyst for rechargeable Li–O_2 batteries, Nanoscale 7 (2015) 11833–11840, https://doi.org/10.1039/C5NR02487K.
[150] B. Rani, J.K. Yadav, P. Saini, A.P. Pandey, A. Dixit, Aluminum–air batteries: current advances and promises with future directions, RSC Adv. 14 (2024) 17628–17663, https://doi.org/10.1039/D4RA02219J.
[151] P. Zhang, W. Peng, J. Miao, G. Ren, Y. Wang, Y. Li, P. Zhang, Evolution of the solid-liquid interface using a novel hybrid corrosion inhibitor to improve Al-air battery performance, J. Energy Chem. 104 (2025) 69–78, https://doi.org/10.1016/j.jechem.2024.12.041.
[152] A. Kongara, A.K. Samuel, G. Kapadia, A.K. Chandiran, Mechanically rechargeable zinc-air batteries for two- and three-wheeler electric vehicles in emerging markets, Commun. Mater. 5 (2024) 244, https://doi.org/10.1038/s43246-024-00662-6.
[153] K.K. Mishra, P.K. Maurya, A.K. Mishra, Dual electrolyte based aluminium air battery using $NiCo_2O_4$–$MoSe_2$ hybrid nanocomposite, Int. J. Hydrog. Energy 69 (2024) 252–260, https://doi.org/10.1016/j.ijhydene.2024.05.032.
[154] P. Goel, D. Dobhal, R.C. Sharma, Aluminum–air batteries: A viability review, J. Energy Storage 28 (2020) 101287, https://doi.org/10.1016/j.est.2020.101287.
[155] B. Zhu, Z. Liang, D. Xia, R. Zou, Metal-organic frameworks and their derivatives for metal-air batteries, Energy Storage Mater. 23 (2019) 757–771, https://doi.org/10.1016/j.ensm.2019.05.022.
[156] G. Gnana kumar, A. Farithkhan, A. Manthiram, Direct Urea Fuel Cells: Recent Progress and Critical Challenges of Urea Oxidation Electrocatalysis, Adv. Energy Sustain. Res. 1 (2020) 2000015, https://doi.org/10.1002/aesr.202000015.
[157] Y.M.T.A. Putri, M.I. Syauqi, I. Rahmawati, A. Aliyah, A.R. Sanjaya, T.A. Ivandini, Advancements in Ni-based Catalysts for Direct Urea Fuel Cells: A Comprehensive Review, ChemElectroChem 11 (2024) e202300637, https://doi.org/10.1002/celc.202300637.
[158] X. Gao, S. Zhang, P. Wang, M. Jaroniec, Y. Zheng, S.-Z. Qiao, Urea catalytic oxidation for energy and environmental applications, Chem. Soc. Rev. 53 (2024) 1552–1591, https://doi.org/10.1039/D3CS00963G.
[159] G. Das, J.-H. Choi, P.K.T. Nguyen, D.-J. Kim, Y.S. Yoon, Anion Exchange Membranes for Fuel Cell Application: A Review, Polymers 14 (2022) 1197, https://doi.org/10.3390/polym14061197.

[160] J. Yoon, J.M. Kim, Y.-h Lin, G.M. Geise, B.S. Beckingham, D.-J. Kim, Impact of a Novel Nickel-Based Catalyst and Phenyl-Acrylate-Based Anion-Exchange Membrane in a Direct Urea Fuel Cell, Energy Fuels 38 (2024) 12274–12281, https://doi.org/10.1021/acs.energyfuels.4c00929.
[161] Z. Lin, C. Zhang, P. Su, P. Qiao, J. Guo, Electrochemical membranes for rare earth mine water treatment: Sequential removal of rare earth ions and ammonia nitrogen, J. Hazard. Mater. 489 (2025) 137668, https://doi.org/10.1016/j.jhazmat.2025.137668.
[162] S. Goswami, S.J. Phukan, G. Gupta, R.K. Pai, S. Rana, M. Roy, P. Kumar, S. Garai, Direct Urea Fuel Cells: A Review on Roadmap, Mechanism, Bottleneck, and Future Perspective, Energy Fuels 39 (2025) 6709–6727, https://doi.org/10.1021/acs.energyfuels.4c05534.
[163] Y.M.T.A. Putri, T.W. Chamberlain, V. Degirmenci, J. Gunlazuardi, Y.K. Krisnandi, R.I. Walton, T.A. Ivandini, Crystallization of NiCo MOF-74 on a Porous NiO Film as an Anode for the Urea/H_2O_2 Fuel Cell, ACS Appl. Energy Mater. 6 (2023) 2497–2507, https://doi.org/10.1021/acsaem.2c03938.
[164] E.T. Sayed, A.H. Alami, M.A. Abdelkareem, T. Wilberforce, S.K. Kamarudin, A. G. Olabi, Real direct urea fuel Fell operation using standalone Ni-based metal-organic framework prepared by ball mill at room temperature, Energy 305 (2024) 132164, https://doi.org/10.1016/j.energy.2024.132164.
[165] M. Ravipati, S. Badhulika, Solvothermal synthesis of hybrid nanoarchitectonics nickel-metal organic framework modified nickel foam as a bifunctional electrocatalyst for direct urea and nitrate fuel cell, Adv. Powder Technol. 34 (2023) 104087, https://doi.org/10.1016/j.apt.2023.104087.
[166] C. Munoz-Cupa, Y. Hu, C. Xu, A. Bassi, An overview of microbial fuel cell usage in wastewater treatment, resource recovery and energy production, Sci. Total. Environ. 754 (2021) 142429, https://doi.org/10.1016/j.scitotenv.2020.142429.
[167] P.P. Rajesh, M.T. Noori, M.M. Ghangrekar, Improving Performance of Microbial Fuel Cell by Using Polyaniline-Coated Carbon–Felt Anode, J. Hazard. Toxic. Radioact. Waste 24 (2020) 04020024, https://doi.org/10.1061/(ASCE)HZ.2153-5515.0000512.
[168] R. Bhande, M.T. Noori, M.M. Ghangrekar, Performance improvement of sediment microbial fuel cell by enriching the sediment with cellulose: Kinetics of cellulose degradation, Environ. Technol. Innov. 13 (2019) 189–196, https://doi.org/10.1016/j.eti.2018.11.003.
[169] A. Rezaei, S. Aber, D.J. Roberts, A. Javid Ga, Synthesis and study of $CuNiTiO_3$ as an ORR electrocatalyst to enhance microbial fuel cell efficiency, Chemosphere 307 (2022) 135709, https://doi.org/10.1016/j.chemosphere.2022.135709.
[170] Y. Liu, S. Guo, J. Wang, C. Li, Fundamental development and research of cathodic compartment in microbial fuel cells: A review, J. Environ. Chem. Eng. 10 (2022) 107918, https://doi.org/10.1016/j.jece.2022.107918.
[171] S. Li, X. Zhu, H. Yu, X. Wang, X. Liu, H. Yang, F. Li, Q. Zhou, Simultaneous sulfamethoxazole degradation with electricity generation by microbial fuel cells using Ni-MOF-74 as cathode catalysts and quantification of antibiotic resistance genes, Environ. Res. 197 (2021) 111054, https://doi.org/10.1016/j.envres.2021.111054.
[172] M. Xu, L. Wu, M. Zhu, Z. Wang, Z.-H. Huang, M.-X. Wang, Self-supporting nitrogen-doped reduced graphene oxide@ carbon nanofiber hybrid membranes as high-performance integrated air cathodes in microbial fuel cells, Carbon 193 (2022) 242–257, https://doi.org/10.1016/j.carbon.2022.03.024.
[173] H. Zarenezhad, S. Mahini, A. Rezaei, S. Aber, A. Khataee, R. Teimuri-Mofrad, Porphyrin-enhanced microbial fuel cell with PCN-600 electrocatalyst for efficient oxygen reduction reaction and eco-friendly energy generation, Chem. Eng. J. 495 (2024) 153540, https://doi.org/10.1016/j.cej.2024.153540.
[174] M.T. Noori, C.I. Ezugwu, Y. Wang, B. Min, Robust bimetallic metal-organic framework cathode catalyst to boost oxygen reduction reaction in microbial fuel cell, J. Power Sources 547 (2022) 231947, https://doi.org/10.1016/j.jpowsour.2022.231947.
[175] M.A. Costa de Oliveira, A. D'Epifanio, H. Ohnuki, B. Mecheri, Platinum Group Metal-Free Catalysts for Oxygen Reduction Reaction: Applications in Microbial Fuel Cells, Catalysts 10 (2020) 475, https://doi.org/10.3390/catal10050475.
[176] X. Li, D. Li, Y. Zhang, P. Lv, Q. Feng, Q. Wei, Encapsulation of enzyme by metal-organic framework for single-enzymatic biofuel cell-based self-powered biosensor, Nano Energy 68 (2020) 104308, https://doi.org/10.1016/j.nanoen.2019.104308.
[177] C. Yang, H. Pang, X. Li, X. Zheng, T. Wei, X. Ma, Q. Wang, C. Wang, D. Wang, B. Xu, Scalable Electrocatalytic Urea Wastewater Treatment Coupled with Hydrogen Production by Regulating Adsorption Behavior of Urea Molecule, Nano-Micro Lett. 17 (2025) 159, https://doi.org/10.1007/s40820-024-01585-0.
[178] C. Wang, H. Lu, Z. Mao, C. Yan, G. Shen, X. Wang, Bimetal Schottky Heterojunction Boosting Energy-Saving Hydrogen Production from Alkaline Water via Urea Electrocatalysis, Adv. Funct. Mater. 30 (2020) 2000556, https://doi.org/10.1002/adfm.202000556.
[179] J. Ge, Z. Liu, M. Guan, J. Kuang, Y. Xiao, Y. Yang, C.H. Tsang, X. Lu, C. Yang, Investigation of the electrocatalytic mechanisms of urea oxidation reaction on the surface of transition metal oxides, J. Colloid Interface Sci. 620 (2022) 442–453, https://doi.org/10.1016/j.jcis.2022.03.152.
[180] X. Zhang, S. Feizpoor, M. Humayun, C. Wang, Urea oxidation reaction electrocatalysts: Correlation of structure, activity, and selectivity, Chem. Catal. 4 (2024) 100840, https://doi.org/10.1016/j.checat.2023.100840.
[181] Q. Zhang, F.M.D. Kazim, S. Ma, K. Qu, M. Li, Y. Wang, H. Hu, W. Cai, Z. Yang, Nitrogen dopants in nickel nanoparticles embedded carbon nanotubes promote overall urea oxidation, Appl. Catal. B Environ. Energy 280 (2021) 119436, https://doi.org/10.1016/j.apcatb.2020.119436.
[182] P. Wang, X. Gao, M. Zheng, M. Jaroniec, Y. Zheng, S.Z. Qiao, Urine electrooxidation for energy–saving hydrogen generation, Nat. Commun. 16 (2025) 2424, https://doi.org/10.1038/s41467-025-57798-3.
[183] K. Zhang, H. Yang, X. Han, S. Wang, X. Liu, T. Zou, J. Li, J. Zhang, H. Zhang, Y. Han, Electrocatalytic Urea-Assisted Hydrogen Production over a Bifunctional Cobalt Hydrogen Phosphite Catalyst, Ind. Eng. Chem. Res. 63 (2024) 22403–22410, https://doi.org/10.1021/acs.iecr.4c04262.
[184] Y. Zhang, Y. Lei, Y. Yan, W. Cai, J. Huang, Y. Lai, Z. Lin, Enhancing hydrogen production capability from urine-containing sewage through optimization of urea oxidation pathways, Appl. Catal. B Environ. Energy 353 (2024) 124064, https://doi.org/10.1016/j.apcatb.2024.124064.
[185] S. Sanati, R. Abazari, A.M. Kirillov, Bimetallic NiCo Metal–Organic Frameworks with High Stability and Performance Toward Electrocatalytic Oxidation of Urea in Seawater, Inorg. Chem. 63 (2024) 15813–15820, https://doi.org/10.1021/acs.inorgchem.4c01850.
[186] H. Yu, W. Xu, H. Chang, G. Xu, L. Li, J. Zang, R. Huang, L. Zhu, B. Yu, Electrocatalytic Ni-Co Metal Organic Framework for Efficient Urea Oxidation Reaction, Processes 11 (2023) 3035, https://doi.org/10.3390/pr11103035.
[187] Y. Xu, R. Wang, C. Feng, X. Zhang, N. Wang, Q. Zhang, M. Xie, Y. Xu, Y. Jiao, J. Chen, Controlling the electronic structure of Fe-MOF electrocatalyst for enhanced water splitting and urea oxidation: A plasma-assisted approach, J. Colloid Interface Sci. 650 (2023) 1290–1300, https://doi.org/10.1016/j.jcis.2023.07.034.
[188] L. Wu, M. Zhang, Z. Wen, S. Ci, V_8C_7 decorating CoP nanosheets-assembled microspheres as trifunctional catalysts toward energy-saving electrolytic hydrogen production, Chem. Eng. J. 399 (2020) 125728, https://doi.org/10.1016/j.cej.2020.125728.
[189] Z. Li, H. Feng, M. Song, C. He, W. Zhuang, L. Tian, Advances in CoP electrocatalysts for water splitting, Mater. Today Energy 20 (2021) 100698, https://doi.org/10.1016/j.mtener.2021.100698.
[190] S. Yuan, Y. Wu, L. Huang, Z. Zhang, W. Chen, Y. Wang, Engineering $Ni_{0.85}Se$/$CoSe_2$ heterojunction for enhanced bifunctional Catalysis in Urea-Assisted hydrogen production, J. Colloid Interface Sci. 683 (2025) 981–994, https://doi.org/10.1016/j.jcis.2025.01.005.
[191] J.-M. Huo, S.-N. Li, Z.-L. Ma, J. Meng, Q.-G. Zhai, Y. Wang, Interfacial engineering of the hetero-coordinated Ru–O-M clusters in MOF/LDH structures for boosting urea-assisted water splitting, J. Solid. State Chem. 343 (2025) 125160, https://doi.org/10.1016/j.jssc.2024.125160.
[192] G. Huang, C. Wang, D. Bukhvalov, Y. Yang, J. Gao, F. Han, X. Yang, C. Wang, Hetero-interface triggering dynamic Ni(3+) active species in reduced Ru-doped NiCo-MOF to boost urea-assisted overall water splitting, Int. J. Hydrog. Energy 145 (2025) 84–94, https://doi.org/10.1016/j.ijhydene.2025.06.044.
[193] C. Chen, L. Jin, L. Hu, T. Zhang, J. He, P. Gu, Q. Xu, J. Lu, Urea-oxidation-assisted electrochemical water splitting for hydrogen production on a bifunctional heterostructure transition metal phosphides combining metal–organic frameworks, J. Colloid Interface Sci. 628 (2022) 1008–1018, https://doi.org/10.1016/j.jcis.2022.08.127.
[194] D. Weerakoon, B. Bansal, L.P. Padhye, A. Rachmani, L. James Wright, G. Silyn Roberts, S. Baroutian, A critical review on current urea removal technologies from water: An approach for pollution prevention and resource recovery, Sep. Purif. Technol. 314 (2023) 123652, https://doi.org/10.1016/j.seppur.2023.123652.
[195] I. El Gheriany, M.H. Abdel-Aziz, E.-S.Z. El-Ashtoukhy, G.H. Sedahmed, Electrochemical removal of urea from wastewater by anodic oxidation using a new cell design: An experimental and modeling study, Process. Saf. Environ. Prot. 159 (2022) 133–145, https://doi.org/10.1016/j.psep.2021.12.055.
[196] X. Wang, J.-P. Li, Y. Duan, J. Li, H. Wang, X. Yang, M. Gong, Electrochemical Urea Oxidation in Different Environment: From Mechanism to Devices, ChemCatChem 14 (2022) e202101906, https://doi.org/10.1002/cctc.202101906.
[197] T. Guha, G. Gopal, A. Mukherjee, R. Kundu, Fe_3O_4-urea nanocomposites as a novel nitrogen fertilizer for improving nutrient utilization efficiency and reducing environmental pollution, Environ. Pollut. 292 (2022) 118301, https://doi.org/10.1016/j.envpol.2021.118301.
[198] Q. Yang, Y. Guo, J. Xu, X. Wu, B. He, E.R. Blatchley, J. Li, Photolysis of N-chlorourea and its effect on urea removal in a combined pre-chlorination and UV_{254} process, J. Hazard. Mater. 411 (2021) 125111, https://doi.org/10.1016/j.jhazmat.2021.125111.
[199] Y. Gao, B. Vinnerås, P. Simha, Partitioning behavior and crystallization of urea, salts and water during stepwise dehydration of acidified human urine by evaporation, Sci. Total. Environ. 966 (2025) 178709, https://doi.org/10.1016/j.scitotenv.2025.178709.
[200] T.O. Ajiboye, O.D. Ogunbiyi, E.O. Omotola, W.J. Adeyemi, O.O. Agboola, D. C. Onwudiwe, Urine: Useless or useful "waste"? Results Eng. 16 (2022) 100522 https://doi.org/10.1016/j.rineng.2022.100522.
[201] V. Singh, G. Ahmed, S. Vedika, P. Kumar, S.K. Chaturvedi, S.N. Rai, E. Vamanu, A. Kumar, Toxic heavy metal ions contamination in water and their sustainable reduction by eco-friendly methods: isotherms, thermodynamics and kinetics study, Sci. Rep. 14 (2024) 7595, https://doi.org/10.1038/s41598-024-58061-3.
[202] R. Bhabal, S. Gupta, R. Fernandes, M. Gupta, N. Patel, Bifunctional CoPBO/Co-MOF composite electrocatalyst for energy-efficient hydrogen evolution by urea-assisted water splitting, Int. J. Hydrog. Energy 116 (2025) 299–311, https://doi.org/10.1016/j.ijhydene.2025.03.100.
[203] Y. Zheng, P. Kannan, V. Linkov, H. Wang, S. Ji, High-valence tungsten doping induces lattice expansion in Mo–Cu metal-organic framework-derived metal oxide-carbon composite (W@Mo–Cu MOF-MOCC) for enhanced urea

electrooxidation catalysis, Int. J. Hydrog. Energy 192 (2025) 152231, https://doi.org/10.1016/j.ijhydene.2025.152231.
[204] X. Xu, Q. Deng, H.-C. Chen, M. Humayun, D. Duan, X. Zhang, H. Sun, X. Ao, X. Xue, A. Nikiforov, K. Huo, C. Wang, Y. Xiong, Metal-Organic Frameworks Offering Tunable Binary Active Sites toward Highly Efficient Urea Oxidation Electrolysis, Research 2022 (2022) 12, https://doi.org/10.34133/2022/9837109.
[205] C.P. O'Brien, R.K. Miao, A. Shayesteh Zeraati, G. Lee, E.H. Sargent, D. Sinton, CO_2 Electrolyzers, Chem. Rev. 124 (2024) 3648–3693, https://doi.org/10.1021/acs.chemrev.3c00206.
[206] S. Ashraf, O. Gohar, M.Z. Khan, U. Tariq, J. Ahmad, R.J. Awan, K. Zheng, Ju Rehman, M.R. Abdul Karim, H.A. Ishfaq, Z. Said, M. Motola, N. Han, M. B. Hanif, Exploring the frontiers of electrochemical CO_2 conversion: A comprehensive review, Nano Mater. Sci. (2024), https://doi.org/10.1016/j.nanoms.2024.05.005.
[207] A. Kaliyaperumal, P. Gupta, Y.S.S. Prasad, A.K. Chandiran, R. Chetty, Recent Progress and Perspective of the Electrochemical Conversion of Carbon Dioxide to Alcohols, ACS Eng. Au 3 (2023) 403–425, https://doi.org/10.1021/acsengineeringau.3c00030.
[208] M. Marchese, G. Buffo, M. Santarelli, A. Lanzini, CO_2 from direct air capture as carbon feedstock for Fischer-Tropsch chemicals and fuels: Energy and economic analysis, J. CO2 Util. 46 (2021) 101487, https://doi.org/10.1016/j.jcou.2021.101487.
[209] M.A. Sabri, S. Al Jitan, D. Bahamon, L.F. Vega, G. Palmisano, Current and future perspectives on catalytic-based integrated carbon capture and utilization, Sci. Total. Environ. 790 (2021) 148081, https://doi.org/10.1016/j.scitotenv.2021.148081.
[210] G. Liu, S. Sun, H. Sun, Y. Zhang, J. Lv, Y. Wang, J. Zeng, Z. Yan, C. Wu, Integrated CO_2 capture and utilisation: A promising step contributing to carbon neutrality, Carbon Capture Sci. Technol. 7 (2023) 100116, https://doi.org/10.1016/j.ccst.2023.100116.
[211] Z. Jin, Y. Guo, C. Qiu, Electro-Conversion of Carbon Dioxide to Valuable Chemicals in a Membrane Electrode Assembly, Sustainability 14 (2022) 5579, https://doi.org/10.3390/su14095579.
[212] B. Belsa, L. Xia, F.P. García de Arquer, CO_2 Electrolysis Technologies: Bridging the Gap toward Scale-up and Commercialization, ACS Energy Lett. 9 (2024) 4293–4305, https://doi.org/10.1021/acsenergylett.4c00955.
[213] M.S. Sajna, S. Zavahir, A. Popelka, P. Kasak, A. Al-Sharshani, U. Onwusogh, M. Wang, H. Park, D.S. Han, Electrochemical system design for CO_2 conversion: A comprehensive review, J. Environ. Chem. Eng. 11 (2023) 110467, https://doi.org/10.1016/j.jece.2023.110467.
[214] X. Li, Q.-L. Zhu, MOF-based materials for photo- and electrocatalytic CO_2 reduction, EnergyChem 2 (2020) 100033, https://doi.org/10.1016/j.enchem.2020.100033.
[215] C.A.R. Pappijn, M. Ruitenbeek, M.-F. Reyniers, K.M. Van Geem, Challenges and Opportunities of Carbon Capture and Utilization: Electrochemical Conversion of CO_2 to Ethylene, Front. Energy Res. 8 (2020) 2020, https://doi.org/10.3389/fenrg.2020.557466.
[216] K.A. Adegoke, N.W. Maxakato, Electrocatalytic CO_2 conversion on metal-organic frameworks derivative electrocatalysts, J. CO2 Util. 69 (2023) 102412, https://doi.org/10.1016/j.jcou.2023.102412.
[217] Y.Y. Birdja, E. Pérez-Gallent, M.C. Figueiredo, A.J. Göttle, F. Calle-Vallejo, M.T. M. Koper, Advances and challenges in understanding the electrocatalytic conversion of carbon dioxide to fuels, Nat. Energy 4 (2019) 732–745, https://doi.org/10.1038/s41560-019-0450-y.
[218] R.M. Arán-Ais, D. Gao, B. Roldan Cuenya, Structure- and Electrolyte-Sensitivity in CO_2 Electroreduction, Acc. Chem. Res. 51 (2018) 2906–2917, https://doi.org/10.1021/acs.accounts.8b00360.
[219] Q.-J. Wu, J. Liang, Y.-B. Huang, R. Cao, Thermo-, Electro-, and Photocatalytic CO_2 Conversion to Value-Added Products over Porous Metal/Covalent Organic Frameworks, Acc. Chem. Res. 55 (2022) 2978–2997, https://doi.org/10.1021/acs.accounts.2c00326.
[220] J.-M. Huang, X.-D. Zhang, J.-Y. Huang, D.-S. Zheng, M. Xu, Z.-Y. Gu, MOF-based materials for electrochemical reduction of carbon dioxide, Coord. Chem. Rev. 494 (2023) 215333, https://doi.org/10.1016/j.ccr.2023.215333.
[221] J. Meng, Y. Wang, C. Jia, Z.-L. Ma, L.-T. Yan, R.-T. Wang, L.-Y. Shao, P. Zhang, W.-Y. Yuan, X.-B. Zhao, C. Zhao, Q.-G. Zhai, Ultra-stabilized Cu^{2+} sites in conductive MOF/t-Cu_2O interface for benchmark CO_2 reduction, Nano Energy 141 (2025) 111077, https://doi.org/10.1016/j.nanoen.2025.111077.
[222] T. Van Phuc, S.G. Kang, J.S. Chung, S.H. Hur, Highly selective metal-organic framework-based electrocatalyst for the electrochemical reduction of CO_2 to CO, Mater. Res. Bull. 138 (2021) 111228, https://doi.org/10.1016/j.materresbull.2021.111228.
[223] X.-Y. Wu, J.-F. Lu, S. Zou, J. Zhao, S.-L. Hou, Z.-H. Zhu, H. Xu, S.-J. Liu, H.-R. Wen, Reducing the Coordination Number of Bismuth Sites in Metal-Organic Framework to Enhance the Performance of Electrochemical CO2 Reduction Over a Wide Potential Range, Adv. Funct. Mater. n/a 2504928, https://doi.org/10.1002/adfm.202504928.
[224] H.-J. Ho, A. Iizuka, E. Shibata, Carbon Capture and Utilization Technology without Carbon Dioxide Purification and Pressurization: A Review on Its Necessity and Available Technologies, Ind. Eng. Chem. Res. 58 (2019) 8941–8954, https://doi.org/10.1021/acs.iecr.9b01213.
[225] A. Al-Mamoori, A. Krishnamurthy, A.A. Rownaghi, F. Rezaei, Carbon Capture and Utilization Update, Energy Technol. 5 (2017) 834–849, https://doi.org/10.1002/ente.201600747.
[226] B.H. Davis, Fischer–Tropsch synthesis: current mechanism and futuristic needs, Fuel Process. Technol. 71 (2001) 157–166, https://doi.org/10.1016/S0378-3820(01)00144-8.
[227] H. Taylor, Catalysis. Volume IV. Hydrocarbon Synthesis, Hydrogenation and Cyclization, 760, J. Am. Chem. Soc. 79 (1957) 760, https://doi.org/10.1021/ja01560a081.
[228] H. Mahmoudi, M. Mahmoudi, O. Doustdar, H. Jahangiri, A. Tsolakis, S. Gu, M. LechWyszynski, A review of Fischer Tropsch synthesis process, mechanism, surface chemistry and catalyst formulation, Biofuels Eng. 2 (2017) 11–31, https://doi.org/10.1515/bfuel-2017-0002.
[229] N. Davoodian, A. Nakhaei Pour, M. Izadyar, A. Mohammadi, M. Vahidi, Fischer–Tropsch synthesis over a novel cobalt catalyst supported on UiO-66, J. Iran. Chem. Soc. 18 (2021) 1043–1050, https://doi.org/10.1007/s13738-020-02091-x.
[230] N. Abas, E. Kalair, A. Kalair, Qu Hasan, N. Khan, Nature inspired artificial photosynthesis technologies for hydrogen production: Barriers and challenges, Int. J. Hydrog. Energy 45 (2020) 20787–20799, https://doi.org/10.1016/j.ijhydene.2019.12.010.
[231] D.K. Dogutan, D.G. Nocera, Artificial Photosynthesis at Efficiencies Greatly Exceeding That of Natural Photosynthesis, Acc. Chem. Res. 52 (2019) 3143–3148, https://doi.org/10.1021/acs.accounts.9b00380.
[232] A. Alhebshi, E. Sharaf Aldeen, R.S. Mim, B. Tahir, M. Tahir, Recent advances in constructing heterojunctions of binary semiconductor photocatalysts for visible light responsive CO_2 reduction to energy efficient fuels: A review, Int. J. Energy Res. 46 (2022) 5523–5584, https://doi.org/10.1002/er.7563.
[233] J. Ran, M. Jaroniec, S.-Z. Qiao, Cocatalysts in Semiconductor-based Photocatalytic CO_2 Reduction: Achievements, Challenges, and Opportunities, Adv. Mater. 30 (2018) 1704649, https://doi.org/10.1002/adma.201704649.
[234] N. Heidary, T.G.A.A. Harris, K.H. Ly, N. Kornienko, Artificial photosynthesis with metal and covalent organic frameworks (MOFs and COFs): challenges and prospects in fuel-forming electrocatalysis, Physiol. Plant. 166 (2019) 460–471, https://doi.org/10.1111/ppl.12935.
[235] S. Mandal, S. Yoosefi, A.K. Mengele, S. Rau, A. Pannwitz, Active molecular units in metal organic frameworks for artificial photosynthesis, Inorg. Chem. Front. 11 (2024) 7682–7755, https://doi.org/10.1039/D4QI01363H.
[236] T. Zhang, W. Lin, Metal–organic frameworks for artificial photosynthesis and photocatalysis, Chem. Soc. Rev. 43 (2014) 5982–5993, https://doi.org/10.1039/C4CS00103F.
[237] Y. Li, T. Kong, S. Shen, Artificial Photosynthesis with Polymeric Carbon Nitride: When Meeting Metal Nanoparticles, Single Atoms, and Molecular Complexes, Small 15 (2019) 1900772, https://doi.org/10.1002/smll.201900772.
[238] Y. Wang, J.-X. Wei, H.-L. Tang, L.-H. Shao, L.-Z. Dong, X.-Y. Chu, Y.-X. Jiang, G.-L. Zhang, F.-M. Zhang, Y.-Q. Lan, Artificial photosynthetic system for diluted CO_2 reduction in gas-solid phase, Nat. Commun. 15 (2024) 8818, https://doi.org/10.1038/s41467-024-53066-y.
[239] L.-Z. Dong, L. Zhang, J. Liu, Q. Huang, M. Lu, W.-X. Ji, Y.-Q. Lan, Stable Heterometallic Cluster-Based Organic Framework Catalysts for Artificial Photosynthesis, Angew. Chem. Int. Ed. 59 (2020) 2659–2663, https://doi.org/10.1002/anie.201913284.
[240] G. Lan, Y. Fan, W. Shi, E. You, S.S. Veroneau, W. Lin, Biomimetic active sites on monolayered metal–organic frameworks for artificial photosynthesis, Nat. Catal. 5 (2022) 1006–1018, https://doi.org/10.1038/s41929-022-00865-5.
[241] R.N. Rosa, The Role of Synthetic Fuels for a Carbon Neutral Economy, C 3 (2017) 11, https://doi.org/10.3390/c3020011.
[242] W. Wang, S. Zhang, Q. Liu, Y. Bai, T. Jiang, B. Guo, C. Liu, Z.L. Wang, D. Luo, Self-powered carbon-neutral system, Cell. Rep. Phys. Sci. 5 (2024), https://doi.org/10.1016/j.xcrp.2024.101871.
[243] Q. Wang, C. Pornrungroj, Artificial photosynthetic processes using carbon dioxide, water and sunlight: can they power a sustainable future? Chem. Sci. 16 (2025) 18990–19011, https://doi.org/10.1039/D5SC03976B.
[244] Y. Kang, T. Kim, K.Y. Jung, K.T. Park, Recent Progress in Electrocatalytic CO_2 Reduction to Pure Formic Acid Using a Solid-State Electrolyte Device, Catalysts 13 (2023) 955, https://doi.org/10.3390/catal13060955.
[245] Y.A. Alli, A. Bamisaye, M.O. Bamidele, N.O. Etafo, S. Chkirida, A. Lawal, V. O. Hammed, A.S. Akinfenwa, E. Hanson, C. Nwakile, K.O. Kazeem, R. J. Ayanwunmi, A.S. Ige, J.R. Parga Torres, H. Al Nageim, Transforming waste to wealth: Harnessing carbon dioxide for sustainable solutions, Results Surf. Interfaces 17 (2024) 100321, https://doi.org/10.1016/j.rsurfi.2024.100321.
[246] V. Ram, S.R. Salkuti, An Overview of Major Synthetic Fuels, Energies 16 (2023) 2834, https://doi.org/10.3390/en16062834.
[247] S.A.S. Mohammed, W.Z.N. Yahya, M.A. Bustam, M.G. Kibria, Elucidation of the Roles of Ionic Liquid in CO_2 Electrochemical Reduction to Value-Added Chemicals and Fuels, Molecules 26 (2021) 6962, https://doi.org/10.3390/molecules26226962.
[248] J. Zhong, X. Yang, Z. Wu, B. Liang, Y. Huang, T. Zhang, State of the art and perspectives in heterogeneous catalysis of CO_2 hydrogenation to methanol, Chem. Soc. Rev. 49 (2020) 1385–1413, https://doi.org/10.1039/C9CS00614A.
[249] D. Kordus, J. Jelic, M. Lopez Luna, N.J. Divins, J. Timoshenko, S.W. Chee, C. Rettenmaier, J. Kröhnert, S. Kühl, A. Trunschke, R. Schlögl, F. Studt, B. Roldan Cuenya, Shape-Dependent CO_2 Hydrogenation to Methanol over Cu_2O Nanocubes Supported on ZnO, J. Am. Chem. Soc. 145 (2023) 3016–3030, https://doi.org/10.1021/jacs.2c11540.
[250] S. Kattel, P.J. Ramírez, J.G. Chen, J.A. Rodriguez, P. Liu, Active sites for CO_2 hydrogenation to methanol on Cu/ZnO catalysts, Science 355 (2017) 1296–1299, https://doi.org/10.1126/science.aal3573.

[251] A. Beck, M. Zabilskiy, M.A. Newton, O. Safonova, M.G. Willinger, J.A. van Bokhoven, Following the structure of copper-zinc-alumina across the pressure gap in carbon dioxide hydrogenation, Nat. Catal. 4 (2021) 488–497, https://doi.org/10.1038/s41929-021-00625-x.
[252] H. Zhou, Z. Chen, A.V. López, E.D. López, E. Lam, A. Tsoukalou, E. Willinger, D. A. Kuznetsov, D. Mance, A. Kierzkowska, F. Donat, P.M. Abdala, A. Comas-Vives, C. Copéret, A. Fedorov, C.R. Müller, Engineering the Cu/Mo_2CT_x (MXene) interface to drive CO_2 hydrogenation to methanol, Nat. Catal. 4 (2021) 860–871, https://doi.org/10.1038/s41929-021-00684-0.
[253] L.-L. Ling, X. Guan, X. Liu, X.-M. Lei, Z. Lin, H.-L. Jiang, Promoted hydrogenation of CO_2 to methanol over single-atom Cu sites with Na^+-decorated microenvironment, Natl. Sci. Rev. 11 (2024), https://doi.org/10.1093/nsr/nwae114.
[254] A. Álvarez, A. Bansode, A. Urakawa, A.V. Bavykina, T.A. Wezendonk, M. Makkee, J. Gascon, F. Kapteijn, Challenges in the Greener Production of Formates/Formic Acid, Methanol, and DME by Heterogeneously Catalyzed CO_2 Hydrogenation Processes, Chem. Rev. 117 (2017) 9804–9838, https://doi.org/10.1021/acs.chemrev.6b00816.
[255] J. Goldemberg, Ethanol for a Sustainable Energy Future, Science 315 (2007) 808–810, https://doi.org/10.1126/science.1137013.
[256] A.E. Farrell, R.J. Plevin, B.T. Turner, A.D. Jones, M. O'Hare, D.M. Kammen, Ethanol Can Contribute to Energy and Environmental Goals, Science 311 (2006) 506–508, https://doi.org/10.1126/science.1121416.
[257] A. Cao, G. Liu, L. Wang, J. Liu, Y. Yue, L. Zhang, Y. Liu, Growing layered double hydroxides on CNTs and their catalytic performance for higher alcohol synthesis from syngas, J. Mater. Sci. 51 (2016) 5216–5231, https://doi.org/10.1007/s10853-016-9823-9.
[258] R. Angamuthu, P. Byers, M. Lutz, A.L. Spek, E. Bouwman, Electrocatalytic CO_2 Conversion to Oxalate by a Copper Complex, Science 327 (2010) 313–315, https://doi.org/10.1126/science.1177981.
[259] P. Ji, K. Manna, Z. Lin, X. Feng, A. Urban, Y. Song, W. Lin, Single-Site Cobalt Catalysts at New $Zr_{12}(\mu_3\text{-}O)_8(\mu_3\text{-}OH)_8(\mu_2\text{-}OH)_6$ Metal–Organic Framework Nodes for Highly Active Hydrogenation of Nitroarenes, Nitriles, and Isocyanides, J. Am. Chem. Soc. 139 (2017) 7004–7011, https://doi.org/10.1021/jacs.7b02394.
[260] B. An, Z. Li, Y. Song, J. Zhang, L. Zeng, C. Wang, W. Lin, Cooperative copper centres in a metal–organic framework for selective conversion of CO_2 to ethanol, Nat. Catal. 2 (2019) 709–717, https://doi.org/10.1038/s41929-019-0308-5.
[261] N. Zou, J. Chen, T. Qiu, Y. Zheng, Direct hydrogenation of CO_2 to ethanol at ambient conditions using Cu(i)-MOF in a dielectric barrier discharge plasma reactor, J. Mater. Chem. A 11 (2023) 10766–10775, https://doi.org/10.1039/D3TA00314K.
[262] S.G. Nnabuife, A.K. Hamzat, J. Whidborne, B. Kuang, K.W. Jenkins, Integration of renewable energy sources in tandem with electrolysis: A technology review for green hydrogen production, Int. J. Hydrog. Energy 107 (2025) 218–240, https://doi.org/10.1016/j.ijhydene.2024.06.342.
[263] T. Tran-Phu, R. Daiyan, X.M.C. Ta, R. Amal, A. Tricoli, From Stochastic Self-Assembly of Nanoparticles to Nanostructured (Photo)Electrocatalysts for Renewable Power-to-X Applications via Scalable Flame Synthesis, Adv. Funct. Mater. 32 (2022) 2110020, https://doi.org/10.1002/adfm.202110020.
[264] J. Leverett, G. Baghestani, T. Tran-Phu, J.A. Yuwono, P. Kumar, B. Johannessen, D. Simondson, H. Wen, S.L.Y. Chang, A. Tricoli, A.N. Simonov, L. Dai, R. Amal, R. Daiyan, R.K. Hocking, Direct Observation of Electron Donation onto the Reactants and a Transient Poisoning Mechanism During CO_2 Electroreduction on Ni Single Atom Catalysts, Angew. Chem. Int. Ed. 64 (2025) e202424087, https://doi.org/10.1002/anie.202424087.
[265] A.K. Mageed, M. Ali Alsaffar, M.A.R. Abdel Ghany, K.A. Sukkar, B.V. Ayodele, Advances in synthesis and application of cobalt and nickel-based nanomaterials for catalytic reforming of hydrocarbons and oxygenates to hydrogen-rich syngas, J. Ind. Eng. Chem. 144 (2025) 1–17, https://doi.org/10.1016/j.jiec.2024.09.022.
[266] M. Bagheri, M.A.O. Lourenço, J.K. Dangbegnon, N.B.D. Monti, L. Mafra, F. Pirri, J. Zeng, Green Synthesis of MOF-Based Materials for Electrochemical Reduction of Carbon Dioxide, ChemSusChem 18 (2025) e202400684, https://doi.org/10.1002/cssc.202400684.
[267] P. Lu, S. Singh, A. Gonzalez, G. Gadikota, Tunable Electrochemical Reactive Carbon Dioxide Capture and Conversion to Produce Syngas Using Highly Dispersed Nickel Catalyst, ACS Sustain. Chem. Eng. 13 (2025) 5963–5973, https://doi.org/10.1021/acssuschemeng.5c00653.
[268] Y. Chen, J. Wei, M.S. Duyar, V.V. Ordomsky, A.Y. Khodakov, J. Liu, Carbon-based catalysts for Fischer–Tropsch synthesis, Chem. Soc. Rev. 50 (2021) 2337–2366, https://doi.org/10.1039/D0CS00905A.
[269] N.C. Shiba, Stoichiometric perovskites as new class supports for Fe and Co in Fischer Tropsch Synthesis: A review, J. CO2 Util. 99 (2025) 103151, https://doi.org/10.1016/j.jcou.2025.103151.
[270] Q. Zhai, H. Huang, T. Lawson, Z. Xia, P. Giusto, M. Antonietti, M. Jaroniec, M. Chhowalla, J.-B. Baek, Y. Liu, S. Qiao, L. Dai, Recent Advances on Carbon-Based Metal-Free Electrocatalysts for Energy and Chemical Conversions, Adv. Mater. 36 (2024) 2405664, https://doi.org/10.1002/adma.202405664.
[271] A. Badreldin, Y. Li, A critical appraisal of advances in integrated CO_2 capture and electrochemical conversion, Chem. Sci. 16 (2025) 2483–2513, https://doi.org/10.1039/D4SC06642A.
[272] S.C. Jesudass, S. Surendran, G. Janani, T.-H. Kim, U. Sim, Redistributing the Electronic States of 2D-Covalent Organic Frameworks for Electrochemical Energy Applications, Adv. Energy Mater. 13 (2023) 2301918, https://doi.org/10.1002/aenm.202301918.
[273] W. Wu, H. Zhou, Y. Liu, Y. Pan, Q. Chen, Y. Zhang, J. Mao, W. Ma, P. Yu, Enhanced electrochemical CO_2 reduction coupled with urea oxidation using bifunctional atomically dispersed CuNi catalysts, Nano Res. 18 (2025) 94907051, https://doi.org/10.26599/NR.2025.94907051.
[274] Y.M. Mao, K. Ramya, S. Goel, Miniaturized Microbial Fuel Cells for Smart Devices: Application and Power Generation, Int. J. Precis. Eng. Manuf. -Green. Tech. 12 (2025) 19, https://doi.org/10.1007/s40684-025-00778-1.
[275] J.-T. Ren, L. Chen, H.-Y. Wang, W.-W. Tian, Z.-Y. Yuan, Water electrolysis for hydrogen production: from hybrid systems to self-powered/catalyzed devices, Energy Environ. Sci. 17 (2024) 49–113, https://doi.org/10.1039/D3EE02467A.
[276] S. Nangan, Y. Ding, A.Z. Alhakemy, Y. Liu, Z. Wen, Hybrid alkali-acid urea-nitrate fuel cell for degrading nitrogen-rich wastewater, Appl. Catal. B Environ. Energy 286 (2021) 119892, https://doi.org/10.1016/j.apcatb.2021.119892.
[277] H. Jiang, J. Xia, L. Jiao, X. Meng, P. Wang, C.-S. Lee, W. Zhang, Ni single atoms anchored on N-doped carbon nanosheets as bifunctional electrocatalysts for Urea-assisted rechargeable Zn-air batteries, Appl. Catal. B Environ. Energy 310 (2022) 121352, https://doi.org/10.1016/j.apcatb.2022.121352.
[278] H. Rastin, D. Dell'Angelo, A. Sayede, M. Badawi, S. Habibzadeh, Green and sustainable metal-organic frameworks (MOFs) in wastewater treatment: A review, Environ. Res. 282 (2025) 122087, https://doi.org/10.1016/j.envres.2025.122087.
[279] A.M. Wright, M.T. Kapelewski, S. Marx, O.K. Farha, W. Morris, Transitioning metal–organic frameworks from the laboratory to market through applied research, Nat. Mater. 24 (2025) 178–187, https://doi.org/10.1038/s41563-024-01947-4.
[280] A. Anastasopoulou, H. Furukawa, B.R. Barnett, H.Z.H. Jiang, J.R. Long, H. M. Breunig, Technoeconomic analysis of metal–organic frameworks for bulk hydrogen transportation, Energy Environ. Sci. 14 (2021) 1083–1094, https://doi.org/10.1039/D0EE02448A.
[281] D. DeSantis, J.A. Mason, B.D. James, C. Houchins, J.R. Long, M. Veenstra, Techno-economic Analysis of Metal–Organic Frameworks for Hydrogen and Natural Gas Storage, Energy Fuels 31 (2017) 2024–2032, https://doi.org/10.1021/acs.energyfuels.6b02510.
[282] W.H.D. Goh, H.S. Lau, W.F. Yong, An integrated life cycle assessment and techno-economic analysis: Evaluation on the production of polymers of intrinsic microporosity (PIM-1) and UiO-66-NH_2 as membrane materials, Sci. Total. Environ. 892 (2023) 164582, https://doi.org/10.1016/j.scitotenv.2023.164582.
[283] E. Hanson, C. Nwakile, V.O. Hammed, Carbon capture, utilization, and storage (CCUS) technologies: Evaluating the effectiveness of advanced CCUS solutions for reducing CO_2 emissions, Results Surf. Interfaces 18 (2025) 100381, https://doi.org/10.1016/j.rsurfi.2024.100381.
[284] S. Anantharaj, Ru-tweaking of non-precious materials: the tale of a strategy that ensures both cost and energy efficiency in electrocatalytic water splitting, J. Mater. Chem. A 9 (2021) 6710–6731, https://doi.org/10.1039/D0TA12424A.
[285] O.E. Fayemi, E.O. Atofarati, O.R. Kanu-Uchenna, C.C. Enweremadu, Seawater electrolysis for hydrogen production: Challenges, innovations, and future pathways, Int. J. Green. Energy 23 (2025) 1–22, https://doi.org/10.1080/15435075.2025.2572703.
[286] W. Wang, D. Chen, F. Li, X. Xiao, Q. Xu, Metal-organic-framework-based materials as platforms for energy applications, Chem 10 (2024) 86–133, https://doi.org/10.1016/j.chempr.2023.09.009.
[287] I. Ullah, M. Zaheer, Enhancing activity and stability of bimetallic metal-organic frameworks (MOFs) for overall electrochemical water splitting through nanocomposite formation, Int. J. Hydrog. Energy 105 (2025) 179–188, https://doi.org/10.1016/j.ijhydene.2025.01.213.
[288] F.-Y. Chen, Z.-Y. Wu, Z. Adler, H. Wang, Stability challenges of electrocatalytic oxygen evolution reaction: From mechanistic understanding to reactor design, Joule 5 (2021) 1704–1731, https://doi.org/10.1016/j.joule.2021.05.005.
[289] D. Chakraborty, A. Yurdusen, G. Mouchaham, F. Nouar, C. Serre, Large-Scale Production of Metal–Organic Frameworks, Adv. Funct. Mater. 34 (2024) 2309089, https://doi.org/10.1002/adfm.202309089.
[290] J. Chen, K. Shen, Y. Li, Greening the Processes of Metal–Organic Framework Synthesis and their Use in Sustainable Catalysis, ChemSusChem 10 (2017) 3165–3187, https://doi.org/10.1002/cssc.201700748.
[291] P. Dhumal, P. Bhadane, B. Ibrahim, S. Chakraborty, Evaluating the path to sustainability: SWOT analysis of safe and sustainable by design approaches for metal–organic frameworks, Green. Chem. 27 (2025) 3815–3850, https://doi.org/10.1039/D5GC00424A.
[292] M. Ficher, T. Bauer, A.-L. Ligozat, A comprehensive review of the end-of-life modeling in LCAs of digital equipment, Int. J. Life Cycle Assess. 30 (2025) 20–42, https://doi.org/10.1007/s11367-024-02367-x.
[293] P. Vitale, N. Arena, F. Di Gregorio, U. Arena, Life cycle assessment of the end-of-life phase of a residential building, Waste Manag. 60 (2017) 311–321, https://doi.org/10.1016/j.wasman.2016.10.002.
[294] F. Ullah, K. Hasrat, W. Abdelfattah, N. Ben Khedher, M. Mu, S. Wang, Comprehensive life cycle analysis of monocrystalline and polycrystalline solar PV panels in Nanjing, China: Effects on the environment, performance, and recycling opportunities, Chem. Eng. J. 522 (2025) 167775, https://doi.org/10.1016/j.cej.2025.167775.
[295] J. Rimu, Organisations beyond Brundtland: a definition of corporate sustainability based on corporate values, J. Sustain. Dev. 11 (2018) 184–193, https://doi.org/10.5539/jsd.v11n5p184.
[296] V. Singh, Environment, Development, and Sustainability, in: V. Singh (Ed.), Textbook of Environment and Ecology, Springer Nature Singapore, Singapore, 2024, pp. 327–339.
[297] A.H. Assen, K. Adil, Y. Belmabkhout, Lab-scale insights into green metal–organic framework sorbents for gas separation or purification, Curr. Opin. Green. Sustain. Chem. 49 (2024) 100948, https://doi.org/10.1016/j.cogsc.2024.100948.

[298] V. Eke, T. Sahu, K.K. Ghuman, M. Freire-Gormaly, P.G. O'Brien, A comprehensive review of life cycle assessments of direct air capture and carbon dioxide storage, Sustain. Prod. Consum. 55 (2025) 217–241, https://doi.org/10.1016/j.spc.2025.02.017.
[299] B. Farasati Far, N. Rabiee, S. Iravani, Environmental implications of metal–organic frameworks and MXenes in biomedical applications: a perspective, RSC Adv. 13 (2023) 34562–34575, https://doi.org/10.1039/D3RA07092A.
[300] C. Capello, G. Wernet, J. Sutter, S. Hellweg, K. Hungerbühler, A comprehensive environmental assessment of petrochemical solvent production, Int. J. Life Cycle Assess. 14 (2009) 467–479, https://doi.org/10.1007/s11367-009-0094-4.
[301] O.V. Kharissova, B.I. Kharisov, C.M. Oliva González, Y.P. Méndez, I. López, Greener synthesis of chemical compounds and materials, R. Soc. Open. Sci. 6 (2019) 191378, https://doi.org/10.1098/rsos.191378.
[302] C.A. Grande, R. Blom, A. Spjelkavik, V. Moreau, J. Payet, Life-cycle assessment as a tool for eco-design of metal-organic frameworks (MOFs), Sustain. Mater. Technol. 14 (2017) 11–18, https://doi.org/10.1016/j.susmat.2017.10.002.
[303] H.U. Escobar-Hernandez, Y. Quan, M.I. Papadaki, Q. Wang, Life Cycle Assessment of Metal–Organic Frameworks: Sustainability Study of Zeolitic Imidazolate Framework-67, ACS Sustain. Chem. Eng. 11 (2023) 4219–4225, https://doi.org/10.1021/acssuschemeng.2c07276.
[304] M. Kalaj, K.E. Prosser, S.M. Cohen, Room temperature aqueous synthesis of UiO-66 derivatives via postsynthetic exchange, Dalton Trans. 49 (2020) 8841–8845, https://doi.org/10.1039/D0DT01939A.
[305] Z. Chen, X. Wang, H. Noh, G. Ayoub, G.W. Peterson, C.T. Buru, T. Islamoglu, O. K. Farha, Scalable, room temperature, and water-based synthesis of functionalized zirconium-based metal–organic frameworks for toxic chemical removal, CrystEngComm 21 (2019) 2409–2415, https://doi.org/10.1039/C9CE00213H.
[306] S.-Y. Pan, Y.-Y. Hsiao, S. Negi, B.M. Matsagar, K.C.W. Wu, Green Synthesis of Waste-Derived Metal–Organic Frameworks for Organic Substance Extraction from Piggery Wastewater as Biofertilizers, ACS Sustain. Chem. Eng. 12 (2024) 17793–17805, https://doi.org/10.1021/acssuschemeng.4c07030.
[307] H.L. Choi, H. Yang, J. Woo, J.-H. Mun, T.-H. Bae, Upcycling PET Waste into High-Performance Metal–Organic Frameworks: Sustainable Synthesis of MIL-53(Al) for Gas Separation and Storage, Korean J. Chem. Eng. (2025), https://doi.org/10.1007/s11814-025-00538-6.
[308] J. Li, S. Zhang, Y. Hua, Y. Lin, X. Wen, E. Mijowska, T. Tang, X. Chen, R.S. Ruoff, Facile synthesis of accordion-like porous carbon from waste PET bottles-based MIL-53(Al) and its application for high-performance Zn-ion capacitor, Green. Energy Environ. 9 (2024) 1138–1150, https://doi.org/10.1016/j.gee.2023.01.002.
[309] A.V. Desai, E. Lizundia, A. Laybourn, D.N. Rainer, A.R. Armstrong, R.E. Morris, S. Wuttke, R. Ettlinger, Green Synthesis of Reticular Materials, Adv. Funct. Mater. 34 (2024) 2304660, https://doi.org/10.1002/adfm.202304660.
[310] E.S. Sowbakkiyavathi, P. Dhandapani, S. Ramasamy, J.H. Oh, I. In, S.J. Lee, A. Subramania, Recent advances in MOFs, MOF-derived materials and their composites as electrocatalysts for hydrogen production, RSC Sustain. (2025), https://doi.org/10.1039/D5SU00199D.
[311] K. Jayaramulu, S. Mukherjee, D.M. Morales, D.P. Dubal, A.K. Nanjundan, A. Schneemann, J. Masa, S. Kment, W. Schuhmann, M. Otyepka, R. Zboril, R. A. Fischer, Graphene-Based Metal–Organic Framework Hybrids for Applications in Catalysis, Environmental, and Energy Technologies, Chem. Rev. 122 (2022) 17241–17338, https://doi.org/10.1021/acs.chemrev.2c00270.
[312] L. Liu, H. Lian, H. Deng, W. Zhang, MXene-supported Ni–Co bimetallic MOF 2D lamellar membrane for enhanced electrochemical oxygen reactions and Li–O_2 battery, Sci. Rep. 15 (2025) 13995, https://doi.org/10.1038/s41598-025-98982-1.
[313] H. Wang, L. Meng, S. Shang, H. Liu, M. Zhang, H. Wu, Nickel-constructing interfaces of multiheterostructure on self-supporting electrode for efficient overall urea-water splitting, Appl. Surf. Sci. 640 (2023) 158288, https://doi.org/10.1016/j.apsusc.2023.158288.
[314] S. Liu, L. Song, R. Liu, L. Li, D. Yang, S. Yuan, X. Dai, Controlled One-Step Synthesis of MOF-on-MOF Cocatalysts for Two-Channel Electrocatalytic Conversion of CO_2 to Formic Acid, Small 19 (2023) 2304808, https://doi.org/10.1002/smll.202304808.
[315] F.-F. Wang, W.-Y. Sun, Cu-MOF and CuBi Double-Perovskite Composites for Selective CO2 Electroreduction to HCOOH, ACS Sustain. Chem. & Eng. 12 (2024) 15651–15658, https://doi.org/10.1021/acssuschemeng.4c06093.
[316] L. Figueroa-Quintero, D. Villalgordo-Hernández, J.J. Delgado-Marín, J. Narciso, V.K. Velisoju, P. Castaño, J. Gascón, E.V. Ramos-Fernández, Post-Synthetic Surface Modification of Metal–Organic Frameworks and Their Potential Applications, Small Methods 7 (2023) 2201413, https://doi.org/10.1002/smtd.202201413.
[317] H. Lin, Y. Xu, B. Wang, D.-S. Li, T. Zhou, J. Zhang, Postsynthetic Modification of Metal−Organic Frameworks for Photocatalytic Applications, Small Struct. 3 (2022) 2100176, https://doi.org/10.1002/sstr.202100176.
[318] T. Gadzikwa, P. Matseketsa, The post-synthesis modification (PSM) of MOFs for catalysis, Dalton Trans. 53 (2024) 7659–7668, https://doi.org/10.1039/D4DT00514G.
[319] Y. Jiang, Y.-P. Deng, R. Liang, N. Chen, G. King, A. Yu, Z. Chen, Linker-Compensated Metal–Organic Framework with Electron Delocalized Metal Sites for Bifunctional Oxygen Electrocatalysis, J. Am. Chem. Soc. 144 (2022) 4783–4791, https://doi.org/10.1021/jacs.1c10295.
[320] X. Ao, Y. Gu, C. Li, Y. Wu, C. Wu, S. Xun, A. Nikiforov, C. Xu, J. Jia, W. Cai, R. Ma, K. Huo, C. Wang, Sulfurization-functionalized 2D metal-organic frameworks for high-performance urea fuel cell, Appl. Catal. B Environ. Energy 315 (2022) 121586, https://doi.org/10.1016/j.apcatb.2022.121586.
[321] M. Zhang, J. Zhou, X. Guo, X. Zeng, L. Shi, T. Zhang, Y. He, X. Zhou, S. Shan, K. Yao, Amine-functionalized MIL-101 sorbents modified with alkali metal cations for enhanced CO_2 capture and electroreduction conversion, Chem. Eng. J. 515 (2025) 163668, https://doi.org/10.1016/j.cej.2025.163668.
[322] H. Zhu, S. Yuan, Y. Wang, Z. Zhang, Z. Zhao, K. Yang, Z. Feng, J. Lu, X. Liu, F. Sun, J. Zhang, Recent advances and future research directions in polyoxometalate-based water electrolysis for hydrogen production, Polyoxometalates 5 (2026) 9140112, https://doi.org/10.26599/POM.2026.9140112.
[323] J. Hu, S. Xu, Y. Meng, Polyoxometalates (POMs) Memristors/Neuromorphic Devices: From Structure Engineering to Material and Function Integration, Nanomaterials 16 (2026) 425, https://doi.org/10.3390/nano16070425.
[324] I. Gregorovic, N. Lotfian, R. Khajavian, S. Maity, M. Mirzaei, S.S. Mal, M. Aureliano, A. Rompel, Polyoxometalates in environmental remediation and energy storage, Environ. Sci. Nano 13 (2026) 1295–1346, https://doi.org/10.1039/D5EN00964B.
[325] M. Liu, S. Lu, G. Hu, Y. Jiang, T. Li, S.-S. Wang, N. Wang, Q. Dai, Z. Jia, A polyoxometalate-anchored Ni MOF for high-efficiency, selective H_2O_2 electrosynthesis, J. Mater. Chem. A 14 (2026) 5806–5815, https://doi.org/10.1039/D5TA07266B.
[326] T.-F. Yao, G.-P. Yang, Y.-Y. Wang, Boosting Efficient Electrocatalytic CO_2 Reduction by Two-Dimensional Polyoxometalate@Metal−Organic Framework Composites with Asymmetric Sites, Chin. J. Struct. Chem. 45 (2026) 100948, https://doi.org/10.1016/j.cjsc.2026.100948.
[327] T. Bao, Y. Wu, C. Tang, Y. Xi, Y. Zou, P. Shan, C. Zhang, W. Drożdż, A. R. Stefankiewicz, P. Yuan, C. Yu, C. Liu, Highly Ordered Conductive Metal-Organic Frameworks with Chemically Confined Polyoxometalate Clusters: A Dual-Functional Electrocatalyst for Efficient H_2O_2 Synthesis and Biomass Valorization, Adv. Mater. 37 (2025) 2500399, https://doi.org/10.1002/adma.202500399.
[328] Z. Naghshbandi, A. Salimi, A. Feizabadi, Hierarchical assembled sulfur-doped MoFe polyoxometalate/ZIF-67 on Ni foam: A novel and efficient electrocatalyst for water splitting and urea oxidation, J. Electroanal. Chem. 999 (2025) 119580, https://doi.org/10.1016/j.jelechem.2025.119580.
[329] Y. Zhang, C. Li, L. Shu, Y.-L. Teng, B.-X. Dong, Research on the Construction of a Series of Transition Metal-Substituted Keggin-Type TMSPOMs@PCN-224 Composites through the Encapsulation Method and Their Electron Transfer Mechanism in CO_2RR, Inorg. Chem. 63 (2024) 11592–11603, https://doi.org/10.1021/acs.inorgchem.4c00840.
[330] M. Souto, K. Strutyński, M. Melle-Franco, J. Rocha, Electroactive Organic Building Blocks for the Chemical Design of Functional Porous Frameworks (MOFs and COFs) in Electronics, Chem. Eur. J. 26 (2020) 10912–10935, https://doi.org/10.1002/chem.202001211.
[331] Y. Jiang, J. Ren, Y. Yuan, B.E. Keshta, Y. Zhang, X. Guan, Y. He, D. Zhao, B. Chen, Covalent organic frameworks for gas storage and separation, Chem. Soc. Rev. 55 (2026) 4522–4584, https://doi.org/10.1039/D5CS01537E.
[332] Z. Wang, C. Yan, H. Peng, I. Shakir, G. Ma, Y. Xu, Covalent organic frameworks for metal–gas batteries: fundamentals and applications, Chem. Soc. Rev. 55 (2026) 2776–2830, https://doi.org/10.1039/D5CS00900F.
[333] S. Kong, X. Zhang, N. Xu, X. Wang, Recent advances in polyoxometalate–covalent organic framework composites: rational design, structural modulation, and application perspectives, Dalton Trans. (2026), https://doi.org/10.1039/D6DT00064A.
[334] Y.-L. Yang, Y.-R. Wang, L.-Z. Dong, Q. Li, L. Zhang, J. Zhou, S.-N. Sun, H.-M. Ding, Y. Chen, S.-L. Li, Y.-Q. Lan, A Honeycomb-Like Porous Crystalline Hetero-Electrocatalyst for Efficient Electrocatalytic CO_2 Reduction, Adv. Mater. 34 (2022) 2206706, https://doi.org/10.1002/adma.202206706.
[335] Z. Liang, G. Zhou, H. Tan, Y. Mou, J. Zhang, H. Guo, S. Yang, H. Lei, H. Zheng, W. Zhang, Constructing $Co_4(SO_4)_4$ clusters within metal–organic frameworks for efficient oxygen electrocatalysis, Adv. Mater. 36 (2024) 2408094, https://doi.org/10.1002/adma.202408094.
[336] R.S. Mane, S. Mane, V. Somkuwar, N.V. Thombre, A.V. Patwardhan, N. Jha, A novel hierarchically hybrid structure of MXene and bi-ligand ZIF-67 based trifunctional electrocatalyst for zinc-air battery and water splitting, Battery Energy 2 (2023) 20230019, https://doi.org/10.1002/bte2.20230019.
[337] Y. Duan, H. Liu, H. Zhang, S. Ke, S. Wang, M. Dou, F. Wang, Conductive bimetal organic framework nanorods decorated with highly dispersed Co_3O_4 nanoparticles as bi-functional electrocatalyst, Nanotechnology 33 (2022) 145601, https://doi.org/10.1088/1361-6528/ac3d66.
[338] Y. Lian, W. Yang, C. Zhang, H. Sun, Z. Deng, W. Xu, L. Song, Z. Ouyang, Z. Wang, J. Guo, Unpaired 3d electrons on atomically dispersed cobalt centres in coordination polymers regulate both oxygen reduction reaction (ORR) activity and selectivity for use in zinc–air batteries, Angew. Chem. Int. Ed. 59 (2020) 286–294, https://doi.org/10.1002/anie.201910879.
[339] W. Li, C. Wu, H. Ren, W. Fang, L. Zhao, K.N. Dinh, Hybrid Cobalt and Iron Based Metal Organic Framework Composites as Efficient Bifunctional Electrocatalysts towards Long-Lasting Flexible Zinc-Air Batteries, Batter. & Supercaps 3 (2020) 1321–1328, https://doi.org/10.1002/batt.202000163.
[340] H. Pourfarzad, M. Shabani-Nooshabadi, M.R. Ganjali, Novel bi-functional electrocatalysts based on the electrochemical synthesized bimetallicmetal organic frameworks: Towards high energy advanced reversible zinc–air batteries, J. Power Sources 451 (2020) 227768, https://doi.org/10.1016/j.jpowsour.2020.227768.

[341] N. Pan, H. Zhang, B. Yang, H. Qiu, L. Li, L. Song, M. Zhang, Conductive MOFs as bifunctional oxygen electrocatalysts for all-solid-state Zn–air batteries, Chem. Commun. 56 (2020) 13615–13618, https://doi.org/10.1039/D0CC05569G.
[342] M.-c Zhang, M.-y Liu, M.-x Yang, X.-x Liu, S.-y Shen, J.-s Wu, W.-b Pei, Copper-cobalt bimetallic conductive metal–organic frameworks as bifunctional oxygen electrocatalyst in alkaline and neutral media, J. Solid. State Chem. 325 (2023) 124133, https://doi.org/10.1016/j.jssc.2023.124133.
[343] F. Lan, G. Huang, Y. Cao, X. Zhang, R. Wang, J. Chen, Enhancing oxygen reduction reaction in microbial fuel cell by Cu-metal organic framework@ Fe-metal organic framework (Cu-MOF@Fe-MOF) as cathode catalyst, J. Environ. Chem. Eng. 13 (2025) 115448, https://doi.org/10.1016/j.jece.2025.115448.
[344] F. Zhao, L. Kang, S. Ding, J. Long, S. Wang, Multilevel Pore Structure and Heterointerface Regulation from an MOF-on-MOF Template to Achieve Ultralong Cyclic Zinc–Air Batteries, ACS Appl. Nano Mater. 9 (2026) 6788–6799, https://doi.org/10.1021/acsanm.6c00477.
[345] M. Wang, Y. Song, H. Diao, W. Sun, S. Dong, D. Yuan, MOFs meet COFs: Ultra-low Ru loaded oxygen reduction reaction electrocatalyst with biomimetic branch-leaf structure for rechargeable Zn-air batteries, J. Energy Storage 109 (2025) 115229, https://doi.org/10.1016/j.est.2024.115229.
[346] J. Zhang, G. Li, S. Zhang, J. Shao, X. Zhang, Y. Liu, P. Krivoshapkin, E. Krivoshapkina, S. Zhang, H. Chen, Facile modulation of hierarchical structures in biomass-derived carbon via metal–organic framework-mediated assembly for enhanced oxygen and carbon dioxide reduction reactions, Nano Res. 19 (2026) 94908149, https://doi.org/10.26599/nr.2026.94908356.
[347] C. Zhang, L. Yuan, C. Liu, Z. Li, Y. Zou, X. Zhang, Y. Zhang, Z. Zhang, G. Wei, C. Yu, Crystal engineering enables cobalt-based metal–organic frameworks as high-performance electrocatalysts for H_2O_2 production, J. Am. Chem. Soc. 145 (2023) 7791–7799, https://doi.org/10.1021/jacs.2c11446.
[348] A. Mijajlović, J. Milikić, A. Jovanović, M. Lisnichuk, M. Fabian, B. Šljukić, D. Stanković, La-MOF/MXene catalyst for efficient two-electron oxygen reduction to H_2O_2, J. Electroanal. Chem. 1011 (2026) 120105, https://doi.org/10.1016/j.jelechem.2026.120105.
[349] S.N. Cruz-Orellana, P. Acevedo-Peña, R. Borja-Urby, E. Reguera, Tailoring the Metal Composition in MOF-Based Electrocatalysts for Enhanced OER and ORR in Zinc–Air Batteries, J. Alloy. Compd. 1062 (2026) 187639, https://doi.org/10.1016/j.jallcom.2026.187639.
[350] X. Zhang, X. Fang, K. Zhu, W. Yuan, T. Jiang, H. Xue, J. Tian, Fe-doping induced electronic structure reconstruction in Ni-based metal-organic framework for improved energy-saving hydrogen production via urea degradation, J. Power Sources 520 (2022) 230882, https://doi.org/10.1016/j.jpowsour.2021.230882.
[351] N.Q. Tran, Q.M. Le, T.T.N. Tran, T.-K. Truong, J. Yu, L. Peng, T.A. Le, T.L. H. Doan, T.B. Phan, Boosting urea-assisted natural seawater electrolysis in 3D leaf-like metal–organic framework nanosheet arrays using metal node engineering, ACS Appl. Mater. Interfaces 16 (2024) 28625–28637, https://doi.org/10.1021/acsami.4c04342.
[352] H. Jiang, S. Bu, Q. Gao, J. Long, P. Wang, C.-S. Lee, W. Zhang, Ultrathin two-dimensional nickel-organic framework nanosheets for efficient electrocatalytic urea oxidation, Mater. Today Energy 27 (2022) 101024, https://doi.org/10.1016/j.mtener.2022.101024.
[353] X. Fu, B. Pu, L. Pan, R. Ming, Q. Lv, X. Chen, L. Tian, Composition regulation of Ni-BDC MOF architecture to enhance electrocatalytic urea oxidation in alkaline solution, Mater. Chem. Front. 8 (2024) 3272–3279, https://doi.org/10.1039/D4QM00550C.
[354] Y. Wang, C. Wang, H. Shang, M. Yuan, Z. Wu, J. Li, Y. Du, Self-driven Ru-modified NiFe MOF nanosheet as multifunctional electrocatalyst for boosting water and urea electrolysis, J. Colloid Interface Sci. 605 (2022) 779–789, https://doi.org/10.1016/j.jcis.2021.07.124.
[355] S. Zheng, Y. Zheng, H. Xue, H. Pang, Ultrathin nickel terephthalate nanosheet three-dimensional aggregates with disordered layers for highly efficient overall urea electrolysis, Chem. Eng. J. 395 (2020) 125166, https://doi.org/10.1016/j.cej.2020.125166.
[356] H. Xu, K. Ye, K. Zhu, J. Yin, J. Yan, G. Wang, D. Cao, Template-directed assembly of urchin-like CoS_x/Co-MOF as an efficient bifunctional electrocatalyst for overall water and urea electrolysis, Inorg. Chem. Front. 7 (2020) 2602–2610, https://doi.org/10.1039/D0QI00408A.
[357] T.T.N. Tran, J. Yu, N.D. Hai, L. Peng, T.A. Le, P.D.N. Tran, K.T.L. Trinh, T. Trần-Phú, N.Q. Tran, Suppression of passivation on $NiMoO_4$ microrod by ultrathin metal-organic-framework nanosheets in urea-assisted natural seawater splitting, J. Colloid Interface Sci. 702 (2025) 138946, https://doi.org/10.1016/j.jcis.2025.138946.
[358] J. Zhang, S. Huang, P. Ning, P. Xin, Z. Chen, Q. Wang, K. Uvdal, Z. Hu, Nested hollow architectures of nitrogen-doped carbon-decorated Fe, Co, Ni-based phosphides for boosting water and urea electrolysis, Nano Res. 15 (2022) 1916–1925, https://doi.org/10.1007/s12274-021-3810-4.
[359] J.-M. Huo, S.-N. Li, Z.-L. Ma, J. Meng, Q.-G. Zhai, Y. Wang, Interfacial engineering of the hetero-coordinated Ru–OM clusters in MOF/LDH structures for boosting urea-assisted water splitting, J. Solid. State Chem. 343 (2025) 125160, https://doi.org/10.1016/j.jssc.2024.125160.
[360] S. Li, Y. Zhang, X. Yu, Z. Wang, G. Zhang, Z. Zhao, Z. Yan, X. Xiao, One-step electrodeposition synthesis of amorphous NiCoFe $(OH)_x$/NF as an efficient catalyst for urea-assisted overall water splitting, Electrochim. Acta 463 (2023) 142803, https://doi.org/10.1016/j.electacta.2023.142803.
[361] H. Tang, Z. Sun, S. Fan, S. Feng, L. Li, L. Fang, C. Wang, Fe-Doped CoNi layered hydrogencarbonate hierarchical Nano-Array assisted growth of ZIF-67 as an efficient OER/UOR bifunctional catalyst reaction for Overall Urea-Water electrolysis, Chem. Eng. J. 491 (2024) 152023, https://doi.org/10.1016/j.cej.2024.152023.
[362] Z. Gao, Y. Wang, L. Xu, Q. Tao, X. Wang, Z. Zhou, Y. Luo, J. Yu, Y. Huang, Optimizing local charge distribution of metal nodes in bimetallic metal–organic frameworks for efficient urea oxidation reaction, Chem. Eng. J. 433 (2022) 133515, https://doi.org/10.1016/j.cej.2021.133515.
[363] A. Acharya, K. Mandal, N. Kumari, K. Chatterjee, Synergistic Inclusion of Reaction Activator and Reaction Accelerator to Ni-MOF Toward Extra-Ordinary Performance of Urea Oxidation Reaction, Small 21 (2025) 2407377, https://doi.org/10.1002/smll.202407377.
[364] R. Abazari, S. Sanati, P. Stelmachowski, Q. Wang, A. Krawczuk, J. Goscianska, M. Liu, Water-stable pillared three-dimensional Zn–V bimetal–organic framework for promoted electrocatalytic urea oxidation, Inorg. Chem. 63 (2024) 5642–5651, https://doi.org/10.1021/acs.inorgchem.4c00053.
[365] Z. Yan, Y. Zhou, M. Huang, TEA-Mediated deprotonation engineering of self-supported thiophene based Ni-MOF electrocatalysts for efficient alkaline oxygen evolution and urea oxidation reactions, Fuel 420 (2026) 138949, https://doi.org/10.1016/j.fuel.2026.138949.
[366] T.X. Nguyen, H.C. Chen, C.K. Peng, T.M. Zheng, T.Y.P. Nguyen, Y.R. Lin, Y.G. Lin, K.S. Chuang, Y.H. Su, H.Y. Huang, Ligand-Engineered MOF Catalyst Enabled Energy-Efficient Urea-Assisted Hydrogen Generation, Adv. Funct. Mater. (2026) e32036, https://doi.org/10.1002/adfm.202532036.
[367] D. Liu, X. Guo, T. Yang, A. Kong, D. Lv, Y. Yang, X. Cui, R. Liu, Self-Supported Asymmetric Ce— O— Ni Sites Reconstructed From Biscuit-Like MOFs for Efficient Urea Oxidation and Zn-Urea Battery Applications, Adv. Funct. Mater. 36 (2026) e17562, https://doi.org/10.1002/adfm.202517562.
[368] M. Bhosale, A.M. Teli, P.J. Morankar, R.U. Amate, A.A. Patil, C.-W. Jeon, Interfacial coupling-driven catalytic enhancement in self-supported NiMnCr LDH coupled with bimetallic NiMn MOF nanoarchitectures for energy-efficient overall water splitting and urea oxidation, Int. J. Hydrog. Energy 229 (2026) 154735, https://doi.org/10.1016/j.ijhydene.2026.154735.
[369] S. Maji, D. Kundu, S. Sarkar, P. Ghorai, S.K. Tudu, N.C. Murmu, P. Banerjee, In-Situ Grown Mixed-Linker Based Redox-Active Cd (II)-Metal Organic Framework on Nickel Foam: A Self-Supported Trifunctional Electrocatalyst for Energy-Efficient Urea-Assisted Overall Water Splitting, ChemPlusChem 91 (2026) e202500717, https://doi.org/10.1002/cplu.202500717.
[370] Y. Wang, M. Wang, Z. Zhang, Q. Wang, Z. Jiang, M. Lucero, X. Zhang, X. Li, M. Gu, Z. Feng, Y. Liang, Phthalocyanine Precursors To Construct Atomically Dispersed Iron Electrocatalysts, ACS Catal. 9 (2019) 6252–6261, https://doi.org/10.1021/acscatal.9b01617.
[371] Z. Xin, J. Liu, X. Wang, K. Shen, Z. Yuan, Y. Chen, Y.-Q. Lan, Implanting polypyrrole in metal-porphyrin MOFs: enhanced electrocatalytic performance for CO_2RR, ACS Appl. Mater. Interfaces 13 (2021) 54959–54966, https://doi.org/10.1021/acsami.1c15187.
[372] M. Li, M. Tang, P. Xue, H. Dai, T. He, Z. Wang, A binder-free, well-integrated metal–organic frameworks@ polypyrrole nanofilm electrocatalyst for highly efficient and selective reduction of carbon dioxide, Mater. Today Energy 30 (2022) 101140, https://doi.org/10.1016/j.mtener.2022.101140.
[373] L.-Z. Dong, Y.-F. Lu, R. Wang, J. Zhou, Y. Zhang, L. Zhang, J. Liu, S.-L. Li, Y.-Q. Lan, Porous copper cluster-based MOF with strong cuprophilic interactions for highly selective electrocatalytic reduction of CO_2 to CH_4, Nano Res. 15 (2022) 10185–10193, https://doi.org/10.1007/s12274-022-4681-z.
[374] A.P. Periasamy, R. Ravindranath, S.M.S. Kumar, W.-P. Wu, T.-R. Jian, H.-T. Chang, Facet-and structure-dependent catalytic activity of cuprous oxide/polypyrrole particles towards the efficient reduction of carbon dioxide to methanol, Nanoscale 10 (2018) 11869–11880, https://doi.org/10.1039/C8NR02117A.
[375] B. Shao, D. Huang, R.K. Huang, X.L. He, Y. Luo, Y.L. Xiang, Lb Jiang, M. Dong, S. Li, Z. Zhang, Metal-Organic Framework Supported Low-Nuclearity Cluster Catalysts for Highly Selective Carbon Dioxide Electroreduction to Ethanol, Angew. Chem. 136 (2024) e202409270, https://doi.org/10.1002/anie.202409270.
[376] Z.-H. Zhao, J.-R. Huang, P.-Q. Liao, X.-M. Chen, Highly efficient electroreduction of CO_2 to ethanol via asymmetric C-C coupling by a metal-organic framework with heterodimetal dual sites, J. Am. Chem. Soc. 145 (2023) 26783–26790, https://doi.org/10.1021/jacs.3c08974.
[377] K. Zhao, Y. Liu, X. Quan, S. Chen, H. Yu, CO_2 electroreduction at low overpotential on oxide-derived Cu/carbons fabricated from metal organic framework, ACS Appl. Mater. Interfaces 9 (2017) 5302–5311, https://doi.org/10.1021/acsami.6b15402.
[378] M. Perfecto-Irigaray, J. Albo, G. Beobide, O. Castillo, A. Irabien, S. Pérez-Yáñez, Synthesis of heterometallic metal-organic frameworks and their performance as electrocatalyst for CO_2 reduction, RSC Adv. 8 (2018) 21092–21099, https://doi.org/10.1039/C8RA02676A.
[379] S.-M. Hwang, S.Y. Choi, M.H. Youn, W. Lee, K.T. Park, K. Gothandapani, A. N. Grace, S.K. Jeong, Investigation on electroreduction of CO_2 to formic acid using $Cu_3(BTC)_2$ metal-organic framework (Cu-MOF) and graphene oxide, ACS Omega 5 (2020) 23919–23930, https://doi.org/10.1021/acsomega.0c03170.
[380] M.-J. Liu, S.-M. Cao, B.-Q. Feng, B.-X. Dong, Y.-X. Ding, Q.-H. Zheng, Y.-L. Teng, Z.-W. Li, W.-L. Liu, L.-G. Feng, Revealing the structure-activity relationship of two Cu-porphyrin-based metal-organic frameworks for the electrochemical CO_2-to-HCOOH transformation, Dalton Trans. 49 (2020) 14995–15001, https://doi.org/10.1039/D0DT02683B.
[381] W.-W. Yuan, J.-X. Wu, X.-D. Zhang, S.-Z. Hou, M. Xu, Z.-Y. Gu, situ transformation of bismuth metal-organic frameworks for efficient selective electroreduction of

CO_2 to formate, J. Mater. Chem. A. 8 (2020) 24486–24492, https://doi.org/10.1039/D0TA08092F.
[382] L. Liu, K. Yao, J. Fu, Y. Huang, N. Li, H. Liang, Bismuth metal-organic framework for electroreduction of carbon dioxide, Colloids Surf. A Physicochem. Eng. Asp. 633 (2022) 127840, https://doi.org/10.1016/j.colsurfa.2021.127840.
[383] Z.W. Yang, J.M. Chen, Z.L. Liang, W.J. Xie, B. Zhao, L.N. He, Anodic Product-Derived Bi-MOF as Pre-catalyst for Cathodic CO_2 Reduction: A Novel Strategy for Paired Electrolysis, ChemCatChem 15 (2023) e202201321, https://doi.org/10.1002/cctc.202201321.
[384] J.-X. Wu, S.-Z. Hou, X.-D. Zhang, M. Xu, H.-F. Yang, P.-S. Cao, Z.-Y. Gu, Cathodized copper porphyrin metal-organic framework nanosheets for selective formate and acetate production from CO_2 electroreduction, Chem. Sci. 10 (2019) 2199–2205, https://doi.org/10.1039/C8SC04344B.
[385] Y. Deng, S. Wang, Y. Huang, X. Li, Structural reconstruction of Sn-based metal–organic frameworks for efficient electrochemical CO_2 reduction to formate, Chin. J. Chem. Eng. 43 (2022) 353–359, https://doi.org/10.1016/j.cjche.2022.03.006.
[386] M. Lee, A. De Riccardis, R.V. Kazantsev, J.K. Cooper, A.K. Buckley, P. W. Burroughs, D.M. Larson, G. Mele, F.M. Toma, Aluminum metal-organic framework triggers carbon dioxide reduction activity, ACS Appl. Energy Mater. 3 (2020) 1286–1291, https://doi.org/10.1021/acsaem.9b02210.
[387] J. Bok, S.Y. Lee, B.-H. Lee, C. Kim, D.L.T. Nguyen, J.W. Kim, E. Jung, C.W. Lee, Y. Jung, H.S. Lee, Designing atomically dispersed Au on tensile-strained Pd for efficient CO_2 electroreduction to formate, J. Am. Chem. Soc. 143 (2021) 5386–5395, https://doi.org/10.1021/jacs.0c12696.
[388] D. Wang, S. Dong, L. Wen, W. Yu, Z. He, Q. Guo, X. Lu, L. Wang, S. Song, J. Ma, Highly selective electrocatalytic reduction of CO_2 to HCOOH over an in situ derived hydrocerussite thin film on a Pb substrate, Chemosphere 291 (2022) 132889, https://doi.org/10.1016/j.chemosphere.2021.132889.
[389] J.N. Yue, Y. Wang, J. Meng, L.Y. Shao, T.S. He, B.L. Sun, L.X. Xie, Q.G. Zhai, Microfluidic printing-induced dynamic splitting of conductive MOF to expose high-density active sites for boosted CO_2 electroreduction, Small 22 (2026) e00018, https://doi.org/10.1002/smll.202600018.
[390] J. Jang, E.P. Delmo, Y. Liu, G. Liu, Y. Wang, T. Li, M. Shao, Effective modulation of multifunctional Cu-metal organic frameworks coordination structure for a selective CH_4 production via CO_2RR, Appl. Catal. B Environ. Energy 393 (2026) 126751, https://doi.org/10.1016/j.apcatb.2026.126751.
[391] Z. Xin, P. Liu, X. Pan, S. Zheng, L. Deng, K. Shen, S. Ding, R. Chen, Nanocavity-confined Cu_2O in porphyrin-based MOF for steering CO_2 electroreduction toward hydrocarbons, J. Mater. Chem. C. (2026), https://doi.org/10.1039/d6tc00305b.
[392] S. Kong, C. Qiu, C. Zhang, H. Ma, C. Wei, F. Yu, G. Sun, C. Chi, Y. Hu, B.S. Yeo, Multi-timescale transformations in MOF-modified copper oxide during electrochemical CO_2 reduction, Nano Energy 152 (2026) 111884, https://doi.org/10.1016/j.nanoen.2026.111884.

Sheraz Muhammad is a Ph.D. student at Guangxi Normal University, China, under the supervision of Prof. Xiulin Yang. His doctoral research focuses on developing metal–organic frameworks (MOFs) as efficient electrocatalysts to enhance performance and stability in energy conversion applications. He earned his Master's degree from Abdul Wali Khan University Mardan, Pakistan (under the supervision of Dr. Nida Ambreen), where he specialized in catalysis. Muhammad Sheraz has authored multiple publications, including research and review articles, in high-impact and reputable journals, contributing to advancements in electrocatalysis and materials science.

Hao Sun, received his bachelor degree in Biopharmaceutical Engineering in 2020, Henan University, China, received his PhD degree in Molecular Biology at the Autonomous University of Madrid, Spain, in early 2025, during which time he completed his PhD thesis at the Spanish National Research Council, and then from April 2025 to now doing a post-doctoral researcher at the University College of London, UK, in the area of nano-biomedicine and catalysis.

Sana Zahoor is a Ph.D. student at Guangxi Normal University, China. She earned her Master's degree from Abdul Wali Khan University Mardan, Pakistan, where she specialized in catalysis and biotechnology, and has authored multiple research and review articles in high-impact and reputable journals.

Sumayya Khan is a Ph.D. student at Guangxi Normal University, China, under the supervision of Prof. Xiulin Yang. Her doctoral research focuses on developing efficient electrocatalysts to enhance performance and stability in energy conversion applications. She earned her Master's degree from Abdul Wali Khan University Mardan, Pakistan, where she specialized in catalysis. Sumayya Khan has authored multiple publications in high-impact and reputable journals, contributing to advancements in electrocatalysis and materials science.

Rahmat Ullah completed his Masters in Physical Chemistry from the University of the Punjab. He is currently pursuing his doctoral research at Guangxi Normal University. His research centers on the rational design of MOF-derived electrocatalysts and advanced composite materials for sustainable energy conversion. He aims to develop efficient and environmentally friendly materials for advanced energy technologies.

Biao Fu is a Master's student at Guangxi Normal University, China, under the supervision of Prof. Xiulin Yang. His research focuses on the oxygen reduction reaction (ORR), and he has published excellent articles in high-impact journals.

Sana Ullah is a Ph.D. student at the Institute for Advanced Study, Shenzhen University, China. He earned his Master's degree from Abdul Wali Khan University Mardan, Pakistan, where he specialized in catalysis. Sana Ullah has authored multiple research articles in high-impact and reputable journals, contributing to advancements in materials science.

Dr. Tayirjan Taylor Isimjan is a Staff Scientist at the Saudi Arabia Basic Industries Corporation (SABIC), based at the King Abdullah University of Science and Technology (KAUST). He co-supervises Ph.D. students through international collaborations, including partnerships with Guangxi Normal University. His research specializes in advanced materials for clean energy and catalysis—specifically high-entropy alloys, metal borides, and metal–organic frameworks (MOFs)—with applications in water splitting, fuel cells, and electrochemical CO_2 reduction. In collaboration with Prof. Xiulin Yang's group, he has co-authored numerous high-impact publications, maintaining an h-index of 40.

Prof. Shohreh Azizi is a Senior Researcher at the UNESCO–UNISA Africa Chair in Nanoscience and Nanotechnology, University of South Africa, and an NRF C2-rated researcher. Her work focuses on biological wastewater treatment and nanotechnology-based solutions for industrial and municipal wastewater, including acid mine-drainage. She has a strong record of publications, research funding, and international collaborations, contributing to sustainable environmental technologies.

Prof. Xiulin Yang is a Professor and Vice Dean at the School of Chemistry and Pharmaceutical Sciences, Guangxi Normal University (GXNU), China. He earned his Ph.D. in Physical Chemistry from the Chinese Academy of Sciences in 2013 and conducted postdoctoral research at KAUST (2013–2018). Since joining GXNU, his work focuses on advanced nanomaterials for clean energy applications, including water splitting, fuel cells, and CO_2 electroreduction. He has published over 150 SCI papers (h-index of 48), held multiple patents, and served on several international journal editorial boards.